INVESTIGATION OF G-QUADRUPLEX FORMING MOTIFS AS POTENTIAL THERAPEUTIC TARGETS IN HUMAN-INFECTING PATHOGENS

Ph.D. Thesis

By

AAKRITI SINGH

MEHTA FAMILY SCHOOL OF BIOSCIENCES AND BIOMEDICAL ENGINEERING

INDIAN INSTITUTE OF TECHNOLOGY INDORE

AUGUST 2025

INVESTIGATION OF G-QUADRUPLEX FORMING MOTIFS AS POTENTIAL THERAPEUTIC TARGETS IN HUMAN-INFECTING PATHOGENS

A THESIS

Submitted in partial fulfillment of the
requirements for the award of the degree
of
DOCTOR OF PHILOSOPHY

by

AAKRITI SINGH

MEHTA FAMILY SCHOOL OF BIOSCIENCES AND BIOMEDICAL ENGINEERING

INDIAN INSTITUTE OF TECHNOLOGY INDORE

AUGUST 2025

INDIAN INSTITUTE OF TECHNOLOGY INDORE

I hereby certify that the work which is being presented in the thesis entitled **INVESTIGATION OF G-QUADRUPLEX FORMING MOTIFS AS POTENTIAL THERAPEUTIC TARGETS IN HUMAN-INFECTING PATHOGENS** in the partial fulfillment of the requirements for the award of the degree of **DOCTOR OF PHILOSOPHY** and submitted in the **MEHTA FAMILY SCHOOL OF BIOSCIENCES AND BIOMEDICAL ENGINEERING, Indian Institute of Technology Indore**, is an authentic record of my own work carried out during the time period from August 2021 to August 2025 under the supervision of Prof. Amit Kumar, Professor, Mehta Family School of Biosciences and Biomedical Engineering.

The matter presented in this thesis has not been submitted by me for the award of any other degree of this or any other institute.

AakritiSingh 12.12.25.
Signature of the student with date

(AAKRITI SINGH)

This is to certify that the above statement made by the candidate is correct to the best of my knowledge.

Signature of Thesis Supervisor with date 12.12.25

(PROF. AMIT KUMAR)

AAKRITI SINGH has successfully given her Ph.D. Oral Examination held on **12th December 2025**.

Signature of Thesis Supervisor with date 12.12.25

(PROF. AMIT KUMAR)

ACKNOWLEDGEMENT

"It always seems impossible until it's done."

— Nelson Mandela

The last four years have been a journey filled with numerous challenges, learning, and growth, made possible by the support of many people to whom I am deeply indebted.

I am profoundly grateful to *God* for granting me the health, strength, and perseverance required to complete this work. This endeavor would not have been possible without the support, endless love, care, and motivation of my family, including *my mother, father, and my younger brother*. I express my appreciation for their presence and utmost patience through the highs and lows of this journey. They believed in me even when I didn't.

I owe my deepest gratitude to my mentor, *Prof. Amit Kumar*, for providing me with the opportunity to work under his guidance and for his patience and encouragement throughout my doctoral journey. His constant motivation, insightful suggestions, and unwavering belief in my abilities have always been a source of inspiration. Over the past four years, working under his mentorship, I not only mastered experimental techniques and writing skills but also inculcated the values of hard work, professional integrity, and core life lessons, which I will carry with me throughout my life. Even through our fair share of ups and downs, he never failed to stand by my side as a mentor, always encouraging me to give my best.

I am also grateful to my PSPC members, *Dr. Abhijeet Joshi* and *Prof. Sharad Gupta* for their consistent evaluation of my research work. I am especially thankful to *Sharad Sir* for his kind and motivating words and the thought-provoking questions that inspired me to explore my research more deeply. I extend my sincere thanks to the *Head and DPGC*, *Mehta Family School of Biosciences and Biomedical Engineering* for their constant support in various capacities, and to other faculty members for fostering an encouraging and healthy environment.

I would be remiss in not mentioning my collaborators, *Dr. Tarun Kumar Sharma* (NIPER Mohali) and *Prof. Manjula Kalia* (Regional Centre for Biotechnology), for their contributions to the completion of my research projects by carrying out crucial experimental studies. I'd also like to acknowledge *Prof. Suhas Joshi*, Director, and the entire IIT Indore community for providing the platform, infrastructure, and facilities required to complete my research work.

This journey would have been incomplete without the dedicated support of IIT Indore staff members, to whom I express my deepest appreciation: *Mr. Arif Patel*, *Mr. Gaurav Singh,* and *Mr. Amit Kumar Mishra (MFS-BSBE office); Mr. Kinny Pandey* and *Dr. Ravinder Kumar* (SIC facility); *Mr. Tapesh Parihar* and *Mr. Rahul Shrivas* (Academics section); *Mr. Roshan Bhatia*, *Mrs. Neha Jain*, and *Ms. Divya Bangar* (Finance section).

I would like to acknowledge my colleagues for their cooperation, assistance during experiments, and for creating a fun, friendly and collaborative work environment. In particular, I am grateful to my seniors, *Mrs. Neha Jain* and *Mr. Uma Shankar,* who mentored me during the initial months of my doctoral work, guiding me in experimental techniques. They not only made the lab a positive and welcoming place to work but also outside the lab, created a cherishing atmosphere and made mundane festival days exciting during COVID times. My heartfelt appreciation goes out to my dear friends and colleagues, *Mr. Ashmad Kumar Nayak* and *Ms. Priya Gupta* for their unwavering love and support throughout these years, both professionally and personally. Their presence made the journey far more memorable, through shared breakfasts, lunches, tea and coffee breaks, and dinners; celebrating festivals together; countless hangouts; and collaboratively planning experiments and interpreting data, each moment has been deeply cherished. I would also like to acknowledge my colleagues, *Mr. Krishna Singh*, *Mr. Aritra Chakraborty*, *Ms. Pronamika Chetia*, *Ms. Sakshi Shukla, Ms. Mansee Patel, Ms. Aditi Kumari Pramod,* and *MSc students*. Together, we made a great team, and it was amazing working alongside all of them. I am also profoundly grateful to my friend *Ms. Kritika Malik* for her care, emotional support, and constant motivation. The countless cups of tea and coffee, along with mandatory snacks, the long

scientific and life-lesson conversations, late-night lab stays during experiments, and numerous other memories shared with her will always remain close to my heart. I would also like to extend my thanks and love to *Ms. Gunjan Nagpure* for instilling warmth and positivity in me during the most difficult days. I thank my friends *Ms. Kavita Singh* and *Mr. Saurabh Yadav* for offering their time, comfort, and support during my lowest days. I would also like to appreciate *Dr. Sanchit Gupta*, for always boosting me with positivity and happiness, pushing me to do better each day, helping me with the silliest of things, and never failing to offer his love, warmth, and support.

I would also like to extend my appreciation to *Mr. Sibasish Barik* for being a part of my doctoral journey.

Beyond academia, I am extremely thankful to my friends *Mrs. Ragini Singh and Ms. Shreya Rai*, for their utmost motivation and encouragement for the entire journey. Furthermore, I would like to extend my gratitude to my flatmates, *Neha Di, Nilima Di, Ekta Di, Deepshikha Di,* and *Tamanna Singh,* who made my stay in DA worthwhile and always ensured that I smiled on the gloomiest of days.

Lastly, I would like to thank the Department of Biotechnology (DBT), New Delhi, India, for providing me with my JRF and SRF fellowships, which enabled me to conduct my thesis work efficiently.

Dedicated

To

My Parents

&

My brother

SYNOPSIS

Introduction

G-quadruplex structures, often abbreviated as G4s, are distinctive non-canonical secondary structures. These structures form in guanine-rich nucleic acid sequences, including both DNA and RNA. G-tetrads, which are the building blocks of G4s, arise through the association of four guanines in a cyclic Hoogsteen-hydrogen bond base pairing. At least two or more planar G-tetrads are stacked on top of each other to form G4s and stabilized by monovalent cations such as potassium or sodium[1]. G4s display topological polymorphism, based on the involvement of a single strand (intramolecular) or multiple strands (intramolecular)[2]. G4s also exhibit varied topologies depending on the polarity of the strands participating in the structure formation: parallel, antiparallel, or hybrid. The distribution of G4s is non-random in the genome[3]. These structures are more prevalent in telomeres, gene promoters, replication origins, 5' and 3' UTRs, and introns, and therefore play significant roles in gene regulation.

Based on their distribution and unique structural and functional features, G4s have garnered attention as attractive therapeutic targets in diseases such as cancer and neurological disorders. Apart from their functional relevance in the eukaryotic genome, G4s also serve as critical regulatory elements in the prokaryotic genome that influence pathogenicity, stress adaptation, and gene expression, making them important targets for therapeutic intervention[4].

G4 structures in bacterial genomes predominantly regulate cellular mechanisms such as transcription and translation. There exist several reports highlighting the functional significance of G4 structures in pathogenic bacteria, including their role in antigenic variation in *Neisseria gonorrhoeae*, and secretion systems in *Mycobacterium tuberculosis*[5,6]. Promoter regions in *Klebsiella pneumoniae* have also been reported to contain G-quadruplex motifs influencing gene regulation, while the G4s present in *Neisseria meningitidis* and *Vibrio cholerae* are associated with pathogenicity[6,7].

An equally compelling dimension is the occurrence of G-quadruplexes within viral genomes, such as flaviviruses, filoviruses, and coronaviruses. For example, in *Zika* virus, conserved RNA G4s span structural and non-structural genes, suggesting functional relevance within the Flaviviridae family[2]. Several ligands, such as Phen-DC3, BRACO-19, TMPyP4, and PDS, have shown potential to stabilize bacterial and viral GQs[9].

Another key element in G4 biology is G4-binding proteins (also called G-quadruplex binding proteins or G4BPs). G4BPs are a diverse group of proteins that specifically recognize and interact with G-quadruplex (G4) structures[10]. The interaction of these proteins with G4 structures regulates the stability of G4 structures, and is central in governing fundamental cellular mechanisms. An in-depth study is required to clarify the relationship between G4s, their locations in the genome, and their protein-binding features. Given the crucial role of G4 structures in regulation of the survival and virulence of clinically important pathogens, comprehensive structural and functional studies of these structures are necessary. Their significance remains underexplored in microbes, in comparison to eukaryotes. This highlights the need for alternative therapeutic approaches to tackle infections caused by such pathogens, against which where current antimicrobials stand ineffective. Hence, the present study addresses the requirement for the identification of bio-molecular targets and supports the development of potent antimicrobials as an alternative strategy to combat antimicrobial resistance.

Scope and Objective

This study concerns the identification and characterization of conserved G4 motifs in pathogenic microbes (*Acinetobacter baumannii* and Japanese Encephalitis Virus) through the application of in silico, biophysical, and cell-based studies. It also investigates the interaction between G4-binding proteins and G4 structures, thereby contributing to the recognition of these motifs as regulatory potential antimicrobial therapeutic targets.

The study was accomplished by addressing the following objectives:

1. Characterization of G-quadruplex structures in genes involved in survival and pathogenesis of *Acinetobacter baumannii*

2. G-quadruplex structures within the hfq gene regulate RNA–protein interactions in *Acinetobacter baumannii*
3. Role of RNA G-quadruplexes in Japanese Encephalitis Virus genome and their recognition as prospective antiviral targets

Chapter contributions

Chapter 1 provides an overview of the subject area, a thorough literature review, and discusses the scope of the thesis.

Chapter 2 discusses the material and methodology employed. Herein, we have explained the concepts involved in various biophysical methods used for characterization, validation, and function of G4s, such as 1D ^{1}H NMR spectroscopy, Circular Dichroism (CD) spectroscopy, Electrophoretic Mobility Shift Assay (EMSA), Fluorescence Titration Assay, and Isothermal Titration Calorimetry (ITC). Cell-based assays, including quantitative-RT-PCR, mTFP reporter-based assay, and Biofilm formation assay, etc., are also described.

Chapter 3 elucidates the genome mining of completely sequenced strains of *Acinetobacter baumannii* to identify conserved putative G-quadruplex motifs using in-house bioinformatic tools and G4Hunter analysis. Initially, in silico analysis revealed the presence of ~49 GQ motifs in the *A. baumannii* reference genome. On functional annotation and conservation analysis, eight highly conserved motifs (AB_PGQs) located in genes linked to bacterial survival, virulence, and biofilm formation were identified. These motifs were characterized in vitro by 1D ^{1}H NMR, CD spectroscopy, and thermal melting assays, confirming stable G4 formation. Interaction studies with the G4-binding ligand BRACO-19 (via fluorescence titration assay, CD spectroscopy and CD Melting, ITC, and NMR broadening) revealed high affinity and significant structural stabilization. Functionally, BRACO-19 exposure reduced mTFP-reporter gene expression, downregulated expression of G4-harboring genes, inhibited bacterial growth, and reduced biofilm thickness, collectively demonstrating that targeting G-quadruplex structures could be an effective strategy to combat multidrug-resistant *A. baumannii*. This is the first study to offer a comprehensive insight into evolutionarily conserved G-quadruplex motifs in *A. baumannii*, proposing a new avenue for developing therapeutics against this drug-resistant pathogen.

Chapter 4 describes the existence, structural characterization, and regulatory potential of two-tetrad G-quadruplex motifs within the hfq gene of *Acinetobacter baumannii*. The *hfq* gene contains seven tandem repeats, as identified through in silico analysis; consequently, a full-length putative G4-forming sequence spanning the entire repeat region and a truncated sequence covering a single repeat were selected for analysis in both RNA and DNA sequences. Through biophysical experiments (NMR, CD spectroscopy, EMSA, fluorescence titration assay, and ITC), both full-length and truncated RNA/DNA sequences displayed characteristic G4 structural features, showing interaction and affinity for the ligand BRACO-19. Interaction studies through CD and Fluorescence titration spectroscopy, and EMSA demonstrated the recognition of these G4 motifs by the Hfq protein, particularly its glycine-rich C-terminal domain, with preferential interaction with hfq RNA G4s. Quantitative RT-PCR assay confirmed the stabilization of these G4 structures downregulates the expression of hfq transcripts. In summary, this work highlighted a RNA-based regulatory mechanism with potential as an antimicrobial target against this drug-resistant pathogen.

Chapter 5 describes the systematic identification of RNA G-quadruplex motifs within the Japanese Encephalitis Virus (JEV) genome using bioinformatic prediction, which were highly conserved across all completely sequenced JEV isolates. Upon gene annotation, eight conserved motifs were identified, located in key structural and non-structural genes, which were structurally confirmed to adopt stable parallel GQ topologies through NMR and CD spectroscopy. The interaction and stabilizing effects of the GQ-binding ligand BRACO-19 were demonstrated by ThT displacement assays, gel retardation, CD Spectroscopy, CD Melting, Fluorescence titration assay, ITC, and NMR line-broadening experiments exhibiting high-affinity binding. Functional studies, including mTFP reporter assay and cell-based antiviral studies, revealed ligand-mediated stabilization of JEV-GQs resulted in downregulation of viral gene expression, replication inhibition, reduced infectious titers and protein expression, highlighting viral RNA G-quadruplexes as promising alternative antiviral targets.

Chapter 6 focuses on the conclusion and future prospects of this thesis work. It highlights on the in-depth structural and functional studies of conserved G-quadruplex motifs across diverse multi-drug resistant (MDR) bacterial and viral pathogens to better understand their role in the regulation of essential genes. Further investigation of G4-protein interactions, in vivo analysis of GQ-targeting ligands, and the development of ligand derivatives with improved specificity and targeted cellular delivery are needed to translate these fundamental insights into clinically feasible antimicrobial therapies. In particular, the evaluation of these alternative therapeutic strategies as a combinatorial treatment may provide a new horizon in the management of emerging and re-emerging infectious diseases.

References

(1) Rhodes, D.; Lipps, H. J. G-Quadruplexes and Their Regulatory Roles in Biology. *Nucleic Acids Res* **2015**, *43* (18), 8627–8637. https://doi.org/10.1093/nar/gkv862.

(2) Burge, S.; Parkinson, G. N.; Hazel, P.; Todd, A. K.; Neidle, S. Quadruplex DNA: Sequence, Topology and Structure. *Nucleic Acids Res* **2006**, *34* (19), 5402–5415. https://doi.org/10.1093/nar/gkl655.

(3) Kledus, F.; Dobrovolná, M.; Mergny, J.-L.; Brázda, V. Asymmetric Distribution of G-Quadruplex Forming Sequences in Genomes of Retroviruses. *Sci Rep* **2025**, *15* (1), 76. https://doi.org/10.1038/s41598-024-82613-2.

(4) Sato, K.; Knipscheer, P. G-Quadruplex Resolution: From Molecular Mechanisms to Physiological Relevance. *DNA repair* **2023**, *130*, 103552. https://doi.org/10.1016/j.dnarep.2023.103552.

(5) Zhang, Z.; He, X.; Yuan, G. Formation and Recognition of G-Quadruplex Relevant for Pilin Antigenic Variation in Neisseria Gonorrhoeae. *Can. J. Chem.* **2012**, *90* (1), 34–38. https://doi.org/10.1139/v11-092.

(6) Mishra, S. K.; Shankar, U.; Jain, N.; Sikri, K.; Tyagi, J. S.; Sharma, T. K.; Mergny, J.-L.; Kumar, A. Characterization of G-Quadruplex Motifs in espB, espK, and Cyp51 Genes of Mycobacterium Tuberculosis as Potential Drug Targets. *Molecular Therapy Nucleic Acids* **2019**, *16*, 698–706. https://doi.org/10.1016/j.omtn.2019.04.022.

(7) Jain, N.; Shankar, U.; Kumar, A. Conserved G-Quadruplex Motifs Regulate Gene Expression in Neisseria Meningitidis. *ACS Infect Dis* **2022**, *8* (4), 728–743. https://doi.org/10.1021/acsinfecdis.1c00383.

(8) Shankar, U.; Jain, N.; Majee, P.; Kodgire, P.; Sharma, T. K.; Kumar, A. Exploring Computational and Biophysical Tools to Study the Presence of G-Quadruplex Structures: A Promising Therapeutic Solution for Drug-

Resistant Vibrio Cholerae. *Front Genet* **2020**, *11*, 935. https://doi.org/10.3389/fgene.2020.00935.

(9) Majee, P.; Pattnaik, A.; Sahoo, B. R.; Shankar, U.; Pattnaik, A. K.; Kumar, A.; Nayak, D. Inhibition of Zika Virus Replication by G-Quadruplex-Binding Ligands. *Molecular Therapy - Nucleic Acids* **2021**, *23*, 691–701. https://doi.org/10.1016/j.omtn.2020.12.030.

(10) Santos, T.; Salgado, G. F.; Cabrita, E. J.; Cruz, C. G-Quadruplexes and Their Ligands: Biophysical Methods to Unravel G-Quadruplex/Ligand Interactions. *Pharmaceuticals* **2021**, *14* (8), 769. https://doi.org/10.3390/ph14080769.

(11) Shu, H.; Zhang, R.; Xiao, K.; Yang, J.; Sun, X. G-Quadruplex-Binding Proteins: Promising Targets for Drug Design. *Biomolecules* **2022**, *12* (5), 648. https://doi.org/10.3390/biom12050648.

LIST OF PUBLICATIONS

Publications from thesis

Published

1. **Singh A**, Jain N, Shankar U, Sharma TK, Kumar A. Characterization of G-quadruplex structures in genes involved in survival and pathogenesis of *Acinetobacter baumannii* as a potential drug target. Int J Biol Macromol. 2024 Jun;269(Pt 1):131806. doi: 10.1016/j.ijbiomac.2024.131806. Epub 2024 Apr 25. PMID: 38670179.

2. **Singh A**, Majee P, Mishra L, Prajapat SK, Sharma TK, Kalia M, Kumar A. Role of RNA G-Quadruplexes in the Japanese Encephalitis Virus Genome and Their Recognition as Prospective Antiviral Targets. ACS Infect Dis. 2025 Mar 14;11(3):558-572. doi: 10.1021/acsinfecdis.4c00507. Epub 2024 Oct 22. PMID: 39436355.

Submitted

3. **Singh A**, Kumar A. G-Quadruplex structures within the hfq gene regulate RNA–Protein interactions in *Acinetobacter baumannii*. *Journal of Structural Biology* (Submission ID: JSB-25-154)

Publications apart from thesis

1. Jain N, Shankar U, **Singh A**, Sharma TK, Kumar A. G-quadruplex motifs in Neisseria gonorrhoeae as anti-gonococcal targets. Appl Microbiol Biotechnol. 2023 Aug;107(16):5145-5159. doi: 10.1007/s00253-023-12646-6. Epub 2023 Jul 6. PMID: 37410137.

2. Gupta A, Mathew R, Anand A, Bhardwaj T, **Singh A**, Singh K, Kumar A, Mishra PR, Sharma TK. A DNA aptamer-based assay for the detection of soluble ST2, a prognostic biomarker for monitoring heart failure. Int J Biol Macromol. 2024 Jan;256(Pt 1):128295. doi: 10.1016/j.ijbiomac.2023.128295. Epub 2023 Nov 21. PMID: 37992929.

3. Choudhury SD, Ghosh S, Kumar P, Bhardwaj A, Singh K, **Singh A**, Kumar A, Basu B, Giri R, Choudhury D. Attenuation of c-Myc expression in breast cancer by hesperidin-mediated stabilization of its promoter proximal G quadruplex region. Int J Biol Macromol. 2025 Apr 11;309(Pt 4):143000. doi: 10.1016/j.ijbiomac.2025.143000. Epub 2025 April 8. PMID: 40222510.

TABLE OF CONTENTS

LIST OF FIGURES

LIST OF TABLES

NOMENCLATURE

λ	Wavelength
ε	Extinction coefficient
π	Pi
Å	Angstrom
°C	Degree centigrade
°	Degree
Δ	Delta
µL	Microliter
mL	Milliliter
L	Liter
nm	Nanometer
LL	Loop length
nM	Nanomolar
µM	Micromolar
mM	Millimolar
M	Molar
Sec	Seconds
mins	Minutes
h	Hour

ACRONYMS

A	Adenine
AB_PGQ	*Acinetobacter baumannii* PGQs
C	Cytosine
CD	Circular dichroism
cDNA	Complimentary DNA
CLSI	Clinical & Laboratory Standards Institute
DNA	Deoxyribonucleic acid
D:N	Drug:nucleotide (DNA/RNA)
DMEM	Dulbecco's Modified Eagle's medium
DMSO	Dimethyl sulfoxide
EDTA	Ethylenediaminetetraacetic acid
EMSA	Electrophoretic mobility shift assay
EBV	Epstein-Barr Virus
FBS	Fetal bovine serum
G	Guanine
G4s	G-quadruplexes
G4BP	G-quadruplex-Binding Proteins
G4IPDB	G-quadruplex structure (G4) Interacting Proteins DataBase
HBV	Hepatitis B Virus
HCV	Hepatitis C Virus
HEK	Human embryonic kidney cell line
Hfq	Host factor for Qβ replicase protein
hfq	Host factor for Qβ replicase protein gene
HIV	Human immunodeficiency virus
IC_{50}	Ligand concentration that inhibits fifty percent of the total
ITC	Isothermal titration calorimetry
JEV	Japanese Encephalitis Virus
JEV-PGQ	Japanese Encephalitis Virus PGQs

LB	Luria Bertani
MERS-CoV	Middle East Respiratory Syndrome Coronavirus
MTT	3-(4,5-Dimethylthiazol-2-yl)-2,5-Diphenyltetrazolium Bromide)
mTFP	Monomeric teal fluorescent protein
NMR	Nuclear magnetic resonance
ORF	Open reading frame
PAGE	Polyacrylamide gel electrophoresis
PCR	Polymerase chain reaction
PDB	Protein Data Bank
PGQs	Putative G-quadruplex-forming sequences
qRT-PCR	Quantitative real time PCR
RNA	Ribonucleic acid
SARS-CoV	Severe Acute Respiratory Syndrome Coronavirus
SARS-CoV-2	Severe Acute Respiratory Syndrome Coronavirus 2
T	Thymine
T_m	Melting Temperature
ThT	Thioflavin T
U	Uracil

CHAPTER 1

INTRODUCTION

Chapter 1

Introduction

1.1 Infectious Diseases

Infectious diseases have profoundly affected human societies worldwide throughout history. Prior to the advent of modern medical science, the widely held notion remained that divine wrath, astrological alignments, or miasmas primarily caused infectious diseases[3]. The idea that living organisms are the causative agents for diseases was initially disregarded when proposed by Girolamo Fracastoro in the 16th century[4]. It was in the late 19th century, that the concept of microorganisms causing infectious diseases was put forward through the germ theory of disease. The germ theory of disease, proposed by Robert Koch, is widely known as Koch's postulates, which established a causal relationship between microorganisms and disease[5]. These were a landmark in the history of infectious diseases, supporting the linkage of microbes and diseases. Microbes are microscopic life forms, which include bacteria, fungi, viruses, and protozoa, a subset of which act as pathogens. These pathogens, which act as infectious agents, are usually comprised of the following groups: Bacteria, Viruses, Fungi, Protozoa, Helminths.

Infectious diseases remain a central global health concern due to their ability to cause widespread morbidity and mortality, and disruption of societies and economies. It is one of the leading causes of global deaths, second only to heart disease. The threat of infectious diseases is intensified by the persistent emergence of new, previously unrecognized, and re-emerging epidemics with global repercussions. The terms "emerging and reemerging diseases (EIDs)", coined by Joshua Lederberg in 1987, underscored the microbial threat to human health[6,7]. EIDs can be categorized into two groups: newly emerging and reemerging infectious diseases.

1.1.1 Newly emerging infectious diseases

These diseases refer to infections that have newly emerged in a human host or population[8]. Examples include:

- HIV/AIDS [emerged in the early 1980s in the USA]
- SARS-CoV [emerged in China in 2002–2003]
- MERS-CoV [first identified in Saudi Arabia in 2012]
- SARS-CoV-2 [first detected in Wuhan, China in late 2019]

1.1.2 Re-emerging infectious diseases

These diseases refer to infections that reappear in a population after a significant decline or eradication, often in a more aggressive form or a new geographic location. Examples include:

- Tuberculosis (TB) [re-emergence due to multidrug-resistant strains[9]]
- Diphtheria [re-emergence due to incomplete vaccination and antimicrobial resistance[10]]
- Measles [re-emergence due to declining vaccination coverage[11]]
- Cholera [periodic resurgences due to poor sanitation[12]]

EIDs have profoundly shaped the course of the health history of humans and caused immeasurable harm. They remain a persistent human threat. Despite advances in public health, vaccination, and treatment, which have significantly reduced their impact, ongoing awareness, vigilance, and innovation of effective strategies remain essential to address both current and future threats.

1.1.3 Factors contributing to the emergence of infectious diseases

The key drivers of emergence primarily include the following factors:

- *Zoonotic spillover*: Most reported EIDs are transmitted from animals to humans, often due to close contact through wildlife trade, wet markets, or hunting and scavenging[13]. E.g., HIV, SARS-CoV.
- *Ecological disruption*: Deforestation, urbanization, expansion of agricultural areas, disrupt ecosystems as a result bringing humans into closer contact with wildlife reservoirs[14]. E.g., Nipah Virus.

- *Globalization*: Increased international travel of humans to distant places has accelerated the spread of infectious disease-causing pathogens across borders[15]. E.g., Zika virus, SARS-CoV.
- *Breakdown of Public Health Measures*: Conflict, displacement, and poor health infrastructure disrupt vaccination, sanitation, and disease surveillance, enabling outbreaks[16]. Eg., Measles and polio re-emergence.
- *Climate Change*: Rapidly changing temperature and rainfall patterns affect the distribution of disease vectors like mosquitoes, which are the causative agents or hosts for several infectious diseases. Eg., Malaria and dengue.
- *Antimicrobial resistance*: Genomic mutation in pathogens, due to chemical exposure and/or exposure to antibiotics, lateral gene transfer results in the acquisition of drug resistance or adaptation to new hosts[17]. E.g., MDR-TB, MRSA (Methicillin-resistant *Staphylococcus aureus*, CRAB (Carbapenem-resistant *Acinetobacter baumannii*).

"The enemy was the microbial world, and over the centuries, it has killed more people than all of man's wars combined."

- Tess Gerritsen, Gravity

1.2 Antimicrobial resistance (AMR) - A silent pandemic

Antibiotics have long been considered one of the finest breakthroughs of the 20th century. However, the true challenge that exists is the rapid surge of antibiotic resistance in hospitals, communities, and the surrounding environment, which accompanies their widespread use[17]. The remarkable genetic adaptability of microbes, coupled with human antibiotic abuse, has led to the mining of diverse resistance genes and the exploitation of multiple pathways of lateral gene transfer. This has resulted in the accretion of resistance in microorganisms, e.g., bacteria, viruses, fungi, and parasites, against almost every antibiotic introduced into the environment to kill them. It makes standard treatments ineffective, enabling infections to persist and spread, escalating the risk of severe illness and death[18].

1.2.1 Causes of AMR

- **Selective Pressure:** The usage of antimicrobial agents creates a selective pressure for organisms able to endure the exposure to such agents. As a result, susceptible ones die, whereas the resistant ones survive and multiply to become the dominant ones in the population[18].
- **Mutation:** Microbes undergo rapid reproduction and undergo prompt adaptations to new environmental conditions. In this process, they acquire random genetic mutations that are passed on to subsequent generations. Some of these mutations may confer resistance to drugs, thereby aiding in their survival upon exposure to antimicrobial agents.
- **Gene Transfer:** Microbes, such as bacteria, are able to exchange genetic material amongst each other through processes such as conjugation, transformation, and transduction. This enables the transfer of resistance genes among others, to spread quickly between different species and strains. This, in turn, provides the advantage of survival to these microbes compared to those lacking such resistance genes.
- **Inappropriate antimicrobial usage:** The problem of antimicrobial resistance is worsened by the misuse and overuse of antimicrobials. For example, the prescription of antibiotics against a viral infection, or an undiagnosed illness, or an incomplete treatment regimen against an infection; self-medication without medical supervision, consumption of expired drugs, or drugs without proper prescription[19,20]. All of these factors may individually or in combination contribute to the development of resistance in microorganisms[21].
- **Animal and Agricultural Use:** The practice of antibiotic addition to agricultural feed contributes to the promotion of resistance in microbes. Additionally, their usage in livestock and aquaculture disease prevention, growth promotion, facilitates resistance acquisition. This also increases the possibility of human transmission through the food chain[22].

AMR is a multifactorial issue shaped by both natural microbial evolution and human actions. The major contributors include the overuse and misuse of

antimicrobials, inadequate infection control, environmental contamination, and the inherent ability of microbes to adapt and exchange resistance genes. Coordinated action across healthcare, agriculture, policy, and public awareness is required in order to address these concerns.

1.2.2 Global significance and impact of AMR

- **Global public health threats:** AMR has arisen to become an urgent menace to global public health in the 21st century[23]. In 2019, it directly caused 1.27 million deaths, and if not checked, the number is projected to rise to about 10 million by 2050[18].
- **Economic burden:** AMR imposes a grave economic burden on healthcare systems, governments, and society at large. This burden is further amplified due to extended hospital stays, increased consultations, and expensive medications as a last line of defense[24]. Consequently, access to existing high-cost therapies is hindered due to limited resources. AMR could result in economic losses that have the potential to reach $100 trillion USD by 2050[25]. Middle and low-income countries are anticipated to bear the worst effects as resistance acquisition outruns new antimicrobial alternatives[24,26].
- **Threat to modern medicine:** AMR threatens the foundation of modern medicine by reducing the treatment efficacy that depends on reliable antimicrobials. Surgeries, cancer therapies, organ transplants, and the management of chronic diseases all rely on successful infection prevention and treatment. These medical procedures become fatal when antimicrobials fail. Routine infections, such as urinary tract infections (UTIs), pneumonia, and sepsis, also become increasingly challenging to treat[24]. As resistance spreads, first-line antibiotics lose their potency, and even second- or third-line drugs may prove ineffective, leading to more frequent treatment failures, more protracted illness, greater complications, and higher mortality[27]. Hence, AMR not only complicates daily healthcare but also risks reversing decades of progress attained in controlling infectious diseases.

Therefore, without urgent action to suppress the ongoing rise of AMR, the world is entering a "post-antibiotic era" where even minor infections may turn out to be life-threatening and are at a loss for medical advances. Continuous awareness of infectious diseases and progress in control measures is essential to support effective public health responses.

"We need a comprehensive strategy that acknowledges the deep connections between human, animal, and environmental health."

—Nikolaj Gilbert, President and CEO of PATH

1.2.3 Mechanisms of acquisition of AMR

There exist multiple mechanisms through which bacteria acquire resistance to antimicrobials. The primary ones include:

Drug inactivation

Bacteria can reduce the efficacy of drugs through either enzymatic degradation (e.g., β-lactamases hydrolyzing β-lactam antibiotics) or chemical modification (e.g., acetyltransferases, phosphotransferases, or adenyltransferases modifying aminoglycosides) by producing various enzymes, thereby rendering them inactive.

- Enzymatic Degradation

Bacteria produce enzymes that have the potential to break down the administered antibiotic, making it inactive. The most prominent example being β-lactamases, which are a diverse class of enzymes that hydrolyze the β-lactam ring of penicillins, cephalosporins, and related antibiotics, destroying their antibacterial activity[28]. Another example is the inactivation of tetracycline by enzymatic oxidation mediated by the tetX gene product, which degrades tetracycline molecules[29,30].

- Chemical Group Transfer

Bacteria can also chemically modify antibiotics by the addition of small functional groups that block its target binding ability. This is most commonly achieved through acetylation, phosphorylation, or adenylation, catalyzed by diverse transferase enzymes[31]. *Acetylation* targets drugs such as aminoglycosides (e.g., gentamicin), chloramphenicol, streptogramins, and even some fluoroquinolones,

and is the most versatile mechanism[32,33]. *Phosphorylation* and *adenylation* mainly target aminoglycosides, modifying hydroxyl or amino groups on the drug molecule to prevent its interaction with bacterial ribosomes[31].

These mechanisms highlight the genetic plasticity of bacteria and the diverse set of enzymatic tools deployed by them to survive antibiotic pressure.

Restricted drug uptake

Bacteria possess intrinsic resistance that limits the uptake of antimicrobial agents. This is mainly achieved through the bacterial cell membrane. The Lipopolysaccharide layer (LPS) layer in gram-negative bacteria confers innate resistance to the uptake of antimicrobial agents[34]. In case of mycobacteria, which consist of a high lipid-containing outer membrane, the uptake of hydrophilic drugs gets restricted, as compared to hydrophobic drugs (eg. Rifampicin, fluoroquinolones)[35,36]. In case of bacterial species such as Mycoplasma, which lack a cell wall, there occurs inherent resistance to all cell-wall targeting agents (β-lactams and glycopeptides)[37]. The absence of an outer membrane in gram-positive bacteria limits their drug uptake inhibition. However, the dense peptidoglycan layer in enterococci restricts the uptake of polar compounds, consequently providing aminoglycoside resistance[38]. Strains of *Staphylococcus aureus,* also known as VISA (Vancomycin-Intermediate S. aureus) strains, have recently developed vancomycin resistance. One mechanism involves unexplained cell wall thickening, which impedes drug penetration and confers intermediate resistance[39,40]. For bacteria with prominent outer membranes, such as Gram-negatives, the entry of hydrophilic molecules commonly occurs through porin channels. A decreased number of expressed porins and altered porin selectivity due to mutations lead to limited drug uptake via porin channels[35]. *Enterobacteriaceae* frequently develop carbapenem resistance by downregulating or eliminating porin expression[41]. Perturbations in porin structure due to mutations have been observed in *Enterobacter aerogenes* (imipenem and cephalosporin resistance) and *Neisseria gonorrhoeae* (β-lactam and tetracycline resistance)[42–44]. Biofilm formation represents another significant barrier to antimicrobial penetration[45]. Pathogens like *Pseudomonas aeruginosa* in the lung, or complex gut biofilm

communities, embed within a polysaccharide, protein, and extracellular DNA matrix that limits antimicrobial diffusion. This matrix necessitates higher drug concentrations for efficacy, while the sessile, slow-growing state of embedded bacteria exhibits reduced susceptibility to antibiotics targeting active cell division[46]. Moreover, biofilms facilitate horizontal gene transfer due to close cellular proximity, enhancing the transfer of resistance genes within these microbial communities[47].

Alteration of Drug targets

Bacteria can acquire resistance through modification of intracellular drug targets. For example, β-lactam resistance in Gram-positive bacteria often involves structural alterations and/or the number of penicillin-binding proteins (PBPs), which are transpeptidases essential for cell wall peptidoglycan synthesis. Changes in PBP quantity,such as increased expression of low-affinity PBPs or structural alterations (e.g., PBP2a in *S. aureus* from the *mecA* gene) reduce or prevent drug binding[48,49]. Gram-negative bacteria possess intrinsic glycopeptide and lipopeptide resistance, for e.g., vancomycin and daptomycin respectively, due to their thick LPS barrier[50]. Vancomycin resistance in enterococci (VRE) and *S. aureus* (VRSA) arises from *van* genes that structurally alter peptidoglycan precursors, lowering its binding ability[48,51]. Daptomycin resistance involves *mprF*-mutation resulting in positively charged membrane and blocking calcium binding required for the drug's action[52–54]. In case of ribosomal subunit targeting, the main mechanisms involved in conferring resistance include mutation of the ribosome (aminoglycosides, oxazolidinones), methylation of the ribosomal subunit (aminoglycosides, macrolides), or ribosomal protection (tetracyclines). These mechanisms interfere with the ribosomal-drug binding[29,55,56]. Resistance to fluoroquinolones, which target synthesis of nucleic acids, arises via structural mutations in DNA gyrase (*gyrA*) in gram-negative bacteria, which diminishes the drug's binding ability. In gram-positives, similar resistance occurs via mutations in *grlA*, which encodes topoisomerase IV[57,58].

Bypass of metabolic pathways

Bacteria acquire antibiotic resistance through bypass of metabolic pathways by rerouting or replacing drug-inhibited biochemical steps with alternative enzymes that preserve essential cellular functions under antibiotic pressure. This process commonly involves horizontal gene transfer of resistance determinants encoding drug-insensitive isoenzymes or the selection of enzymatic variants with reduced drug affinity, which together restore metabolic flux despite pharmacological blockade. A classical example is resistance towards metabolic pathway inhibitors such as sulfonamides and trimethoprim, where acquisition of plasmid-encoded *sul* genes produces a drug-resistant dihydropteroate synthase, and *dfr* genes encode trimethoprim-insensitive dihydrofolate reductases[59,60]. Similarly, chromosomal mutations or overproduction of resistant dihydropteroate synthase (DHPS) and dihydrofolate reductase (DHFR) variants disrupt antibiotic binding at the enzyme's active site while allowing normal substrate processing, thereby maintaining folate biosynthesis and ensuring bacterial survival in the presence of these agents. [61,62].

Drug efflux

Bacteria express efflux pumps which primarily function to export intracellular toxic substances or various compounds (multi-drug [MDR] efflux pumps). These are expressed constitutively or induced under suitable conditions and resistance is mainly developed via transport channel mutation, the capability of which is affected by the available carbon source[34,63].

There exist mainly bacterial efflux pump types, categorized on the basis of structure and energy source:

(i) ATP-binding cassette (ABC) family
(ii) Multidrug and toxic compound extrusion (MATE) family
(iii) Small multidrug resistance (SMR) family
(iv) Major facilitator superfamily (MFS)
(v) Resistance-nodulation-cell division (RND) family[64].

Most efflux pumps transport substrates across the cytoplasmic membrane acting as single-component systems, while RND pumps form tripartite complexes spanning

the whole cell envelope, acting as multi-component systems [65,66]. Gram-positive bacteria mainly rely on chromosomal MATE and MFS pumps for intrinsic resistance, whereas gram-negatives use all five families, with RND pumps being especially clinically significant.

Viruses usually follow a different route for development of resistance as compared to other microbes. The term "antimicrobial resistance" is more accurately applicable in the case of bacteria, fungi, and parasites. However, viruses can develop antiviral resistance in response to antiviral drugs, the mechanisms of which are listed below:

Genetic Mutation

A virus's mutation rate is defined as the likelihood of a specific nucleotide change during a single genome replication. Drug resistance development depends not only on mutation rates but also on rate of viral replication, progeny fitness, and possible compensatory mutations, collectively referred to as the "resistance rate." The mutation rates of RNA viruses is higher than DNA viruses. This is considered partly a consequence of the error-prone nature of the polymerases utilized for viral genome replication. The daily virion numbers of HIV and HCV are 10^9 and 10^{12}, respectively[67]. These enormous virions, coupled with mutation rates of approximately 10^{-4}, lead to a massive genetic diversity, creating a dynamic "quasi-species" swarm of variants. Mutations in viral genes encoding viral enzymes or structural proteins reduce the binding or effectiveness of antiviral drugs, leading to resistance.

Another pathway for resistance development involves missense mutations in thymidine kinase (TK) or DNA polymerase enzymes, which retain the enzymatic activity but lower the drug's binding affinity. These mutations occur roughly 100 times less frequently in viruses grown in culture but are known to underpin clinical drug resistance in HSV, HCMV etc.A result of genetic mutation is target modification, which is one of the most frequent and clinically relevant mechanisms through which viruses develop antiviral drug resistance. It refers to mutations in the viral protein or enzyme that act as direct antiviral drug targets. These mutations

alter the structure or function of the target such that the drug loses its binding ability, reducing or eliminating its inhibitory effect[68]. Antiviral resistance is achieved through several mutation-based alterations of the drug targets. Point mutations, involving single-nucleotide changes, can lead to amino acid replacement in the drug target that either obstructs drug binding directly or alters the binding site's conformation. For example, in HIV, mutations in the active sites of protease and reverse transcriptase enzymes prevent inhibitor binding leading to drug resistance. In some cases, multiple mutations occur to provide high-level resistance or to offset the fitness cost imposed by initial resistance mutations, like resistance to HIV protease inhibitors often involves multiple mutations that change the enzyme's shape or charge properties[69]. Additionally, allosteric mutations, those occurring at sites distant from the drug-binding pocket,can induce structural changes that diminish drug efficacy[70]. To further enhance viral replication, compensatory mutations may develop, restoring fitness compromised by initial resistance-conferring alterations. In hepatitis B virus (HBV), mutations such as M204V/I in the polymerase gene confer resistance to lamivudine, and additional mutations like L180M and V173L enhance resistance and viral fitness[71].

Selective Pressure

The use of antiviral drugs creates selective pressure, favoring the survival and replication of resistant viral strains.

Recombination and Reassortment

Recombination can bring together multiple resistance mutations from different viral strains into a single genome. This accelerates the emergence of multidrug-resistant viruses, as seen in HIV, where recombination has been shown to create viruses with new patterns of resistance mutations not present in either parent strain. Recombination occurs when two different viral genomes exchange genetic material within a host cell. When a host cell is co-infected with two genetically distinct viruses, their genomes can undergo crossover events. This process can generate progeny viral variants with unique combinations of genetic mutations, including those conferring resistance to antiviral drugs[72]. Recombination also helps in the

maintenance of genetic diversity in viral populations, which can enhance adaptability and the likelihood of resistance emerging under drug pressure.

Some RNA viruses, like influenza (which has eight genome segments), possess an extra route for acquiring resistance, i.e., reassortment. When two viral strains co-infect a cell, their genome segments can reassort randomly, in any combination, producing new viral strains. This in turn, can allow a poorly transmissible but drug-resistant strain to mix with a highly infectious, drug-sensitive strain, producing progeny that are both drug-resistant and highly infectious. For example, the 2009 H1N1 pandemic strain arose through reassortment of eight segments originating from avian (two), swine (five from two continents), and human (one) viruses[73]. Although this new virus was not drug-resistant, it spread widely because most people below age 60 lacked immunity. Fortunately, its initial global spread did not result in severe illness on a catastrophic scale, and only a few cases of oseltamivir resistance were reported during the first year.

1.2.4 Possible strategies to combat AMR

AMR is a relentless global health issue that jeopardizes current therapeutic strategies and requires immediate preventive measures. Addressing this challenge requires a comprehensive, multifaceted approach involving individual practices, healthcare systems, and expansion of global surveillance networks. In parallel, accelerating the development of new therapeutics through rigorous scientific research is critical, particularly as resistance continues to outrun the discovery of conventional antibiotics. The limited selection of molecular targets highlights the lack of new and effective treatment strategies to fight antimicrobial resistance. While primary research focus traditionally highlights upon proteins and enzymes as drug targets, there is growing interest in exploration of non-traditional targets such as structured nucleic acid elements within pathogenic bacterial and viral genome. Unlike conventional approaches, nucleic acid-targeting strategies directly interfere with bacterial or viral genomes and transcripts. These structured nucleic-acid elements play critical roles in gene expression, regulation of survival, and virulence in pathogens, and genome stability. These elements are also often highly conserved and therefore offering the advantage of precise, structure-specific and

attractive drug targets. Nucleic acid structures, such as G-quadruplexes (G4s), internal ribosome entry sites (IRES), hairpins, pseudoknots, and riboswitches, have emerged as promising non-protein targets for novel antibacterial and antiviral therapies. Targeting these conserved and functionally essential nucleic acid structures represents a promising avenue in antimicrobial drug target identification, particularly for addressing infections associated with multidrug-resistant pathogens where existing treatment strategies become saturated.

1.3 Nucleic acid secondary structures as therapeutic targets

Nucleic acids, DNA and RNA, are the fundamental biomolecules responsible for the storage, transmission, and expression of genetic information. Each nucleic acid is composed of repeating structural units called nucleotides, which consist of a nitrogenous base (purines: adenine, guanine; pyrimidines: cytosine, thymine [in DNA], and uracil [in RNA]), a pentose sugar (deoxyribose in DNA, ribose in RNA), and a phosphate group. The secondary structures formed by these nucleic acids arise from specific sequence-driven interactions such as base pairing, base stacking, and sometimes, interactions with metal ions or other small molecules. Apart from their primary sequence, nucleic acids adopt intricate secondary structures through intra- and inter-strand base pairing governed by hydrogen bonds. While the canonical Watson–Crick base pairing paradigm underlies the canonical helix structure, various sequence-specific and environmental factors allow nucleic acids to adopt alternative, non-canonical conformations that are functionally important. Broadly, nucleic acid secondary structures can be categorized into canonical and non-canonical configurations.

Nucleic acid secondary structures represent an exciting frontier in antimicrobial drug development, offering novel mechanisms that complement traditional protein-targeting approaches. These structures, formed through intra- and inter-molecular base pairing interactions, create unique molecular targets that can be exploited for therapeutic intervention against both bacterial and viral pathogens.

1.3.1 Canonical secondary structures

DNA

The understanding of canonical secondary structures of nucleic acids was revolutionized in 1953 when James Watson and Francis Crick discovered the double helical model of DNA. This B-form DNA, which adopts a right-handed helix, is the most prevalent and stable form of intracellular DNA. In this form, two strands having opposite polarity run parallel to each other, spiraling around a central axis, stabilized by Watson-Crick hydrogen-bond base pairing (A-T and G-C) and base stacking interactions (Figure 1.1)[74]. Furthermore, the presence of major and minor grooves provides a structural platform for protein–DNA interactions, essential for regulation and replication. While B-DNA is the most abundant & stable structure formed readily physiologically, DNA also adopts other unusual conformations such as, A-form and Z-form. These conformations differ in their helical geometry, physiological requirements, and biological significance. The A-form adopts a right-handed helix, shorter and broader than B-form DNA. This form is usually observed in dehydrating conditions or in RNA–DNA hybrids[75]. The Z-form adopts a left-handed helix and occurs in regions with purine-pyrimidine-rich sequences, alternating in a zig-zag form[76]. These structural entities are instrumental in genetic recombination, transcriptional regulation[77].

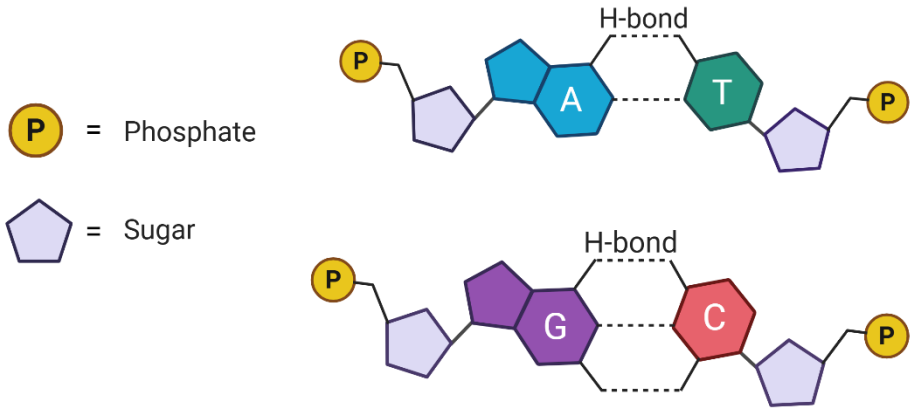

Figure 1.1. The base-pair complementation in canonical nucleic acid secondary structures. Thymine is replaced by Uracil in RNA.

RNA

RNA, unlike DNA is generally exhibits a single-stranded intramolecular folding governed by the same Watson–Crick base pairing rules, in which Thymine is replaced by Uracil (A-U instead of A-T). This gives rise to diverse secondary structural motifs, including stem-loops, bulges, and internal loops, which are further stabilized by base stacking[78,79]. RNA usually adopts a single-stranded conformation but can form double-stranded regions via intramolecular base pairing, folding into A-form helical structures. Notably, this form is more compact and occurs frequently in viral genomes, RNA interference pathways, and ribonucleoprotein complexes[80,81]. Stem-loops or hairpins result from intra-strand base pairing, characterized by a double-stranded stem and a loop[82]. These motifs are ubiquitously found in mRNAs, non-coding RNAs, form structural elements in ribozymes and riboswitches, act as key regulators in translation and transcription termination, and are vital to the folding of tRNA[83,84]. Internal loops, bulges, and multibranch loops arise from non-complementary regions within double-stranded stems, and contribute to complex tertiary folding and ligand recognition[85].

1.3.2 Non-Canonical secondary structures

In addition to canonical structures adopted by DNA and RNA, there exists a range of non-canonical secondary structures like G-quadruplexes, i-motifs, hairpins, triplex DNA, cruciform structures, etc. These structures are not merely structural oddities but have been implicated in the dynamic modulation of gene expression, telomere maintenance, genome stability, chromatin remodeling, and disease pathogenesis. Structural motifs such as G-quadruplexes and triplexes are increasingly recognized as therapeutic targets, opening new avenues for drug design. For instance, G-quadruplexes have been linked to transcriptional repression of proto-oncogenes such as *MYC*, *KRAS*, and *BCL2*, and their stabilization, due to their promoter-enrichment and therefore suggesting a tumor-suppressive potential. Expanded G-rich repeats able to form G-quadruplex or triplex structures, such as those formed in *C9orf72* and *FMR1*, have been linked to neurodegenerative diseases, including amyotrophic lateral sclerosis (ALS) and fragile X syndrome.

Moreover, i-Motifs and triplexes have been associated with epigenetic dysregulation in cancer. Furthermore, G-quadruplex-forming sequences within bacterial and viral genomes have been implicated in virulence gene expression, replication, and latency, as observed in HIV-1 and Epstein–Barr virus, indicating their relevance in infectious diseases. Collectively, non-canonical nucleic acid structures have gained attention as novel therapeutic targets for intervention in cancer, neurodegeneration, and antimicrobial resistance, thereby opening new avenues for drug design.

The main scope of this research explores the presence, formation, and biological implications of G-quadruplex structures in bacterial and viral pathogens, and the same is discussed further.

1.3.3 G-quadruplex structures

Ivar Bang, in 1910, first documented the gel-forming properties of guanylic acid solutions, providing the first indication that guanine-rich nucleic acid sequences could aggregate to form higher-order structures[86]. The concept of self-assembly of guanines into planar guanine tetrads (G-tetrads) via Hoogsteen hydrogen bonding was then introduced by Gellert, Lipsett, and Davies in 1962 using X-ray diffraction[87]. This laid the molecular foundation for the first experimental evidence for what would later be termed G-quadruplexes (G4s). Over two decades later, Sen and Gilbert (1988) provided a more biologically relevant context by demonstrating that synthetic oligonucleotides with guanine-rich sequences could form stable four-stranded quadruplex structures under physiological conditions in vitro[88]. G4s have since been identified throughout eukaryotic, prokaryotic, and viral genomes. Their structural and functional versatility has attracted significant attention in gene regulation, genome maintenance, and disease pathogenesis.

1.3.4 Structural features of G-quadruplexes

The formation and stability of G4s are governed by unique hydrogen bonding interactions distinct from classical Watson-Crick base pairing and cation co-ordination. G4s formation takes place when four guanine bases are arranged

cyclically in a plane to give rise to a G-quartet. In each G-quartet, N1 of a guanine forms a hydrogen bond with the O6 of the adjacent guanine. The N2 (amino group) can form hydrogen bonds with the N7 of neighboring guanines. This results in a cyclic network of eight hydrogen bonds per quartet, providing significant enthalpic stabilization. Multiple G-quartets stack atop each other via π–π interactions between their aromatic guanine rings, resulting in the G4 structure (Figure 1.2). The central cavity created by the stacked quartets is negatively charged due to the alignment of O6 carbonyl groups from the guanines[89,90]. This highly electronegative environment is unfavourable and requires neutralization by cation coordination, between or within the quartets. The insertion of suitable monovalent cations, primarily potassium (K^+) and sodium (Na^+) into this cavity is crucial for supporting G4 folding and maintaining structural integrity. Among monovalent ions, K^+ provides the highest stabilization due to its ideal ionic radius (~1.33 Å), which allows it to fit snugly between adjacent G-quartets and directly coordinate with eight O6 atoms from two quartets. In contrast, the smaller Na^+ ion (~0.95 Å) typically coordinates within a single quartet plane, offering less efficient stabilization. Moreover, K^+ owing to its high intracellular concentration (~140 mM) is considered to be more physiologically relevant than that of Na^+ (~10 mM)[91]. The relative effectiveness of these ions in stabilizing G-quadruplexes follows the trend: $K^+ > Na^+ >> Li^+$, with Li^+ being less effective in providing stabilization, due to its suboptimal coordination geometry and high hydration energy. Additionally, divalent cations such as Mg^{2+} and Ca^{2+} do not typically stabilize G4 structures directly; however, they can influence folding indirectly by modulating the overall ionic strength or interacting with loop residues.

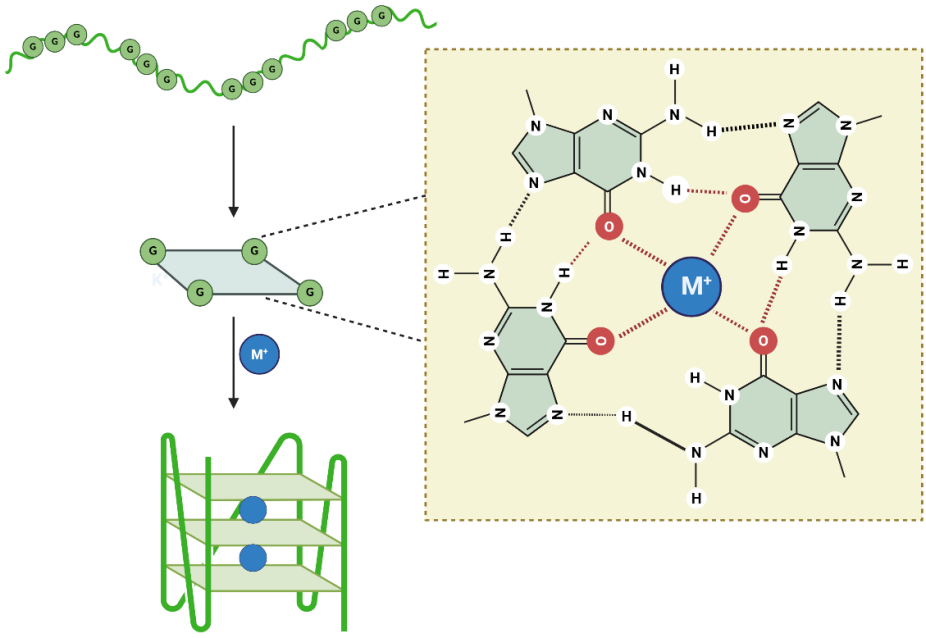

Figure 1.2. Depiction of self-association of the guanines in guanine-rich nucleic acid sequences forming a G-quartet structure that, upon further stacking, forms the G-quadruplex structure, stabilized by a monovalent cation.

G4 structures display considerable topological diversity influenced by several factors, including the relative strand orientation (parallel, antiparallel, or hybrid), the type of monovalent cation present (typically K^+ or Na^+), the glycosidic bond conformation (syn or anti), the number of nucleic acid strands involved (intramolecular or intermolecular), the number of stacked G-quartets. The orientation of the strands participating in G4 structure formation contributes in determining the G4 topology. A G4 is termed parallel if the polarities of all the strands are aligned in the same direction with respect to one another. In contrast, if each strands are aligned in opposite polarity with respect to the adjacent strands, an anti-parallel G4 is formed[92]. Hybrid topologies have also been observed, which consist of a mixed parallel-antiparallel strand orientation[93].

The conformation of glycosidic bonds of guanine bases refers to the torsion angle between the bases and their sugar moiety, classified as syn or anti. This affects the local base orientation and dictates G-quadruplex topology[94]. All guanines adopt the anti-conformation in parallel G4s, leading to uniform strand orientation and propeller-type loops, commonly observed in RNA G4s and certain DNA G4s in

potassium-rich conditions[95]. On the other hand, alternating syn–anti conformations, which enable strand reversals are observed in antiparallel G4s, inducing lateral or diagonal loop formation, as exemplified by the sodium-stabilized human telomeric G4 structure[96]. Hybrid topologies, such as those observed in K^+-stabilized human telomeric DNA, exhibit guanines in mixed syn and anti-conformation to accommodate parallel and antiparallel strands within the same structure[97].

G4s can adopt intramolecular (monomeric) or intermolecular (multimeric) structure based on the involvement of one or more nucleic acid strands, respectively, in structure formation. Intramolecular G-quadruplexes are formed from a single strand which represent majority of biologically relevant G4s. They fold rapidly and exhibit great conformational diversity. In contrast, intermolecular G-quadruplexes involve two (bimolecular) or four (tetramolecular) strands. These multimeric structures are generally less physiologically abundant but serve as valuable framework for studying G4 folding and ligand binding [3]. The number of strands directly influences G4 folding kinetics, topology, and structural polymorphism.

The number of stacked G-quartets in a G4 structure has a direct influence on its topology, stability, and biological relevance. The algorithm usually employed to predict putative G4-forming motifs is:

$$G_XN_{L1}G_XN_{L2}G_XN_{L3}G_XN_{L4}$$

(where $x \geq 3$, N can be any base including guanine, and L depicts the loop length). Multiple computational tools are available for identifying putative G4-forming sequences, which primarily rely on the G-tract length and the intervening loops to define the consensus sequence[98,99]. Most well-characterized G4s consist of three stacked G-quartets. However, in vivo functional G4s may not always follow this canonical model and exhibit deviations from this consensus sequence. Although two-quartet G4s are generally less stable thermodynamically, their formation has been validated by NMR and CD studies, and they are increasingly recognized in regulatory regions, such as promoters and untranslated regions, particularly in RNA [100–102]. Despite lower intrinsic stability, two-quartet G4s contribute to the

structural and functional diversity of quadruplex motifs across genomes. This exemplifies the structural diversity and complexity of G4s, highlighting the need for a more refined approach towards their prediction and characterization. The structural heterogeneity of G4s confers on them specific folding dynamics and protein recognition capacity.

RNA G-quadruplexes (rG4s) present a distinguished class of non-canonical secondary structures adopted by guanine-rich RNA sequences. While both DNA and RNA G-quadruplexes share a similar core architecture of stacked guanine tetrads, stabilized by Hoogsteen hydrogen bond base pairing and monovalent cations, there has been relatively less focus on RNA G-quadruplex structures in prokaryotic contexts. Their structural features differ fundamentally from those of DNA-G4s, due to the presence of ribose 2′-hydroxyl group, which provides steric constraints and stabilizes the C3′-endo sugar puckering[103,104]. This confers rG4s with their characteristic preference for parallel topology, as a direct consequence of anti N-glycosidic bond conformation, limiting their structural heterogeneity. Comparatively, a wider structural polymorphism is observed in DNA G4s, which can adopt parallel, antiparallel, and hybrid topologies. Notably, rG4s also demonstrate greater thermodynamic stability compared to DNA-G4s, more likely because of the 2′-hydroxyl group, which enhances intramolecular interactions promoting extensive hydrogen bonding and base stacking interactions and less hydration. These structural variations between DNA and RNA G4s not only define their unique biological functionality but also affect their potential as targets for therapeutic intervention. Like DNA G4s, rG4s have been reported to be involved in different cellular mechanisms such as, regulation of RNA processing, translation, localization, and their dysregulation has been linked with diseases such as cancer, and neurodegenerative diseases[105]. Although these structures have been implicated in viral infections, the level of research landscape in this area is still emerging and remains insufficient. Moreover, the significance of rG4s in bacteria has received even limited attention, both of which have been elaborated in the present thesis work. Their increasing functional recognition highlights the

importance of their therapeutic targeting in the context of bacterial and viral pathogens.

1.4 G-quadruplex Binding Proteins as therapeutic targets

A diverse range of proteins selectively recognize and bind to G4s, and are referred to as G-quadruplex binding proteins (G4BPs). These G4BPs serve as key regulators of G4-associated biological processes by modulating G4 folding, stability, and function. Subsequently, their misregulation has been associated with cancer, neurodegenerative diseases, and viral infections, upholding them as promising therapeutic targets[106].

For example, nucleolin and NM23-H2 modulate the transcription of the c-MYC promoter, which is greatly implicated in cancer development and progression. Reduced NM23-H2 levels lower c-MYC expression, leading to apoptosis, but also increasing the metastatic potential[107]. In neurological diseases, G4BPs are implicated through the regulation of rG4-containing mRNAs. For example, disruption of mRNA transport and translation of various other mRNAs due to reduced FMRP expression in Fragile X syndrome; modulation of rG4-mediated translation by hnRNP H/F overexpression in glioblastoma[108,109]; DDX3X-mediated transcript expression associated with oxidative phosphorylation, having direct implications in Huntington's, Alzheimer's, and Parkinson's disease, etc[110]. In case of viral infections, nucleolin and hnRNP A2/B1 promote HIV-1 transcription by stabilizing and unfolding G4s in the long terminal repeat (LTR) promoter, respectively[111,112]. Additionally, an explicit interaction of SARS-CoV-2 G4s with the viral helicase nsp13 has also been reported[113].

Therefore, investigation of G4–protein interactions offers valuable insights into novel intervention strategies, particularly in disease contexts where aberrant G4 formation or resolution contributes to pathogenesis. As we already know, and so has been reported through scientific evidence, that G4 structures are equally crucial in bacterial genome functioning, the functional significance of G4BPs is yet to be elucidated in bacterial contexts. While their identities and functional impact has been explored in eukaryotes and viruses, the same remains relatively elusive in case of bacteria. The possibility of G4BPs in bacteria emerging as important regulators

of nucleic acid structure and function, with implications for gene regulation, bacterial physiology, and potential antimicrobial therapy, and their comparative studies across bacterial species may highlight their key roles in regulation of bacterial physiology and pathogenicity as well as species-specific functioning and conservation. Therefore, uncovering the mechanisms of G4-G4BP interaction, their full spectrum, and roles represent a significant frontier in bacterial molecular biology and provides an appealing approach for potential therapeutic targets alongside G4 structures against clinically relevant bacteria.

1.5 Aim and Scope of the Thesis

Antibiotics transformed medicine in the 1930s–1940s by enabling the effective treatment of pathogenic bacterial infections[114]. Moreover, the development of antiviral drugs occurred more gradually compared to antibiotics, but have significantly transformed the treatment landscape for viral infections[115]. However, the overuse and misuse of antibiotics, a high rate (30–50 %) of incorrect prescriptions, and the expanded antibiotic usage in agriculture and livestock have contributed in the recent acceleration of Antimicrobial resistance (AMR)[116]. Antimicrobial resistance is a long-standing, silent pandemic that has become an increasingly serious global public health crisis in the 21st century, as identified by the World Health Organization (WHO)[117]. In 2019, AMR contributed deaths counted to approximately 4.95 million globally, far exceeding COVID-19 pandemic first-wave death estimates[23,118].

A major obstacle in the fight against AMR is the lack of pharmaceutical investment in the development of new antibiotics, due to high costs and limited profitability, resulting in a gap in innovation. AMR continues to worsen by each passing day. The WHO's July 2024 updated list of emerging pathogens marks a strategic shift in global health preparedness, promoting a broader, family-based framework rather than targeting individual pathogens. A key update in the 2024 list is the inclusion of Prototype Pathogens, selected based on pathogenic relevance and biological understanding. These serve as research models to enable the formulation of broad-spectrum medical countermeasures that can be rapidly adapted to related emerging and re-emerging pathogens. This revised approach addresses the limitations of

earlier lists by embracing a more proactive, adaptable, and forward-looking strategy to confront both known and emerging pandemic threats.

Among the pathogens posing an emerging public health risk is *Acinetobacter baumannii* arising from its rapidly surfacing multidrug-resistance. *Acinetobacter baumannii* is a rapidly adapting, extensively drug-resistant pathogen that poses a growing global public health challenge. Its remarkable capacity to withstand antibiotics and persist in clinical environments positions it as a major contributor to the AMR crisis and a priority pathogen for novel therapeutic strategies. Likewise, Japanese encephalitis virus (JEV) is an emerging public health threat due to its geographic spread, severe health impacts, lack of specific treatments, and complex transmission dynamics. Its emergence and significantly rising disease burden contribute to the AMR crisis indirectly.

This thesis aims to investigate the presence, structural characterisation, and functional analysis of conserved G4-forming motifs in human-infecting pathogens, with a specific focus on *Acinetobacter baumannii* and Japanese Encephalitis Virus (JEV). By integrating in silico prediction, biophysical validation, and cell-based analyses, this work seeks to establish the therapeutic significance of these motifs as regulatory elements within the genomes of clinically relevant pathogens. Additionally, the study explores the formation of two G-tetrad DNA/RNA G4s in the genome of *Acinetobacter baumannii* and the interaction between these G4 structures and G4-binding protein (G4BPs). Collectively, this work helps to gain a better perspective on how these non-canonical structures and their interactions with specific proteins contribute to microbial gene regulation and pathogenicity.

The scope of this thesis encompasses the therapeutic exploration of G4 motifs and G4BPs as antimicrobial targets, particularly in the context of drug-resistant bacterial and viral infections through:

- In silico identification of highly conserved and structurally stable G4 motifs across *A. baumannii* and JEV genomes using established G4-predictive algorithms.

- Confirmation of G4 formation, topology, and stability through experimental techniques such as NMR spectroscopy, circular dichroism (CD) spectroscopy, Thioflavin T probe fluorescence assay, electrophoretic mobility shift assay (EMSA).
- Further validation of quadruplex structure formation through interaction and binding analysis of the G4s with well-known G4-binding ligands through biophysical studies including CD spectroscopy, EMSA, Fluorescence titration assay, NMR spectroscopy, Isothermal calorimetric titration analysis.
- Cell-based studies to assess the regulatory impact of selected G4 motif stabilization on gene expression through quantitative real-time PCR, reporter gene assay, biofilm-formation assay, immunoblotting, etc.
- Investigation of protein–G4 interactions, to elucidate their role in modulating G4 stability.

To summarize, this thesis is confined to pathogenic systems of high clinical relevance and does not extend to commensal or non-pathogenic microbes. The research findings discussed herein aim to advance the understanding of the relevance of G-quadruplex structures, interaction with specific G4 binding ligands, their role in gene regulation, and protein-G4 interaction in pathogens and contribute to the development of novel G4/G4BP target based therapeutic strategies.

1.6 Organization of the thesis

The entire thesis is organized into six chapters, a summary which is discussed below:

Chapter 1 presents a brief background of the research work covered in the thesis, offering a concise overview of emerging and re-emerging infectious diseases and the factors contributing to their emergence. It discusses the global threat of antimicrobial resistance posed by these diseases, its underlying causes, and its broader implications. It also outlines the strategies employed to combat AMR with particular emphasis on targeting nucleic acid secondary structures, precisely G-quadruplexes. The chapter also highlights the structural characteristics and biological relevance of G4s in bacterial and viral genomes, including the formation

of stable two-tetrad G4s and their interactions with G4-binding proteins (G4BPs) in context of a bacterial genome. It concludes with a brief summary of the aim and scope of the thesis.

Chapter 2 presents an overview of the materials and methodologies adopted in the studies presented in the thesis. It also summarizes the instrumentation techniques used, along with their underlying working principles.

Chapter 3 investigates conserved genomic G4 motifs in *Acinetobacter baumannii*. It outlines the pathogen's clinical significance, details the conservation of certain G4 motifs across multiple strains, and presents their biophysical characterization. Interaction with G4-specific ligand and cellular assays confirm the G4 formation and regulation in modulating gene expression associated with *A. baumannii* infection.

Chapter 4 elaborates on the characterisation of two-tetrad G-quadruplex motifs within the *hfq* gene of *A. baumannii*. Biophysical and interaction assays confirmed the stable formation of DNA/RNA G4 and selective recognition by the Hfq protein, particularly with RNA. Stabilization of these motifs reduced *hfq* expression, indicating a potential RNA-based regulatory mechanism for therapeutic intervention.

Chapter 5 elucidates the importance of evolutionarily conserved RNA G4 motifs in the genome of Japanese Encephalitis Virus, identified bioinformatically and structurally validated by multiple biophysical assays. It also demonstrates the functional studies revealing suppression of viral gene expression and replication upon G4 stabilization, positioning JEV-GQs as potential antiviral targets.

Chapter 7 presents the concluding remarks and future perspectives of the thesis work.

CHAPTER 2

MATERIALS, METHODS, AND INSTRUMENTATION

Chapter 2

Materials, Methods, and Instrumentation

2.1 Materials

Oligonucleotides

All DNA and RNA oligonucleotides used in biophysical analyses, including G-quadruplex-forming sequences and control sequences (both G4 and non-G4-forming), were purchased from Sigma-Aldrich (St. Louis, MO, USA) and Integrated DNA Technologies (Iowa, USA), or produced via *in vitro* transcription. The list of oligonucleotides used in this study are listed below in Table 2.1.

Table 2.1. List of oligonucleotide sequences used in the entire study.

Sl. No.	**G4 motif**	**Sequence**
1	AB_PGQ1	AAGTGGGCGTGTTGGGTGCGGGCATGATGGGTGCC
2	AB_PGQ2	GAACGGGTACAAGTGGGTAACTATATGGGTATGAATCAGGGCCGT
3	AB_PGQ3	ATTTGGGCTAAAGGGCACGGGTTTATGAGTGGGTATA
4	AB_PGQ4	GAACGGGAGGGGGACACCTTCGGGTGTGCTGGGTTTT
5	AB_PGQ5	ACATGGGCTTTCGGGACATGGGCGGGAAGG
6	AB_PGQ6	TTTAGGGGCAGGTTTTCGGGTAGGTTGGGTCTATGCGGGTAAA
7	AB_PGQ7	GATTGGGCAGGGTGCCGAGGGCATTATTTTGGGGTGTA
8	AB_PGQ8	ATTCGGGCTTTCGGGTCAGGCTGGGCATCGGCAATGGGGCGTA
9	*hfq*_RNA	GGCUUCGGUGGCCAAGGCGGCUUCGGUGGUCAAGGUGGCUUCGGUG
10	truncated hfq_RNA	GGCUUCGGUGGCCAAGG
11	*hfq*_DNA	GGCTTCGGTGGCCAAGGCGGCTTCGGTGGTCAAGGTGGCTTCGGTG
12	truncated hfq_DNA	GGCTTCGGTGGCCAAGG
13	Env_1	GCUCUUGGGUCACAGGAAGGAGGCCUCCA
14	Env_2	GAGCCUGGGACUUUGGCUCCAUUGGAGGGGUCUUC
15	NS3_1	GACCAAGGUGGAAUUAGGGGAGGCAGCAAA
16	NS3_2	GGCACUGGUUAUGGGAGAUGGGUUUCCAAGGAUGAC
17	NS3_3	GAGUCAGGAAAAGGAUCCGUGGUUCCAGGCGGGG
18	NS5_1	GGAAAAGGGGAAGGCCCGGGGGCAGGACGCUAAAA
19	NS5_2	GGUAUUGGGUUAGUGGAGCCGCUGGCAAUGUGGUGCAC
20	NS5_3	GCUAAAGGAAGCAGGGCCAUUUGGUUCAUGUGGCUUGG

Reagents and Kits

All reagents and antibodies used in the study are listed below in Table 2.2.

Table 2.2. List of reagents, antibodies and kits used in the entire study.

Sl. No.	Company	Reagent
1	HiMedia	Potassium chloride (KCl)
2	HiMedia	Sodium chloride (NaCl)
3	HiMedia	Lithium chloride (LiCl)
4	HiMedia	Magnesium chloride ($MgCl_2$)
5	HiMedia	Sodium Hydroxide (NaOH)
6	HiMedia	Potassium Phosphate Dibasic (K_2HPO_4)
7	HiMedia	Potassium Dihydrogen Phosphate (KH_2PO_4)
8	HiMedia	Sodium Phosphate Dibasic (Na_2HPO_4)
9	HiMedia	Sodium Dihydrogen Phosphate (NaH_2PO_4)
10	HiMedia	Ammonium chloride (NH_4Cl)
11	HiMedia	Ethylenediaminetetraacetic acid (EDTA)
12	HiMedia	Urea
13	HiMedia	Agarose Low EO
14	HiMedia	Luria Bertani Broth, Miller
15	HiMedia	Luria Bertani Agar, Miller
16	HiMedia	Brain Heart Infusion (BHI) Broth
17	Sigma	Triton™ X-100
18	Sigma	3-(Trimethylsilyl) propionic-2,2,3,3-d4 acid sodium salt (DSS)
19	HiMedia	MTT (3-(4, 5-dimethylthiazol-2-yl)-2, 5-diphenyl tetrazolium bromide)
20	G-Biosciences	Tween 20
21	Sigma	10mM dNTP Mix
22	HiMedia	Taq Polymerase
23	Sigma	Adenosine 5′-triphosphate disodium salt hydrate
24	Sigma	Guanosine 5′-triphosphate sodium salt hydrate
25	Sigma	Cytidine 5′-triphosphate disodium salt
26	Sigma	Uridine 5′-triphosphate trisodium salt hydrate
27	Sigma	Spermidine
28	Sigma	Thioflavin T

29	Sigma	BRACO19 hydrochloride
30	Sigma	TMPyP4
31	Sigma	2-Mercaptoethanol
32	Sigma	Agarose Type VII
33	Promega	CellTiter-Glo®
34	HiMedia	Phenylmethylsulfonyl fluoride (PMSF)
35	Sigma	Protease inhibitor cocktail (PIC)
36	HiMedia	SDS
37	Merck Millipore	PVDF membrane
38	HiMedia	Sodium pyruvate
39	Takara Bio USA, Inc.	PrimeScript™ cDNA Synthesis Kit
40	Applied Biosystems	PowerUp SYBR Green Master Mix
41	Takara Bio USA, Inc.	Trizol reagent (RNAiso Plus)
42	HiMedia	DMEM
43	Gibco	FBS
44	HiMedia	L-15
45	HiMedia	L-Glutamine
46	Hyclone	MEM
47	HiMedia	Penicillin-Streptomycin
48	HiMedia	Trypsin - EDTA Solution
49	Gibco	PBS
50	NEB	NdeI
51	NEB	XhoI
53	GeneTex (GTX100118)	GAPDH
54	GeneTex (GTX131359)	JEV-NS5
55	GeneTex (GTX125868)	JEV-NS3
56	Jackson ImmunoResearch (715-035-150)	Peroxidase AffiniPure Donkey Anti-Mouse IgG (H+L)
57	Jackson ImmunoResearch (711-035-152)	Peroxidase AffiniPure Donkey Anti-Rabbit IgG (H+L)
58	Qiagen	QIAprep Spin Miniprep Kit
59	Qiagen	QIAquick Gel Extraction Kit
60	Qiagen	QIAquick PCR Purification Kit
61	HiMedia	HiPurA® Plasmid DNA Midiprep Purification Kit
62	HiMedia	HiPurA® Bacterial Genomic DNA Purification Kit

Cell lines

Human embryonic kidney cell lines (HEK293T), Neuro2a (mouse neuroblastoma), C6/36, and Vero cell lines were procured from the cell repository of the National Center for Cell Sciences (NCCS) Pune, India.

HEK293T cells were cultured in Dulbecco's Modified Eagle's Medium (DMEM) media supplemented with 10 % Fetal Bovine Seum (FBS) and 1 % Penicillin-Streptomycin solution.

Neuro2a cells were cultured in DMEM media, Vero cells in Eagle's Minimum Essential Medium (MEM), and C6/36 cells in Leibovitz's L-15 medium. All culture media were supplemented with 10% fetal bovine serum (FBS), 100 µg/ml Penicillin-streptomycin solution, and 2 mM L-glutamine.

2.2 Sample Preparation

2.2.1 Oligonucleotide preparations

The desalted, purified oligonucleotides were reconstituted in Milli-Q water following the manufacturer's instructions. The stock concentration of the oligonucleotides was calculated by measuring absorption at 260 nm (A_{260}) in denaturing buffer using the Beer-Lambert's law, with provided molar extinction coefficients. The stock solutions were stored at 4 °C for short-term and -20 °C for long-term preservation until further use.

2.2.2 In vitro transcription

DNA templates containing the T7 RNA promoter, along with forward and reverse primers, were designed and procured from Sigma-Aldrich (St. Louis, MO, USA). Templates for in vitro transcription were generated by PCR amplification. RNA transcripts were synthesized using in-house purified T7 RNA Polymerase and the synthesized transcripts were purified by running 15 % denaturing PAGE. The gels were analyzed through UV shadowing, and RNAs were extracted from the gel and purified using ethanol precipitation. The concentration of oligonucleotides used in each experiment was quantified by measuring the absorbance value at 260 nm. The molar extinction coefficients were calculated using the IDT OligoAnalyzer tool.

2.2.3 One-dimensional proton Nuclear Magnetic Resonance spectroscopy

Oligonucleotide samples were prepared in potassium phosphate buffer (KPO_4) (10 mM, pH 7.5, 100 mM K^+) using a 9:1 H_2O:D_2O solvent ratio, with a final volume of 200 µl. Sodium trimethylsilylpropanesulfonate (DSS) served as the internal reference in all experiments. This sample solution was transferred into Shigemi NMR tubes for subsequent analysis.

For NMR Broadening experiment, 200 µl volume of ligand solution (200 µM) was prepared under similar conditions as described above. Oligonucleotide solutions were then titrated into the ligand solution based on the desired drug-to-nucleic acid (D:N) ratio.

2.2.4 Circular Dichroism spectroscopy

Each Circular Dichroism (CD) spectrum was recorded using oligonucleotide samples at a final concentration of 10 µM in KPO_4 buffer (10 mM, pH 7.5) supplemented with four different cations, *viz.* K^+, Na^+, Mg^{2+}, or Li^+ (100 mM each) in separate experiments. Prior to CD spectral and thermal denaturation analyses, the samples were denatured at 95 ºC for 10 mins followed by slow reannealing at room temperature.

For ligand titration assays, the ligand was incrementally added to the oligonucleotide sample based on the drug-to-nucleic acid (D:N) ratio, followed by the acquisition of CD spectra and thermal denaturation profiles.

2.2.5 Electrophoretic mobility shift assay (EMSA)

Both test (G4-forming sequences) and control oligonucleotides (Bcl2, cKit as positive controls; non-G4-forming mutant as negative control) were prepared at a final concentration of 10 - 15 µM in KPO_4 buffer (10 mM, pH 7.5) containing 100 mM of either K^+, Na^+, Mg^{2+}, or Li^+. Samples were denatured at 95 °C for 10 minutes and then slowly cooled to room temperature.

For ligand and protein interactions, EMSA was performed with oligonucleotides titrated against BRACO-19 (0 - 100 µM) or incubated with purified protein (40 µM) for 30 min and 1 h, respectively, at room temperature.

2.2.6 ThT probe light-up and displacement assay

Oligonucleotides (5 μM) and their corresponding mutant sequences were prepared in KPO_4 buffer (10 mM, pH 7.5, 100 mM K^+). Thioflavin T (ThT) solution was prepared at 10 μM in the same buffer, and a 25 μM ligand solution was similarly prepared for subsequent addition.

2.2.7 Fluorescence titration assay

Two solutions, A and B, were prepared in KPO_4 buffer (10 mM, pH 7.5, 100 mM K^+) and BSA (40 μg/ml) in water. Oligonucleotides (20 - 30 μM) were added exclusively to Solution A, while the ligand BRACO-19 was included in both solutions. Solution A was heated at 95 °C for 10 minutes and then slowly cooled to room temperature to allow proper G4 refolding. Solution B was dispensed into wells (50 μL per well) and titrated with serial dilutions of Solution A.

2.2.8 Isothermal titration calorimetry (ITC)

For ITC experiment, oligonucleotide samples were dissolved in KPO_4 buffer (10 mM, pH 7.5, 100 mM K^+) and heated at 95 ºC for 10 minutes followed by slow cooling at room temperature. The working solution of the ligand (BRACO-19) was prepared in the same buffer, and both oligonucleotide and ligand solutions were thoroughly degassed before titration.

2.2.9 Fluorescence spectroscopy

Working solutions of proteins (5 μM) and oligonucleotides were prepared in KPO_4 buffer (10 mM, pH 7.5, 100 mM K^+). Oligonucleotide samples were added to the protein samples in increasing Nucleic acid/Protein (N/P) ratios ranging from 0 to 2.0.

2.3 Methodology and Instrument Specifications

2.3.1 In-silico methods

2.3.1.1 Bacterial genome retrieval

The complete genome sequences of all the available of the bacterial strains and viral isolates under study were downloaded from the NCBI Genome

(https://www.ncbi.nlm.nih.gov/genome) and subjected to G4 motif prediction analysis.

2.3.1.2 Tools used for G-quadruplex mining

Numerous computational tools exist for predicting G-quadruplex (G4) motifs within nucleic acid sequences, most of which rely on searching for a specific regular expression. Our lab has developed a custom Python-based algorithm, accessible via the G4IPDB database server, to predict G4 motifs in any given input sequence. We also cross-verified our results using established algorithms from other research groups. Subsequent analyses included conservation assessment through clustering and functional annotation of predicted G4s based on their genomic location and associated genes, using NCBI GenBank coordinates. A schematic representation of the genome mining workflow used for G4 motif prediction in this thesis is represented in Figure 2.1.

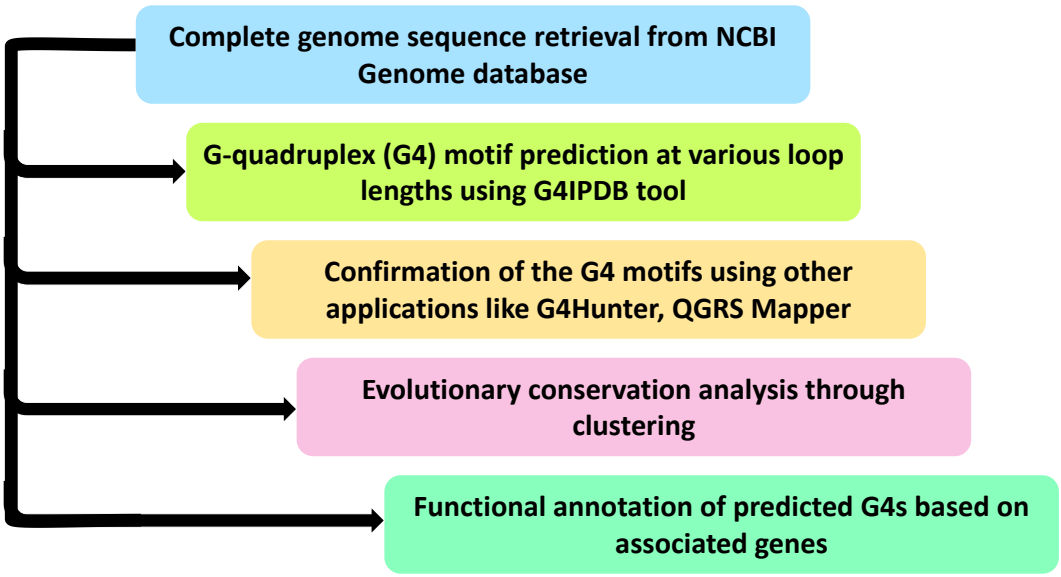

Figure 2.1. Flowchart depicting workflow of in-silico analysis used for genome mining of G4 motifs.

2.3.1.3 Principle of the G4 prediction tools.

G4IPDB

G4IPDB server is an in-house G4 prediction tool developed to predict the G4 motifs in a given sequence[119]. The second updated version of the tool is available at

http://people.iiti.ac.in/~amitk/bsbe/ipdb/update/tool.html. The whole input sequence is scanned to search for a regular expression based on the consensus sequence given below:

$$G_YN_{L1}G_YN_{L2}G_YN_{L3}G_Y$$

Where G represents Guanine; N is any nucleotide including Adenine, Cytosine, Thymine and Guanine, Y is the Guanine tract and can lie between the range 2 - 7, while L is the loop length which can vary from 1 - 20 nucleotides. In a G4 motif, L can vary, but Y usually remains constant. The tool performs a G4 motif search in both strands, Sense and Antisense, providing a comprehensive list of G4s within the input sequence. For each G4 motif predicted, the tools give the cG and cC score based on the number of Guanines and Cytosines in the motif. A higher cG/cC score indicates a higher propensity of the sequence to form a G4 structure both in vitro and in vivo[99].

QGRS Mapper

QGRS Mapper is a web-based tool designed for the identification and analysis of putative G-quadruplex-forming G-rich sequences (QGRS) within the provided nucleic acid sequence and can be accessed at http://bioinformatics.ramapo.edu/QGRS/[120]. It allows users to predict G4 motifs in genomic (e.g., promoters, telomeres) as well as RNA sequences, including alternatively processed pre-mRNAs. The tool uniquely maps the location of QGRS in the context of RNA processing sites, helping the investigation of their contribution to gene expression regulation. Additionally, QGRS Mapper provides an interactive graphical visualization of the output data, which displays the alternative RNA products along with their QGRS distribution.

G4Hunter

The G4Hunter tool predicts G4 motifs on the basis of the G-richness and G-skewness of the input sequence [3]. It is available as both a Python-based standalone script (https://github.com/LacroixLaurent/G4Hunter) and a web server (http://bioinformatics.ibp.cz). For each G4 motif predicted, the tool assigns a quadruplex propensity score, with higher scores indicating a greater likelihood of

G4 formation in vitro. Unlike G4IPDB and QGRS Mapper, G4Hunter does not rely on classical regular expressions, enabling the prediction of non-classical G4 motifs that deviate from the canonical consensus sequence.

2.3.1.4 Identification of evolutionarily conserved G4 motifs

The G4 motifs of all the available completely sequenced bacterial strains and viral isolates were clustered either manually or using the NCBI Nucleotide BLAST tool to evaluate the percent conservation of the motifs. The criteria for a G4 motif to be considered evolutionarily conserved were deemed to be present in ≥ 90 % of the genomes for that particular species.

2.3.1.5 Functional Annotation

The predicted G4 motifs were functionally annotated based on the genes harboring them. G4 motifs located within 500 nucleotides upstream of a gene were considered to be in the promoter region. In contrast, those present in the open reading frame (ORF) regions were considered to be in the coding region. Additionally, the motifs were also classified based on their presence in the sense and antisense strand with respect to the gene direction. The distribution of the G4s predicted through different prediction tools along with their genomic location and the genes were represented using R/ShinyCircos accessible at http://shinycircos.ncpgr.cn/[121]. The consensus logo of the selected G4 motifs studied in the current thesis work were generated using WebLogo server[122].

2.3.2 One dimensional proton Nuclear Magnetic Resonance (1D ^{1}H NMR) Spectroscopy

Nuclear Magnetic Resonance (NMR) spectroscopy is a powerful technique employed for analyzing the molecular structure and dynamics. Among the various NMR techniques available, one-dimensional (1D) NMR spectroscopy serves as a fundamental method, offering critical insights into molecular structure, composition, and interactions[123,124]. The realization of the significance of NMR spectroscopy in structural biology came early on, with the revelation of proteins being dynamic entities rather than just being static structures, as elucidated by the

X-ray studies of that era. Thereafter, NMR spectroscopy has been employed to provide an atomic resolution of dynamic biomolecular motions.

The principle underlying NMR spectroscopy is that specific non-zero spin angular momentum nuclei possess a magnetic moment, which interacts with an external magnetic field (B_0). When such nuclei containing samples are exposed to a strong magnetic field, they align either parallel or anti-parallel to the field, creating a net magnetization. This equilibrium is disturbed upon the application of a radiofrequency (RF) pulse, causing the nuclei to wobble or precess and emit signals that the NMR spectrometer can detect. The precessional frequency of these emitted signals, known as the *Larmor frequency* ($\omega = \gamma B_0$) (in MHz), is directly proportional to the magnetic field strength (B_0) (in MHz/T) and the gyromagnetic ratio (γ) of the nucleus (in T). Only nuclei with a spin angular momentum are NMR-active, characterized by nuclear spin quantum number (I) and is NMR detectable. For example, NMR active nuclei with $I \neq 0$, such as ^{1}H and ^{13}C ($I = 1/2$), while NMR inactive nuclei with $I = 0$, such as ^{12}C, ^{16}O, ^{32}S[124].

As hydrogen atoms are abundant and highly sensitive to NMR detection, Proton (^{1}H) NMR Spectroscopy remains of the most widely employed NMR. It yields detailed information about the number of protons and the surrounding environment within a molecule. The frequency difference between a sample proton and a reference signal, represented as *chemical shift*, a key parameter in proton NMR spectroscopy. This shift is influenced by the electronic environment of the proton, including shielding or de-shielding effects produced from neighboring atoms, functional groups, or π-electron clouds. The atomic-level resolution of NMR is associated with the occurrence of chemical shifts and analysis of these shifts, signal splitting (spin-spin coupling), and integration (relative proton count), which provide structural insights into molecular connectivity. It also elucidates information regarding molecular composition through the identification of functional groups and the analysis of complex mixtures[124].

In a 1D NMR spectrum, resonance intensity is displayed along a single frequency axis and chemical shift is expressed in ppm relative to an internal reference compound:

$$\delta\ (ppm) = \ 10^6 \frac{\nu - \nu_0}{\nu_0}$$

where ν is the observed signal frequency in Hz and ν_0 is that of the internal reference. Different data sets recorded at different magnetic field strengths can be compared on the basis of their chemical shifts expressed in ppm. Standard references include tetramethylsilane (TMS) for organic solvents, 2,2-dimethyl-2-silapentane-5-sulfonic acid (DSS) for water-based solvents. Additionally, the NMR data is also calibrated along the water signal. Moreover, an interaction between two compounds or macromolecules can be detected based on the change in chemical shifts, for example, a change in the chemical shifts of substance A upon addition of substance B denotes an interaction between the two[125].

NMR spectroscopy is extensively utilized to study G-quadruplex structures under physiologically relevant solution conditions. Unlike extended double-helical DNA structures such as B-DNA which are devoid of global interaction information, G-quadruplexes exhibit globular folding, allowing the detection of global interaction information. NMR Spectroscopy is a powerful tool for analyzing the G-quadruplex secondary structures in DNA/RNA. The imino protons of guanines involved in G-tetrad formation display characteristic chemical shifts in the range of 10 – 12.5 ppm[126]. This region is well-differentiated from the imino resonances arising from other DNA conformations, including duplex, single-stranded, or other secondary structures. For example, the duplex DNA structures exhibit chemical shifts in the 13 - 14 ppm region arising out of Watson-Crick hydrogen bonding[127]. Hence, the imino resonances of guanines involved in Hoogsteen-hydrogen bond base pairing, which is the hallmark of G4, gives a clear and direct indication of its formation and interactions with small molecules or ligands[128].

In the research work presented in the thesis, NMR spectroscopic studies were carried out using Bruker AVANCE III 400/500 MHz (BioSpin International AG, Switzerland) spectrometer equipped with a 5 mm broadband (BBI) inverse probe. All the data were recorded at 25 °C. All the NMR data processing and analysis was performed using TopSpin v4.0.6 software (academic license).

2.3.3 Circular Dichroism (CD) Spectroscopy

Circular Dichroism Spectroscopy, an absorption spectroscopy, utilizes circularly polarized light to study the structural properties of optically active chiral compounds. Circular dichroism represents the differential absorption of left and right-handed circularly polarized light and occurs when a chiral optically active molecule preferentially absorbs one direction of the circularly polarized light, which can be measured and quantified.

$$\text{Circular dichroism} = \Delta A = A_L - A_R$$

Here, A_L and A_R denote the absorptions of left and right circularly polarized respectively.

CD Spectroscopy is usually employed to study the higher order structure of biological macromolecules. It finds its primary application in analysis of secondary structure or conformation of macromolecules, particularly proteins and nucleic acids. Additionally, changes in the CD spectra depict the dynamic changes in the secondary structure of a macromolecule upon interaction with small molecules, cations or other macromolecules, as well as with changing chemical environment due to changing temperature, ionic strength, pH, or denaturants[129].

The CD spectrum is often expressed in degrees of ellipticity, θ, which is a measure of the ellipticity of the polarization:

$$tan\,\theta = \frac{E_L - E_R}{E_L + E_R}$$

where E is the magnitude of the electric field vector.

The CD signal displayed by any biological macromolecule usually provides a signature for a given secondary structure, which is referred to as its signature CD spectrum. CD spectroscopy has been widely used for the primary structural characterization of G-quadruplex structures. G4 structure differences arising due to differential G-quartet stacking, strand directionality give rise to characteristic signature CD spectral profiles. G-quadruplex structures display three distinct topologies, namely, parallel, anti-parallel and hybrid or mixed. The signature spectra for these topologies are classified on the basis of their wavelength maxima

and minima, which is ~265 nm maximum, ~245 nm minimum for parallel, ~295 nm maximum, ~260 nm minimum for anti-parallel and ~295 nm maximum, ~260 nm maximum, ~245 nm minimum for hybrid G4 structures.

Furthermore, interactions of G4 structures with cations or ligands induce conformational changes that are reflected in the CD spectra, offering insights into the stabilizing or destabilizing effects of the ligands.

CD Spectroscopy can also be employed in elucidating the stabilizing effect of cations or ligands on the thermal stability of G4 structures. The stability is usually quantified in terms of melting temperature (T_m) assessed through a change in the CD signals, with increasing concentration of the cations or ligands, and depicted as ΔT_m. The higher the Tm, the higher the stability of G4 structures (Figure 2.2).

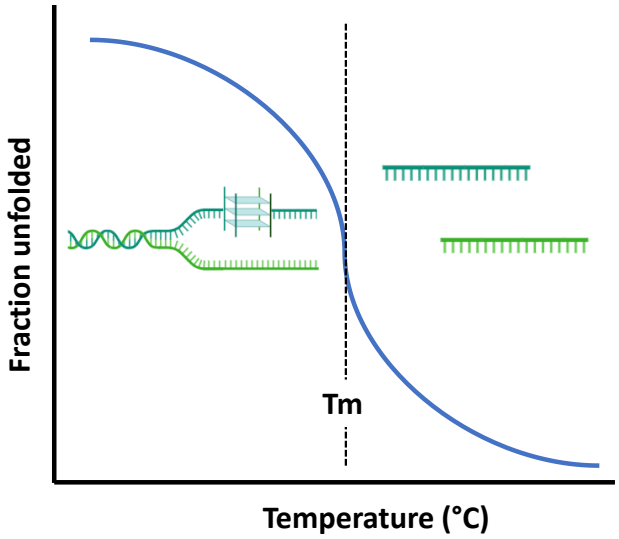

Figure 2.2. Depiction of thermal denaturation profile of a G-quadruplex structure.

In the current research work, CD spectroscopic experiments were performed at 25 °C with a scanning rate of 50 nm/min using Jasco J-815 Spectropolarimeter (Jasco Hachioji, Tokyo, Japan). The instrument was equipped with a Peltier Junction temperature controller. Spectra were recorded in a 1 mm path length cuvette with a wavelength range set from 220 to 320 nm. To avoid signal contribution from buffer components, a blank spectrum was recorded before each measurement and subtracted from the sample's CD spectrum prepared in the same buffer. For CD

spectroscopic titrations with cation, the concentration of salt was increased with each subsequent titration.

CD Melting analysis was performed for every sample within a temperature range of 25 °C - 95 °C. The ramp rate was set to 2 °C/min for each experiment. For ligand titrations, the ligand was subsequently added until the specified Drug/Nucleic acid (D/N) ratios were reached, and spectral and thermal melting analyses were performed.

2.3.4 Electrophoretic Mobility Shift Assay (EMSA)/ Gel retardation Assay

EMSA is a widely used technique, to analyze the size and molecularity of the biological macromolecules. The underlying mechanism of the assay is that molecules exhibit in different electrophoretic mobilities when resolved on a native polyacrylamide or agarose gel based on their size and charge[130]. G4 structures adopt two conformations: intra- and inter-molecular. An intramolecular G4 structure results from the association of guanines involved in quadruplex formation from a single nucleic acid strand. An intermolecular G4 structure arises when the guanines involved in structure formation are present in multiple strands. Consequently, an intermolecular G4 migrates slowly compared to an intramolecular G4, due to its increased molecular weight.

To assess the molecularity of a G4 structure, a corresponding linear mutant sequence is loaded alongside the G4 sequence. The mutant sequence is designed to lack sufficient guanines, rendering it incapable of folding into a G4 structure. The G4 structure migrates faster than the mutant sequence, exhibiting an intramolecular topology, owing to its compact folding. On the other hand, an intermolecular G4 sequence migrates more slowly than its mutant sequence when loaded on native PAGE (Figure 2.3). In the studies presented in this thesis, Native PAGE was performed by running a 15 - 18% polyacrylamide gel in 1X TBE buffer. After polymerization, the gels were assembled into a Bio-Rad Mini-PROTEAN Tetra Vertical Electrophoresis unit. For each G4 motif, a mutant oligonucleotide of similar length (G substituted with T), and standard G4-forming sequences, *ckit 22* and *bcl-2* along were loaded as negative and positive controls respectively. Prior to loading, samples were mixed with 6X orange dye and electrophoresed at 70 V at

4 °C until the dye front reached three-fourths of the gel length. Gels were stained with ethidium bromide and imaged using the ImageQuant LAS4000 system (GE Healthcare, Sweden).

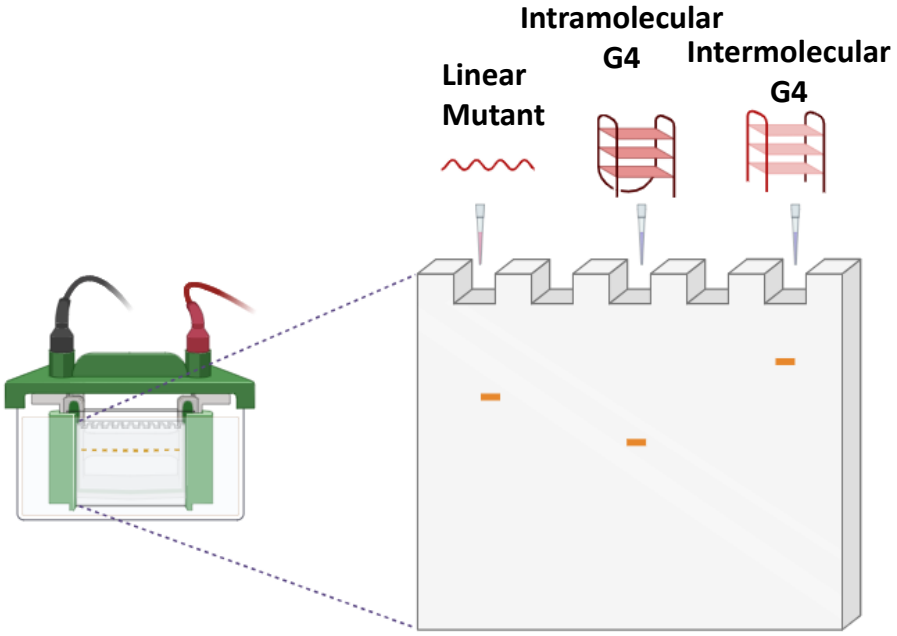

Figure 2.3. Schematic representation of EMSA depicting molecularity of G4 structure with respect to linear mutant in Native PAGE.

Gel retardation assay can also be exploited to study the interaction of ligands or proteins with G4 motifs. The addition of these molecules results in changes to the secondary structure and molecular weight of the nucleic acids. This altered molecular weight results in a shift of the migration pattern of the nucleic acid-ligand/protein complexes (Figure 2.4). For ligand-G4 interaction and protein-G4 interaction analysis, the complexes were then resolved on 3% agarose gels prepared in 1X TBE buffer and run on ice at 55 V using the Bio-Rad Mini-Sub Cell GT system. Gels were visualized with the ImageQuant LAS4000 system (GE Healthcare, Sweden).

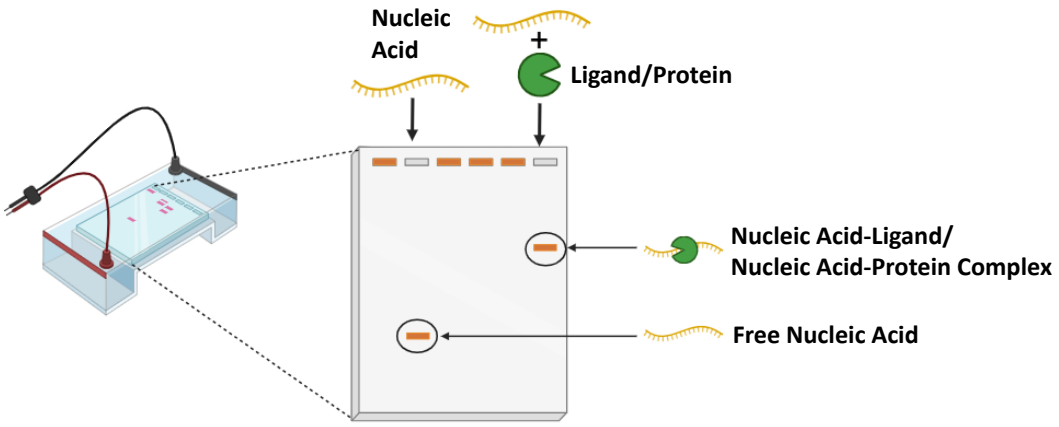

Figure 2.4. Schematic representation of EMSA depicting shift in band mobility of G4 structure upon interaction with ligand or protein molecule in agarose gel.

2.3.5 Fluorescence titration assay

Fluorescence is the emission of light by a molecule (fluorophore) arising due to the transition of an excited electron from its first excited or higher energy state to ground state. The excitation is caused by photon absorption by a molecule in the singlet ground level, promoting it to higher excited energy level. Upon returning back to the ground level after a finite time (10^{-8} s), the emitted energy is lower than that absorbed and therefore emitting at a longer wavelength. The surrounding chemical environment affects the energy amount released in emission[131]. Fluorescence efficiency is determined by factors such as the molecular extinction coefficient and the quantum yield, which can be correlated to absorption and fluorescent efficiency of the molecule. A fluorophore bound associated with a biological macromolecule is susceptible to conformational changes that can result in either enhancement or photo-quenching. These changes in fluorescence intensity is exploited to assess binding affinity and specificity of small molecules/ligands/protein towards macromolecules (nucleic acids/protein).

In the current study, we employed this approach to detect the change in fluorescence intensity of the small molecule/protein upon binding to the nucleic acid. The fluorescence titration experiments have been performed on Synergy H1 multi-mode microplate reader (BioTek Instruments, Winooski, VT, USA) using 96 well Corning half area black plate at 25 ºC to investigate ligand-nucleic acid interaction. Fluorescence spectroscopy measurements were performed using Fluorolog®-3

Spectrofluorometer (Horiba Scientific, Jobin Yvon, Palaiseau, France) operated by FluorEssence software (Horiba Scientific, Jobin Yvon, Palaiseau, France). The excitation and emission wavelengths of each small molecule were determined by observing their absorption and fluorescence spectra, respectively. We used fluorescence analysis in the following experiments:

2.3.5.1 Thioflavin T light-up assay

The oligonucleotides, both G4 motif and mutant sequences (5 μM), were heated at 95 °C and gradually annealed at room temperature. Thioflavin T (10 μM) solution was added to the oligonucleotide solution, thoroughly mixed, and incubated for 15 mins. Fluorescence intensities were recorded at the emission wavelength of 495 nm following excitation at 425 nm in a Corning half-area black plate using the BioTek microplate reader Synergy H1 system.

2.3.5.2 Thioflavin T Displacement Assay

A two-molar equivalent Thioflavin T (10 μM) solution was added to the reannealed oligonucleotides (5 μM), and fluorescence measurements were detected after a 10 min incubation at room temperature. Subsequently, five molar equivalents of G4-specific ligands (BRACO-19, TMPyP4) were added to each oligonucleotide-ThT mixture and incubated for 30 mins, and fluorescence intensity measured. The fluorescence intensity of ThT alone (without oligo) was also recorded to subtract the background interference. The percent displacement of ThT was calculated using the equation:

$$\text{ThT Displacement } (\%) = 100 - [100 \times \frac{F_I - F_b}{F_{I_0} + F_b}]$$

Where F_I is the fluorescence of the oligonucleotide + ThT sample in the presence of G4 ligand, F_{I_0} is the fluorescence of the oligonucleotide + ThT sample in the absence of G4 ligand, and F_b is the fluorescence of ThT alone.

2.3.5.3 Fluorescence Titration Assay

All oligonucleotide samples were subjected to serial dilution, and each reaction was performed in a set of duplicates, with a final reaction volume of 50 μl per well in a

Corning half-area 96-well black plate. The final well in series served as a blank control and did not contain an oligonucleotide. The ligand (BRACO-19) solution was titrated with the oligonucleotide solution, and the fluorescence response was monitored. Fluorescence emission was measured at 440 nm with excitation at 360 nm. The fluorescence signal recorded from the blank control well was used to subtract from all other wells, to avoid any interference from buffer components. Data was analyzed using Sigma Plot 15.0 software (Systat Software, Chicago, IL, USA). The equilibrium binding was modeled using the following equation:

$$f = \frac{B_{max1} \times \text{abs (x)}}{K_{d1} \times \text{abs (x)}} + \frac{B_{max2} \times \text{abs (x)}}{K_{d2} \times \text{abs (x)}}$$

Where B_{max_1} and B_{max_2} denote the maximum number of binding sites, K_{d_1} and K_{d_2} denote the equilibrium dissociation constants.

2.3.5.4 Fluorescence spectroscopy

Steady-state fluorescence measurements were conducted on a Fluorolog®-3 Spectrofluorometer (Horiba Scientific, Jobin Yvon, Palaiseau, France), controlled via FluorEssence software. Oligonucleotide solutions were titrated into the protein samples (5 μM) with increasing nucleic acid-to-protein (N/P) ratios ranging from 0 to 2.0 at 25 °C. Emission spectra were recorded from 285 to 420 nm, with excitation at 274 nm, corresponding to tyrosine absorption. Data were processed and analyzed using OriginPro (OriginLab Corporation).

2.3.6 Isothermal titration calorimetry assay (ITC)

Isothermal titration calorimetry (ITC) is a valuable and highly robust technique providing information about the molecular interactions and binding affinities of nucleic acid and ligand molecules and depicting a complete thermodynamic profile of this macromolecular interaction[132,133]. ITC has established a promising role in studying a wide range of biomolecular interactions and a key role in affinity-based small-molecule screening, offering a reliable approach to determine the affinity between two interacting molecules[133–135]. A major advantage offered by ITC is the absence of modification requirements for interacting partners, such as the use of fluorescent tags or solid surface immobilization.

The technique utilizes a sensitive calorimeter that directly measures the heat absorbed or released during the binding events due to the interaction between two molecules[133]. The heat measured enables the determination of important thermodynamic parameters, including association constant (K_a), stoichiometry (n), enthalpy (ΔH), and entropy (ΔS). These parameters are calculated using the equation:

$$\Delta G = - RT \ln K_a = \Delta H - T\Delta S$$

Where ΔG is the Gibbs' free energy, R is the universal gas constant, and T is the temperature.

The microcalorimeter contains two cells: a reference cell and a sample cell. The reference cell is filled with degassed water while the sample cell is filled with the sample of interest, into which the binding molecule is introduced gradually using an injection syringe (Figure 2.5). A heat-sensing device evaluates the temperature difference between these two cells. Initially the temperature difference is zero, which changes upon injection of reactant into the sample cell, as the interaction takes place between the sample and reactant. The temperature difference arises due to the heat change taking place upon binding interactions between the two, which is recorded by the calorimeter[136]. This is reported to the heaters, which restores the temperature difference between the reference and sample cell. The observed heat change is recorded after each injection in an individual reaction, which is plotted against the time of injection to generate a binding isotherm (Figure 2.5). The key thermodynamic parameters are then subsequently derived from this binding isotherm[137].

In the present thesis work, oligonucleotides were added into the sample cell into which the ligand molecule was titrated, both of which were prepared in the same 1x KPO_4 buffer. All the calorimetric titrations were carried out at 25 °C by injecting 1.77 µl - 1.66 µl aliquots of ligand solution into oligonucleotide sample solution at 120 s intervals, for a total of 22 injections. A separate reaction was performed by titrating the ligand solution at same concentration into the buffer solution to analyze the heat of dilution, for each experiment. The binding isotherm generated from this ligand-buffer titration was subtracted from that of ligand-sample titration and fitted

with appropriate binding equation of two-site binding mode provided in the MicroCal Origin software version 7 (Microcal Software Inc. Northampton, MA, USA) which yielded the reaction binding constants.

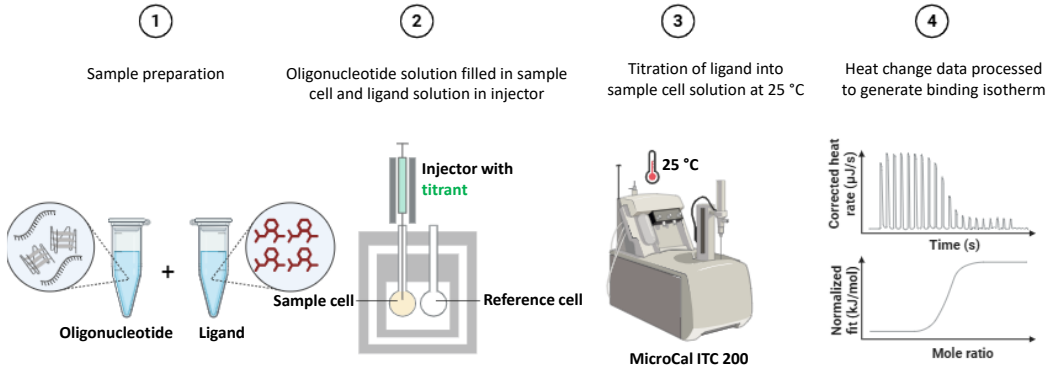

Figure 2.5. Workflow depicting an ITC titration to generate a binding isothermogram. (Adapted from Biorender)

2.3.7 Reporter gene assay

Reporter gene assays are frequently utilized to investigate gene expression and regulation. This technique relies on the usage of a reporter gene, placed downstream of a regulatory target sequence. Based on the activation or repression of this target sequence, the expression of the reporter gene changes, which can be quantified using different detection methods[138]. The detection methods are straightforward and typically include easily detectable gene products such as luminescence or fluorescence, making the technique quite convenient and reliable. Reporter gene assays are widely used to examine the impact of G4 structure formation on gene expression. This is achieved by linking a G4-forming sequence to a reporter gene sequence, such as Green Fluorescent Protein (GFP) or luciferase, and analyzing it through reporter gene expression. Additionally, the addition of ligands on G4 structures can stabilize them, resulting in impeding the progression of ribosomal assembly, and regulating the translation process. This can aid in analyzing the effect of small molecules on stabilization of G4 structures in vivo[139]. Standard reporter-based assays include the luciferase assay, β-galactosidase assay, and green fluorescent protein (GFP) having detection methods of luminescence, color and fluorescence.

In our experimental setup, we have utilized the monomeric teal fluorescent protein (mTFP) gene as a reporter gene. We have employed a molecular cloning-based strategy to insert the G4 motif adjacent to the mTFP gene and assessed the effect of its stabilization through reporter gene expression upon ligand exposure.

Cloning

This method employed recombinant molecular cloning, involving restriction digestion, ligation, and subsequent bacterial transformation. Herein, the vector (either pCAG-mTFP/ mTFP-pET43a+) was digested with the restriction enzymes *NdeI* and *XhoI*. The G4 motif was inserted right after the mTFP gene start codon using an overhang-containing, G4-specific forward primer incorporating an *NdeI* restriction site, and a common reverse primer having an *XhoI* restriction site. The insert which was the amplified G4-mTFP PCR product (~728 - 735 bp) was gel extracted, and both insert and vector were double digested using the same restriction enzymes. The digested fragments were then ligated in a 3:1 ratio of insert: vector using T4 DNA ligase. The ligation product was subsequently transformed into *E. coli* DH5α strains, and positive colonies were confirmed by colony PCR. The resulting positive plasmids were isolated, and further validated by double restriction digestion and plasmid PCR.

mTFP expression analysis

In Escherichia coli cells

The recombinant G4-mTFP-pET43a^{+} constructs were transformed into *E. coli* Rosetta strain. A primary culture was grown overnight at 37 °C from these transformed cells and used for inoculating a secondary culture. The secondary culture was grown till $O.D._{600}$ = 0.3 and treated with the ligand at the specified concentration for 45 mins. Thereafter the mTFP protein expression was induced using 0.5 mM Isopropyl β-D-1-thiogalactopyranoside (IPTG) for 4 hours. After that, the cells were harvested, fixed using 5% paraformalydehyde and mounted on a glass slide and covered with a cover-slip. The slides were then visualized using confocal microscopy (Olympus), and acquired images were analyzed using Olympus Fluoview software.

In HEK293T cells

The recombinant pCAG-G4-mTFP constructs were transfected in human embryonic kidney (HEK293T) cells, using the calcium phosphate method in a six-well plate provided with coverslips. The cells were subsequently treated with specified concentrations of the ligand after 4 h of transfection, and the mTFP expression level was observed after 24 h of treatment using a fluorescence microscope. ImageJ software was used for comparative fluorescence intensity analysis. Statistical significance was determined using a Two-Way ANOVA to identify significant differences between untreated and treated sets of wild-type and mutant samples. Data were analyzed using GraphPad Prism software version 8.0.2 and represented as mean ± SD.

2.3.8 Growth Inhibition assay

A growth inhibition assay is most commonly used to evaluate the effectiveness of compounds, such as antibiotics, small molecules or ligand in preventing the growth of bacteria. The change in bacterial growth can be monitored, either visually or through optical density measurements and accordingly determine the minimum inhibitory concentration (MIC) of a compound and assess its antibacterial efficacy. In the work presented in the thesis, we performed MTT assay to analyze the inhibitory effect of G4 binding ligand on bacterial growth.

MTT growth inhibition assay

MTT assay is a colorimetric assay utilized to assess cell viability and proliferation[140]. MTT is a yellowish, water soluble tetrazolium salt 3-(4,5-dimethylthiazol)-2,5 diphenyl-tetrazolium bromide which gets enzymatically converted to formazan, a water-insoluble form, in metabolically active cells[141,142]. The MTT assay can be divided into two stages:

Stage 1: The conversion of MTT to intense purple-blue colored formazan in viable cells by the dehydrogenase enzymatic activity of live cells. This formazan and forms insoluble crystals upon cellular interaction[143].

Stage 2: Dissolution of formazan crystals for spectrophotometric quantification.

One of the advantages offered by this assay includes the simultaneous measurement of multiple samples using a 96-well-plate reader[144]. MTT assay was performed for investigating the inhibitory effect on *A. baumannii* cell growth upon exposure to the ligand (BRACO-19). The bacteria were cultured in BHI broth media at 220 rpm, 37°C until they reached $O.D._{600}$ = 0.5. Then, the culture was diluted to $O.D._{600}$ = 0.08 using fresh media. This culture was then again diluted 150 fold using fresh media, and 50µl was transferred to each well of a 96-well plate. Dilutions were prepared from the stock solution (400 µM) of BRACO-19 using fresh BHI media and added to the respective wells, of which last well served as blank (without ligand). The experiment was performed in triplicates. The plates were incubated at 37 °C for 24 h, post which, 10 µl of MTT (stock solution of 10 mg/ml) was added to each well and incubated further for 4 h. The formazan crystals were dissolved by addition of 100 µl DMSO, and absorbance was recorded using a microplate reader (BioTek) at 570 nm. The data obtained was analyzed via Graphpad Prism software.

2.3.9 Total RNA isolation and cDNA synthesis

Total RNA isolation and cDNA synthesis involves a two-step protocol. In the first step, total RNA was extracted TRIzol reagent (Invitrogen) from bacterial cells, both ligand-treated and untreated sets by centrifugation and washing steps to isolate purified RNA. The concentration and purity of isolated RNA were measured using a Nanodrop (Thermoscientific) and quantified in ng/ul and A260/A280, respectively. In the second step, 2 µg of purified RNA was used as a template for cDNA synthesis a 20 µl reaction by PrimeScript cDNA synthesis kit (Takara Bio USA, Inc.) according to the manufacturer's instruction (Figure 2.6).

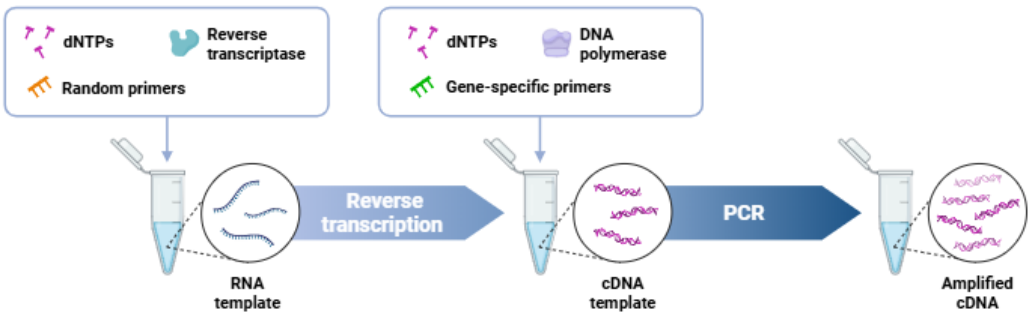

Figure 2.6. Schematic workflow depicting a two-step RT-PCR reaction. (Adapted from Biorender)

2.3.10 Quantitative reverse transcription PCR (qRT-PCR)

qRT-PCR is a sensitive and modified version of the normal PCR reaction used to detect and quantify RNA levels, reflecting the differential gene expression. The technique involves the conversion of RNA to its complementary DNA (cDNA) using reverse transcriptase enzyme, which then serves as a template for PCR amplification. The amount of DNA product is detected in real-time during each cycle using either fluorescent dyes or probes[145].

Fluorescent Dyes

These are non-specific sequence-independent dyes that intercalate into the amplified dsDNA and emit a fluorescence signal. The fluorescence intensity increases with increasing DNA amplification over time[146].

DNA Probes

These are sequence-dependent probes that are labeled with a fluorescent reporter dye and a quencher. The probe and the quencher bind to the specified sequence in the amplified DNA, and when the probe is encountered by the polymerase, the reporter dye is cleaved. Upon separation of the probe from the quencher, fluorescence signal is emitted (Figure 2.7)[146].

In the current thesis work, we used a fluorescent dye-based (SYBR-Green) system to detect gene expression. SYBR-Green is a nucleic acid intercalating fluorophore which binds with the dsDNA and emits fluorescence to be detected by the fluorescence detector.

We employed qRT-PCR to investigate the difference in gene expression of *A. baumannii* G4 harboring motifs on treatment with G4 binding ligand: BRACO-19. The reaction was carried out out in a PCR master reaction mix consisting of 1X iTaq Universal SYBR Green Supermix (Bio-Rad Laboratories, Inc.)/Applied Biosystems PowerUp SYBR Green Master Mix, 0.5 µM of each primer and 10 - 50 ng of cDNA as the template. The final reaction volume was kept 10 – 20 µL in a 96-well PCR plate and reaction was performed on a QuantStudio 3 Real-Time PCR System (Applied Biosystems, USA), with 16S rRNA serving as the housekeeping gene. All the samples for the PCR reaction were prepared in duplicates, and the expression of the 16s rRNA was used as a reference for data normalization.

The thermo-cycling conditions used were as follows: initial hold of 2 mins at 50°C; initial denaturation at 95°C for 10 mins followed by 40 cycles of 95°C for 15 s and 60°C for 1 min, and a final extension at 72°C for 10 mins. Data were analyzed using the comparative ΔΔCt method. The proportionate change in gene expression was assessed by change in expression of the target gene in treated as compared to untreated. Statistical analysis was performed using unpaired t-test in GraphPad Prism v 8.0.2 (GraphPad Software, San Diego, CA).

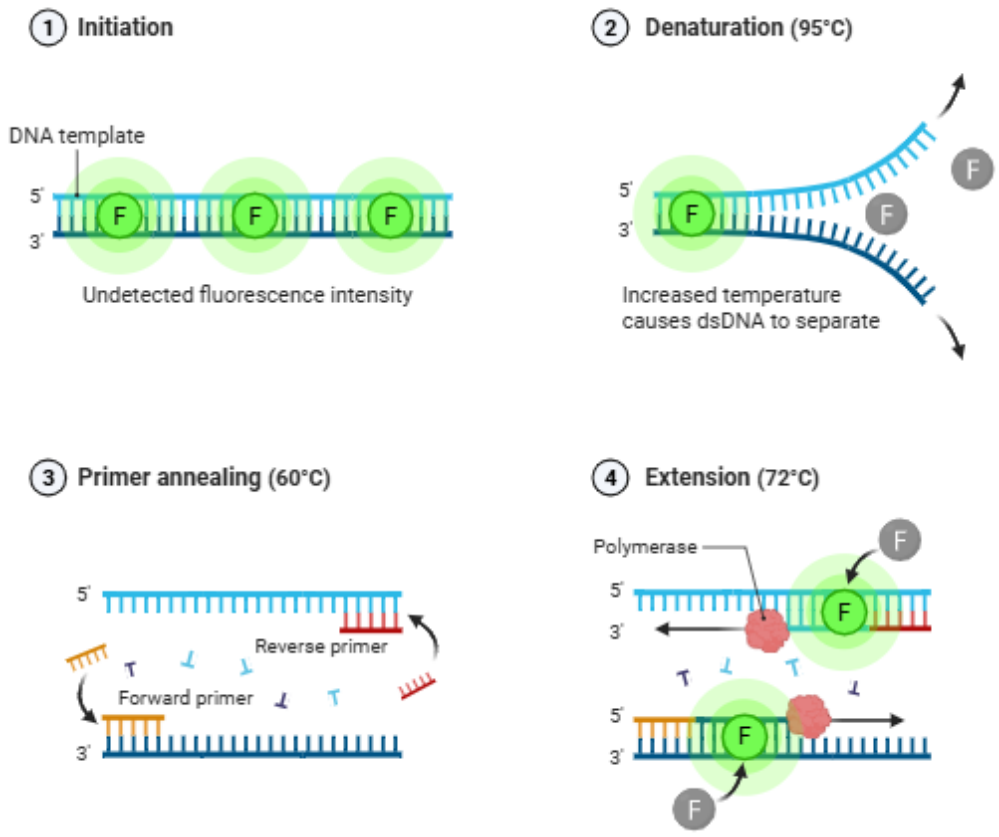

Figure 2.7. Diagrammatic representation of steps of a qRT-PCR reaction. (Adapted from Biorender.)

2.3.11 Biofilm Formation

Biofilm formation is a key stress response mechanism adopted by bacteria, aiding their survival in adverse conditions, and acting as a major contributor to antimicrobial resistance. Biofilm formation can occur both on biotic and abiotic surfaces[147].

In this study, we examined the ability of *A. baumannii* establish biofilms on glass coverslips, to assess effect of G4 binding ligand in particular. A 0.4 McFarland suspension of *A. baumannii* was diluted hundred-fold in BHI broth, then treated with BRACO-19 (25 µM, 12 µM, 6.25 µM). The treated and untreated sets of bacterial cells were incubated undisturbed on coverslips placed in a 12-well plate for 48 h 37 °C in presence of 5 % CO_2 (Figure 2.8). Following incubation, the cells were fixed using 4% paraformaldehyde, stained with DAPI (10 µg/ml), and

visualized using a confocal laser scanning microscope with Z-stack imaging. Acquired images were processed using FluoView software.

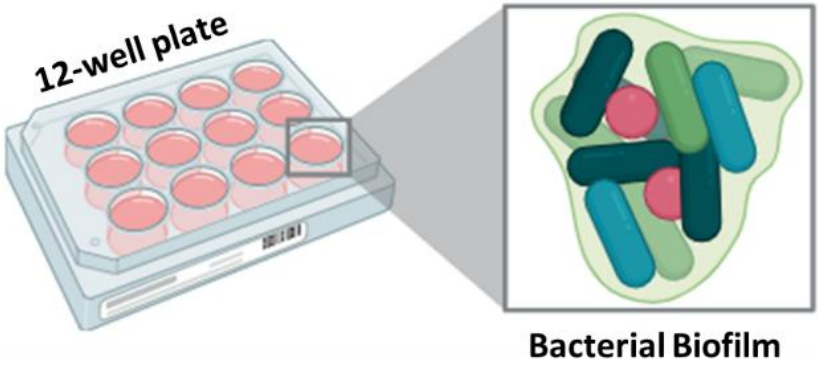

Figure 2.8. Diagrammatic representation of bacterial biofilm formation in a 12-well plate.

2.3.12 Cloning and expression of Hfq protein

The hfq gene (A1S_3785) from *Acinetobacter baumannii* was amplified by PCR and cloned into the *NdeI* and *XhoI* restriction sites of the pET-43.1a(+) vector representing the full-length Hfq protein. A truncated version of Hfq (Hfq ΔCTD) was similarly amplified, using the same forward primer and an alternative reverse primer, and then cloned in a similar manner. Both constructs were expressed in *Escherichia coli* Rosetta cells. Cultures of recombinant *E. coli* Rosetta were grown overnight in Luria Bertani broth at 37 °C. Protein expression was induced by adding 0.25 mM isopropyl β-D-thiogalactopyranoside (IPTG) to the cultures at $O.D._{600}$ = 0.8, followed by incubation for 16–18 hours at 18 °C. Cells were harvested, washed with 1× PBS, and resuspended in a lysis buffer containing 50 mM Tris (pH 7.5), 1 M NaCl, 1 M urea, 1 mM β-mercaptoethanol, 5% glycerol, 1 mM PMSF, 0.1 mg/ml DNase I, and 1 M $MgCl_2$. After vortexing, homogenization, and sonication, the lysate was clarified by centrifugation. The supernatant was heated at 95 °C for 15 minutes, centrifuged again, treated with RNase A (30 µg/ml) at 37 °C for 1 hour, and re-clarified. The recombinant proteins, fused with a His-tag, were purified using Ni-NTA agarose column after the lysate was loaded onto a pre-equilibrated Ni-NTA column and allowed to bind for 1 h. The column was then washed with buffers containing 50 mM and 100 mM imidazole, and the

recombinant protein was eluted using a buffer with 500 mM imidazole. Eluted fractions were pooled and dialyzed against a buffer containing 50 mM Tris (pH 7.5), 350 mM NH_4Cl, 1 mM EDTA, 0.05 % Triton X-100, and 5% (v/v) glycerol. The purified proteins were visualized by running SDS-PAGE 15 % (for full-length Hfq) and 18 % (for Hfq Δ*CTD*) gels. Protein concentrations were determined by measuring absorbance at 280 nm, using an extinction coefficient (ε = 2980 M^{-1} cm^{-1}) calculated with the Expasy ProtParam Tool (https://web.expasy.org/protparam/).

2.3.13 Viral Cellular Assays

The Japanese Encephalitis Virus (JEV) isolate Vellore P20778 (GenBank accession no. AF080251) was propagated in C6/36 cells.

Virus infection and Cell viability assay

All viral infection studies were carried out by exposing cells to JEV in incomplete growth medium at specified multiplicity of infection (MOI) for 1 h. Subsequently, cells were washed with 1X PBS and replenished with complete medium. Cells were administered with specified BRACO-19 concentrations for 24 h post-infection. Cells were then harvested for cell viability assays, RNA isolation, and Western blot analysis, while culture supernatants were stored for virus titration using plaque assay. Each experiment was performed in biological triplicates.

Cell viability was assessed using the CellTiter-Glo® assay kit following the manufacturer's instructions. The percentage of cell viability was calculated according to the following equation:

$$\frac{\text{ATP luminescence of experimental condition}}{\text{ATP luminescence for untreated control}} \times 100$$

The values were normalized to the values of the untreated control.

RNA isolation, qRT - PCR, and Western Blotting

Total RNA was isolated using TRIzol reagent. cDNA was synthesized using Bio-Rad iScript cDNA synthesis kit. Quantitative real-time PCR (qRT-PCR) was carried out on a QuantStudio 6 system (Applied Biosystems) using SYBR Green dye to

quantify JEV RNA levels, with GAPDH serving as the internal control. Each qRT-PCR reaction was performed in duplicates.

For Western Blot analysis, cells were lysed in ice-cold lysis buffer for 1 h at 4 °C and supernatant containing the protein was collected. The lysis buffer consisted of 150 mM NaCl, 1 % Triton X-100, 50 mM Tris-HCl (pH 7.5), 1 mM PMSF, and a protease inhibitor cocktail. Protein concentration in the stored cell lysates were quantified using the BCA assay. Prior to electrophoresis, samples were denatured by heating at 95 °C for 10 mins in 5X loading dye (40% glycerol, 20% β-mercaptoethanol, 0.04% bromophenol blue, 6% SDS, 0.25 M Tris-HCl, pH 6.8). Equal amounts of protein were loaded onto SDS-PAGE gels and transferred to PVDF membranes for immunoblotting. Blots were visualized using the Bio-Rad Gel Doc XR+ system, and band intensities were quantified using ImageJ software.

CHAPTER 3

CHARACTERIZATION OF G-QUADRUPLEX STRUCTURES IN GENES INVOLVED IN SURVIVAL AND PATHOGENESIS OF *ACINETOBACTER BAUMANNII* AS POTENTIAL DRUG TARGETS

Chapter 3

Characterization of G-quadruplex structures in genes involved in survival and pathogenesis of *Acinetobacter baumannii* as potential drug targets

3.1 Introduction

As per the World Health Organization (W.H.O.), multidrug-resistant (MDR) bacterial infections are among the top 10 growing threats to human health. This ever-increasing concern has raised apprehension about the emergence of community-acquired and nosocomial infections. The most commonly reported bacteria accounting for MDR-related nosocomial infections include *Acinetobacter baumannii*, *Enterococcus faecium, Staphylococcus aureus, Klebsiella pneumoniae, Pseudomonas aeruginosa,* and *Enterobacter sp.* among which *A. baumannii* tops the critical priority pathogen list[148–150]. *A. baumannii* belongs to the genus *Acinetobacter* which comprises of ~50 species and stands as one of the most important pathogens amongst the genus, with high mortality rate[151]. The bacteria has a unique ability to survive in the hospital environment and develop resistance to antibiotics, hence leading to troublesome hospital outbreaks and therapeutic challenges for reported infections[152]. The bacteria are primarily found to colonize the skin and fluid-filled organ systems of the body such as the oropharynx, respiratory secretions, and the digestive tract[153]. The occurrence of infection caused by this bacteria is comparatively higher among immunocompromised individuals, particularly those having a longer duration of hospital stay[154]. The notorious pathogen, *A. baumannii* has developed extensive resistance to most first-line drugs leaving only a few therapeutic options available for treatment. The available options include Polymyxins (Colistin), certain Tetracyclines (Tigecycline), Carbapenems, and specific combinatorial therapies. However, these options also come with the complications of adverse side effects or limited clinical data[155]. Therefore, developing effective therapeutic strategies to combat

infections associated with these resistant strains of *A. baumannii* still remains a challenge and needs to be dealt with urgently.

Nucleic acid-based therapeutics have recently emerged as a novel strategy to combat human diseases[156–159]. In recent times, along with the duplex canonical form of nucleic acids, various non-canonical structures are being reported to be formed in eukaryotes and prokaryotes[2,160,161]. Among the multiple non-canonical structures, G-quadruplexes (G4s) are the most stable and are involved in the regulation of gene expression in the genomes of mammals[162], viruses[158], bacteria[163,164], protozoa[165], and plants[166,167]. Owing to their crucial involvement in normal cellular functioning and physiology, which is based on their location in the genome, these structures have attracted considerable attention. G4s are actively involved in human diseases such as cancer[168], neurodegenerative diseases[169], and pathogenic infections[170]. Varied roles have been reported for G4s in bacterial pathogens including the regulation of gene expression in host-pathogen interactions, efflux pumps, nutrient metabolism, etc., contributing to virulence and the survival of the pathogen[171–173]. However, information regarding the importance of these structures in bacterial genomes and their efficacy as therapeutic targets for bacterial infections is inadequate. Studies focusing on the role of these secondary structures have been reported for commonly associated pathogenic bacteria, namely *N. gonorrhoeae,* implicating the role of G4 in antigenic variation[174], gene regulation in *E. coli*[175], biofilm formation in *P. aeruginosa*, secretion system in *M. tuberculosis*[172], etc. These structures are also frequently associated with nutrient absorption and metal transport in *Paracoccus denitrificans*[176], *Salmonella enterica*[160], and *Helicobacter pylori*[177]. The promoter regions of *Klebsiella pneumoniae* are also reported to harbor G-quadruplex motifs that regulate their respective gene regulation. The genome of *Neisseria meningitidis*[171] and *Vibrio cholerae*[178] are also enriched in the G4 motifs and are associated with essential functions, including pathogenesis. Though some bacterial genomes are explored for the role of G-quadruplex motifs, a large number of them are yet to be investigated, *A. baumannii* is one of them. Most of the bacterial genomes explored to date for the role of G-quadruplex motifs were

GC-rich, while *A. baumannii* has a relatively low GC content (39%). Their location and function in this pathogen would help elucidate the importance of these non-canonical structures in microbial genomics.

In the present chapter, the characterization of evolutionary conserved G4 motifs was performed in the nosocomial pathogen's genome using bioinformatics, biophysical, and cellular-based assays. We identified eight G4 motifs in the genome of *A. baumannii* that play a critical role in bacterial growth, biofilm formation, and pathogenesis. According to existing literature, the formation of DNA G4s within putative G4- forming sequences (PGQPGQs) can be correlated with the formation of corresponding RNA G-quadruplex structures due to sequence homology. The usage of DNA sequences for G-quadruplex investigations is usually preferred due to their efficiency and cost-effectiveness, providing a foundation for the analysis of analogous RNA sequences. Consistent with this approach, DNA oligonucleotides were employed in our in vitro analyses to simulate the G4s in the *Acinetobacter baumannii* genome. All eight selected G-quadruplex motif sequences were able to form stable secondary structures *in vitro* and *in vivo*. The G-quadruplex-specific small molecule, BRACO-19 showed strong affinity and selectivity towards the PGQs and negatively affected the expression of G-quadruplex harboring genes. Collectively, this study reinforces the credible role of G-quadruplex structures in *A. baumannii* genome attracting attention towards targeting of G-quadruplex structures in this bacterium as a therapeutic strategy.

3.2 Material and Methods

3.2.1 Genome mapping and prediction of G-quadruplex forming motifs

Completely sequenced strains of *A. baumannii* were retrieved from the NCBI Genome database (http://www.ncbi.nlm.nih.gov/genomes). G-quadruplex predictions were performed by using our previously established in-house G-quadruplex prediction tool available at G4IPDB (http://people.iiti.ac.in/~amitk/bsbe/ipdb/index.php)[99]. To mine the putative G-quadruplex sequences in *A. baumannii,* the tool performed predictions using the following regular expression:

$$G_{\{T\}}[N]_{\{L1\}}\ G_{\{T\}}[N]_{\{L2\}}\ G_{\{T\}}[N]_{\{L3\}}\ G_{\{T\}}$$

where G refers to Guanine, T is the length of consecutive Guanine tract, N is any nucleotide including Guanine. L1, L2, and L3 are the variable loop lengths ranging from 1 to 20.

Both sense and antisense strands were explored for putative G-quadruplex motifs in the query sequence. Every prediction was listed and scrutinized for its location in NCBI GenBank. The resultant PGQ motifs were then gene annotated for their functions in the genome of the *A. baumannii* strains using NCBI Database Graphics mode. The G4Hunter tool based on GC skewness was also utilized with varying thresholds for the G-quadruplex prediction. The Circos plots were created using ShinyCircos tool.

3.2.2 Oligonucleotide sample preparation

The desalted DNA oligonucleotides were procured from Sigma-Aldrich (St. Louis, MO, USA) and Integrated DNA Technologies (Coralville, Iowa, USA). Stock solutions of 100μM each were prepared by dissolving the lyophilized samples in water as per the manufacturer's protocol. Before each set of experiments, the oligonucleotide samples were allowed to slowly reanneal at room temperature for 2 hours after the denaturation at 95 °C for 10 mins.

3.2.3 One-dimensional ^{1}H NMR spectroscopy

Proton NMR experiments were performed by using AVANCE 500MHz (BioSpin International AG, Switzerland). The spectra were recorded in a 9:1 ratio of H_2O: D_2O solvent at 298 K with 20 ppm spectral width. All AB_PGQs were dissolved in KPO_4 buffer (10 mM, pH 7.5, 80 mM K^+) at a final concentration of 200 μM, and Sodium trimethylsilylpropanesulfonate (DSS) was chosen as the internal reference. NMR data were processed and analyzed by Topspin v4.0.6 software (academic license).

For the BRACO-19 peak broadening analysis, each AB_PGQ was gradually added to 400 μM of BRACO-19 solution containing 80 mM KCl in the subsequent steps according to the specified D/N ratio.

3.2.4 G-quadruplex probe light-up assay

Thioflavin T (ThT, 2 μM) was used as a G-quadruplex probe and was added to 5 μM AB-PGQs and their respective mutants. Fluorescence intensities were collected at 495 nm using an excitation wavelength of 425 nm in a half-area black plate (Corning) using the BioTek microplate reader Synergy H1 system.

3.2.5 Circular Dichroism (CD) Spectroscopy

CD experiments were performed for each oligonucleotide in Tris-Cl buffer (10 mM, pH = 7.4) containing K^+ at 25 °C using Jasco J-815 Spectropolarimeter (Jasco Hachioji, Tokyo, Japan). The spectra were recorded in the wavelength ranging from 220 to 320 nm with a scanning rate of 50 nm/min in a quartz cuvette of 1 mm path length. The final concentration of all oligonucleotides was 20 μM in a final sample volume of 200 μl. Baseline correction using the buffer alone was performed before each experiment. The CD spectral titration analysis was also performed with an increasing concentration of BRACO-19. Recorded spectral data was then normalized and plotted with the help of Sigma plot 14.0 software.

3.2.6 UV Thermal denaturation analysis

Thermal denaturation experiments of AB_PGQs were carried out on a Perkin Elmer Lambda 35 spectrophotometer equipped with a Peltier temperature programmer (PTP 6+6) and water Peltier system PCB-1500. Melting curves of the AB_PGQs were collected at a heating rate of 1 °C/min in increasing concentrations of KCl. Melting of AB_PGQS was also recorded in the presence of BRACO-19 up to a ratio of D/N = 2, where D is the Drug (BRACO-19), and N is the Nucleic Acid (AB_PGQs). The fraction of DNA unfolded was plotted as a function of temperature using Sigma plot 14.0 software.

3.2.7 Gel retardation assay

Native polyacrylamide gel electrophoresis (PAGE) was performed to assess the molecularity of AB_PGQs. 20% native polyacrylamide gel was cast and run in 1X TBE (Tris-Borate- EDTA) buffer containing 80 mM K^+ at 4 °C in a Bio-Rad Mini protean Tetra Vertical Electrophoresis unit at a voltage of 70 V. All the AB_PGQs were diluted to a final concentration of 20 μM in K^+ containing buffer. Linear DNA

oligonucleotides of the same length as that of AB_PGQs served as negative control and standard G-quadruplex forming sequences (ckit22-G4), and its mutant served as a positive control, both of which were prepared under the same parameters as that of AB_PGQs. The gel was visualized using ImageQuant LAS4000 (GE Healthcare, Biosciences Ltd, Sweden) instrument after staining with Ethidium Bromide (EtBr).

3.2.8 Steady-state fluorescence titration study

Fluorescence titration experiments were carried out on a Synergy H1 multi-mode microplate reader, and titrations were performed in a 96-well corning half-area black plate. All the measurements were collected at 25 °C. 5 nM BRACO-19 solution was prepared in KPO_4 buffer (10 mM, pH 7.5, 80 mM K^+) and 20 μM solution of oligonucleotides in the same buffer. For the fluorescence titration study, ligand was added to each of the 12 wells. Gradually, the oligonucleotide was titrated in each well, starting from the first well except the last one that served as blank. Reaction for every PGQ was performed in duplicates with the final reaction volume of 75 μL. Fluorescence was observed at excitation maximum (λ_{ex} = 360 nm of the BRACO-19 molecule) and emission (λ_{em} = 440 nm)[179]. The change in emission fluorescence (ΔF) for all datasets was normalized to the last well (containing no DNA), and the data obtained from the experiment were analyzed using Sigma Plot 14.0 software (Systat Software, Chicago, USA). Two-site saturation model was used to extrapolate the curve between ΔF and DNA concentration. The following equation was employed to fit the data for two receptor binding sites, which provided two different binding affinities, K_{d1} and K_{d2}.

$$f = \frac{B_{max1} \times \text{abs (x)}}{K_{d1} \times \text{abs (x)}} + \frac{B_{max2} \times \text{abs (x)}}{K_{d2} \times \text{abs (x)}}$$

where B_{max} = maximum number of binding sites and K_d = equilibrium dissociation constant.

3.2.9 Isothermal titration calorimetric (ITC) analysis

To determine the binding affinity of BRACO-19 with the AB_PGQs ITC analysis for all eight AB_PGQs, and a linear DNA was performed using MicroCal iTC200

calorimeter (GE Healthcare, Biosciences Ltd., Sweden). All the oligonucleotides were dissolved in 50 mM K^+ containing KPO_4 buffer at the final concentration of 17 µM. 1 mM solution of BRACO-19 dissolved in the same buffer was titrated 22 times against the oligonucleotide added to the ITC cell with an initial injection of 0.4 µl followed by 1.77 µl of the ligand at each step for a duration of 3.54 s at 25 °C. 120 s gap was kept between each injection. The heat of dilution of the ligand was estimated by titrating the same concentration of ligand in the buffer and thereafter subtracting it from the binding isotherms of the oligonucleotide sequences before the curve fitting analysis. Data was obtained in triplicates and analyzed for the determination of association constant by its two-site binding model analysis using Origin scientific software version 7 (Microcal Software Inc. Northampton, MA, USA).

3.2.10 *Acinetobacter baumannii* growth inhibition assay

The minimum inhibitory concentration of BRACO-19 for *A. baumannii* was evaluated using an MTT-based growth inhibition assay, as per the modified protocol mentioned elsewhere[180,181]. BRACO-19 dilutions were prepared in BHI media from the freshly prepared solution of 400 µM and were added to the respective wells; the last well served as blank. The bacteria were cultured in BHI broth media (HiMedia) until they reached $O.D._{600}$ = 0.5. Then, they were diluted to an optical density of 0.08 using fresh BHI media. This culture was then diluted 150 times using fresh BHI media, and 50 µl was transferred to each well of a 96-well plate. The experiment was performed in triplicates. The plates were kept at 37 °C for 24 h, and thereafter 10µl of MTT (stock solution of 10 mg/ml) was added and incubated further for 4 h. The formazan precipitate formed was then diluted using 100 µl DMSO, and the change in absorbance was recorded using a microplate reader (BioTek) at 570 nm. The data obtained was analyzed via Graphpad Prism software.

3.2.11 mTFP-based reporter assay

The AB_PGQ motifs were cloned just after the start codon of the mTFP gene using the forward primer containing *NdeI* site and a reverse primer with *XhoI* site in their

flanking regions. The PCR amplified product and *pET43a*$^{+}$ were then digested with both restriction enzymes and ligated using T4 DNA ligase. The ligated product was then transformed into the *DH5Alpha* strains of *E. coli*. The cloned plasmid from the positive colonies was then isolated and transformed into the *Rosetta* strains. The secondary culture was grown till $O.D._{600}$ = 0.3 and incubated with BRACO-19 (12.5 µM) for 45 mins. Thereafter the protein expression was induced using 0.5 mM Isopropyl β-D-1-thiogalactopyranoside (IPTG) for 4 hours. Then cells were harvested, fixed by using 5% paraformalydehyde, and mounted on a glass slide. The slides were then visualized using confocal microscopy (Olympus). Statistical significance was calculated using t-test to determine significant differences between untreated and BRACO-19 treated samples. Data was analyzed using GraphPad Prism software version 10.2.1. and represented as mean ± SEM.

3.2.12 Total RNA isolation and cDNA synthesis

A. baumannii was grown in 25 ml of BHI media overnight at 37 °C at 220 rpm. The 50 ml BHI media was inoculated with 1% inoculum from overnight culture and incubated at 37 °C at 220 rpm. At $O.D._{600}$ = 0.5, 2 ml of culture was then taken and added to two separate culture tubes for untreated and treated cells, wherein 12.5 µM of BRACO-19 (dissolved in water) was added to the treated set. Both the sets were incubated at 37 °C, 220 rpm for 2 h. Post 2 h, samples were centrifuged at 6000 rpm and immediately preceded for RNA isolation using TRIzol reagent (Invitrogen) according to the manufacturer's instructions. The concentration and purity of the isolated RNA were measured using a NanoDrop (Thermo Scientific) as ng/µL and A_{260}/A_{280}, respectively. Subsequently, 2 µg of total RNA from each sample was used for cDNA synthesis in a 20 µl reaction using PrimeScript cDNA synthesis kit (Takara Bio USA, Inc.) according to the manufacturer's instructions.

3.2.13 Gene expression profiling using real-time quantitative PCR

Quantitative Real-Time PCR (qRT-PCR) was carried out in a PCR master mix containing iTaq Universal SYBR Green Supermix (Bio-Rad Laboratories, Inc.). 0.5 µM of each primer (Table A1) and 5 µL of cDNA template was added in a final reaction volume of 20 µL in a 96-well RT-PCR plate in QuantStudio 3 (Applied

Biosystem, USA). All the samples for the PCR reaction were prepared in duplicates, and the expression of the 16s rRNA housekeeping gene was used as a reference. The thermo-cycling condition used in qRT-PCR was as follows: initial hold of 2 mins at 50 °C; initial denaturation at 95 °C for 10 mins followed by 40 cycles of 95 °C for 15 s and 60 °C for 1 min, and a final extension at 72 °C for 10 mins. Data were analyzed using the comparative $\Delta\Delta C_t$ method, where C_t values of each sample were normalized concerning the control. Statistical analysis was carried out between untreated and BRACO-19 treated samples using t-test, using GraphPad Prism software version 10.2.1. Data was represented as mean ± SEM.

3.2.14 Biofilm formation assay

A. baumannii was grown in 25 ml of BHI media overnight at 37 °C at 220 rpm. 1% inoculum from this overnight culture was then used to inoculate 50 mL of BHI media and incubated at 37 °C at 220 rpm till $O.D._{600}$ = 0.4. The culture was then diluted 100 times and divided into four sets which were treated with 25 µM, 12 µM, 6.25 µM of BRACO-19, and an untreated control on the coverslip in a 12-well plate. All four sets were then incubated at 37 °C. After 48 h, the culture was discarded from the wells, and 1 ml of 4% paraformaldehyde (HiMedia) was added to each well and incubated at 37 °C for 1 h. Subsequently, 10µg/ml DAPI prepared in 1% PBS was then added to each well and again incubated for 2-3 h at 37 °C with 5% CO_2. The coverslips were then carefully taken out from the wells and mounted on the glass slides, and biofilm formation was visualized through Z-scanning performed using confocal microscopy, and analyzed using Olympus Fluoview software. The experiment was performed in duplicates. between untreated and BRACO-19 treated samples. Statistical difference between the control and treated sets was calculated using one-way ANOVA. Data were analyzed using GraphPad Prism software and were represented as mean ± SEM.

3.3 Results

3.3.1 Mining of Conserved Putative G4-forming Sequences in *Acinetobacter baumannii*

A. baumannii has a genomic length of ~3.97 Mb and a GC content of ~39 %. G-quadruplex structures can be formed by motifs having two, three, or four Guanine tracts. Since G-quadruplexes can modulate promoter activity and gene expression when formed on either strand, both sense and antisense strands were evaluated using our previously established G4 prediction tool. We first checked the presence of G-quadruplex motifs in the reference genome of *A. baumannii* (K09-14) using the parameters of Guanine tract ≥2. The *A. baumannii* genome contains a large number of G-quadruplex motifs with a 2G-tract. Though motifs with 2G tract form G-quadruplex conformations, the motifs with ≥3 G-tracts have higher propensity and stability *in-vivo*. Therefore, we explored the *A. baumannii* reference genome for G-quadruplex motifs with G-tract ≥3 and loop length (LL) of 20 nts. The analysis revealed a total of 49 G-quadruplex motifs in the bacterial genome. The G-quadruplex density (G-quadruplex per 1000 bases) for the G-tract ≥3 and LL ≤20 nts was observed to be 0.0123, which was much lesser than the other explored bacteria highlighting the scarcity of these non-canonical structures in the nosocomial pathogen. Out of 49 motifs, 24 were in the sense strand, while 25 were in the antisense strand (Table A2). Furthermore, we also checked the number of G-quadruplex motifs with LL of ≤15, ≤10, ≤7, and ≤5. With a more stringent loop length parameter, the number of G-quadruplex motifs was found to sharply decrease, with a G-quadruplex density of 0.0108, 0.0035, 0.00075, and 0.00025, respectively (Figure 3.1 A, B).

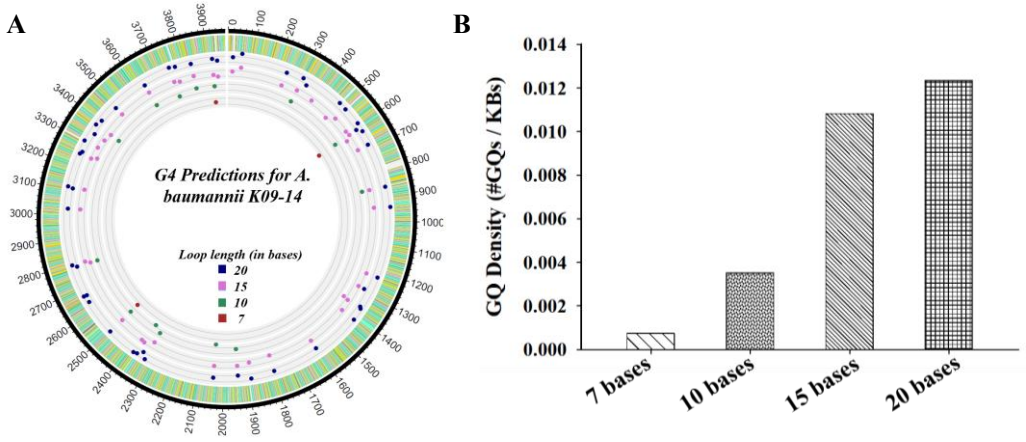

Figure 3.1. (A) Number of G4 motifs represented along with their locations in A. baumannii K09-14 genome predicted using In-house Prediction tool (G4IPDB) represented by Circos Plot (B) G4 density (number of GQs/kilobases) of the G4IPDB predictions.

In recent times, a few non-canonical motifs in the guanine-rich sequences having imperfect G-tracts with bulges in them are also shown to form G-quadruplex conformation in-vitro[182]. Therefore, to include these non-classical motifs in the genome mining of *A. baumannii*, we further explored the bacterial genome using the G4Hunter tool. The tool predicts the G-quadruplex motifs based on Guanine richness and skewness of the sequence and provides a propensity score. A higher score depicts a greater propensity for G-quadruplex formation. The analysis was performed first with a score threshold of 1.2, as they are shown to form G-quadruplex conformation *in-vitro* which resulted in 4272 G4 motifs with a G4 density of 1.07. This higher density might highlight the presence of more non-classical G-quadruplex motifs as compared to the classical ones. With the increasing threshold, a decrease in the number of G-quadruplex motifs was observed, resulting in 1058 with 1.4, 280 with 1.6, 62 with 1.8, and 16 with 2.0 score (Figure 3.2 A). This reflected in a G4 density of 0.266, 0.07, 0.015, and 0.004 for scores 1.4, 1.6, 1.8, and 2.0 respectively (Figure 3.2 B).

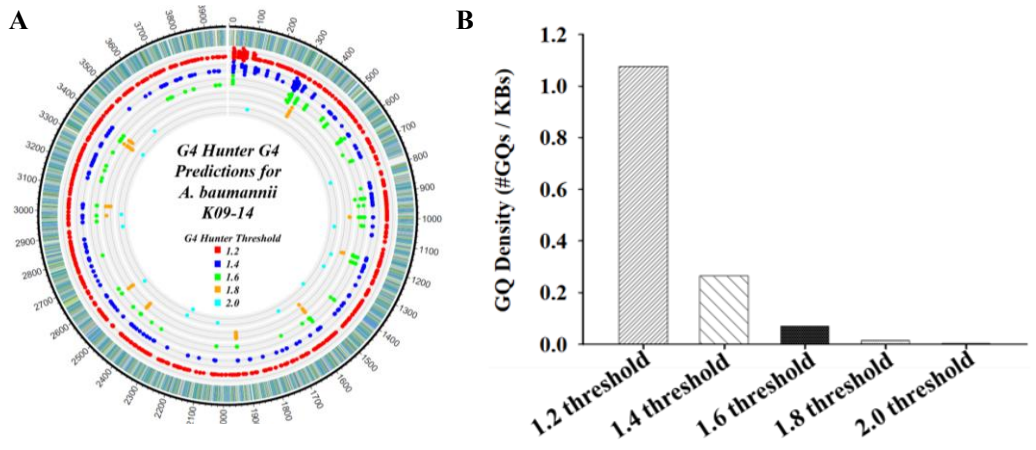

Figure 3.2. (A) Number of G4 motifs represented along with their locations in A. baumannii K09-14 genome predicted using G4Hunter with varying thresholds represented by Circos Plot (B) G4 density (number of G4s/kilobases) of the G4 Hunter predictions.

The evolutionary conserved G-quadruplex motifs might act as critical therapeutic targets as they can be used to target both drug-susceptible and drug-resistant strains of *A. baumannii*. Therefore, we proceeded to perform a BLAST search using the obtained 49 PGQs from reference *A. baumannii* genome, to find the highly conserved potential G-quadruplex (AB_PGQ) motifs against all the 452 completely sequenced *A. baumannii* strains in the NCBI genome database (until September 30, 2022). We received eight unique motifs evolutionary with the conserved-ness of ≥ 90%. On functional annotation, these eight AB_PGQs were found to be associated with the genes involved in essential pathways responsible for the survival and pathogenicity exhibited by the bacteria. One of the G-quadruplex motifs (AB_PGQ4) was located upstream of GO593_12270, a TetR family transcriptional regulator, while the remaining conserved motifs were in the open reading frame of various essential genes. These eight conserved G-quadruplex motifs were selected for biophysical and biomolecular characterization (Figure 3.3, Table 3.1).

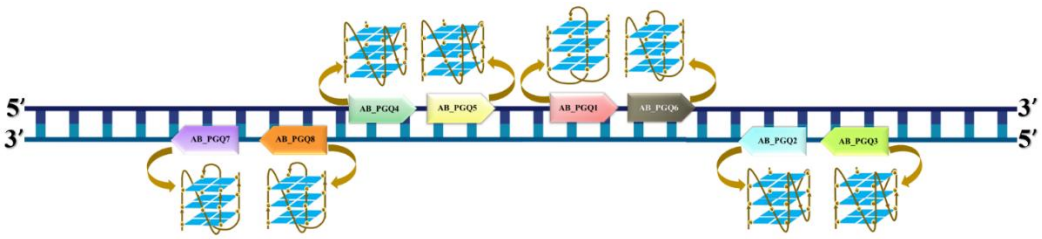

Figure 3.3. Schematic representation of location and strand directionality of PGQs used for biophysical characterization.

Table 3.3.3.1. Table depicting the functional annotation and genes for AB_PGQs.

PGQs	**AB_PGQ1**	**AB_PGQ2**	**AB_PGQ3**	**AB_PGQ4**	**AB_PGQ5**	**AB_PGQ6**	**AB_PGQ7**	**AB_PGQ8**
Sequence	AAGTGGGC GTGTTGGGT GCGGGCATG ATGGGTGCC	GAACGGGT ACAAGTGG GTAACTATA TGGGTATGA ATCAGGGCC GT	ATTTGGGCT AAAGGGCA CGGGTTTAT GAGTGGGTA TA	GAACGGGA GGGGGACA CCTTCGGGT GTGCTGGGT TTT	ACATGGGCT TTCGGGACA TGGGCGGG AAGG	TTTAGGGGC AGGTTTTCG GGTAGGTTG GGTCTATGC GGGTAAA	GATTGGGCA GGGTGCCGA GGGCATTAT TTTGGGGTG TA	ATTCGGGCT TTCGGGTCA GGCTGGGC ATCGGCAAT GGGGCGTA
G4 harboring genes	3-hydroxyacyl-CoA dehydrogenase	Pilus assembly protein PilP	Tetratricopeptide repeat protein	TetR family transcriptional regulator	Aldehyde dehydrogenase	Aminotransferase pyridoxal phosphate-dependent enzyme	Amino acid racemase	MFS transporter
Gene ID	GO593_03275	GO593_04755	GO593_08125	GO593_12270	GO593_14240	GO593_14770	GO593_18755	Aba10324_RS 12040
Potential biological role	Fatty Acid Metabolism	Horizontal gene transfer, twitching motility, adherence, biofilm formation.	Transfer of bacterial virulence factors to host cells, binding to the host cells and inhibition of phagolyso-somal maturation	Regulation of efflux systems	Involved in cellular aldehyde metabolic process	Cellular biosynthetic pathways	D-amino acid metabolism	Adherence and biofilm formation
Position	ORF	ORF	ORF	Upstream of gene	ORF	ORF	ORF	ORF

3.3.2 1D ^{1}H NMR spectral analysis and increase in ThT fluorescence intensity corroborates the formation of G-quadruplex structure in the conserved AB_PGQs

NMR spectroscopy is considered one of the most conventional techniques for affirming the formation of G-quadruplex structures in the solution. The canonical DNA structures containing Watson-Crick Hydrogen bonds show a chemical shift in the 12-14 ppm range, whereas non-canonical DNA conformations like G-quadruplex show a characteristic chemical shift around the 10 - 12 ppm range in ^{1}H NMR spectra. This characteristic chemical shift is solely due to the presence of special Hoogsteen Hydrogen bonds between the imino protons involved in the G-quartet formation of the G-quadruplex structure[128]. Therefore, proton NMR was performed for the AB_PGQs in 80 mM K^{+} containing KPO_4 buffer. The sequences AB_PGQ-3, AB_PGQ-6, and AB_PGQ-7 showed a clear peak in the 10 - 12 ppm range depicting the presence of G-quadruplex structures in the respective solutions. The NMR spectra of AB_PGQ1, AB_PGQ2, AB_PGQ5, and AB_PGQ8 revealed imino proton signals originating from both Watson-Crick base pairings and Hoogsteen base pairings. The presence of Hoogsteen ^{1}H signals in the 10 - 12 ppm range confirms the formation of G-quadruplex structures in the sequence. Additionally, the appearance of Watson-Crick base pairing signals in the 12 - 13.5 ppm range may be attributed to the presence of additional hydrogen bonding interactions between the nucleobases of the loops and/or flanking sequences[183,184]. These extra hydrogen bond interactions might stack upon the G4 tetrad core, contributing to the stabilization of the G-quadruplex structure forming in the sequences. Their appearance in the NMR spectra suggests that these interacting imino protons are protected from solvent exchange, possibly due to specific structural properties of the loop[183,185]. In the NMR spectrum of AB_PGQ4, in addition to the distinctive Hoogsteen ^{1}H signals in the 10 - 12 ppm range characteristic of G-quadruplex structure formation, two additional resonances are observed. The appearance of the two resonances in the NMR spectrum of AB_PGQ4 at 12.1 - 12.3 ppm can be ascribed to the G-register (GR) exchange. This phenomenon usually occurs in the case of extra guanosine residues

present in G tracts (>3) resulting in sliding of G-tracts with respect to one another[186]. This leads to the adoption of multiple folded isomers (GR isomers) by the same sequence based on the incorporation of different Gs of the G tract in the G-tetrad core structure[187,188]. The exchange between these GR isomers termed as GR exchange can lead to the appearance of the imino proton peaks for exchanges occurring relatively slowly on the NMR chemical shift timescale[186]. This is a type of dynamic conformational polymorphism of G-quadruplex structures and has been most commonly found to be associated with promoter regions of genes[188]. The sequence AB_PGQ4 (Table 3.1) also contains such surplus guanosines (G5 tract) in the second G-tract instead of the usual G3-tract and may be capable of showing such dynamic conformational polymorphism (Figure 3.4).

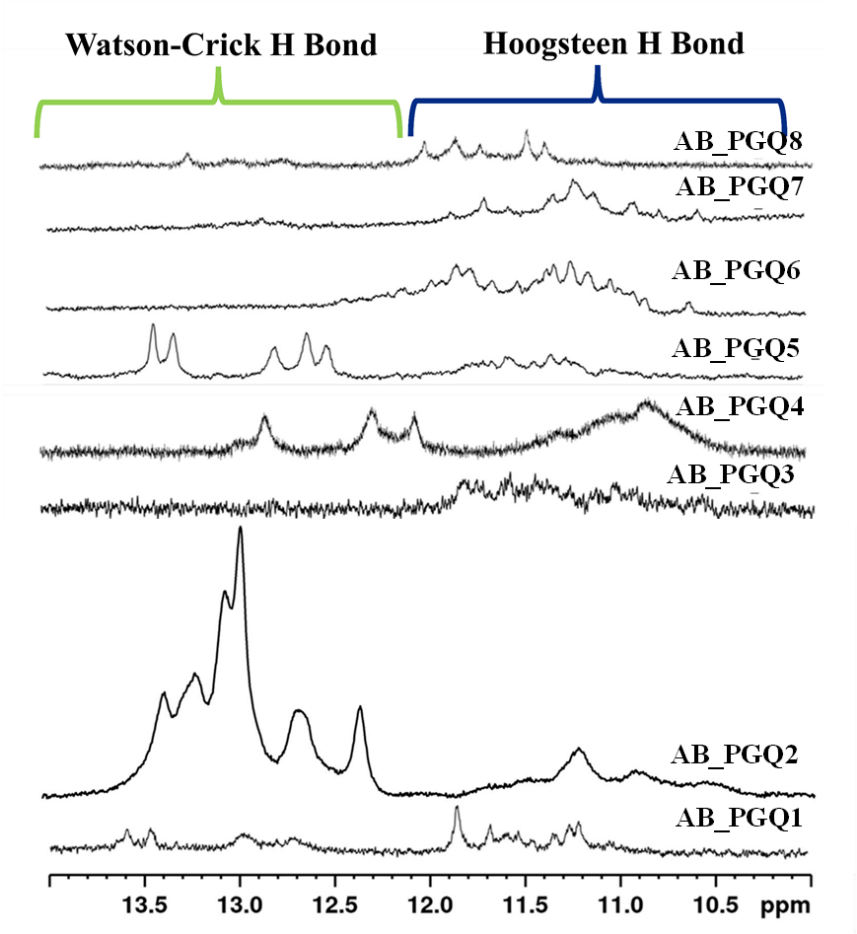

Figure 3.4. 1D 1H NMR spectra of AB_PGQs.

ThT functions as a fluorescent probe that exhibits enhanced fluorescence intensity upon exposure to G-quadruplex structures compared to non-G-quadruplex structures. This characteristic feature of Thioflavin T was exploited for characterizing the formation of G-quadruplex structures in AB_PGQs. All the AB_PGQs showed a multiple-fold increase in the ThT fluorescence intensity as compared to their linear counterparts. This affirmed the formation of G-quadruplex motifs by the AB_PGQ sequences (Figure 3.5).

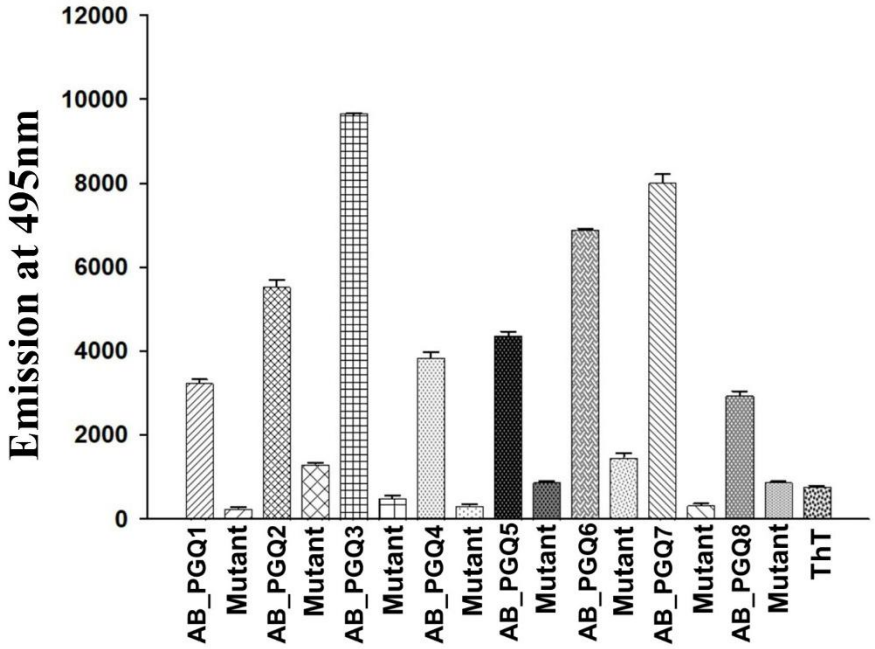

Figure 3.5. ThT Probe Light-up Assay of AB_PGQs w.r.t. to their respective mutants.

3.3.3 *A. baumannii* G-quadruplex motifs displayed varied stable topologies and molecularity in the presence of potassium ion

G-quadruplexes can display a wide variety of topologies as are possible because of varying combinations of the strand directions (5' → 3'), number of G-tetrads, and differences in the composition and size of loop bases, that are not involved in the G-tetrad formation[189,190]. G-quadruplexes are parallel if all the strand orientations are in the same direction, and antiparallel if half strands are in one direction, while the other half in the opposite direction. The anti-parallel structures can be chair or basket-type structures depending on the loop position[190–192].

Hybrid G-quadruplex structures are the ones that have three parallel and one anti-parallel strands[193,194]. CD spectroscopy can be exploited for analyzing the G-quadruplex topologies and following their structural transitions based on the changing environmental conditions. In CD spectroscopy, parallel and anti-parallel conformations have clear spectral signature peaks, where a negative peak at ~240 and positive peak at ~260 signifies a parallel conformation, while a negative peak at ~260nm and positive peak at ~290 nm shows the formation of anti-parallel topology in the solution. Other than these two, a third signature pattern in the CD spectra where a negative peak at ~240 nm and two positive peaks, one at ~260 nm and a second at ~290 nm shows the formation of a hybrid structure[195,196]. This hybrid signature pattern can be a result of either a hybrid conformation or the presence of separate parallel and anti-parallel conformations in the same solution. G-quadruplexes are stabilized by various mono and divalent cations, in which potassium (K^+) surpasses all others. Also, bacteria can survive a significant fluctuation of K^+ concentration ranging from 25 mM to 200 mM. Therefore, CD spectral and melting analysis evaluated G-quadruplex topologies and stability of AB_PGQs in the presence of K^+. The sequences AB_PGQ1 and AB_PGQ8 in the presence of K^+ affirmed the formation of anti-parallel topology as depicted by a positive peak at ~290 nm and a negative peak at ~260 nm. Likewise, AB_PGQ2, AB_PGQ3, and AB_PGQ4 exhibited a parallel topology with a positive peak around ~260 nm and negative peak around ~240 nm; AB_PGQ5, AB_PGQ6 and AB_PGQ7 exhibited a mixed/hybrid G-quadruplex topology showing a significant positive peak at around ~260 nm, and ~290 nm with a negative peak at ~240 nm (Figure 3.6). The increased K^+ concentration further stabilized the AB_PGQs as an increase in the CD ellipticity was observed in a concentration-dependent manner. To determine the significance of the G-rich tract for the G-quadruplex forming ability of AB_PGQs, the central Guanine in each tract was mutated to Thymine, and CD spectral analysis was carried out in the presence of 50 mM K^+. All the mutants showed a negative peak at ~250 nm with a positive peak at ~270 nm and failed to show the signature CD peaks of G-quadruplex conformation.

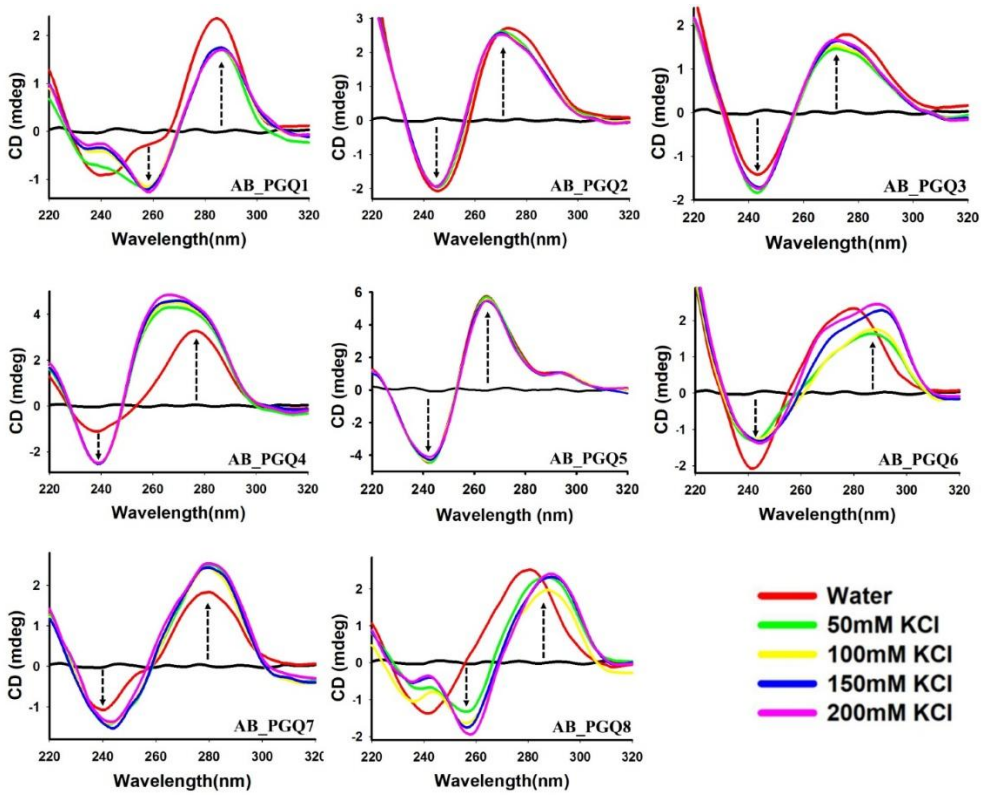

Figure 3.6. CD Spectra of AB_PGQs with the increasing concentration of KCl (0 - 200 mM).

To check the stability of AB_PGQ motifs in the absence and presence of K^+ (50 mM - 200 mM), a thermal melting analysis was performed. Thermal denaturation analysis revealed the stabilizing effect of K^+ on AB_PGQs as, with the increase in the cation concentration, the melting temperature (T_m) was found to increase. The AB_PGQs displayed maximum stability at 200 mM K^+ concentration as the change in melting temperature (ΔT_m) of 18.2 °C for AB_PGQ1, 12.6 °C for AB_PGQ2, 11.2 °C for AB_PGQ3, 6.3 °C for AB_PGQ4, 21.7 °C for AB_PGQ5, 21°C for AB_PGQ7 and 18.9 °C for AB_PGQ8 was observed with respect to the absence of any cation (Figure 3.7 A, B).

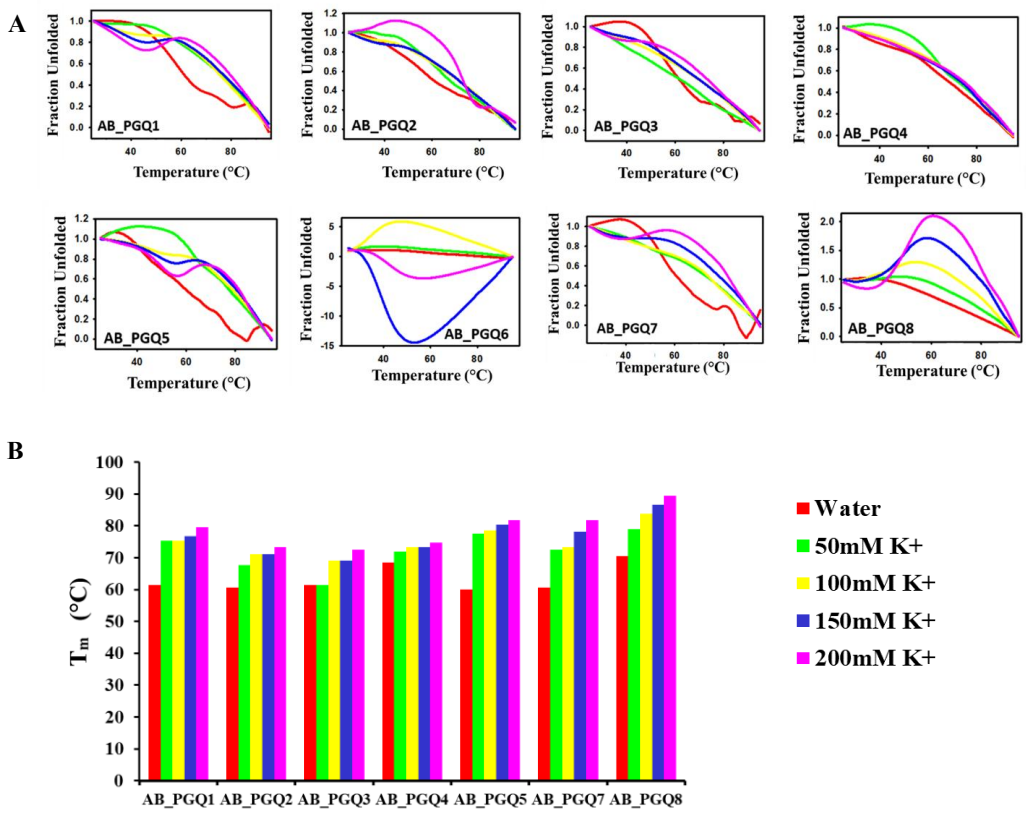

Figure 3.7. (A) UV-Melting spectra of the AB_PGQs with increasing concentration of KCl (0 - 200 mM) (B) Bar-graph depicting melting temperature from UV-Melting study.

We further sought to assess the molecularity of these AB_PGQs by comparing their mobility in the native polyacrylamide gels with their respective mutant counterparts. It is a well-established fact that the folded G-quadruplex structures exhibit faster migration corresponding to an intramolecular topology. In contrast, the ones that exhibit slow migration correspond to an intermolecular conformation[197–199]. It was observed that the migration rate for AB_PGQ1, AB_PGQ2, AB_PGQ3, AB_PGQ4, and AB_PGQ5 were faster than their mutant counterparts suggesting the formation of intramolecular G-quadruplex structure by these PGQs. A known intramolecular G-quadruplex forming sequence, ckit22, and its linear counterpart also showed a similar pattern[200]. Simultaneously, it was observed that the migration rate for AB_PGQ6, AB_PGQ7, and AB_PGQ8 was slower than their mutant counterparts suggesting the formation of intermolecular G-quadruplex structures by these PGQs (Figure 3.8).

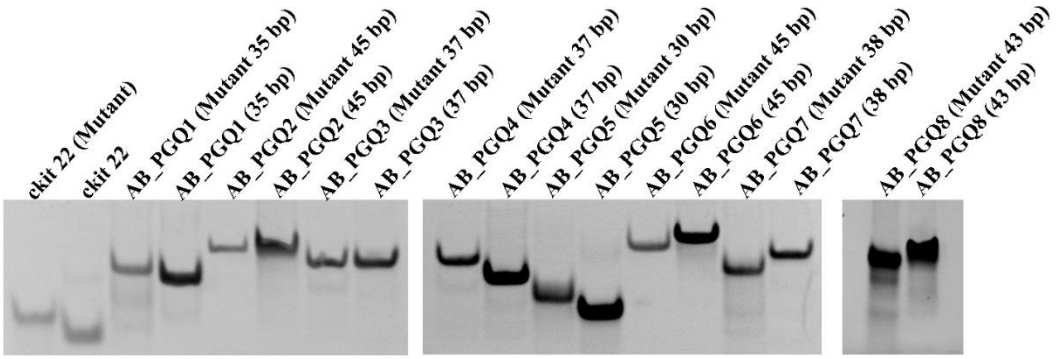

Figure 3.8. Electrophoretic mobility shift assay of AB_PGQs.

3.3.4 The G-quadruplex specific ligand BRACO-19 showed high affinity towards AB_PGQs

Small molecules specific for interacting and binding with G-quadruplex motifs are widely used for the characterization of G-quadruplex forming sequences. BRACO-19 is a G-quadruplex binding ligand that shows high specificity and affinity towards G-quadruplex DNA[201] and has shown a high affinity towards PGQs in various bacterial genomes such as *M. tuberculosis*[164], *K. pneumoniae*[161], and *S. enterica*[160]. Therefore, we first sought to explore the binding affinity of BRACO-19 towards AB_PGQs by using a fluorescence titration assay. This assay exploits the intrinsic fluorescence property of the ligand molecule to determine the interaction revealing the binding affinity between the ligand and receptor. The differential fluorescence intensity quantifies the binding efficiency in the absence and presence of DNA, and binding affinity is obtained in the form of the K_d value (dissociation constant). A successful interaction between the two results in the enhancement or quenching of the ligand fluorescence intensity (F), and the change in fluorescence (ΔF) is plotted against the DNA concentration. The K_d value obtained upon global curve fitting is then used to evaluate the binding affinity of the ligand with each PGQ. In the current study, all the AB_PGQs showed a higher binding affinity for BRACO-19 compared to the linear mutant, which was taken as a negative control (Figure 3.9 A, B). The lowest K_d that signifies the highest affinity of BRACO-19 was observed with AB_PGQ8 (0.0011 µM), while the linear counterpart showed a K_d of 7.67 µM. This higher affinity of BRACO-19 towards AB_PGQs which was equivalent to the affinity of a well-known G-quadruplex

motif of c-Myc (K_d = 0.09 μM), further affirmed the formation of stable G-quadruplex conformation by the *A. baumannii* G4 motifs (Table 3.2). The differential binding affinity of different AB_PGQs could be due to differences in their sequence composition, molecularity, loop sequence, folding pattern, and length of their G motifs[202].

Table 3.2. Table depicting the equilibrium dissociation constant (Kd) values of the AB_PGQs and mutant with BRACO-19 obtained through Fluorescence titration assay.

PGQs	**K_d**
AB_PGQ1	3.538
AB_PGQ2	0.798
AB_PGQ3	0.133
AB_PGQ4	0.103
AB_PGQ5	0.085
AB_PGQ6	0.490
AB_PGQ7	0.670
AB_PGQ8	0.011
Positive control (c-Myc)	0.09
Negative control (Mutant)	7.668

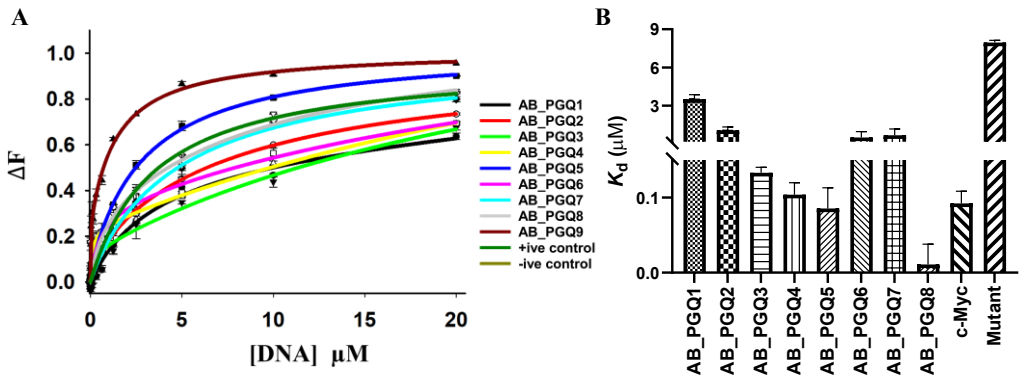

Figure 3.9. Fluorescence titration studies of BRACO-19 with AB_PGQs. (A) Fluorescence binding curves (B) Bar graph representing the dissociation constant (K_d) values of AB_PGQs w.r.t. the mutant obtained by Fluorescence titration analysis.

To further affirm the affinity of the G-quadruplex ligand with AB_PGQs, Isothermal titration calorimetry (ITC) was performed. ITC is a powerful tool for assessing the binding affinity between receptors and ligands at the thermodynamic level. The change in enthalpy (ΔH_1) for AB_PGQ1, AB_PGQ2, AB_PGQ3, AB_PGQ4, AB_PGQ5, AB_PGQ6, AB_PGQ7, and AB_PGQ8 was noted to be -8.0 x 10^3, -1.059 x 10^4, -1.204 x 10^4, -8.671 x 10^3, -1.37 x 10^7, -1.24 x 10^4, -1.363 x 10^4 and -9.494 x 10^3 cal/mol respectively indicating that the AB_PGQs and BRACO-19 complex formation are thermodynamically driven and exothermic in nature (Table 3.3). The exothermic nature of the complex formation strengthens the biological feasibility. The association constant (K_a) was also higher for all the AB_PGQs than the mutant sequence affirming the high affinity of BRACO-19 with the AB_PGQs. The association constant (K_a) for AB_PGQ8 was found to be the highest, i.e., 2.15 x 10^{10} M^{-1}, amongst all the AB_PGQs, whereas the association constant for the mutant sequence lacking G-quadruplex motif was found to be the lowest, i.e., 7.95 x 10^3 M^{-1}. These results were in line with the fact that BRACO-19 has high binding affinity and specificity towards G-quadruplex DNA against DNA sequences lacking G-rich motifs (Figure 3.10).

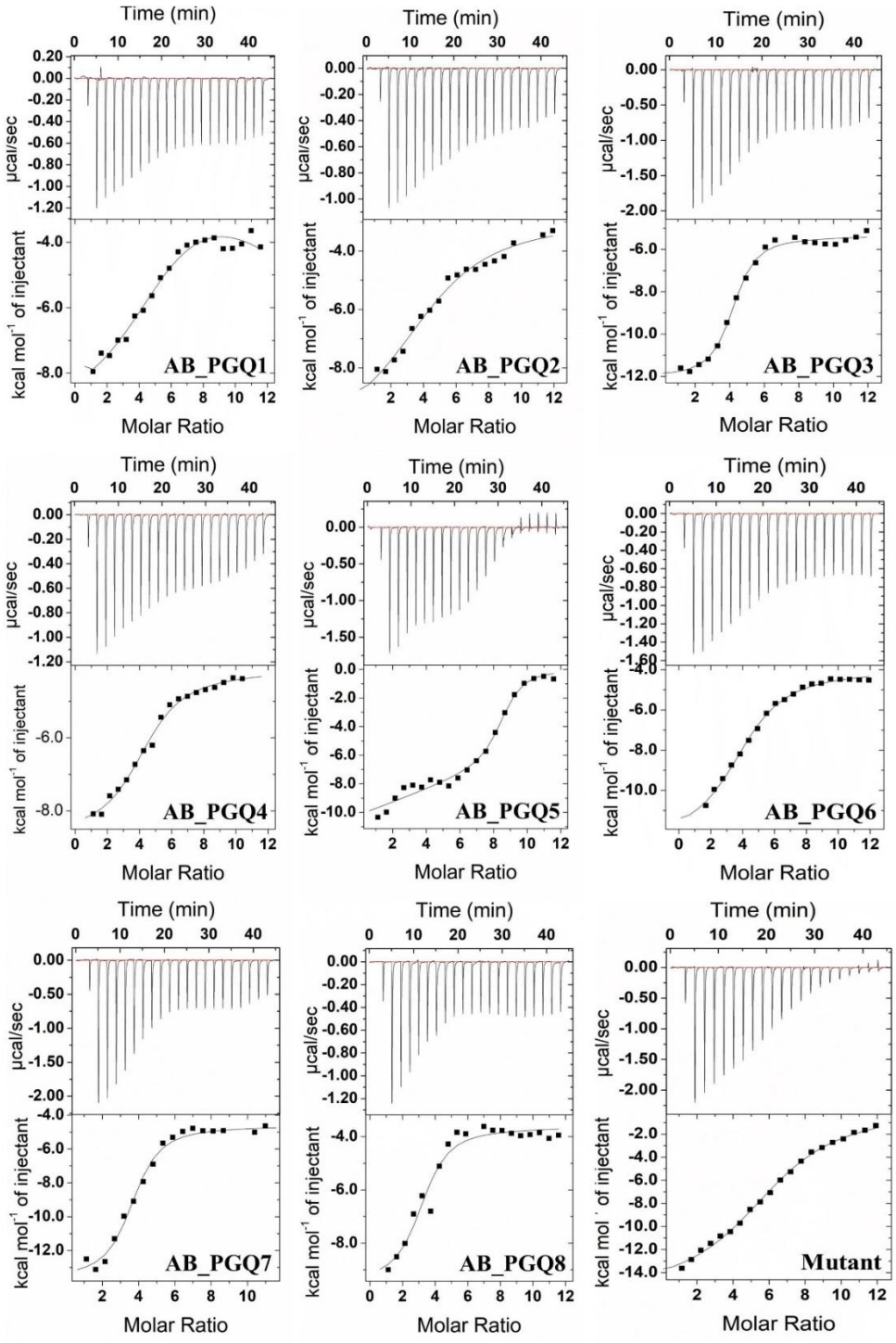

Figure 3.10. ITC thermograms of AB_PGQs and a linear mutant obtained from titration with BRACO-19.

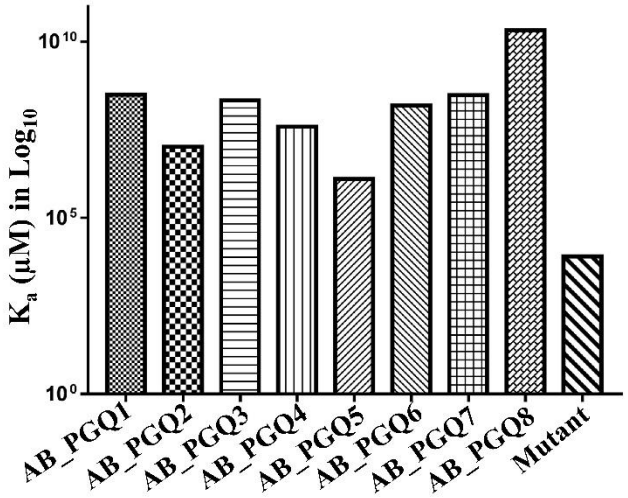

Figure 3.11. Bar graph depicting the association constant (K_a in log_{10}) values of AB_PGQs w.r.t. mutant obtained by ITC analysis.

Table 3.3. Table depicting the dissociation constant and free energy change values of the AB_PGQs and mutant with BRACO-19 obtained through Isothermal Titration Calorimetry

	AB_PGQ1	**AB_PGQ2**	**AB_PGQ3**	**AB_PGQ4**	**AB_PGQ5**	**AB_PGQ6**	**AB_PGQ7**	**AB_PGQ8**	**Mutant**
K_d1	0.0032μM	0.09μM	0.0045μM	0.00257μM	0.78μM	0.0065μM	0.0032μM	0.0465 μM	125.7μM
K_d2	6.5μM	46.5μM	22.1μM	26.1μM	0.79μM	52.35μM	3.88μM	0.086nM	19.3μM
ΔG1	-8.3 kcal/mol	-10.505 kcal/mol	-11.944 kcal/mol	-8.812 kcal/mol	-13615 kcal/mol	-12.362 kcal/mol	-13.458 kcal/mol	-9.529 kcal/mol	11167.5 kcal/mol
ΔS1	12 cal/mol/deg	-3.40 cal/mol/deg	-2.24 cal/mol/deg	5.64 cal/mol/deg	-4.60 cal/mol/deg	-4.34 cal/mol/deg	-6.88 cal/mol/deg	15.4 cal/mol/deg	$4.09x10^4$ cal/mol/deg
ΔH1	$-0.8x10^4$ cal/mol	$-1.06x10^4$ cal/mol	$-1.204x10^4$ cal/mol	$-0.87x10^4$cal/mol	$-1.37x10^7$ cal/mol	$-1.24x10^4$ cal/mol	$-1.36x10^4$ cal/mol	$-0.95x10^4$ cal/mol	$1.22x10^7$ cal/mol

The change in the intensity of the proton peaks in a 1D ^{1}H NMR spectra can also be used to determine the interaction of the ligand with the nucleic acid molecules. BRACO-19 is a 3,6,9-trisubstituted acridine derivative with two side chains containing tertiary amine groups. It includes five different aromatic protons to which specific numbers H1, H2, H3, H4, and H5 are assigned as in Figure 3.12 A. During NMR broadening analysis, it was observed that with the successive addition of the AB_PGQs to the BRACO-19 solution in the presence of 80mM K^{+}, the resonances of all these protons widened. This broadening of the ligand peaks underscores the participation of protons in the complex formation with AB_PGQs[203] (Figure 3.12 B). All eight AB_PGQs showed a similar binding mode with BRACO-19, i.e. through π-π stacking mode of interaction[204].

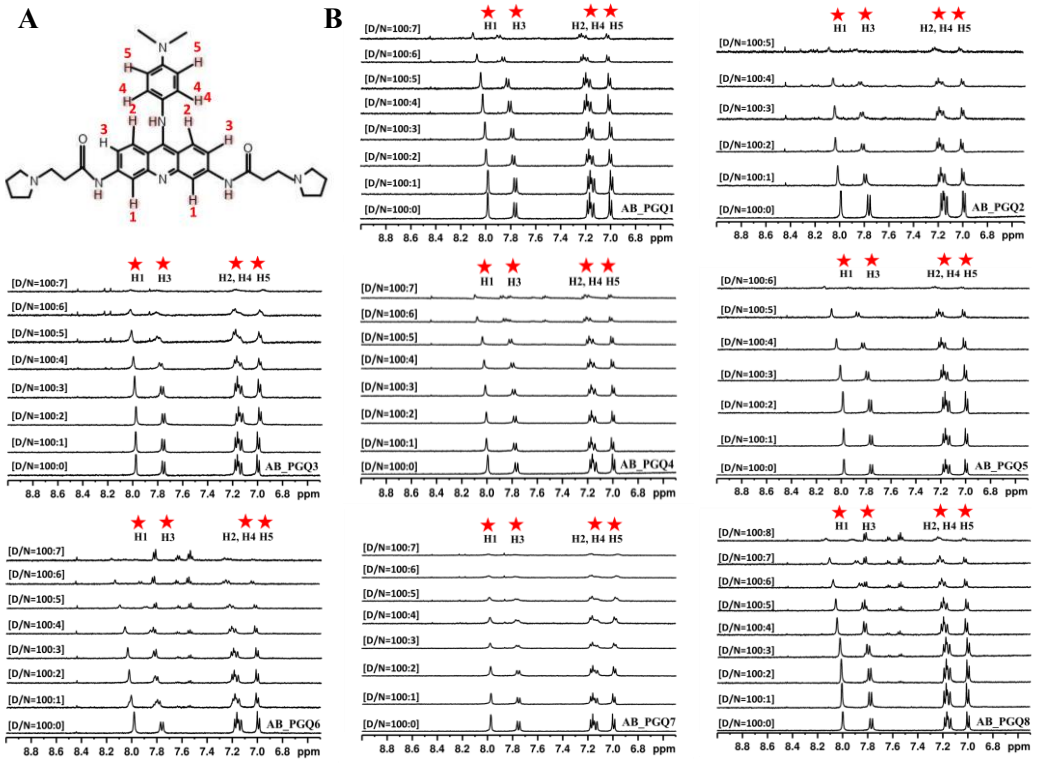

Figure 3.12. (A) Structure of BRACO-19 with the assigned aromatic protons exhibiting peaks in 1D 1H NMR spectra. (B) NMR Broadening Analysis of BRACO-19 on addition of AB_PGQs.

3.3.5 BRACO-19 enhances the stability of *A. baumannii* conserved G-quadruplex motifs

Small molecules can have a stabilizing or destabilizing effect on the G-quadruplex structures. Fluorescence binding, ITC, and NMR broadening revealed the interaction analysis of BRACO-19. To check the effect of BRACO-19 on the conformation and stability of AB_PGQs, CD spectral and thermal melting analysis was performed for AB_PGQs in the increasing concentration of the G-quadruplex ligand. With the gradual addition of BRACO-19 to AB_PGQs, an increase in ellipticity in the positive and negative peaks was observed, whereas the overall topology of the PGQs was maintained (Figure 3.13). This increase in ellipticity helps strengthen the interaction of BRACO-19 and its stabilizing effect on the AB_PGQs[205,206].

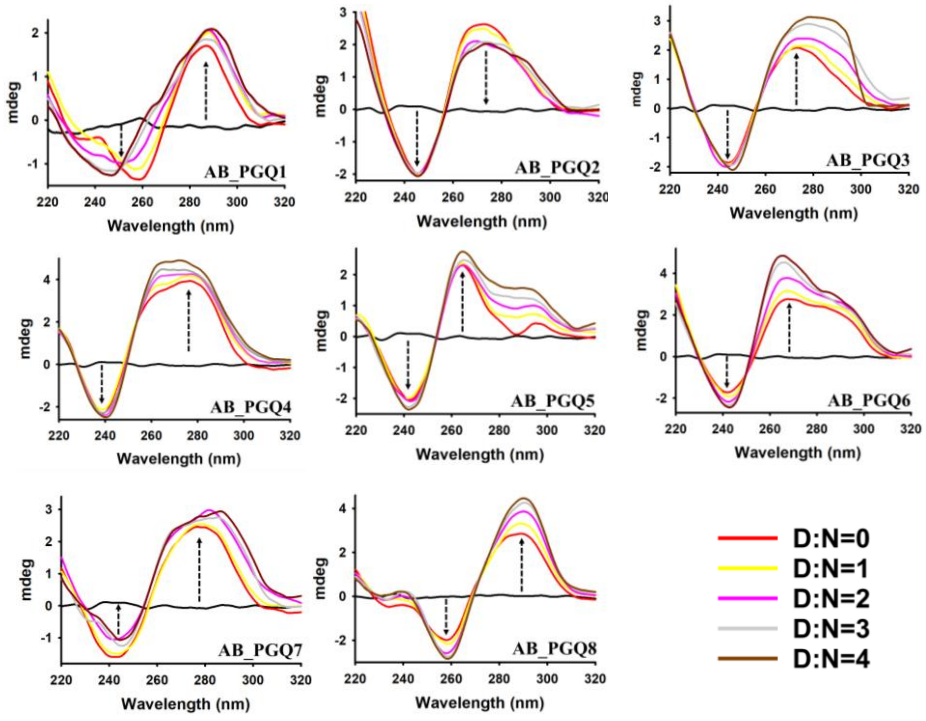

Figure 3.13. CD spectra of AB_PGQs in increasing concentration of BRACO-19.

UV Melting profiles of G-quadruplexes depict their stability based on the respective melting temperature (T_m) values, which tends to increase or decrease with the addition of a ligand. Interaction of the ligand with the G-quadruplex structure and an effect on the stability of the latter can be assessed, based on the difference of

melting temperature (ΔT_m) in absence and presence of the ligand[207]. In our work, when BRACO-19 was added up to a two-molar equivalent (D/N = 2) of the PGQs, an increase in T_m values was observed. Increase in T_m of the G4 structure clearly indicated to a stabilization of the structure which rendered it difficult to unfold. Hence, the thermal denaturation analysis of AB_PGQs in the presence of BRACO-19 depicted a significant increase in their ΔT_m (Figure 3.14. A, B), thereby further affirming the stabilizing effect of the ligand[208].

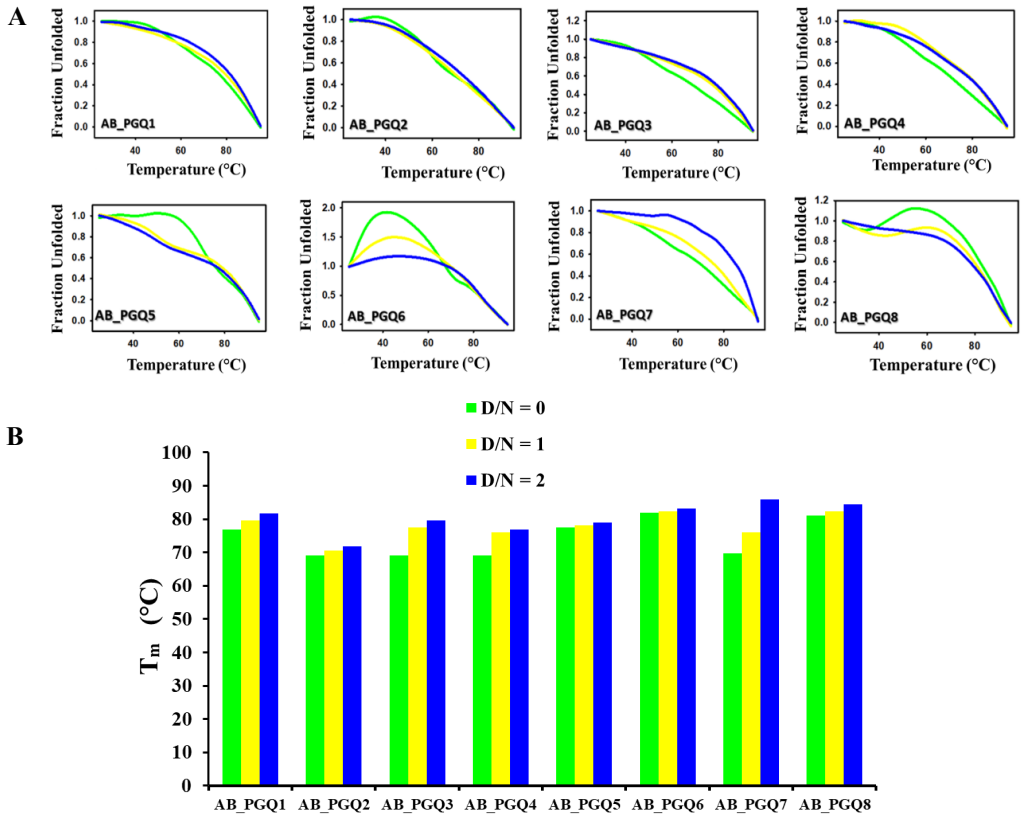

Figure 3.14. (A) UV-Melting spectra of the AB_PGQs with increasing concentration of BRACO-19. (B) Bar-graph depicting melting temperature from UV-Melting study.

3.3.6 *A. baumannii* G-quadruplexes might regulate biological functions

To further check if the G-quadruplex ligand, BRACO-19 would have any effect on the expression of AB_PGQs containing reporter genes, we performed mTFP based reporter assay using *pet43a*$^+$ expression vector system in *Escherichia coli*. For this, we selected two G-quadruplex motifs, one located in the ORF region and the other

in the promoter region (AB_PGQ4). Out of the seven conserved AB_PGQs located in the ORF region, AB_PGQ2 was selected as it was present in the coding region of the essential genes *pilP* that is involved in the horizontal gene transfer, twitching motility, adherence, and biofilm formation. The *AB_PGQ-mTFP-pet43a*$^{+}$ plasmid transformed cells showed a clear expression of mTFP gene in the untreated cells, but the addition of BRACO-19 led to a decrease in the gene expression in both AB_PGQ2 and AB_PGQ4 harboring plasmids, whereas no change was observed in the plasmid containing a linear oligonucleotide instead of the AB_PGQ motif (Figure 3.15). This signifies the stabilization of G-quadruplex motif in the presence of BRACO-19 that might obstruct the gene expression machinery leading to decrease in the mTFP gene expression.

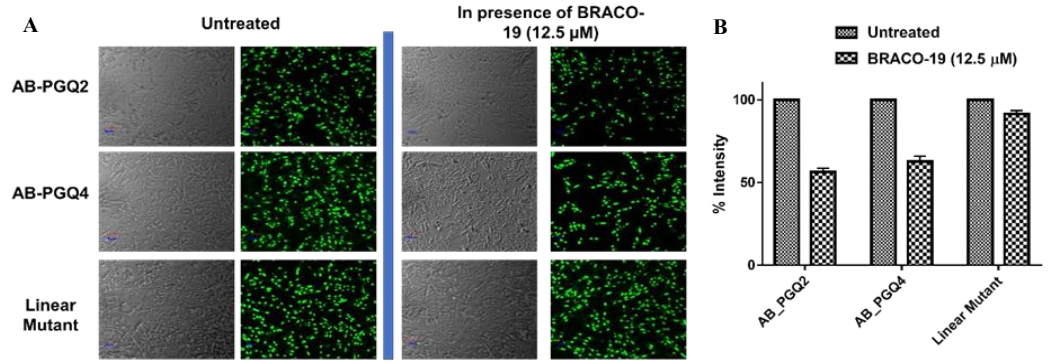

Figure 3.15. (A) The confocal images of untreated and BRACO-19 treated Rosetta cells depicting the expression of mTFP gene. (B) The bar graph depicting the normalized expression of mTFP in AB_PGQs and linear mutant.

3.3.7 BRACO-19 inhibits the growth of *A. baumannii* and affects the expression of AB_PGQ harboring genes

In order to assess the effect of BRACO-19 on the survival of *A. baumannii*, an MTT assay was performed. The ligand decreases the bacterial growth in a concentration-dependent manner, and the IC_{50} value was found to be 25 µM ± 0.1415 (Figure 3.16 A). G-quadruplex formation during biological processes, including replication, transcription, and translation, acts as a roadblock resulting in their attenuation. To analyze the effect of G-quadruplex stabilization in the presence of BRACO-19 on the gene expression of the eight genes harboring evolutionary conserved G-quadruplex motifs, a real-time PCR experiment (RT-PCR) was carried out. In the

presence of BRACO-19 (12.5 µM), the expression of all eight genes was decreased relative to the expression of the control housekeeping gene, thereby depicting the negative role of the G-quadruplex structure stabilization in the gene expression. Interestingly, AB_PGQ7 harboring gene, showed the highest attenuation (80%), followed by AB_PGQ2 (78%), AB_PGQ5 (74%), AB_PGQ6 (64%), AB_PGQ8 (51%), AB_PGQ1 (42%), and AB_PGQ4 (39%). Strikingly, BRACO-19 showed the minimum effect on the expression of AB_PGQ3 (4%) harboring gene that encodes Tetratricopeptide repeat protein (Figure 3.16 B).

The results of this experiment support the hypothesis of the interaction of BRACO-19 with the G-quadruplex structures in the bacterium *in vivo*. This points out the critical role of G-quadruplex structure stabilization in regulating G-quadruplex harboring genes by affecting their gene expression, thus laying down an unexplored avenue for targeting this extremely resistant bacterium.

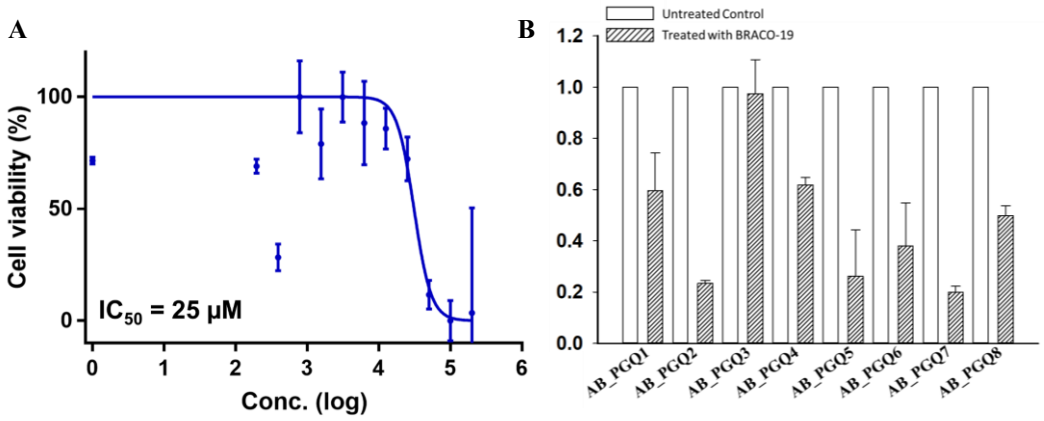

Figure 3.16. (A) MTT based growth inhibition assay of A. baumannii upon treatment with BRACO-19. (B) Fold change in the expression of genes harboring PGQs in A. baumannii treated w.r.t. the untreated culture control.

3.3.8 Effect of BRACO-19 on biofilm formation

A. baumannii is a notorious pathogen, mostly acquired from hospitals. The ability of this bacteria to survive on hospital surfaces has been strongly correlated to its biofilm-forming ability[209,210]. It is an established fact that biofilm-associated pathogens shows decreased antibiotic susceptibility and persistent existence in harsh environments[211,212]. In respect of this, and the presence of PGQs (AB_PGQ2 and AB_PGQ8) in the genes involved in biofilm formation, and the known role of G-quadruplexes in the regulation of transcription and translation of

the harboring genes, we tested the effect of stabilization of G-quadruplexes with BRACO-19 on the biofilm-forming ability of *A. baumannii*.

Therefore, a total of four sets, each of which was treated with a different concentration of BRACO-19 (25 µM, 12 µM, 6.25 µM) and untreated control, were observed under confocal microscopy after 48 h. On observation, it was noted that the thickness of the biofilm formed in the untreated control was the highest, being 17600 nm and with increasing concentration of BRACO-19 the thickness of the biofilm decreased with 25 µM having the least thickness of 9800 nm (Figure 3.17 A, B). These observations confirmed that BRACO-19 affected the biofilm formation by *A. baumannii* which might be due to binding of the ligand to the G-quadruplex motif harboring gene involved in biofilm formation.

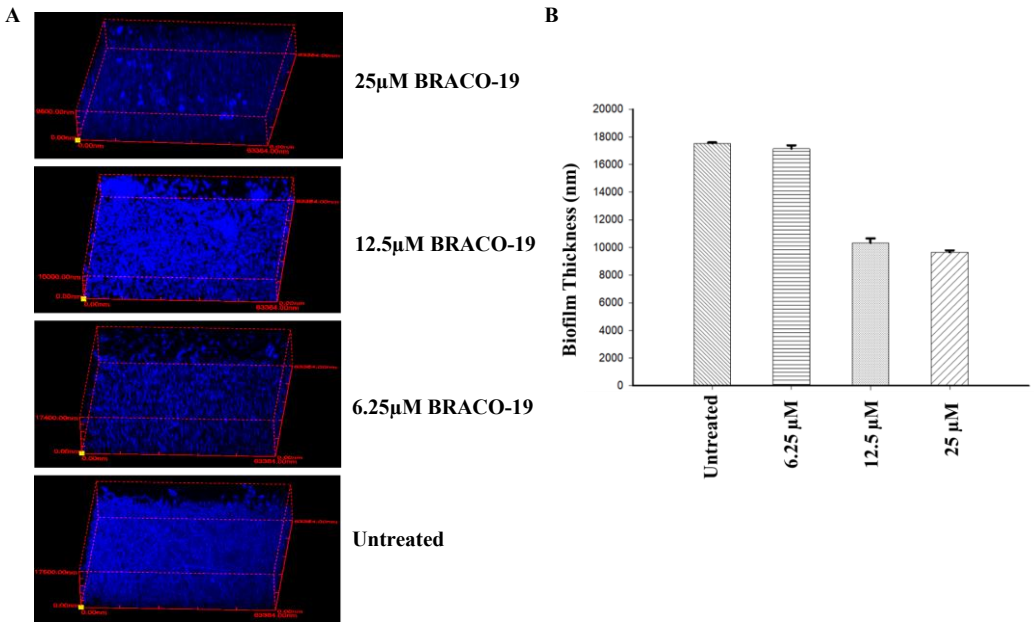

Figure 3.17. (A) Z-scan analysis images of A. baumannii biofilm thickness under varying concentrations of BRACO-19 (25 – 0 µM). (B) Bar graph representing the thickness of biofilm formed.

3.4 Discussion

The presence of G-quadruplex forming sequences and their evolutionary conserved-ness in bacterial and viral genomes raises curiosity about the importance of these structures in their genomes. G-quadruplex forming genes present in the bacterial and viral genomes are involved in the pathogenicity and virulence exhibited by drug-susceptible and drug-resistant strains. Several such genes are also

found to be involved in their survival inside the host or inanimate surfaces from which infections associated with these bacteria are acquired. This opens a new route for targeting such pathogenic bacteria, which have become increasingly drug-resistant. The idea of choosing G-quadruplex structures as a target for drugs was proposed long back in 1998[213]. Though targeting of G-quadruplex structures as a therapeutic option has been achieved in other human diseases, their potential has been relatively less explored against bacterial therapeutics affecting public health.

In this study, we first mined the whole genome of *A. baumannii* to unravel the presence of G-quadruplex motifs in its genome. Our bioinformatics analysis revealed the occurrence of G-quadruplex (classical and non-classical) motifs as predicted by our in-house tool and G4Hunter server. Functional annotation of these G-quadruplex motifs revealed their presence in various essential genes required for bacterial growth, nutrient transport, biofilm formation, and virulence.

Furthermore, we evaluated eight evolutionary conserved G-quadruplex motifs using an array of biophysical and biomolecular techniques. AB_PGQ1 was present in the ORF region of 3-hydroxy acyl-CoA dehydrogenase, which takes part in the fatty acid metabolism[214], while AB_PGQ2 was located in the ORF of pilus assembly protein *pilP,* which is involved in biofilm formation and host cell adhesion of the bacterium[215]. AB_PGQ3 was present in the ORF of tetratricopeptide repeat protein which is supposedly responsible for the transfer of bacterial virulence factors to host cells, binding to the host cells and inhibition of phagolysosomal maturation[216]; AB_PGQ4 was localized at the upstream of TetR family transcriptional regulator that regulates the efflux system by acting as repressors[217]; AB_PGQ5 was present in the ORF of aldehyde dehydrogenase family involved in cellular aldehyde metabolic process[218]; AB_PGQ6 was present in the ORF of aminotransferase pyridoxal phosphate-dependent enzyme taking part in cellular biosynthetic pathways[219]. Likewise, AB_PGQ7 was present in the ORF of amino acid racemase, which is responsible for D-amino acid Metabolism and, therefore, crucial for cell-wall biosynthesis[220], and AB_PGQ8 was present in the ORF of MFS transporter supposedly having a role in adherence and biofilm formation by the bacteria[221]. As a result, the stabilization of G-

quadruplex structures forming in these genes may influence various important metabolic pathways, adherence to host cells, and biofilm-forming ability, thereby affecting the growth and pathogenicity of the bacteria. The biophysical analysis such as NMR and CD spectroscopic analysis confirmed the formation of G-quadruplex structures by all the eight conserved AB_PGQs, and the molecularity of the PGQs was depicted by EMSA analysis. These results further affirmed the precise prediction of G-quadruplex forming motifs by the in-house G-quadruplex prediction tool.

Many G-quadruplex binding ligands have been found to specifically bind and stabilize G-quadruplex structures such as TMPyP4, TMPyP2, PDS, BRACO-19, and naphthalene diimide derivatives, etc., and many more small molecules are still in development[158]. Herein, we used BRACO-19, which showed higher stability and affinity towards AB_PGQs as compared to their linear counterparts. In addition to stabilizing the G-quadruplex structure, the G-quadruplex ligand was also able to inhibit the growth of *A. baumannii in* the micromolar range and affected the expression of G-quadruplex harboring genes. BRACO-19 was found to decrease the expression of these genes upon exposure, hinting at its involvement in the down-regulation of gene transcription. BRACO-19 was also able to impede the formation of biofilm by dysregulation of involved genes in the bacteria. However, it is important to acknowledge that BRACO-19, despite its high binding affinity, lacks adequate specificity towards G-quadruplex structures. Consequently, it becomes imperative to investigate the interaction of these bacterial G-quadruplex structures with alternative ligands or small molecules that provide a desirable balance between affinity and specificity. Furthermore, research efforts dedicated to designing molecules guided by the principles of structure-activity relationships may lead to the discovery of ligands with potent anti-bacterial activity via targeting of these secondary structures. Overall, this work, for the first time, provides an extensive understanding of evolutionarily conserved G-quadruplex motifs in *A. baumannii,* providing an advancing platform for designing therapeutics against this extremely drug-resistant critical pathogen.

3.5 Conclusion

G-quadruplexes have recently gained attention due to their association with several bacterial as well as viral infections affecting public health. The implications of G-quadruplexes in bacteria have been in focus here in light of the rapid development of multi-drug resistance by the pathogenic *A. baumannii*. Herein, we performed bioinformatic analysis to identify DNA G-quadruplex motifs conserved across the genome of *A. baumannii*, and proceeded with biophysical assays to confirm the formation of G-quadruplex structures in-vitro. The interaction and binding affinity between G-quadruplex selective ligand BRACO-19 and identified G-quadruplex motifs were evaluated through a series of experiments. The presence of BRACO-19 also significantly inhibited the expression of reporter gene mTFP containing the AB_PGQs in the *pet43a(+)* expression system. It was also observed that BRACO-19 addition resulted in bacterial growth reduction as well as regulated gene expression and biofilm formation. Given the inherent property of guanine-rich sequences to fold into G-quadruplex structures, both DNA and RNA molecules have the capability to adopt such structures. Although the G4 structures formed by DNA and RNA may exhibit diverse topologies, RNA-derived G4 structures are more thermodynamically stable. Thus, the exploration of potential G4 RNA structures in this pathogen is a viable avenue for research. Moreover, investigating RNA-derived G4 structures in pathogenic bacteria, which have received limited attention thus far, will enhance our comprehension of the role played by RNA G4 structures in diseases associated with these bacteria. In our study, we focused on DNA sequences to investigate G-quadruplex structures in A. baumannii; however, the examination of RNA G4 structures in this bacterium remains a prospective area for future investigation. In essence, our study underscored the probable significance of DNA G-quadruplex structures in the survival and pathogenicity exhibited by *A. baumannii* and their potential to be recognized as an efficient drug target against the bacteria.

CHAPTER 4

G-QUADRUPLEX STRUCTURES WITHIN THE *HFQ* GENE REGULATE RNA-PROTEIN INTERACTIONS IN *ACINETOBACTER BAUMANNII*

Chapter 4

G-Quadruplex structures within the *hfq* gene regulate RNA–protein interactions in *Acinetobacter baumannii*

4.1 Introduction

G-quadruplex structures (G4s) have emerged as significant regulatory structures in bacterial genomes with diverse biological functions that extend far beyond their initial discovery as simple DNA secondary structures[170,222]. These nucleic acid secondary structures are adopted by guanine-rich sequences in DNA and RNA that are formed by G-tetrad stacking and stabilized through co-ordination of monovalent cations, such as K^+ and Na^+[223,224]. While canonical G4s are comprised of three or more tetrads, two-tetrad (2G) G4s have recently emerged as structurally and functionally relevant motifs[225]. Though less stable, they can be stabilized under physiological conditions by cations, molecular crowding, loop interactions, or dimerization[191,223,226]. Their minimal sequence requirement makes them more prevalent than canonical G4s, expanding the regulatory landscape often missed by standard G4 predictors[227,228]. These two-tetrad G4s regulate transcription, translation, and RNA stability, acting as structural roadblocks or protein-binding platforms[229]. Notably, transcriptome-wide analyses demonstrate that most folded RNA G4s (rG4s) in bacteria are of the two-quartet type, particularly enriched in coding regions, and their regulatory impact on gene expression can vary across species[222,230]. Their transient ability to form under physiological conditions allows them to act as dynamic and reversible regulatory switches, particularly advantageous in the context of compact bacterial genomes. The functionality of two-tetrad G4s has not been extensively explored in the context of prokaryotic gene regulation, particularly within clinically relevant bacterial species.

Acinetobacter baumannii is one such notorious opportunistic pathogen associated with multidrug resistance and persistent nosocomial infections[231]. The regulatory mechanisms that enable its adaptation and survival under various environmental stresses are not fully understood. Among the key post-transcriptional

regulators in gram-negative bacteria is Hfq, a RNA chaperone protein. Hfq plays a pivotal role as a central RNA chaperone in the post-transcriptional regulatory networks of Gram-negative bacteria, such as *Acinetobacter baumannii*, required for the activity of most small regulatory RNAs (sRNAs)[232–235]. *A. baumannii* Hfq is distinguished by an unusually long, glycine-rich C-terminal domain, absent in most bacterial homologs[236,237]. This intrinsically disordered domain, rich in glycine, phenylalanine, and glutamine residues, has emerged as a critical player in displaying high-affinity towards RNA, ribo-regulation, and self-regulation of the protein itself in bacteria, such as *E. coli, P. aeruginosa*[232,234,238,239]. Subsequently, the transcript region of *hfq* encoding the CTD domain was found to be guanine-rich.

Additionally, according to recent reports, certain non-canonical RNA-binding roles of Hfq are also accounted, like interaction of Hfq with non-canonical nucleic acid structures such as G-quadruplexes (G4s) in *E. coli*[240]. Functional studies have shown that loss of Hfq or its glycine-rich tail leads to impaired growth, reduced stress tolerance, compromised biofilm formation, and diminished virulence, underscoring its importance in environmental adaptation and pathogenicity[234,237,241]. Similar phenotypes have also been reported for other pathogens, including *Pseudomonas aeruginosa*, *Salmonella enterica*, and *Klebsiella pneumoniae*, etc., where *hfq* mutants exhibit attenuated virulence, defective secretion, reduced adhesion and invasion, and decreased expression of virulence factors[235,242–244]. Results from biochemical assays have also demonstrated that truncation of the *hfq* CTD domain affects Hfq's ability to bind G4 DNA and RNA, leading to reduced genomic instability and altered gene expression profiles[245].

Henceforth, in this study, we investigated the presence and structural features of G4-forming sequences within the *hfq* gene of *Acinetobacter baumannii*, with a particular focus on their interaction with the Hfq protein. Employing an array of biophysical techniques such as Nuclear Magnetic Resonance (NMR), Circular dichroism (CD) Spectroscopy, Electrophoretic Mobility Shift Assay (EMSA), we characterized the formation of two-tetrad G4s in full-length and truncated variants

of *hfq* RNA and DNA (*hfq*_RNA; *truncated hfq*_RNA; *hfq*_DNA; *truncated hfq*_DNA). These G4 structures also demonstrated specific binding to BRACO-19, a well-established G-quadruplex ligand, as observed from Fluorescence Titration Assay and Isothermal Titration Calorimetry (ITC), further validating G4 formation. We further examined the interaction dynamics of these G4 motifs with both the full-length Hfq and Δ*CTD* protein. This integrative analysis reveals a previously unrecognized mode of structural modulation involving G-quadruplexes and the Hfq protein in bacterial gene regulation. Our findings not only expand the current understanding of post-transcriptional control in *A. baumannii* but also identify G4-Hfq complexes as promising targets for antimicrobial intervention. By bridging structural biology with bacterial regulatory networks, this work offers a foundation for future exploration of RNA-protein interactions in microbial pathophysiology and drug development.

4.2 Material and Methods

4.2.1 Reagents

The desalted DNA/RNA oligonucleotides and primers were procured from Integrated DNA Technologies (Coralville, Iowa, USA) and Sigma-Aldrich (St. Louis, MO, USA), respectively. Stock solutions of each were prepared by dissolving the lyophilized samples in Milli-Q water. BRACO-19 (SML0560), TMPyP4 (613560), and Thioflavin T (596200) were purchased from Sigma.

In vitro transcription

Full-length *hfq*_RNA and Mutant RNA were transcribed in vitro. DNA templates containing T7 RNA promoter and forward and reverse primers were designed and procured from Sigma-Aldrich (St. Louis, MO, USA). Templates for in vitro transcription were produced via PCR amplification, and RNAs were transcribed using in-house purified T7 RNA Polymerase. The synthesized transcripts were purified by running samples on 15 % denaturing PAGE.

4.2.2 Bioinformatic Analysis

The *hfq* gene sequence was retrieved from the NCBI Genome database and utilized for putative G4 motif prediction using our in-house G4 prediction tool (G4IPDB)[99]. The tool used the following algorithm for G4 prediction:

$$G\geq_2 N_{L1}\, G\geq_2 N_{L2}\, G\geq_2 N_{L3}\, G\geq_2$$

where G refers to Guanine, N refers to any nucleotide including Adenine, Thymine, Cytosine, and Guanine, and L1, L2, and L3 are the loops having variable lengths.

4.2.3 Cloning and expression of Hfq protein

A. baumannii hfq gene (A1S_3785) was PCR amplified and cloned in NdeI-XhoI site of pET-43.1a^{+} vector. The truncated version Hfq Δ*CTD* was amplified using the same forward primer, but a different reverse primer, cloned and expressed similarly in E. coli Rosetta strain. An overnight culture of E. coli Rosetta carrying the recombinant clones was grown in Luria-Bertani broth at 37 °C overnight. The expression of proteins from the recombinant clones was induced by adding 0.25 mM isopropyl β-D-thiogalactopyranoside (IPTG) to a secondary culture at $O.D._{600}$ = 0.8 and incubated further to grow for 16 - 18 hours at 18 °C. Recombinant proteins were purified as His-tagged fusions using Ni-NTA agarose. Cells were centrifuged, washed in chilled 1x PBS, and the cell pellets were resuspended in lysis buffer [50 mM Tris (pH 7.5), 1 M NaCl, 1 M urea, 1 mM β-mercaptoethanol (β-ME), 5 % glycerol, 1 mM Phenylmethylsulfonyl Fluoride (PMSF), 0.1 mg/ml DNase I, and 1 M $MgCl_2$]. After vortexing, homogenization, and sonication, lysates were clarified by centrifugation. The supernatant was collected and heated at 95 °C for 15 mins, centrifuged, treated with 30 µg/ml RNase A at 37 °C for 1 h, and re-clarified. The lysate was loaded purified using a Ni-NTA column, pre-equilibrated with wash buffer [50 mM Tris (pH 7.5), 1 M NaCl, 1 mM β-ME]. After 1 h of binding, 50 mM and 100 mM imidazole wash buffers were allowed to sequentially pass through the column. The bound protein was finally collected in 500 mM imidazole-containing wash buffer. Eluates were pooled and buffer exchanged against dialysis buffer [50 mM Tris (pH 7.5), 350 mM NH4Cl, 1mM EDTA, 0.05 % Triton-X and 5 % v/v glycerol] through dialysis. The proteins were resolved on

a 15 % (Hfq *FL*) and 18 % (Hfq Δ*CTD*) SDS PAGE gel. Protein concentration was calculated by measuring absorbance at 280 nm (A_{280}), using the molar extinction coefficient (ε = 2980 M^{-1} cm^{-1}) obtained using Expasy ProtParam Tool (https://web.expasy.org/protparam/).

4.2.4 Nuclear magnetic resonance

NMR experiments were carried out on a Bruker AVANCE III 400 MHz spectrometer (BioSpin International AG, Switzerland) attached with a 5 mm broadband inverse (BBI) probe. One-dimensional proton (^{1}H 1D) NMR spectra were recorded at 25 °C using 180 µl samples at oligonucleotide concentrations of 0.4–0.6 mM. Samples were prepared in potassium phosphate (KPO_4) buffer (10 mM, 100 mM K^+, pH 7.5) in 5 mm Shigemi NMR tubes, with DSS (4,4-dimethyl-4-silapentane-1-sulfonic acid) as internal reference compound. Prior to data collection, oligonucleotide samples were denatured by heating at 95 °C for 10 min and reannealed at room temperature for 1 h. For titration studies, DNA/RNA was incrementally added to the BRACO-19 solution. All NMR data were analyzed using TopSpin v4.0.6 software (academic license).

4.2.5 Circular Dichroism (CD) Analysis

CD spectra were recorded using a JASCO J-815 spectropolarimeter with a 1 mm path length quartz cuvette. RNA and DNA samples (5 and 10 µM) were prepared in KPO_4 buffer (10 mM, pH 7.5) supplemented with required K^+ concentration, denatured at 95 °C for 10 minutes, and reannealed at room temperature for 1 h. Samples were scanned at 25 °C with a wavelength range of 200 - 320 nm and a scanning speed of 50 nm/min. For CD titration with ligand and protein, the buffer was supplemented with 100 mM K^+. The ligand and protein were gradually added to the oligonucleotide solution to reach a final ligand: nucleic acid molar ratio (D:N) of 2:1 and protein: nucleic acid molar ratio (P:N) of 5:1, respectively. Baseline correction was performed prior to each experiment, and the resulting data were normalized by subtracting the spectrum of the buffer solution without oligonucleotides. Data plots were generated using SigmaPlot 15.0 software (Systat Software, Chicago, IL, USA).

CD melting experiments with the ligand were conducted using a JASCO J-815 spectropolarimeter fitted with a Peltier temperature control system and a PCB-1500 water circulation unit. Oligonucleotide samples (10 μM) were prepared following the same protocol as used for CD Analysis. Thermal denaturation profiles were recorded at ~265 nm over a temperature range of 25 °C to 95 °C with a ramp rate of 1 °C/min, continuing until a ligand: nucleic acid (D:N) ratio of 2:1 was reached. Normalized absorbance values were plotted against temperature using SigmaPlot 15.0 software (Systat Software, Chicago, IL, USA).

4.2.6 Native PAGE

Native polyacrylamide gel electrophoresis (PAGE) was performed to assess the molecular weight of the *hfq* sequences. 15% - 18 % native polyacrylamide gels were prepared and run in 1X TBE buffer supplemented with 100 mM K^+ at 4 °C using a Bio-Rad Mini-PROTEAN Tetra Vertical Electrophoresis system at 70 V. The oligonucleotide samples were diluted to a final concentration of 15 μM in KPO_4 buffer (10 mM, pH 7.5) with 100 mM cation concentration to assess molecularity. The gel was run till the dye front crossed three-fourths of the gel and then stained with ethidium bromide.

EMSA was also performed to check interaction between BRACO-19 and full-length and *hfq* RNA/DNA. Oligonucleotide solutions were prepared same as which were then titrated with a high concentration of BRACO-19 solution (100 - 0 μM) and incubated for 30 mins at room temperature. The resulting complexes were then resolved on agarose gel (3 %) prepared in 1X TBE buffer and run under cold conditions (on ice) at 55 V.

40 μM concentration of each purified protein was added to the RNA/DNA samples and were allowed to equilibrate for 1 h at room temperature. The resulting complexes were then resolved on agarose gel (3 %) prepared in 1X TBE buffer and run under cold conditions (on ice) at 55 V. All the gels were visualized using the ImageQuant LAS4000 system (GE Healthcare, Sweden).

4.2.7 Fluorescent ThT probe displacement assay

Fluorescence emission spectra were acquired on a BioTek Synergy H1 microplate reader (excitation 425 nm; emission 495 nm). Annealed oligonucleotides (5 μM) and Thioflavin T (10 μM) were prepared in KPO_4 buffer (10 mM, pH 7.5, 100 mM K^+). A 25 μM ligand solution, made in the same buffer, was added, the mixture incubated for 30 min at 25 °C, and fluorescence measured in a Corning half-area 96-well black plate. Each sample was run in duplicate, and the readings averaged. The displacement was calculated as:

$$\text{Displacement (\%)} = 100 - [100 \times (F_I - F_b)/(F_{I_o} - F_b)],$$

where F_I is the fluorescence with ligand, F_{I_o} is the fluorescence without ligand, and F_b is the fluorescence of ThT alone.

4.2.8 Fluorescence Titration Assay

Fluorescence titration experiments were performed using a Synergy™ H1 multi-mode microplate reader (BioTek Instruments, Winooski, VT, USA) at 25 °C. Corning half-area 96-well black plates were utilized for all measurements. All samples were prepared at an initial concentration of 20 μM and subjected to serial dilution. Each condition was assayed in duplicate, with per well reaction volume being 50 μl. The final well in each dilution series served as a blank and contained no oligonucleotide. To monitor the fluorescence response of BRACO-19 upon titration with DNA and RNA, fluorescence emission was measured at 440 nm following excitation at 360 nm. All fluorescence readings were corrected by subtracting the signal from the corresponding blank well. Data analysis was performed using Sigma Plot 15.0 software (Systat Software, Chicago, IL, USA). The equilibrium binding was modeled using the following equation:

$$f = \frac{\text{Bmax1} \times \text{abs (x)}}{K\text{d1} \times \text{abs (x)}} + \frac{\text{Bmax2} \times \text{abs (x)}}{K\text{d2} \times \text{abs (x)}}$$

where B_{max_1} and B_{max_2} represent the maximum number of binding sites, K_{d_1} and K_{d_2} are the equilibrium dissociation constants.

4.2.9 Isothermal titration calorimetric (ITC) analysis

Isothermal titration calorimetry (ITC) experiments were conducted using a MicroCal iTC200 microcalorimeter (GE Healthcare, Biosciences Ltd., Sweden). Oligonucleotide sample was prepared at a concentration of 10 μM, and BRACO-19 was prepared at 1 mM, both in KPO_4 buffer (10 mM, pH 7.5, 100 mM K^+). All titrations were performed at 25 °C by injecting 1.66 μL of BRACO-19 solution into the oligonucleotide solution at 120-second intervals, totaling 22 injections. To account for the heat of dilution, an individual titration was performed by injecting BRACO-19 into buffer alone. The resulting data were buffer-corrected by subtracting the heat of dilution from the binding isotherms. Binding isotherms were fitted using a two-site binding model and analyzed using Origin version 7 (Microcal Software Inc., Northampton, MA, USA).

4.2.10 Fluorescence spectroscopy

Fluorescence measurements were taken using a Fluorolog®-3 Spectrofluorometer (Horiba Scientific, Jobin Yvon, Palaiseau, France) operated by FluorEssence software (Horiba Scientific, Jobin Yvon, Palaiseau, France) at 25 °C. Working solutions of proteins (5 μM) and oligonucleotides were prepared in KPO_4 buffer (10 mM, pH 7.5, 100 mM K^+). Increasing concentrations of full-length and truncated *hfq* DNA and RNA were added in sequential Nucleic acid: Protein (N/P) ratios (0 - 2.0). Emission spectra were recorded in the wavelength range of 285 - 420 nm, using an excitation wavelength (λ_{exc}) of 274 nm (corresponding to Tyrosine). The data plots were generated and analyzed using OriginPro software (© OriginLab Corporation).

4.2.11 Total RNA Isolation and cDNA synthesis

Bacterial Culture and Treatment

Acinetobacter baumannii was cultured overnight at 37 °C (220 rpm) in 25 ml Brain Heart Infusion (BHI) broth. A 50 ml BHI subculture was inoculated with 1 % of this pre-culture and grown under similar conditions until $O.D._{600} = 0.5$ was reached. At this O.D., 2 ml aliquots were distributed into three treatment groups: Untreated control, treated groups ($IC_{12.5}$ and IC_{25}), and incubated at 37 °C (220 rpm) for 2 h.

RNA Isolation

Cells were harvested by centrifugation at 6000 rpm and processed immediately for RNA extraction using RNAIso Plus (Takara) according to the manufacturer's protocol. RNA concentration and purity were quantified using a NanoDrop spectrophotometer (Thermo Scientific), with yield reported as ng/µL and purity assessed by the A_{260}/A_{280} ratio.

cDNA Synthesis

Total RNA (2 µg) was reverse-transcribed in 20 µl reactions using the PrimeScript™ cDNA Synthesis Kit (Takara Bio USA, Inc.), following the manufacturer's instructions.

4.2.12 Gene Expression Profiling by Quantitative Real-Time PCR (qRT-PCR)

qRT-PCR was performed using Applied Biosystems PowerUp SYBR Green Master Mix in 10 µL reaction volumes. Each reaction contained 0.5 µM of gene-specific primers (Table B1) and 10 ng cDNA template. Reaction was set up in duplicates in a 96-well plate and run on a QuantStudio 3 Real-Time PCR System (Applied Biosystems, USA), with 16S rRNA serving as the endogenous reference gene. Thermal cycling parameters were:

Initial hold: 50 °C for 2 min

Denaturation: 95 °C for 10 min

40 cycles: 95 °C for 15 s → 60 °C for 60 s → 72 °C for 5 min

Final extension: 72 °C for 10 min

Gene expression was quantified using the comparative $\Delta\Delta C_t$ method, with target gene C_t values normalized to 16S rRNA and calibrated against untreated controls. Statistical significance between untreated and treated groups was determined by unpaired t-test using GraphPad Prism v 8.0.2 (GraphPad Software, San Diego, CA). Structural details of the hfq constructs amplified in the RT-PCR assay are listed in Table B2.

4.3 Results and Discussion

4.3.1 Mapping of *hfq* G4 structure and Hfq protein

Three G-quartet G4s are well-established for their structural stability and regulatory roles in both prokaryotic and eukaryotic genomes; however, emerging studies highlight the functional relevance of two G-quartet G4s in bacteria. These shorter G4s, though less stable than their 3G or 4G counterparts, are enriched in promoter regions, untranslated regions, and coding sequences, where they modulate gene expression with high structural plasticity. We conducted an in-silico analysis of the *hfq* gene (A1S_3785) and identified a distinct guanine-rich transcript unique to the *Acinetobacter* genus. Genome mining using our in-house G4 prediction tool revealed eleven potential G-quadruplex (PGQ) motifs within this transcript, defined by a G-tract length of ≥2 and loop lengths ranging from 1 to 15 nucleotides. Notably, seven of these motifs, all 2G-tract G4s, were present as tandem repeats within the *hfq* gene sequence corresponding to the C-terminal region of the Hfq protein (Table 4.1).

Table 4.1. List of predicted G4 motifs within the hfq gene.

#	Length (bp)	PG4 Motifs	cG Score	cC Score
1	32	**GG**UGCACAA**GG**UGCA**GG**UUUCCCA GCUCA**GGG**	120	80
2	20	**GG**UAGUCAA**GG**UGGCUUC**GG**	90	30
3	20	**GG**UCAA**GG**CGCU**GG**CUUU**GG**	90	40
4	23	**GG**UGCUCAA**GG**UGCU**GG**CUUC**GG**	100	50
5	17	**GG**CCAA**GG**C**GG**CUUC**GG**	80	50
6	17	**GG**UCAA**GG**U**GG**CUUC**GG**	80	30
7	17	**GG**UCAA**GG**U**GG**CUUC**GG**	80	40
8	17	**GG**UCAA**GG**U**GG**CUUC**GG**	80	40
9	17	**GG**UCAA**GG**U**GG**CUUC**GG**	80	30
10	17	**GG**UCAA**GG**U**GG**CUUC**GG**	80	40

To evaluate the G4-forming potential of these motifs, we selected a 46-nucleotide sequence encompassing the repeat region (*hfq*_RNA) and a shorter 18-nucleotide variant (*truncated hfq*_RNA) for in vitro analysis, along with their corresponding DNA sequences (*hfq*_DNA and *truncated hfq*_DNA) (Table 4.2). To investigate the regulatory relevance of the Hfq protein, we examined the interactions of both full-length Hfq (Hfq *FL*) and C-terminal truncated Hfq (Hfq *ΔCTD*) with all *hfq* RNA/DNA sequences in vitro.

Table 4.2. List of hfq sequences used in the study.

G4	Sequence
hfq_RNA	GGCUUCGGUGGCCAAGGCGGCUUCGGUGGUCAAGGUGGCUUCGGUG
truncated hfq_RNA	GGCUUCGGUGGCCAAGG
hfq_DNA	GGCTTCGGTGGCCAAGGCGGCTTCGGTGGTCAAGGTGGCTTCGGTG
truncated hfq_DNA	GGCTTCGGTGGCCAAGG

4.3.2 Guanine-rich motifs within *hfq* transcript fold into G4 structures in vitro

Nuclear magnetic resonance (NMR) spectroscopy is a widely used technique for probing the structural characterization of macromolecules, including nucleic acids, and therefore a powerful tool for analyzing G4 structures under physiologically relevant solution conditions. Guanine H1 imino protons involved in G4 formation exhibit characteristic chemical shifts in the 10.0 - 12.5 ppm range due to Hoogsteen hydrogen bonding (G:G). In contrast, imino protons involved in duplex Watson-Crick hydrogen bonding (A:U; G:C), typically give rise to chemical shifts in the 12.5 - 14.0 ppm region. To evaluate the G4 formation in the selected RNA/DNA sequences, 1D ^{1}H NMR spectra were recorded for both full-length and truncated *hfq* variants. The presence of imino proton resonances between 10.0 - 12.5 ppm, confirmed the presence of Hoogsteen hydrogen bonds and thus G4 formation in *hfq*_RNA (Figure 4.1). The *truncated hfq*_RNA also exhibited distinct G4 signals, albeit with broader resonances, possibly indicating greater structural dynamics compared to *hfq*_RNA (Figure 4.1). Additionally, resonances in the 12.5 - 13.5 ppm region were also evident in both full-length and truncated sequences, indicating the coexistence of Watson-Crick base-paired structures, likely attributable to flanking duplex elements, as well as the G4 structure. In case of *hfq*_DNA, well-resolved imino proton resonances between 10.0 - 12.5 ppm, comparable to that of RNA, were observed, and *truncated hfq*_DNA also exhibited sharp peaks in the same range, thus hinting at the formation of G4 structure in the DNA counterparts (Figure 4.1). The presence of minor peaks observed in the Watson-Crick region (12.5 - 13.5

ppm) also indicated some conventional base pairing interactions. Collectively, these findings supported the presence of a defined G4 motif in both full-length and truncated *hfq* DNA and RNA constructs, with the truncated sequences able to retain the essential GQ-forming core. This spectroscopic analysis reinforced the in-silico predictions of G4 structure formation by shorter G-rich sequences.

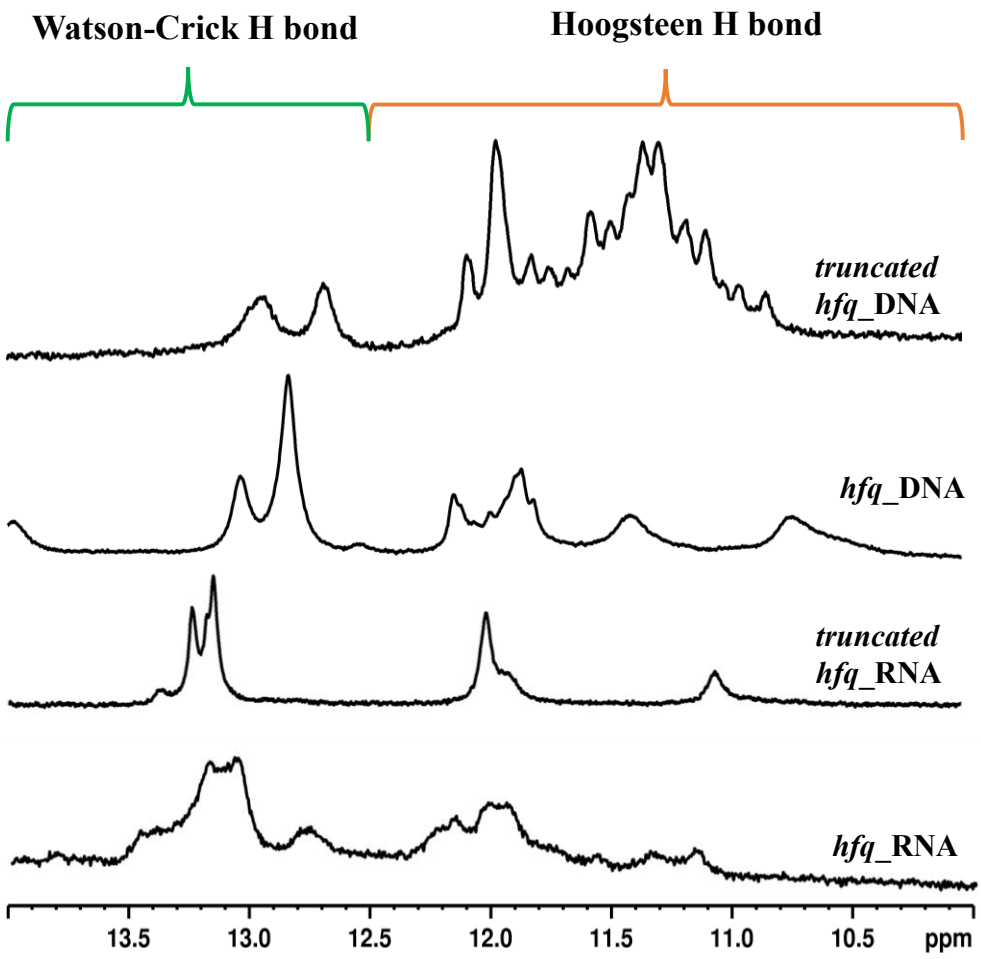

Figure 4.1. 1D 1H NMR spectra of hfq RNA and DNA G4 sequences.

4.3.3 Cation-Driven Topological and Molecular Variability of *hfq*_G4s

Circular dichroism (CD) spectroscopy is a primary analytical tool for characterizing G4 structures, providing unique insights into their topological identification. This technique distinguishes G4 topologies by characteristic spectral profiles; parallel (positive ~260 nm, negative ~240 nm), antiparallel (positive ~290 nm, negative ~260 nm), and hybrid (positive ~260/290 nm, trough ~240 - 260 nm), with RNA

G4s typically adopting a parallel fold. However, DNA G4s can adopt diverse folding patterns.

CD spectroscopy was performed to confirm the G4 folding of selected *hfq* DNA and RNA sequences in the presence of varied monovalent and divalent cations. CD spectrum of *hfq*_RNA revealed a positive peak at ~265 nm and a negative peak at ~240 nm in the presence of 50 mM K^+, which is signature of parallel G4 topology (Figure 4.2 A). These signals were found to be moderately reduced in Na^+, and highly reduced in Li^+ and Mg^{2+}, as compared to those in K^+ for the same RNA concentration. This confirmed the K^+ dependent stabilization of *hfq*_RNA. Titration with increasing K^+ (0 - 200 mM) did not significantly alter the ellipticity beyond 100 mM for *hfq*_RNA (Figure 4.2 B), suggesting stabilization of the folded G4 structure even at low potassium concentrations. The CD spectrum of *truncated hfq*_RNA displayed a similar topology but a slightly reduced ellipticity, suggesting a compact yet stable G4 structure with a less polymorphic folding (Figure 4.2 A), which was in line with the NMR spectroscopy results. CD spectrum of *hfq*_DNA displayed CD peaks characteristic of antiparallel structure with a positive peak around ~285 nm and a negative peak around ~260 nm, though the intensity was significantly lower, likely due to conformational heterogeneity (Figure 4.2 A). In case of *truncated hfq*_DNA, signature peaks suggestive of hybrid G4 structure were observed, with positive peaks centered around ~290 nm, with a secondary peak at ~262 nm and, a negative peak around ~245 nm (Figure 4.2 A). Additionally, both DNA sequences exhibited maximum ellipticity in the presence of K^+, in comparison to other cations, indicating K^+-dependent stabilization. Upon titration with K^+, no significant enhancement in CD signature was detected for both, even at higher K^+ concentrations (Figure 4.2 B). Overall, these results indicated K^+-dependent G4 formation in *hfq*, favored in RNA, and exhibiting less robust folding in DNA.

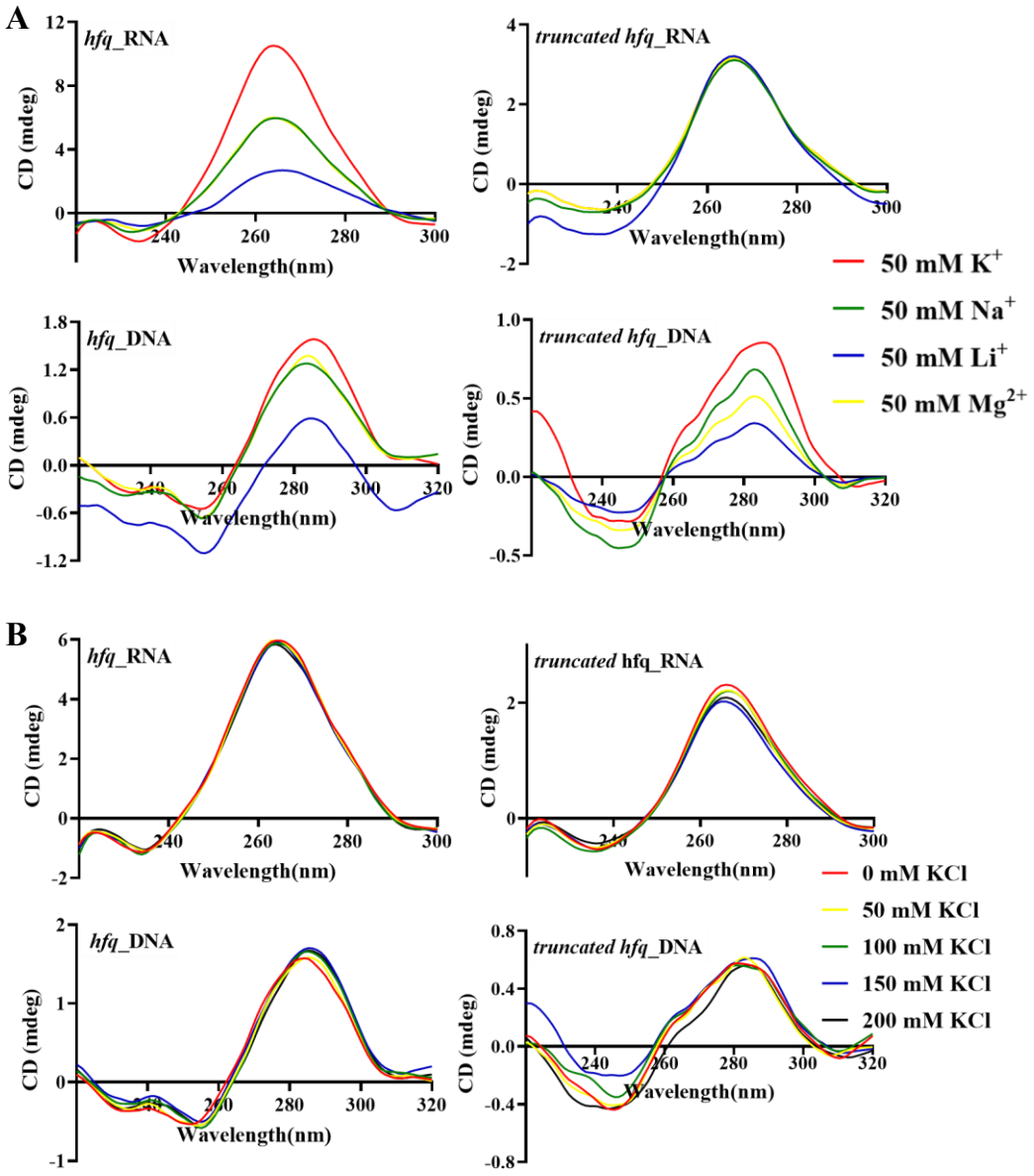

Figure 4.2. (A) CD spectra of hfq RNA and DNA G4 sequences (A) in the presence of different cations (B) increasing K^+ concentrations (0 - 200 mM).

Electrophoretic mobility shift assay (EMSA) is employed for assessing the molecularity and G4 oligomeric structures, which enables the assessment of whether a G-rich sequence forms intramolecular (monomeric) or intermolecular (multimeric) G4 by observation of the migration patterns on native gels[246,247]. An intramolecular G4, is typically compact and monomeric, and migrates as a single, distinct band, while an intermolecular G4 (involving multiple strands) displays slower migration due to its larger size and higher molecular weight[248].

EMSA analysis of *hfq* full-length and truncated sequences was performed to investigate their molecularity by allowing their migration on polyacrylamide gels along with their respective mutants. It was observed that *hfq*_RNA and *truncated hfq*_RNA both migrated slower than their mutants, thereby suggesting intermolecular G4 structure formation in the presence of all four cations (K^+, Na^+, Li^+, Mg^{2+}) (Figure 4.3). The migration was observed to be faster in the case of *hfq*_DNA and *truncated hfq*_DNA, suggesting an intramolecular G4 structure formation in the presence of all four cations (K^+, Na^+, Li^+, Mg^{2+}) (Figure 4.3). A reported intramolecular G4-forming sequence (bcl2), and its mutant counterpart, which served as a positive control alongside *hfq* DNA sequences, also displayed a similar pattern[249].

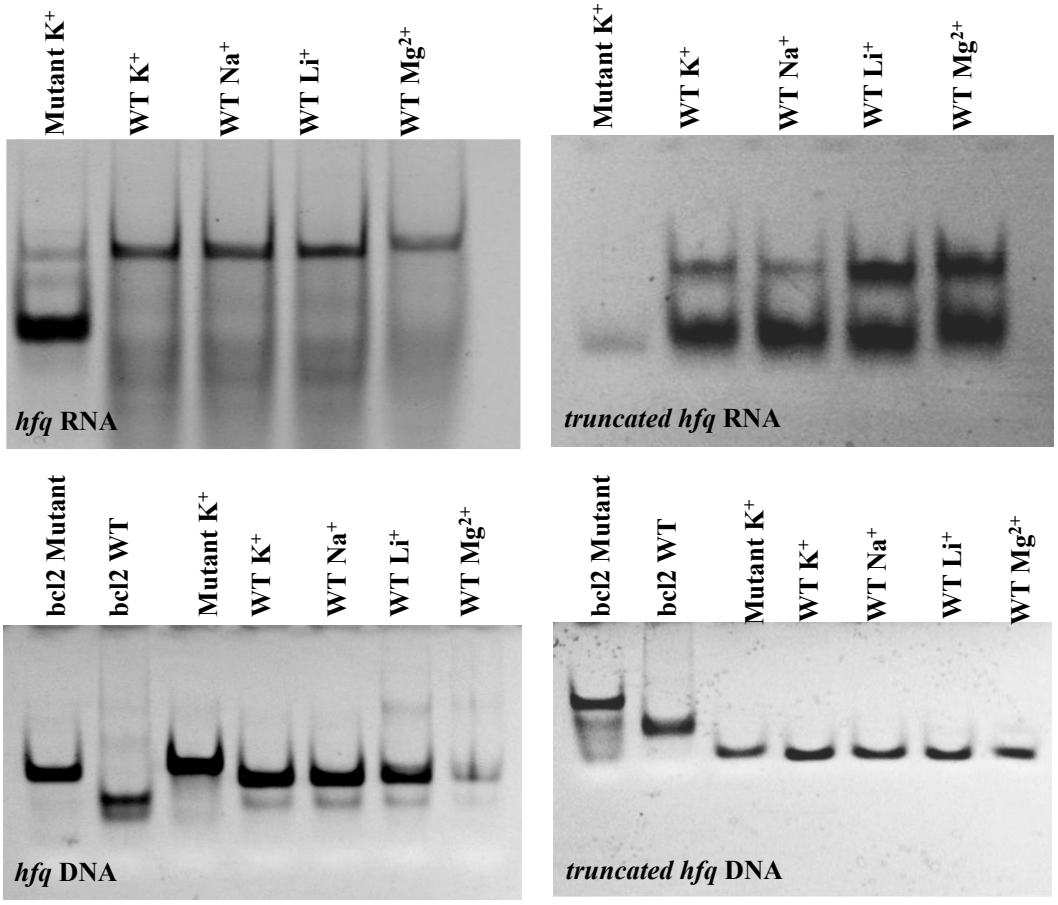

Figure 4.3. Native PAGE analysis depicting molecularity hfq RNA and DNA G4 sequences.

4.3.4 Thioflavin T fluorescence displacement as a readout for *hfq* G4-ligand binding

Thioflavin T (ThT) is a benzothiazole dye that exhibits weak fluorescence in solution but shows fluorescence intensity enhancement upon binding to G-quadruplexes. The ThT probe displacement assay is a fluorescence-based technique used to monitor the binding of small molecules or ligands to G4 structures. The ThT probe displacement assay was employed to evaluate the interaction of well-known G4 binding ligands, BRACO-19 and TMPyP4, with the selected *hfq*_G4 sequences.

A concomitant increase in fluorescence was observed upon ThT binding for all the full-length and truncated *hfq* RNA/DNA sequences, in contrast to the corresponding mutant sequences. Upon addition of the ligands, a reduction in fluorescence intensity was observed, indicative of ThT displacement from its binding sites. This decrease was quantified and expressed as a percentage, providing a sensitive readout for ligand interaction and binding affinity. All the *hfq*_G4s displayed a comparative better displacement with BRACO-19, in comparison to TMPyP4 (Figure 4.4). Overall, the ThT probe displacement assay proved to be an effective tool in both the confirmation of G4 structure formation and the analysis of G4-ligand interaction.

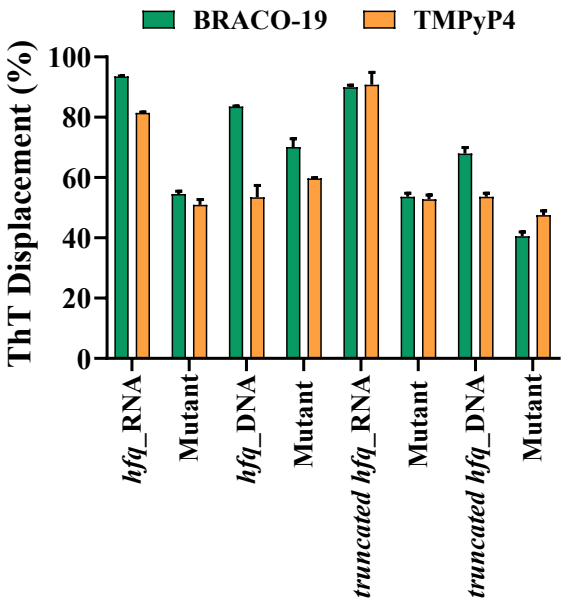

Figure 4.4. ThT displacement assay showing percentage displacement by BRACO-19 and TMPyP4 across wild-type and mutant hfq RNA and DNA G4 sequences.

4.3.5 Ligand responsiveness of *hfq* G4 validated through BRACO-19 binding

To assess the effect of the G-quadruplex-binding ligand BRACO-19 on the folding and stability of *hfq* G4 structures, CD spectra were recorded across increasing ligand-to-nucleic acid molar ratios (D:N) for *hfq*_G4 RNA/DNA sequences. In *hfq*_RNA, the intensity of the positive peak at ~265 nm exhibited minimal shift with increasing BRACO-19 concentration (up to D:N = 4), indicating ligand-independent stabilization of the parallel G-quadruplex topology (Figure 4.5). For *truncated hfq*_RNA, there was a progressive decrease in the overall ellipticity (Figure 4.5). For *hfq*_DNA, the CD signal showed a moderate increase in ellipticity upon BRACO-19 addition, suggesting a ligand-induced stabilization, and the same was observed for *truncated hfq*_DNA (Figure 4.5). These results collectively demonstrated the inherent stability of the *hfq*_RNA G4 as compared to other *hfq* G4 variants, where the structure was stabilized upon ligand addition.

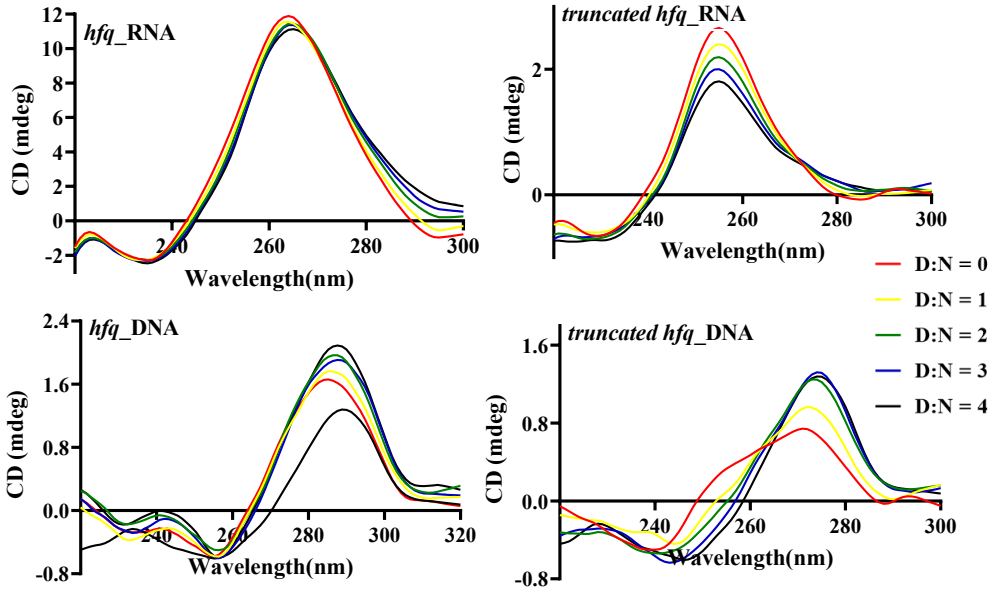

Figure 4.5. CD titration spectra of hfq_RNA (i) and truncated hfq_RNA (ii) with increasing BRACO-19 concentrations (D:N ratios 0 - 4), indicating G4 stabilization.

The CD melting profile provides insights into the stabilizing effect of ligands on G4 structures by evaluating changes in their melting temperature (T_m). To assess the thermal stability of the *hfq* G4s and the stabilizing effect of BRACO-19 on the same, CD melting assays were performed. CD melting spectra were acquired by monitoring the ellipticity at the characteristic wavelength corresponding to the G4 topology, over a temperature range of 25 °C - 95 °C at a controlled rate.

The thermal denaturation was carried out at a ligand-to-nucleic acid molar ratio of 2:1, wherein the T_m showed a significant increase in the presence of BRACO-19 for *hfq*_RNA (3.5 °C), truncated *hfq*_RNA (2.1 °C), *hfq*_DNA (19.6 °C), while a very minimal increase was observed for truncated *hfq*_DNA (0.7 °C) (Figure 4.6). The drastic elevation in T_m reflects a ligand-induced stabilization of the DNA G4 conformation, whereas, *hfq*_RNA G4 showed considerate stability even in absence of the ligand, as evident from the thermal denaturation results. The stabilization of G4 and increase in T_m is consistent with the ability of BRACO-19 to stack at the terminal G-quartets and enhance the structural rigidity of G-quadruplexes[250,251].

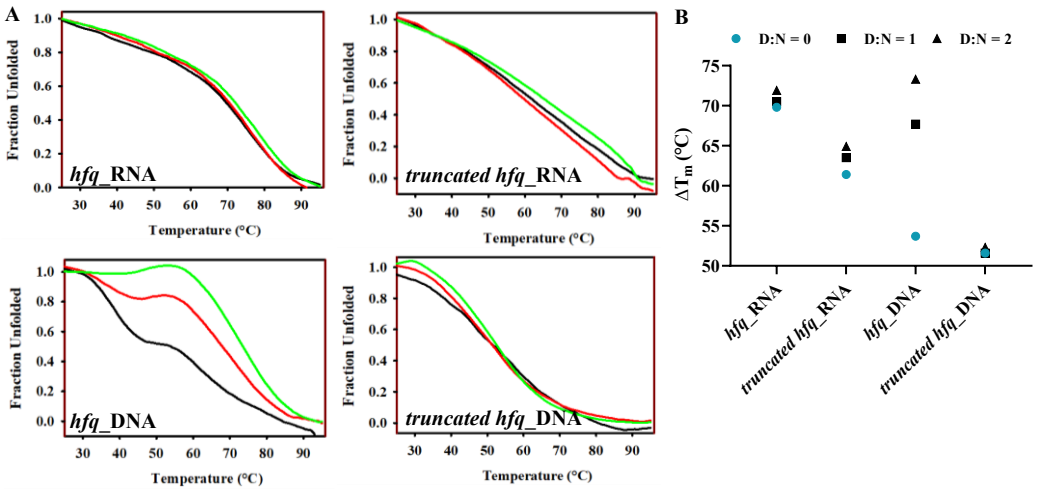

Figure 4.6. Melting temperature shifts (ΔT_m) of hfq RNA and DNA sequences in the absence and presence of BRACO-19 (D:N = 0, 1, 2).

EMSA can also be adapted to investigate the influence of ligands on G4 formation and stability, providing insight into the interaction and affinity of the ligand with these structures. The assay exploits the principle that ligand binding to nucleic acid leads to a reduced electrophoretic mobility on native polyacrylamide or agarose gels due to slower migration of the resulting complex compared to the free nucleic acid, providing a visual readout of interaction between the two[130]. To validate the interaction between BRACO-19 and *hfq* full-length and truncated DNA and RNA G4s, EMSA was performed using increasing concentrations of BRACO-19 (0 - 50 µM). At 50 µM, a shift in mobility was observed for all the bands corresponding to *hfq*_G4s-protein complexes in comparison to the free G4 controls (0 µM), indicating a stable complex formation (Figure 4.7)[252]. This shift suggests binding of BRACO-19 to G4 structure formed in the selected sequences.

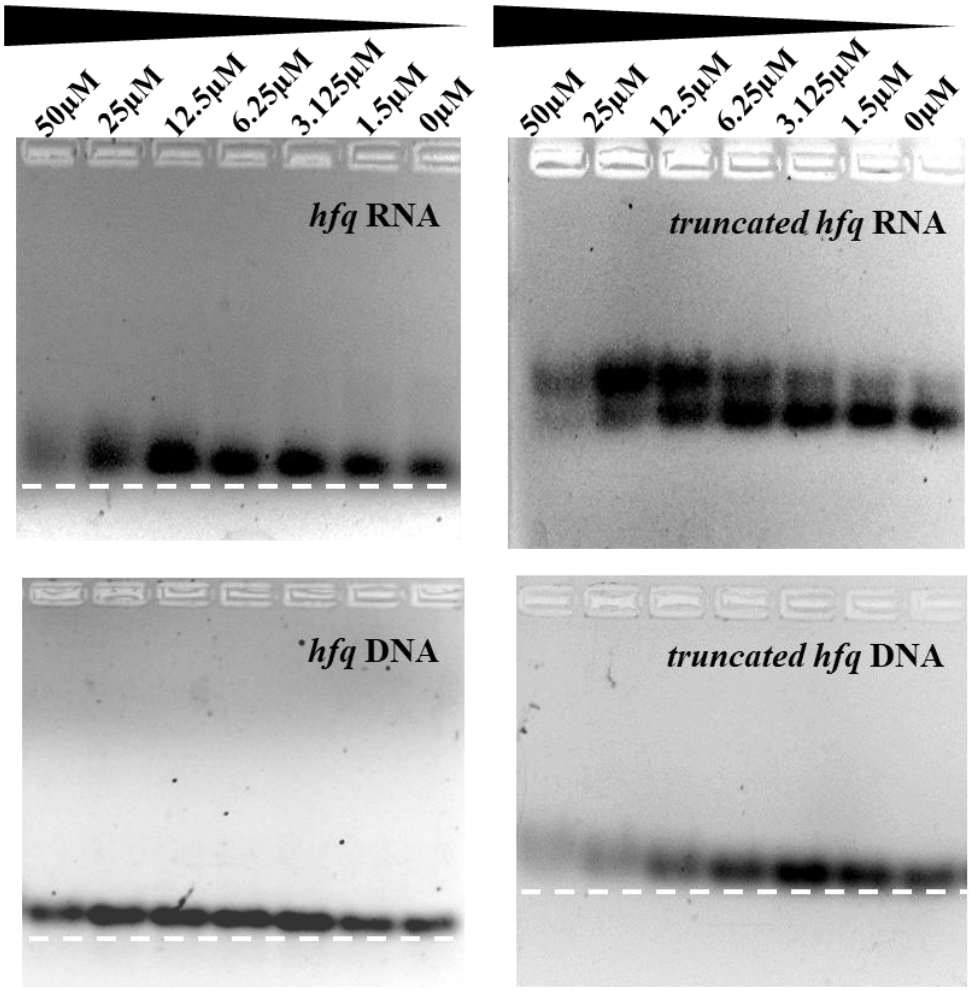

Figure 4.7. EMSA of hfq RNA and DNA sequences with BRACO-19 showing retardation in presence of ligand (50 μM) with respect to free nucleic acid (0 μM).

4.3.6 Robust affinity of BRACO-19 for *hfq*_G4 structures

Fluorescence titration was employed to evaluate the binding of BRACO-19 to *hfq*_G4 RNA/DNA. BRACO-19 exhibits measurable shifts in fluorescence intensity (ΔF) upon interaction with nucleic acids, which, when fitted using a two-site saturation model, yield dissociation constants (K_d). *hfq*_RNA exhibited strong binding with BRACO-19 (K_d = 0.017 μM) indicating a high-affinity interaction. In contrast, *truncated hfq*_RNA showed a comparatively weaker binding (K_d = 1.094 μM), suggesting that structural elements in the full-length RNA enhance better ligand stabilization. These results are consistent with CD NMR data showing an inherently stable parallel G4 topology in the *hfq*_RNA[253,254]. The binding

affinity of BRACO-19 towards *hfq*_DNA was found to be less than *hfq*_RNA (K_d = 0.066 μM). In contrast, *truncated hfq*_DNA showed a comparatively weaker binding (K_d = 0.2 μM). Overall, BRACO-19 displayed preferential and stronger binding to full-length *hfq* RNA, with lower affinity for truncated or DNA sequences (Figure 4.8).

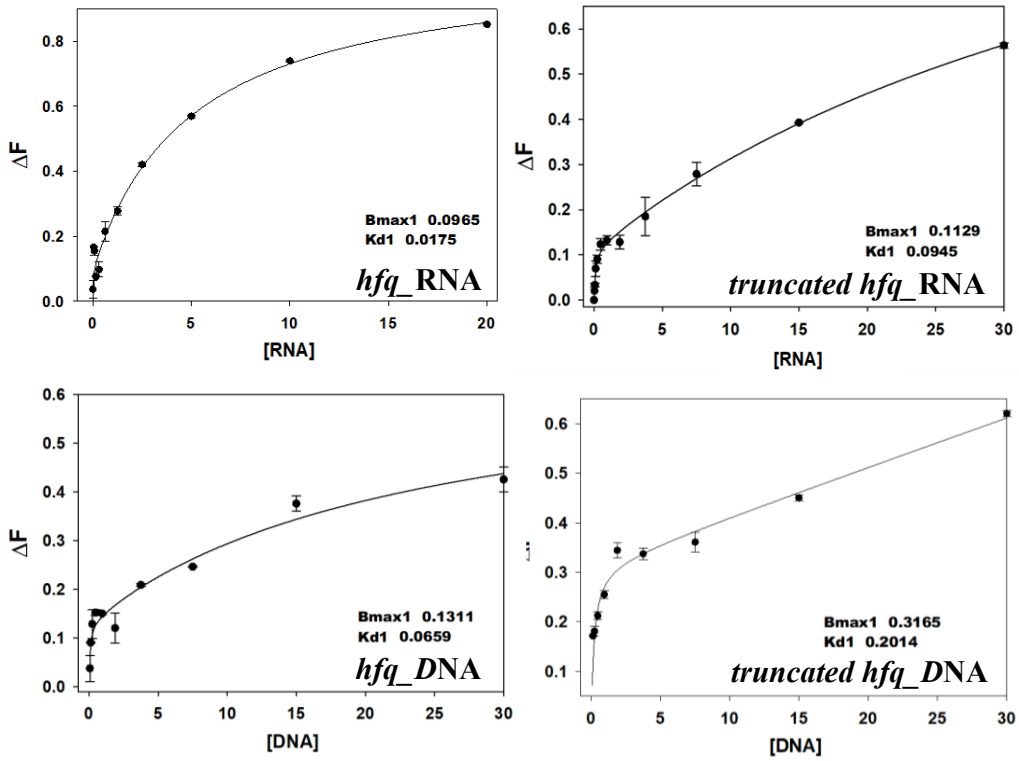

Figure 4.8. Fluorescence titration studies of BRACO-19 with hfq RNA/DNA G4 sequences. Plot after fitting the data obtained due to the interaction of BRACO-19 with the respective hfq by two-mode binding.

Isothermal titration calorimetry (ITC) was utilized to assess the thermodynamic profile of the interaction of BRACO-19 with full-length and truncated *hfq* RNA and DNA G4 sequences. The sequence *hfq*_RNA exhibited a strong exothermic interaction with a sharp sigmoidal binding curve, indicating a high-affinity (K_d = 3.5 nM) and specific recognition by BRACO-19. In contrast, the *truncated hfq*_RNA exhibited a lower dissociation constant (K_d = 0.87 μM), suggesting a probable effect of truncation on ligand accessibility. Similarly, BRACO-19 displayed moderate affinity towards *hfq*_DNA (K_d = 0.58 μM) compared to *hfq*_RNA, whereas the *truncated hfq*_DNA construct exhibited significantly

weaker and less cooperative binding (K_d = 5.4 μM). These results demonstrated that BRACO-19 preferentially interacts with full-length RNA G-quadruplexes, in line with other result analyses (Figure 4.9, Table 4.2). The less pronounced interaction with truncated constructs underscored the role of sequence length in G4 stability and determining ligand affinity. Titration was also performed with corresponding mutant RNA and DNA sequences to evaluate the significance of G4 structure in the binding with BRACO-19, which displayed high K_d values (Table B3).

Table 4.2. Table depicting the values of thermodynamic parameters obtained through Isothermal Titration Calorimetry (ITC) Analysis of the hfq RNA and DNA G4 sequences with BRACO-19.

Parameters	***hfq*_RNA**	***truncated hfq*_RNA**	***hfq*_DNA**	***truncated hfq*_DNA**
K_d1 (μM)	0.004	0.870	5.435	0.581
ΔG1 (cal/mol)	-5.550	-6.051	-5.178	-78.840
ΔS1 (cal/mol/°C)	21.900	8.140	7.340	-258.000
ΔH1 (cal/mol)	-5.002×10^3	-5.847×10^3	-4.994×10^3	-8.529×10^4

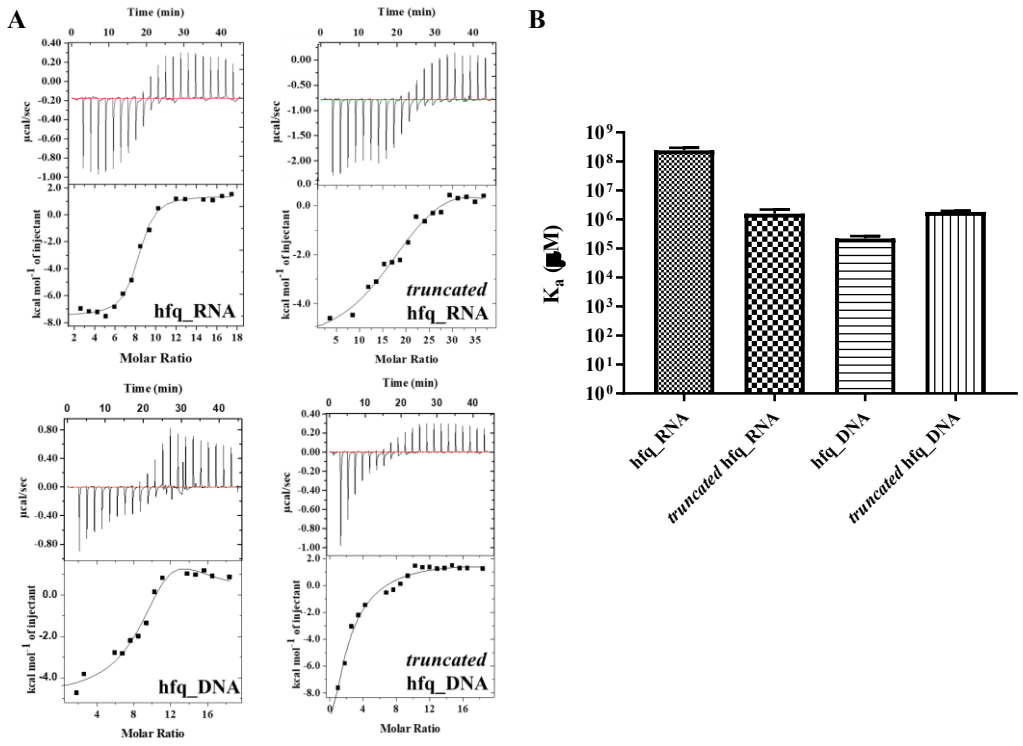

Figure 4.9. (A) ITC binding isotherms of titration of hfq RNA and DNA G4 sequences with BRACO-19. (B) K_a values represented on a log scale for comparative assessment of BRACO-19 affinity from ITC study.

To investigate the molecular interaction between BRACO-19 and *hfq* RNA/DNA G4, 1D proton NMR spectroscopy was employed to monitor chemical shift perturbations and line broadening in the aromatic proton region (6.5 - 8.8 ppm) of BRACO-19 NMR spectrum upon nucleic acid titration. Broadening of proton resonances is indicative of ligand binding, or complex formation, often attributed to intermediate exchange on the NMR timescale. Progressive titration of *hfq*_RNA in BRACO-19 solution resulted in significant line broadening and intensity loss of well-resolved signals (H1, H3, H2/H4, H5), and the consequent appearance of new resonances, indicating strong binding of the ligand to a well-structured *hfq*_RNA G4 structure (Figure 4.9). For *truncated hfq*_RNA, similar broadening was observed, but the effect was less intense and more gradual, suggesting slightly reduced affinity, consistent with fluorescence titration assay results (Figure 4.10). In contrast, *hfq*_DNA showed minimal peak broadening at the same D:N ratio (Figure 4.10), and less intense additional resonances, indicating a comparative

weaker interaction, which may be attributed to the comparatively less stable folding of DNA G4s compared to their RNA counterparts[255]. Similarly, in case of *truncated hfq*_DNA, negligible changes in peak broadening were observed (Figure 4.10), reinforcing the conclusion that BRACO-19 does not significantly interact with this sequence under the tested conditions. Altogether, these NMR results highlight the preferential interaction of BRACO-19 with *hfq* RNA_G4, as compared to the other sequences.

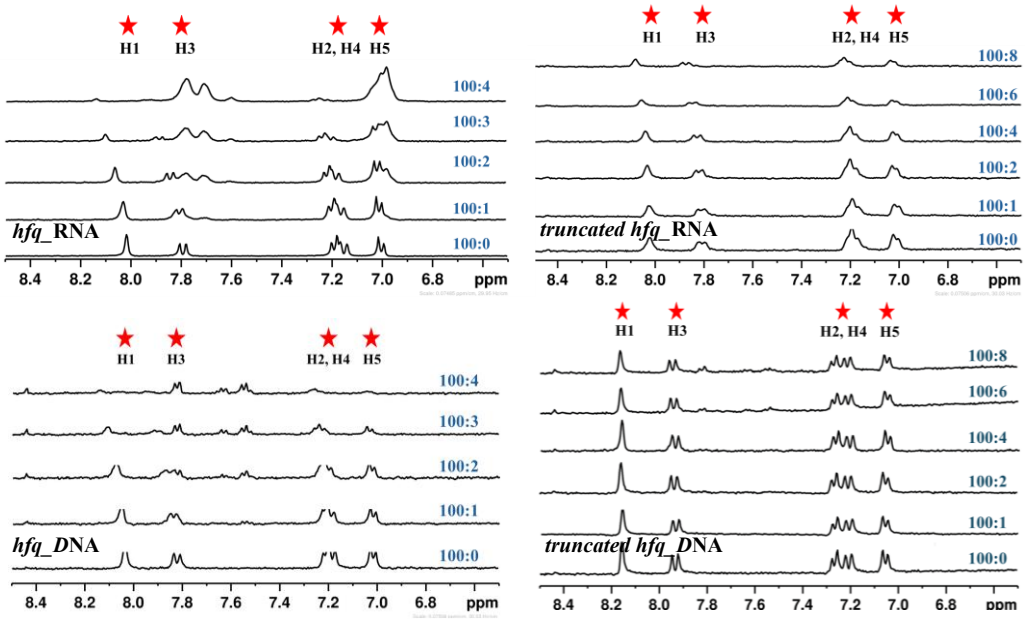

Figure 4.10. 1D 1H NMR peak broadening analysis of BRACO-19 with hfq RNA and DNA G4 sequences.

4.3.7 Recognition of *hfq*_G4 structures by Hfq Protein

To investigate the recognition potential of the full-length and Δ*CTD* Hfq protein towards G4 structures, CD titration spectroscopy was performed with full-length and *truncated hfq* DNA and RNA sequences. Upon titration with Hfq *FL*, a dose-dependent decrease in the positive CD signal at ~265 nm was observed for *hfq*_RNA and *truncated hfq*_RNA, suggesting an interaction of both protein variants with RNA G4 (Figure 4.11). A less pronounced decrease was seen with DNA counterparts, indicating weaker or less specific interactions (Figure 4.11). In contrast, titrations with Hfq *ΔCTD* showed modest and similar spectral changes with all the G4s (Figure 4.11). This may suggest the lack of recognition or

specificity towards RNA/DNA structures due to the truncation of the CTD. The CD titration analysis demonstrated that both the *FL* and *ΔCTD* Hfq variants maintain functional interaction with all nucleic acid targets, though *ΔCTD* with moderately reduced specificity, in comparison to Hfq *FL*. It is also noteworthy to mention that the Hfq *CTD* may be responsible for the differential binding enhancement of RNA G4s in case of titration with Hfq *FL*, consistent with its known role in RNA chaperone activity and multivalent binding[256–258].

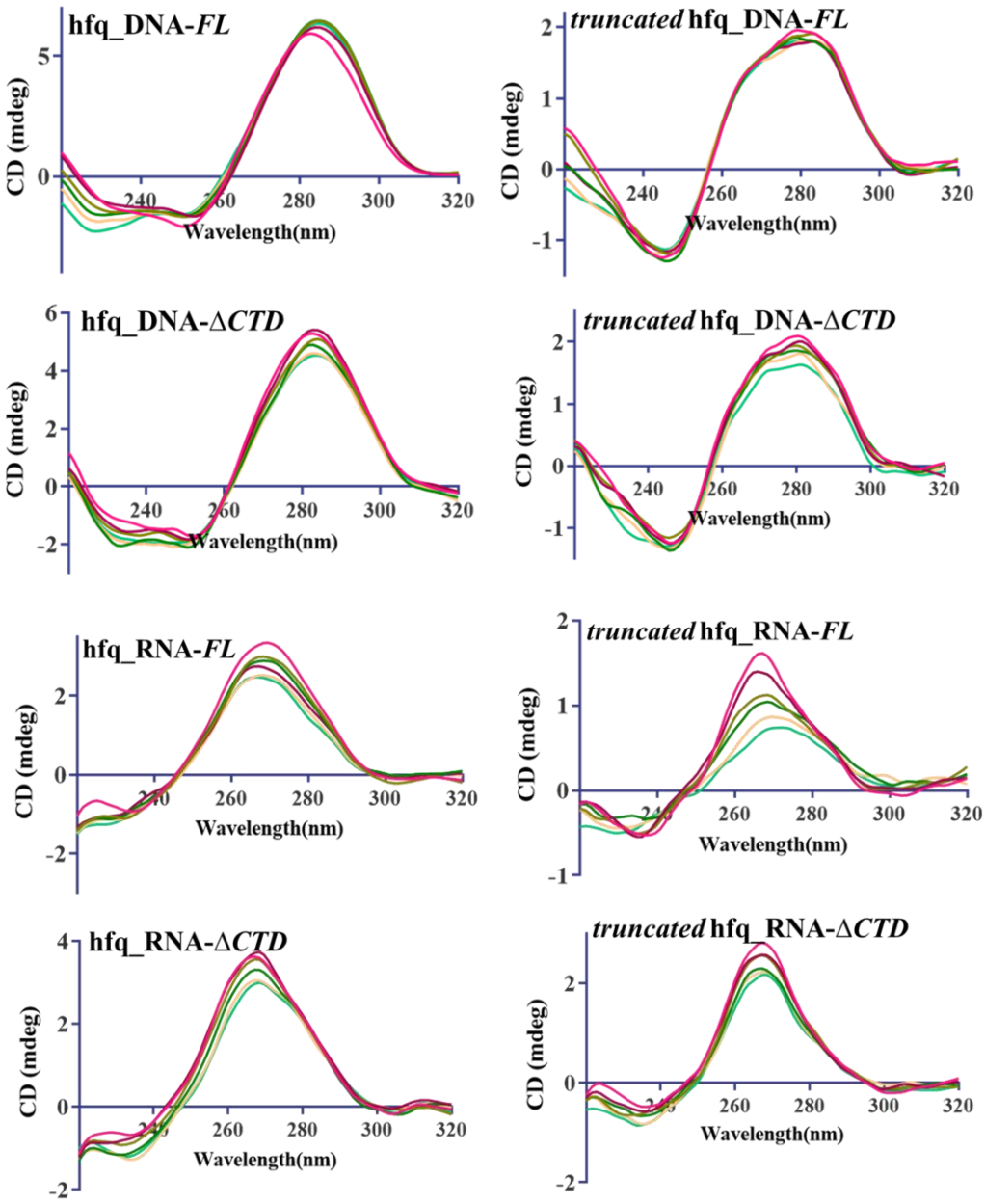

Figure 4.11. CD titration spectra of hfq RNA and DNA G4 sequences with increasing concentrations Hfq FL and ΔCTD protein (P:N = 0 - 5), showing protein-induced conformational changes in G4 structure.

Electrophoretic Mobility Shift Assay (EMSA) was performed to determine the interaction between Hfq protein variants (*FL* and *ΔCTD*) and *hfq* G4 sequences. A clear shift in RNA mobility was observed for *hfq*_RNA in the presence of increasing Hfq *FL* protein concentrations, and clear bands corresponding to complex and free nucleic acid were observed for *truncated hfq*_RNA (Figure 4.12), indicating stable

complex formation. Notably, the intensity and shift pattern diminished with the *ΔCTD* protein, suggesting reduced affinity or altered binding dynamics without the C-terminal domain. In contrast, the *hfq*_DNA and *truncated hfq*_DNA sequences (Figure 4.12) showed minimal to no shift with either protein variant, indicating a lack of significant interaction under the tested conditions.

These findings strengthened the selective binding property of Hfq towards RNA and highlighted the role of Hfq *CTD* in enhancing RNA G4 recognition and binding, while DNA counterparts appeared largely unbound.

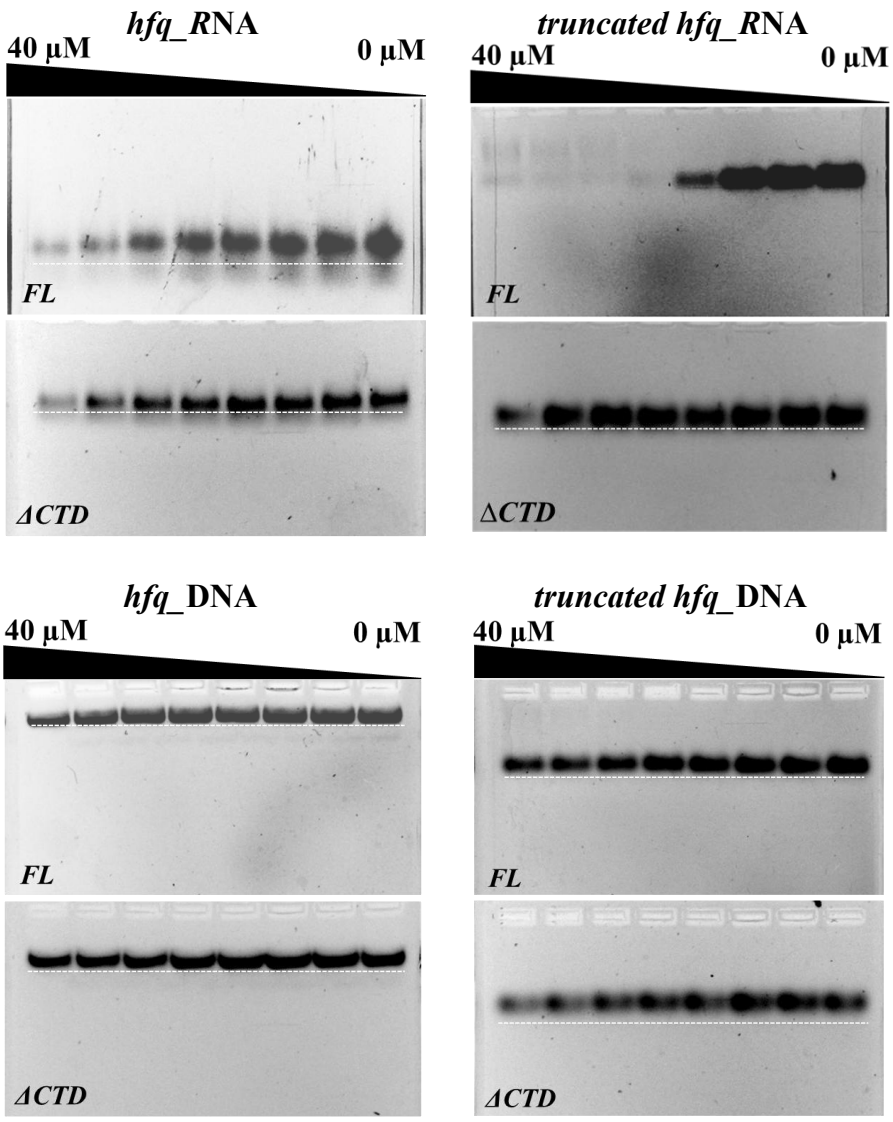

Fig 4.12. EMSA of RNA and DNA G4 sequences with increasing concentrations of FL and ΔCTD Hfq.

4.3.8 Fluorescence Spectroscopy revealed Hfq-G4 interaction

To validate the interaction between Hfq (*FL* and *ΔCTD* variants) and *hfq* DNA and RNA G4 structures, fluorescence emission spectra of the proteins were recorded with subsequent titration of nucleic acid. Upon titration of Hfq *FL* with *hfq*_RNA, a significant red shift in emission maxima was observed with an increase in the fluorescence intensity of the maxima (Figure 4.13). The fluorescence enhancement likely arises from shielding of the fluorophore from solvent or quenching groups which may be an indication of a strong interaction and probable stabilization or

structural rearrangement of protein structure. The overall difference in fluorescence intensity and shift upon titration with *hfq*_RNA were found to be less pronounced in case of *ΔCTD* compared to the *FL* protein, indicating a comparatively weaker interaction (Figure 4.13). In case of *truncated hfq*_RNA, a similar pattern was observed, but the intensity increase was somewhat less and there appeared a lack of cooperative binding pattern (Figure 4.13). For *hfq*_DNA, both *FL* and *ΔCTD* Hfq proteins show little to no significant change in fluorescence emission intensity, suggesting weak or non-structural binding that does not induce major conformational changes in the protein (Figure 4.13). However, for *truncated hfq*_DNA, both protein variants showed an increased fluorescence intensity and emission maximum exhibiting red shift with increasing N/P ratio. This effect was robust for both *FL* and *ΔCTD* proteins, suggesting that CTD may not be solely responsible for this interaction with truncated DNA.

Altogether, fluorescence data revealed that both *FL* and *ΔCTD* Hfq bind RNA far more readily than DNA. The muted response of the ΔCTD mutant underscores the CTD's contribution to high-affinity RNA recognition. *hfq*_DNA, by contrast, displayed little to no binding under these conditions. An exception to this was the *truncated hfq*_DNA construct, which elicited appreciable fluorescence shifts with both Hfq variants, indicating a dispensable role of CTD and possibly a non-specific interaction between the two.

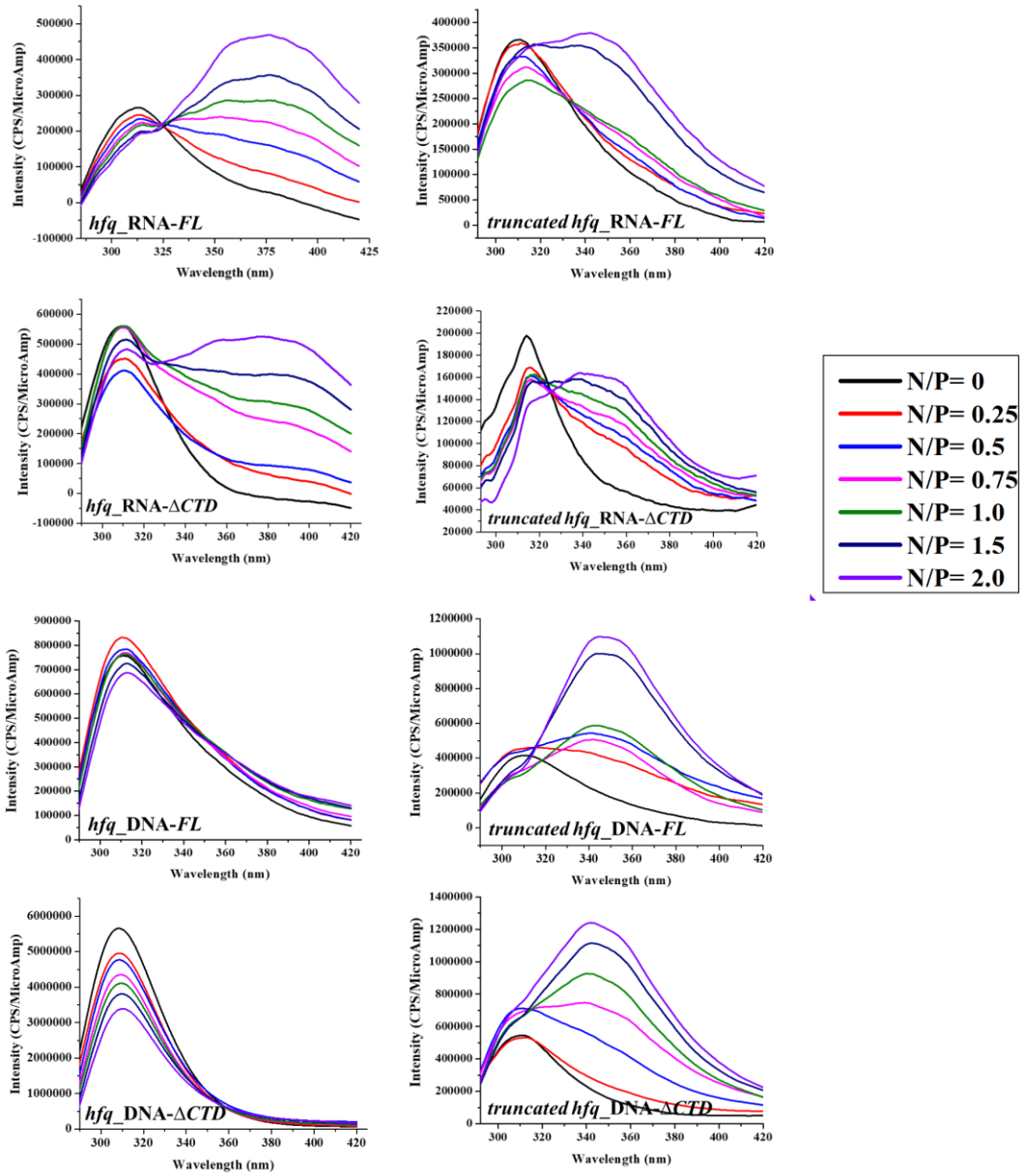

Figure 4.13. Fluorescence titration spectroscopy analysis of Hfq FL and Hfq ΔCTD upon increasing concentrations of hfq RNA and DNA sequences (N/P = 0 - 2.0), indicative of RNA-protein interaction.

4.3.9 Regulation of *hfq* gene expression by BRACO-19

To determine the impact of BRACO-19-mediated G4 stabilization on hfq gene expression constructs, an RT-PCR assay was performed. The RT-PCR analysis examined the transcriptional response of three *hfq* gene constructs: full-length *hfq*, C-terminal truncated *hfq* (ΔCTD), and the glycine-rich region (GRP), following treatment with BRACO-19 at IC_{25} (12.5 µM) and $IC_{12.5}$ (6.25 µM). The IC_{50} value

was selected according to a study performed earlier[251]. Full-length *hfq* transcript levels showed a clear dose-dependent reduction following BRACO-19 treatment with a ~20% decreased expression observed at $IC_{12.5}$, and ~60% of control levels at IC_{25} (Figure 4.14). A slightly less downregulation pattern was observed for ΔCTD *hfq* region (Figure 4.14). The most substantial repression was observed for the GRP *hfq* construct, where transcript levels dropped below 20 % at the higher BRACO-19 concentration (IC_{25}). This suggested the sensitivity of the glycine-rich CTD region alone towards BRACO-19, possibly due to G-rich sequences or a structural predisposition that enabled ligand binding and consequent transcriptional inhibition.

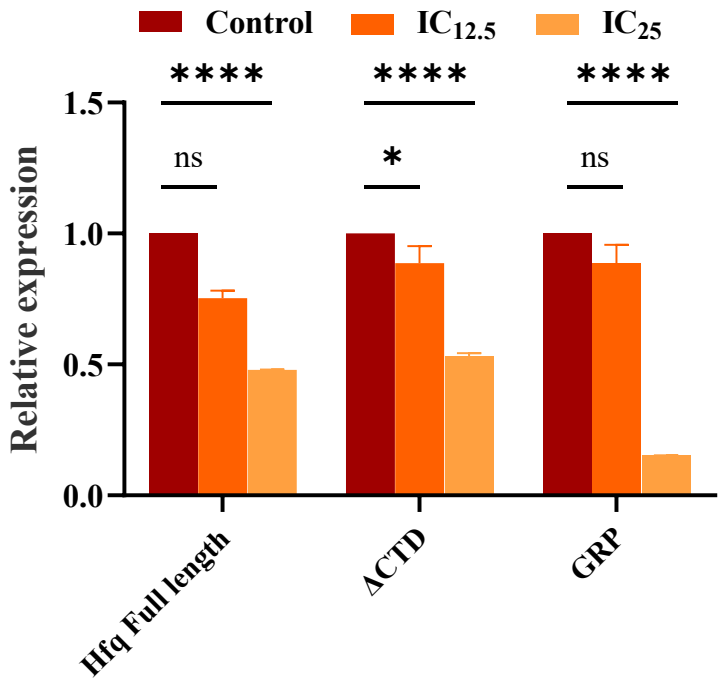

Figure 4.14. RT-PCR analysis of hfq transcript variants (full-length, ΔCTD, GRP domain) upon BRACO-19 treatment ($IC_{12.5}$ and IC_{25}) relative to untreated control.

4.4 Conclusion

The comprehensive exploration of G4 structures within the *hfq* gene of *Acinetobacter baumannii* has illuminated a previously unacknowledged level of regulation in bacterial gene expression. By integrating in silico, biophysical, and biochemical approaches, this study demonstrated that both full-length and

truncated hfq RNA and DNA sequences can form two-tetrad G4 structures in the presence of K^+, particularly RNA G4s being more stable. These G4 structures were recognized and stabilized by the well-characterized G4 ligand BRACO-19 and exhibited a good binding affinity. They also displayed interaction with the Hfq protein, especially its full-length variant, with preferential binding towards RNA G4s over DNA, highlighting the critical role of the glycine-rich C-terminal domain in high-affinity RNA binding. Importantly, the stabilization of *hfq* G4s by BRACO-19 was shown to result in significant expressional downregulation of *hfq* gene fragments, with the most pronounced effect observed in the glycine-rich C-terminal region. This finding underscored the potential of G4-Hfq complexes as dynamic, ligand-responsive regulatory switches in bacterial physiology. The data collectively suggested that G4 structures within the *hfq* transcript could operate as structural roadblocks or protein-binding platforms in the alteration of gene expression, and that targeting these motifs may offer a novel strategy for antimicrobial intervention. Overall, this work revealed the functional versatility of non-canonical nucleic acid structures in microbial adaptation and pathogenicity. It also aided in formulating a basis for future exploration of RNA–protein interactions in clinically relevant bacteria and highlighted the therapeutic potential of G4-targeting ligands in controlling multidrug-resistant pathogens.

CHAPTER 5

RNA G-QUADRUPLEXES IN THE JAPANESE ENCEPHALITIS VIRUS GENOME: UNCOVERING TARGETS FOR ANTIVIRAL INTERVENTION

Chapter 5

RNA G-quadruplexes in the Japanese Encephalitis virus genome: uncovering targets for antiviral intervention

5.1 Introduction

G-quadruplexes (G4s) constitute a subset of non-canonical secondary nucleic acid structures formed by Guanine-rich DNA or RNA sequences. The architecture of G4s comprises a stacked arrangement of G-quartets, wherein four guanine bases are hydrogen-bonded in a planar configuration via Hoogsteen interactions. The G4 structure is stabilized by the co-ordination of certain physiologically relevant monovalent cations, such as Na^+ and K^+ depending upon their ionic radii[260]. G4s can adopt intramolecular conformations originating from a single strand or intermolecular conformations facilitated by the association of different strands. The orientation of the guanines in the tetrad is further defined by the *anti* or *syn* conformation of the N-glycosidic bond which dictates the topology exhibited by the G-quadruplex structures, parallel, anti-parallel, and mixed/hybrid[193]. RNA G4s exclusively exhibit parallel topologies due to their anti-glycosidic conformation, and despite their increased stability compared to DNA G4s, they have received relatively less attention. Recent studies have expanded our understanding of potential G-quadruplex (G4)-forming sequences (PGQPGQs) dispersed across various biologically significant regions, suggesting a widespread presence of RNA PGQPGQs and their pivotal role in the regulating a myriad of cellular functions[261–263].

RNA G-quadruplexes have been identified as key regulators of gene expression having implications in cancer[264,265] and neurological disorders[266]. Another intriguing aspect is the presence of RNA G4s in the viral genome which have been extensively reported in positive as well as negative sense single-stranded RNA viruses such as flaviviruses, filoviruses, and coronaviruses[267]. For instance, RNA-G4s have been noted to play a crucial role in the HIV-1 viral life cycle, specifically in the viral replication system and the initiation of reverse

transcription[268]. Similarly, RNA G4 structures have been implicated in the expression of Ebola virus L gene as well as the C gene of the Hepatitis C virus[269,270]. Additionally, RNA synthesis in HCV is also found to be regulated by the formation of an RNA-G4 structure in the negative sense strand of the virus[271]. The Zika virus, a member of the Flaviviridae family, has also been documented to harbor potential G4s within its RNA genome, spanning both structural and non-structural protein genes[2,272]. These G4s were found to be conserved across the whole flavivirus genus, thereby hinting at their probable role in the viral lifecycle. It is also noteworthy to mention the involvement of RNA G4s in the reduction of viral mRNA translation, in turn affecting antigen presentation and contributing to immune evasion in Epstein-Barr virus[273]. Additionally, the presence of conserved RNA G4s in SARS-CoV-2, SARS-CoV, and MERS-CoV has been observed, and the same has also been validated through biophysical approaches[274]. The importance of RNA G4 structure in hindering SARS-CoV2 infection through limiting the entry of the virus has also been elucidated[275]. Nonetheless, several well-reported G-quadruplex binding ligands have been found to effectively stabilize these viral RNA G4s, consequently exhibiting anti-viral activity. In particular, Phen-DC3, a distinct G-quadruplex ligand demonstrated the ability to impede viral replication in HCV-infected cells[271]. Similarly, another G-quadruplex binding ligand, BRACO-19 has been associated with the inhibition of promoter activity in HIV-1[276]. In another study, TMPyP4 has been identified as a potent inhibitor of RNA G4s involved in replication and gene expression of SARS-CoV-2 virus[277]. Subsequently, in another study directed towards SARS-CoV-2, TMPyP4 was found to present efficacy as an antiviral agent through the stabilization of RNA G-quadruplex structures in the viral genome[278]. Similar to its effect on SARS-CoV-2, the ligand was also found to hinder the growth, replication, and translation of ZIKA virus-infected cells via binding to RNA G4s present in the viral genome[2]. In another recent investigation, PDS, another G-quadruplex binder also demonstrated antiviral efficacy against ZIKV infection through effective binding and stabilization of ZIKV RNA G-quadruplexes in vitro[279]. Given the robust conservation of putative G-quadruplex forming

sequences in the RNA among the respective viral isolates, G-quadruplex binding ligands could be of compelling interest for new antiviral therapies against RNA G-quadruplexes.

We investigated the presence of potential G-quadruplex sequences in the Japanese encephalitis virus (JEV) genome, the most prevalent cause of severe flaviviral encephalitis. JEV is a mosquito-borne arbovirus, particularly widespread in East and Southeast Asian countries and certain regions of the Western Pacific[280]. The global incidence of JEV cases remains uncertain due to inadequate monitoring but reported JEV infections reach approximately 68,000 annually, with around 20,000 fatal cases[281]. The primary demographic affected by JEV is children, carrying a mortality rate of up to 30 %[281]. Survivors, numbering up to 50%, may endure persistent and severe neuropsychiatric complications such as recurrent seizures, memory loss, convulsions, and paralysis[282]. JEV is an enveloped, positive-sense, single-stranded RNA virus with a genome of approximately 11,000 nucleotides, comprising a substantial open reading frame (ORF) flanked by 5′ and 3′ untranslated regions (UTRs). The polyprotein encoded by the ORF, upon cleavage by either viral or cellular proteases yields three structural proteins (SPs) (the capsid, C; pre-membrane, prM; envelope, E) and seven nonstructural proteins (NSPs) (NS1, NS2A, NS2B, NS3, NS4A, NS4B, and NS5)[283]. Despite evidence indicating significant anti-JEV activity of various compounds both in vitro and animal models, there lies a paucity of clinical trials conducted in the past decade[281,284]. The limited availability of anti-JEV therapeutics underscores the insufficient understanding of the molecular underpinnings of JEV pathogenesis. At present, there lies a dearth of specific antiviral therapies for JEV infection, necessitating the identification of novel targets for the development of effective antiviral strategies.

The study in this chapter explored the existence of G-quadruplex structures in the JEV genome using a comprehensive approach, integrating bioinformatics, biophysical, and biological techniques. Initially, G4-prediction algorithms were employed to analyze the JEV genome, predicting the occurrence of putative G4 motifs, followed by an exploration of motif conservation across various JEV

isolates. The conserved motifs were then characterized in terms of their topology and thermodynamic stability using circular dichroism. The interactions between these motifs and the G4-binding ligand BRACO-19 were extensively evaluated through fluorescence probe displacement assay, gel retardation, titration assays utilizing RNA-induced changes in ligand fluorescence, isothermal titration calorimetry (ITC), and NMR peak broadening analysis. Furthermore, cell-based assays were conducted to assess the cytotoxic and antiviral effects of BRACO-19, revealing a dose-dependent reduction in infectious virus titers, viral replication, and translation in JEV-infected cells. The cell-based assay results therefore demonstrated the impact of G-quadruplex-specific ligand on G4-mediated biological processes. This study provides insights into the structural characteristics of RNA G-quadruplexes in the JEV genome, and the elucidated G4-ligand binding represents progress toward the development of potential antiviral targeting JEV infection.

5.2 Material and Methods

5.2.1 Genome-mining studies using bioinformatics analysis

All 378 JEV genome sequences were downloaded from the NCBI genome database and used for the prediction of the putative G4-forming motifs utilizing our in-house G-quadruplex prediction tool (G4IPDB)[99]. The prediction was performed using the algorithm:

$$G{\geq}_2\, N_{1\text{-}7}\, G{\geq}_2\, N_{1\text{-}7}\, G{\geq}_2\, N_{1\text{-}7}\, G{\geq}_2$$

where G refers to Guanine, and N is any nucleotide including Guanine. Both sense and antisense strands were explored for PGQPGQ prediction. The predicted PGQsPGQ were then functionally annotated in the JEV genome using NCBI Database Graphics mode. G-quadruplex prediction was also performed using G4Hunter. Sequence logos of selected RNA G4s were prepared using the WebLogo tool[122].

5.2.2 In vitro transcription

DNA templates containing T7 RNA promoter and forward and reverse primers were designed and purchased from Sigma-Aldrich (St. Louis, MO, USA) (Table

C1). DNA templates for in vitro transcription were produced via PCR amplification. RNAs were transcribed using in-house purified T7 RNA Polymerase and the synthesized transcripts were purified by running 15 % denaturing PAGE. The concentration of the oligonucleotides used for each experiment was determined from UV absorption at 260 nm using molar absorption coefficients as calculated from IDT OligoAnalyzer tool.

5.2.3 ^{1}H Nuclear magnetic resonance (NMR) spectroscopy

^{1}H NMR spectra were recorded at 25 °C using a 400 MHz Bruker Avance III (BioSpin International AG, Switzerland) spectrometer equipped with a 5 mm broadband inverse (BBI) probe. The RNA oligonucleotides were annealed in KPO_4 buffer (10 mM, pH 7.5, 100 mM K^+) at a final concentration of around 0.3-0.5 mM. DSS (4,4-dimethyl-4-silapentane-1-sulfonic acid) was used as an internal reference. The samples were annealed by heating at 95 °C for 10 min and slowly cooled to room temperature. The titration experiments of BRACO-19 were performed with the successive addition of RNA till a ligand to RNA (D:N) ratio of 100:8 was achieved. The acquired NMR spectra were processed and analyzed using Topspin v4.0.6 software (academic license).

5.2.4 Circular Dichroism (CD) Spectroscopy and Melting Analysis

J-815 spectropolarimeter (JASCO) was used to perform the CD experiments. The required temperature was maintained with a continuous supply of nitrogen gas to prevent condensation around the cuvette. The concentration of RNA sample for CD Spectral analysis was maintained at 5 μM in KPO_4 buffer (10 mM, pH 7.5) supplemented with the required concentration of K^+. The sample was heated at 95 °C for 10 minutes and then left to reanneal at room temperature. The spectra were recorded with a wavelength range set to 220 – 300 nm with a scanning speed of 50 nm/min and 0.1 nm interval. For CD Spectroscopy in the presence of ligand, the buffer was supplemented with 100 mM K^+. Ligand was gradually added to the RNA solution till a ligand to RNA (D:N) ratio of 2:1. Baseline correction was performed before each experiment and data were normalized by buffer subtraction. The

obtained data was plotted using SigmaPlot 15.0 software (Systat Software, Chicago, IL, USA).

CD Melting experiments were conducted using a J-815 Spectropolarimeter (JASCO) equipped with a Peltier temperature programmer and water Peltier system PCB-1500. RNA solution (10 μM) was prepared in KPO_4 buffer (10 mM, pH 7.5, 100 mM K^+), heated at 95 °C for 10 mins, and then allowed to cool down at room temperature for 30 mins. The melting curves were monitored at a wavelength of ~265 nm with a temperature range of 25 °C to 95 °C at the rate of 1 °C/min. The melting analysis was carried out till a ligand to RNA (D:N) ratio of 2:1 was attained. The normalized absorbance changes at 265 nm against temperature were plotted using the SigmaPlot 15.0 software (Systat Software, Chicago, IL, USA).

5.2.5 Fluorescence intercalator displacement (FID) assay

FID assay was performed using Thioflavin T (ThT), a fluorescent G-quadruplex probe. The solution of RNA oligonucleotide (5 μM) and their respective mutants was prepared in KPO_4 buffer (10 mM, pH 7.5, 100 mM K^+). 10 μM ThT solution was prepared in the same buffer and fluorescence intensities were collected at 495 nm using an excitation wavelength of 425 nm. The oligonucleotide solution was then added to the ThT solution and fluorescence emission was recorded after 10 mins. Next, 25 μM ligand solution, also prepared in the same buffer was added to the above mixture and incubated for 30 mins, and fluorescence intensity was recorded. All the steps were carried out at 25 °C in a Corning half-area 96-well black plate and fluorescence intensity was measured using the BioTek microplate reader Synergy H1 system.

The experiment was performed in duplicate and fluorescence intensity was averaged. To calculate the percentage of ThT displacement, the following formula was used:

$$\text{ThT Displacement } (\%) = 100 - [100 \times \frac{F_I - F_b}{F_{I_0} + F_b}]$$

where F_I stands for fluorescence with ligand, F_{Io} for fluorescence without ligand, and F_b for fluorescence of ThT alone.

5.2.6 Gel mobility shift assay

Gel mobility shift assay was performed with 15 µM of JEV-PGQ RNAs prepared in KPO_4 buffer (10 mM pH 7.5; 100 mM K^+) after heating at 95 °C for 10 mins and then allowed to cool down at room temperature. The PGQ RNA solution was then titrated with a high concentration of BRACO-19 solution (100 - 0 µM) and incubated for 30 mins at room temperature. The samples were then resolved on 3 % agarose gel prepared in 1X TBE buffer and run under cold conditions in ice at 55 V and stained by ethidium bromide. The gel image was visualized and analyzed using ImageQuant LAS 4000 (GE Healthcare, Biosciences Ltd, Sweden).

5.2.7 Fluorescence titration assay

The Fluorescence titration assays were performed on Synergy™ H1 multi-mode microplate reader using a Corning half-area 96-well black plate at 25 °C. Each sample was prepared in duplicates with a final volume of 75 µl in each well. The JEV PGQ and mutant RNAs prepared at a concentration of 20 µM were serially diluted and the last well was taken as blank (no RNA). For the detection of fluorescence change of BRACO-19 upon titration with RNA, fluorescence emission was recorded at the maximum emission wavelength of 440 nm after being excited at a wavelength of 360 nm. The obtained data were analyzed using Sigma Plot 15.0 software (Systat Software, Chicago, USA) according to the following equation:

$$f = \frac{B_{max1} \times \text{abs (x)}}{K_{d1} \times \text{abs (x)}} + \frac{B_{max2} \times \text{abs (x)}}{K_{d2} \times \text{abs (x)}}$$

where B_{max} = maximum number of binding sites. K_d = equilibrium binding constant

5.2.8 Isothermal titration calorimetric (ITC) analysis

The ITC experiments were carried out using a MicroCal iTC200 isothermal titration calorimeter (GE Healthcare, Biosciences Ltd., Sweden). The RNA solutions were prepared at a concentration of 10 µM and BRACO-19 at a concentration of 1 mM in KPO_4 buffer (10 mM, pH 7.5, 100 mM K^+). All the calorimetric titrations were carried out at 25 °C by injecting 1.6 µl aliquots of BRACO-19 solution into RNA solution at 120 s intervals, for a total of 22 injections. The titration curves were buffer corrected by titrating the same ligand concentration into buffer solution for

calculating the heat of dilution. The obtained values were used to generate the binding isotherms using the Origin scientific software version 7 (Microcal Software Inc. Northampton, MA, USA). A two-site binding mode was used for fitting the data and to determine the binding constants.

5.2.9 mTFP-based reporter assay

The Human Kidney (HEK293T) cell line was procured from the National Centre for Cell Science (NCCS), Pune, India. The JEV-PGQ sequences were cloned in the pCAG-mTFP vector, just after the ATG start codon of the mTFP gene. The forward primers were designed to contain the EcoRI cleavage site at the 5′ end followed by the respective PGQ sequence with the mTFP gene N terminus sequence at the 3′ end. A common reverse primer was used for all the sequences comprising the XhoI cleavage site at the 3′end and the TFP C-terminus sequence at the 5′ end (Table C2). The forward and reverse primers were then used to amplify the ~708 bp fragment comprising the whole mTFP gene along with the JEV-PGQ sequence, using the pCAG-mTFP plasmid as the PCR template. The amplified fragment which is the desired insert, and the plasmid were then individually digested with EcoRI and XhoI, and ligated together to generate the plasmid constructs pCAG-JEV-PGQ-Env_2-mTFP, pCAG-JEV-PGQ-NS3_2-mTFP and pCAG-JEV-PGQ-NS5_1-mTFP. Similarly, the forward and reverse primers were designed to generate the mutant construct pCAG-JEV-Mut-mTFP. The sequence of the constructs was verified by gene sequencing and then transfection was performed in HEK293T cells. The transfected cells were subsequently treated with 5 μM and 10 μM of Braco-19 after 4 h of transfection and the mTFP expression level was observed after 24 h of treatment using a microscope. Statistical significance was calculated using Two-Way ANOVA to determine significant differences between untreated and BRACO-19-treated sets of wild-type and mutant samples. Data was analyzed using GraphPad Prism software version 8.0.2, and represented as mean ± SD.

5.2.10 Cell lines and Virus

Neuro2a (mouse neuroblastoma), C6/36, and Vero cell lines were obtained from the cell repository at the National Centre for Cell Sciences (NCCS), Pune, India.

These cells were tested and found negative for mycoplasma. Neuro2a cells were cultured in Dulbecco's modified Eagle's medium (DMEM), Vero cells were cultured in Eagle's minimum essential medium (MEM) and C6/36 cells were cultured in Leibovitz's (L-15) medium. All media were additionally supplemented with 10% fetal bovine serum (FBS), 100 µg/ml penicillin-streptomycin cocktail, and 2 mM L-glutamine. JEV isolate Vellore P20778 (GenBank accession no. AF080251) was propagated in C6/36 cell line and Vero cells were used to titrate the virus using plaque assays as described earlier[285].

5.2.11 Virus infection, cell treatment and cell viability assay

All virus infection studies were performed by giving JEV infection in incomplete media at indicated MOI for 1 h. Cells were then washed with 1X PBS and complete medium was added. Cells were treated with BRACO-19 at indicated concentrations for 24 h post-infection. Cells were harvested for cell viability assays, RNA isolation, and Western blotting. Culture supernatants were used for virus titration through plaque assay. Every experiment had biological triplicates.

Cell viability assays were performed using the CellTiter-Glo® assay kit as per manufacturer's instructions. The percentage of cell viability was calculated as: [(ATP luminescence for experimental condition)/(ATP luminescence for untreated condition)] × 100 and normalized to untreated control.

5.2.12 RNA isolation, quantitative Real time (qRT)- PCR and Western Blotting

RNA was extracted using Trizol reagent. cDNA was prepared using Bio-Rad iScript cDNA synthesis kit (Cat. # 1708891), and used to set up qRT-PCR on QuantStudio 6 (Applied Biosystems). JEV RNA level and GAPDH (loading control) were determined with SYBR green reagents. qRT-PCR for each sample was done in technical duplicates. The primer sequences used for qRT-PCR are listed in Table C3.

For Western Blotting, cells were lysed using ice-cold lysis buffer for 1 hour (4 °C) and protein was collected in the supernatant. The composition of cell lysis buffer used is: 150 mM NaCl, 1 % Triton X-100, 50 mM Tris-HCl pH 7.5, 1 mM PMSF,

and protease inhibitor cocktail. Protein concentration in cell lysates was estimated by using a BCA assay kit. Before loading, cell lysates were boiled at 95 °C (10 minutes) with 5X loading dye (40 % glycerol, 20 % β-mercaptoethanol, 0.04 % bromophenol blue, 6 % SDS, 0.25 M Tris-HCl pH 6.8) to denature proteins. Equal amount of cell lysates were run on SDS-PAGE and separated proteins were transferred to PVDF membranes for immunoblotting. The blots were visualized using Bio-Rad Gel Doc XR^+ gel documentation system and protein expression was calculated by measuring the band intensity using Image J software.

5.3 Results and Discussion

5.3.1 Identification of putative G-quadruplex forming motifs (PGQs) in the JEV genome

The existence of PGQs has been reported in other flaviviruses such as Zika, and TBEV, and thus we aimed to evaluate the same in JEV having a GC content of 51.5 %. We performed a genome-wide screening of 378 JEV isolates from the NCBI database using our established G-quadruplex prediction tool, examining both the positive (sense) and negative (antisense) strands. While the JEV genome is composed of positive-sense RNA, which acts as a template for both transcription and translation, we also considered the negative antisense strand, synthesized later, which plays a crucial role in viral genome replication. According to computational bioinformatics studies, it has been observed that the density of G-quadruplexes in viruses exhibits a moderate correlation with the G/C content of the viruses. Moreover, a comprehensive analysis indicates that PGQs with short loops are more prevalent and exhibit conservation across various viral taxonomic groups[286]. Hence, our criteria for identifying PGQs included ≥2 guanine tracts and loop lengths of 1-7, resulting in 26 motifs in the sense strand and 12 in the antisense strand. We then conducted a BLAST search to identify highly conserved PGQs across JEV strains, yielding eight conserved PGQs (≥90 %) in essential genes, including NSP (NS3 and NS5) and SP (Envelope protein E) genes with six in sense and two in antisense strand (Figure 5.1). These PGQs were located within the ORF region of crucial genes, including two in the Envelope protein (E), a crucial

mediator of host-cell viral infection. Furthermore, three PGQs were positioned in the NS3 protein gene, contributing a functional role in viral replication and protein maturation[287]. The remaining three PGQs were situated in the coding region of the NS5 gene, i.e. the RNA-dependent RNA polymerase coding gene. It is responsible for the viral genome replication and capping and is one of the highly conserved proteins among JEV and the flavivirus genus[288].

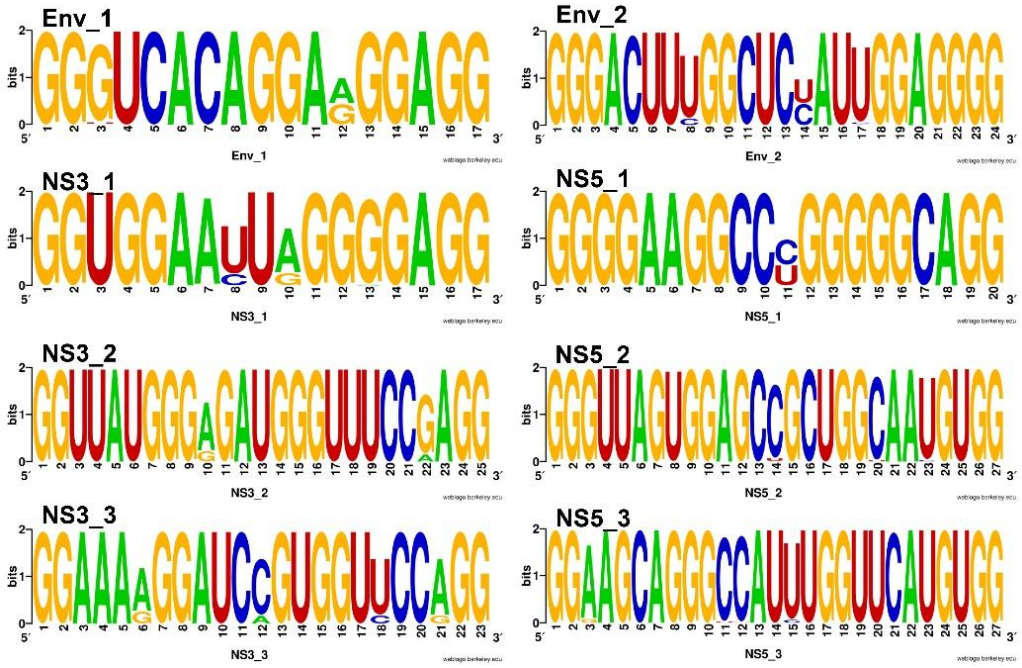

Figure 5.1. WebLogo representation of the predicted PGQ motifs in the JEV genome.

Moreover, viral genomic sequences have been found to harbor G4 motifs that diverge from the conventional criteria of canonical G4s, instead incorporating non-canonical features, including bulges, base pair mismatches, and stem-loop conformations, thereby highlighting the structural diversity and complexity of viral G4s[289–291]. In particular, flaviviruses have been observed to encompass both canonical and non-canonical G4s, with JEV genome embedding more than a hundred such PGQs in their genomes[292]. Although various algorithms are currently accessible for G4 prediction, there exist certain non-canonical G4-forming motifs that evade detection through conventional G4 prediction tools, as reported by investigations[293,294]. To address this, we employed G4-Hunter

assesses G4 propensity based on G/C skewness and G-tract presence, providing a score[98,294]. We set threshold values between 1.0 and 2.0, with a 25-nucleotide window size, considering the typical size of reported G4-forming sequences [294]. A concomitant decrease in the number of G4s with increasing threshold was observed resulting in G4 densities of 29 per kb at threshold 1.0, 8.7 at 1.2, 1.0 at 1.4, 0.09 at 1.6, and none beyond 1.6 (Figure 5.2 A, B). The observed increased density may denote an increased prevalence of non-canonical G-quadruplex motifs relative to their canonical counterparts. In addition, we also predicted the number of G4s using G4IPDB with G-tract ≥2 and varying loop lengths (LL) of ≤15, ≤10, ≤7, ≤5, ≤3 and noted a decrease in the number of GQs with decreasing loop length (LL) (Figure 5.2 C, D). Surprisingly, we did not obtain any PGQs in the sense or anti-sense strands when parameters were set to G-tract ≥3 and loop lengths (LL) of ≤15, ≤10, ≤7, ≤5, ≤3.

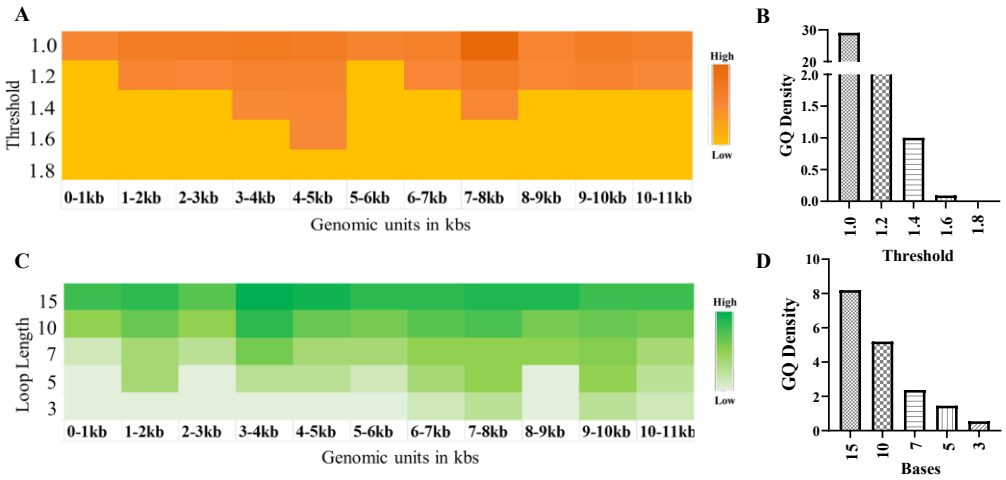

Figure 5.2. Prediction of putative G-quadruplex motifs in JEV reference strain (NC_001437.1) (A) and (C) Heat map representing the number of GQs/kb predicted using G4 Hunter and G4IPDB tool respectively (B) Bar graph representing the GQ density from G4 Hunter and G4IPDB predictions respectively.

5.3.2 Predicted JEV-PGQs form RNA G-quadruplex structures in vitro

Nuclear magnetic resonance (NMR) spectroscopy is widely used for the structural study of macromolecules, such as nucleic acids. It has a unique strength in studying G-quadruplex secondary structures under physiologically relevant solution conditions. The guanine H1 imino protons involved in G-quadruplex structure formation have a characteristic shift when Hoogsteen hydrogen-bonded (G:G),

giving rise to characteristic resonance peaks around 10.0 - 12.5 ppm[128]. This chemical shift region is distinct from imino chemical shifts corresponding to other DNA conformations that appear in the upfield region between 12.5 - 14.0 ppm due to Watson-Crick hydrogen bonding (A:U; G:C)[126]. Hence, the appearance of imino proton resonances in the NMR spectrum provides a clear indication of the formation of G-quadruplex structures in a sequence. To proceed with the determination of G4 structure formation in JEV-PGQs in vitro, we performed 1D ^{1}H NMR spectroscopy. The emergence of characteristic imino proton peaks between 10.0 – 12.0 ppm confirmed the formation of a predominant RNA G-quadruplex structure in the predicted JEV-PGQs (Figure 5.3). While no additional peaks were observed for sequences NS5_1, NS5_2, and NS5_3 beyond 12.5 ppm, some additional peaks were observed for Env_1, Env_2, NS3_1, NS3_2, and NS3_3 PGQs in the region 12.5 - 14.0 ppm. These additional peaks can be attributed to the Watson-Crick base pairing between the bases present in the loop sequences and/or sequences flanking the G4 motif[183,290].

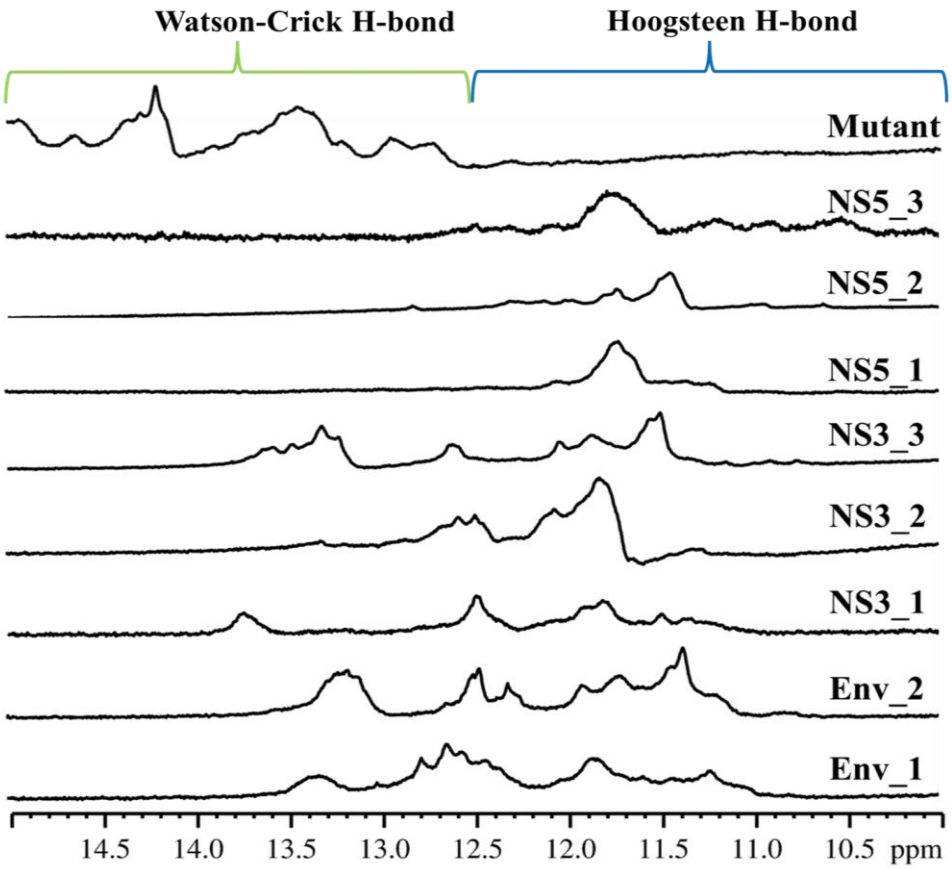

Figure 5.3. 1D 1H NMR Spectra of JEV-PGQs.

5.3.3 The structural topology of JEV-PGQs remained intact in the presence of cations

To experimentally validate the formation of G-quadruplex structures in the selected PGQs, we carried out Circular Dichroism (CD) spectroscopy of the synthesized RNA PGQ sequences. CD spectroscopy is a well-established method used to determine the topology of G-quadruplex structures. RNA G-quadruplexes are reported to exhibit predominantly parallel topology, as compared to the DNA G-quadruplexes which exhibit varied topology, with few exceptions (34, 35). A parallel GQ topology is characterized by the appearance of a positive peak around ~265 nm and a negative peak around ~240 nm[295]. The spectra for each of the PGQs were recorded in an increasing concentration of K^+ ranging from 0 - 200 mM in KPO_4 buffer solution at room temperature. The emergence of signature peaks representative of parallel G-quadruplexes with positive and negative bands at ~265 nm and ~240 nm respectively, for all the PGQs further confirmed the formation of

G-quadruplex in these motifs (Figure 5.4), whereas these signature peaks were absent in the CD spectrum of the mutant sequence (Figure 5.4). It is also noteworthy to mention that, no significant alteration in the CD ellipticity was observed at higher concentrations of K^+ (200 mM), indicating that the PGQs were stabilized in the presence of potassium ions.

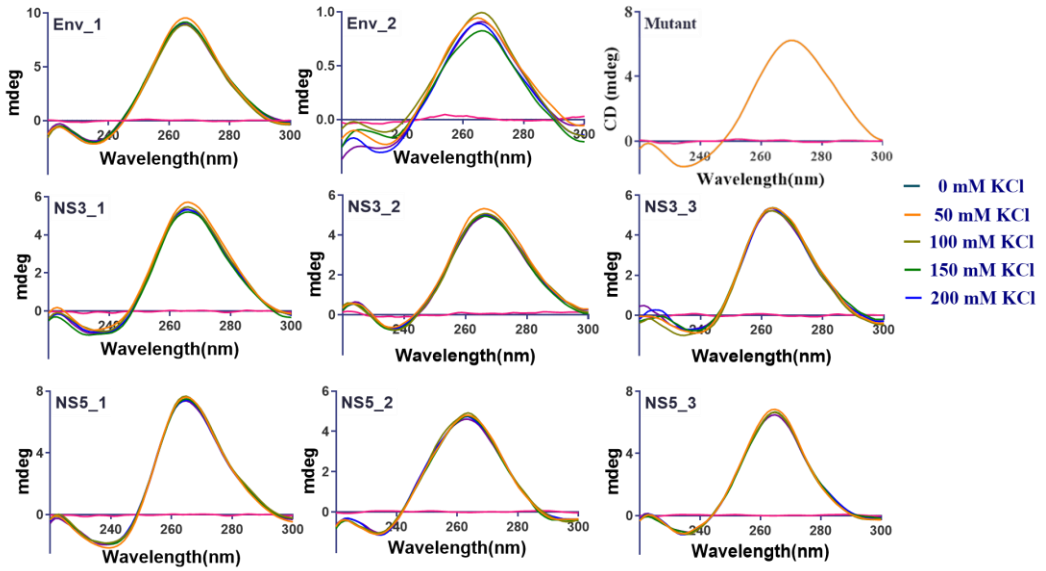

Figure 5.4. CD-Spectra of JEV-PGQs in increasing KCl (0 – 200 mM) concentration.

5.3.4 Presence of JEV-PGQs results in fluorescence enhancement of ThT

Thioflavin T (ThT), a benzothiazole has been reportedly used as a fluorescence light up probe for validating the G4 conformation adopted by sequences due to its increased selectivity towards RNA G-quadruplex structures[296]. A heightened enhancement in fluorescence of ThT serves as a distinctive characteristic of the majority of G4-forming sequences[297]. This property of ThT was employed to determine the interaction and affinity of ligands towards G4s through their competitive ability to displace bound ThT from G4-forming sequences. This approach is based on the G-quadruplex Fluorescent Intercalator Displacement (G4-FID) assay, developed in 2006, where the displacement of ThT from G-quadruplex structures is measured to assess ligand binding.[298,299].

We performed the G4-FID assay to verify G4 structure formation in the identified motifs and to evaluate the interaction of G-quadruplex binding ligands with the

former. The fluorescence intensity of ThT was found to significantly increase upon the addition of JEV-PGQs while the emission intensities of the linear mutant unable to adopt G4 structure was comparable to that of ThT alone (Figure 5.5 A). Henceforth, this confirmed the adoption of G4 structure by the motifs. BRACO-19 and TMPyP4 were selected as representatives of conventional G4 ligands for the displacement assay, both of which exhibit antiviral activity [255,300]. The fluorescence emission decreased drastically upon the addition of these two distinctive G-quadruplex binders, thereby showcasing their ability to displace the ThT bound to the PGQs. This confirmed the interaction of G-quadruplex binding ligands to the PGQs. Additionally, the displacement percent of BRACO-19 was found to be better as compared to TMPyP4, which led us to select BRACO-19 as a potent G4 binding ligand throughout the study (Figure 5.5 B).

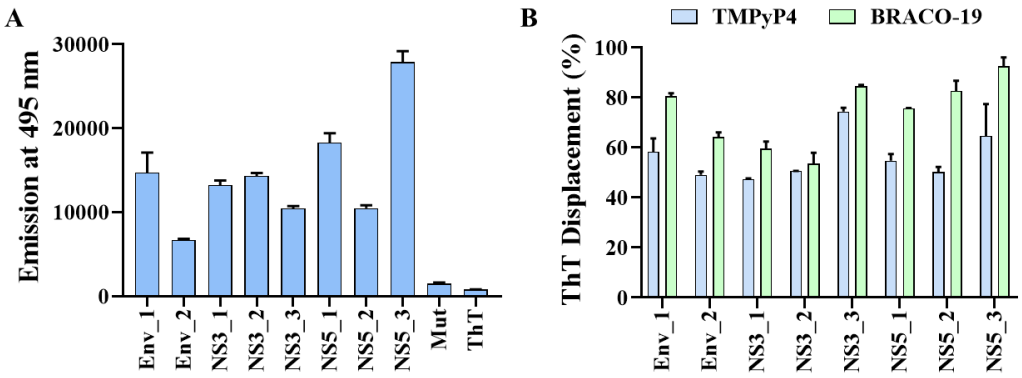

Figure 5.5. Fluorescence Intercalator Displacement (FID) Assay. (A) The fluorescence of Thioflavin T (ThT), obtained by the addition of JEV-PGQs with respect to (w.r.t.) mutant and ThT alone. (B) The percent displacement of ThT from JEV-PGQs with the addition of BRACO-19 and TMPyP4.

5.3.5 Gel retardation assay of JEV-PGQs with BRACO-19 reveals their interaction

Gel retardation assay is a technique initially delineated in 1981, widely employed for evaluating essential details concerning protein-nucleic acid interactions[301–303]. The fundamental principle of the assay lies in the differential electrophoretic mobilities exhibited by molecules based on varied sizes and charges when separated on a native polyacrylamide or agarose gel. This technique is now widely adopted to investigate interactions between ligand and nucleic acids. Typically, binding of

the ligand to free nucleic acid molecules affects the electrophoretic mobility of the latter, yielding slower-migrating species in comparison to unbound nucleic acids[130]. Therefore, the mobility of the ligand-nucleic acid complex is retarded relative to the free nucleic acid and, thus the assay is regarded as gel retardation assay which provides valuable information regarding the binding interactions between them. The aforementioned results offer insights into the interacting capability of BRACO-19 with JEV-PGQ RNAs. To corroborate these observations, we performed a gel retardation assay of each of the JEV-PGQs with BRACO-19. Upon increasing the concentration of BRACO-19 (100 μM), a noticeable retardation in the migration of the band was observed in JEV-PGQ RNAs as compared to ligand unbound PGQ RNA (0 μM) (Figure 5.6 A). The observed alteration in mobilities associated with each PGQ can be attributed to sequence-specific interactions facilitating the formation of a stable complex between BRACO-19 and JEV-PGQ RNAs[252]. In contrast to JEV-PGQs, no significant retardation was observed in the mobility of the mutant taken as negative control. Moreover, we also examined the mobility of JEV-PGQs w.r.t. the mutant, where the mutants were observed to migrate faster than PGQs (Figure 5.6 B).

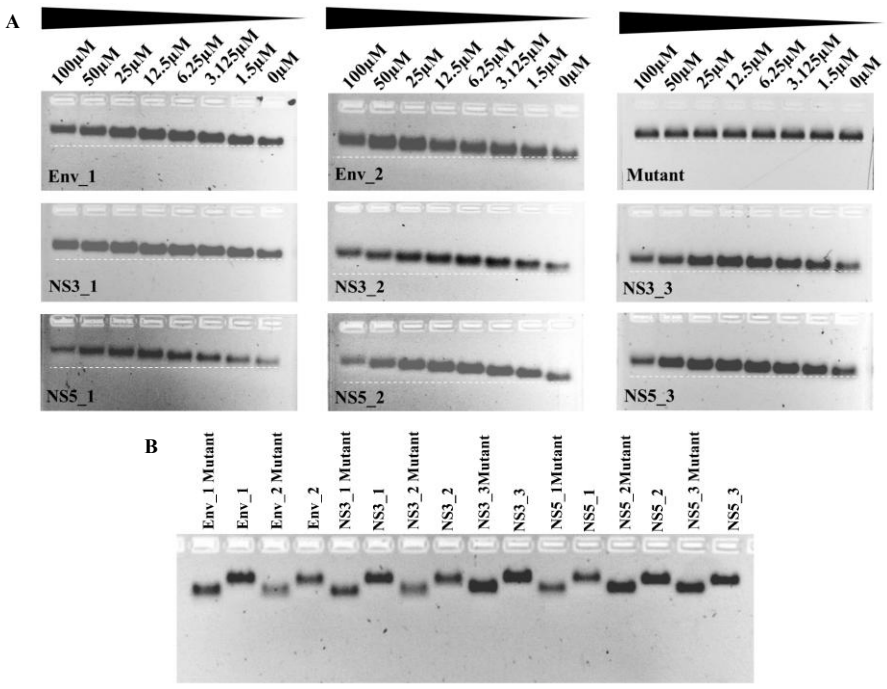

Figure 5.6. Gel retardation assay. (A) with increasing concentration of BRACO-19 (0 - 100 μM) (B) Comparison of mobility of G4 forming sequences w.r.t. mutants.

5.3.6 BRACO-19 induces the stabilization of JEV-PGQs

The impact of the ligand BRACO-19 on the stability of JEV-PGQs was assessed by performing titration of the ligand, BRACO-19 through CD spectroscopy and CD melting experiments. CD spectral analysis stands as a viable method for investigating the RNA secondary structure, offering insights into alterations in the conformation resulting from the introduction of a ligand. An effective G-quadruplex binding ligand is expected to exert a robust stabilizing influence on G-quadruplex structures. We performed CD spectroscopy with all the JEV-PGQs, and BRACO-19 was gradually added to the RNA solution until it reached a 2:1 ligand-to-RNA molar ratio. Remarkably, with the addition of BRACO-19, the positive band at ~265 nm and the negative band at ~240 nm in the CD spectra of JEV-PGQs remained unaltered (Figure 5.7). Therefore, it can be said that the topology of each of the G4 motifs was maintained in presence of BRACO-19.

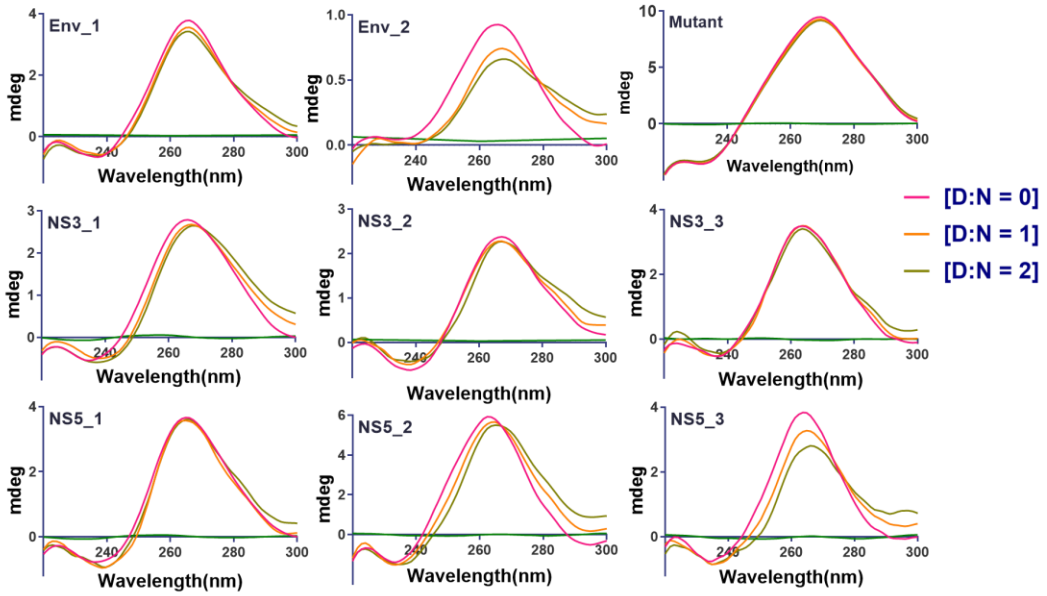

Figure 5.7. CD spectra of JEV-PGQs in increasing BRACO-19 concentration. [(Ligand:RNA) i.e. D:N = 0, D:N = 1 and D:N = 2].

CD melting profile gives information about the stabilizing effect of ligands on G4s in terms of melting temperature (T_m). The acquisition of the CD melting spectra typically involves monitoring the changes in the RNA secondary structure at the wavelength associated with maximum ellipticity (~265 nm) across a temperature range (25 °C to 95 °C). This idea is based upon the presumption of having a fully folded structure at the initial lower temperature and the subsequent complete unfolding of the molecular structure on reaching the highest temperature[304]. In this work, a CD melting study was carried out using BRACO-19 with the ligand-to-RNA ratio of 2:1 as in CD spectroscopy. Subsequently, an increase in melting temperature was observed for all the JEV-PGQs (Figure 5.8 A, B, Table C4). Hence, the elevation in the melting temperature of the PGQs with increasing ligand concentration prompted an interpretation of a stabilizing effect on the former, making it challenging to undergo unfolding.

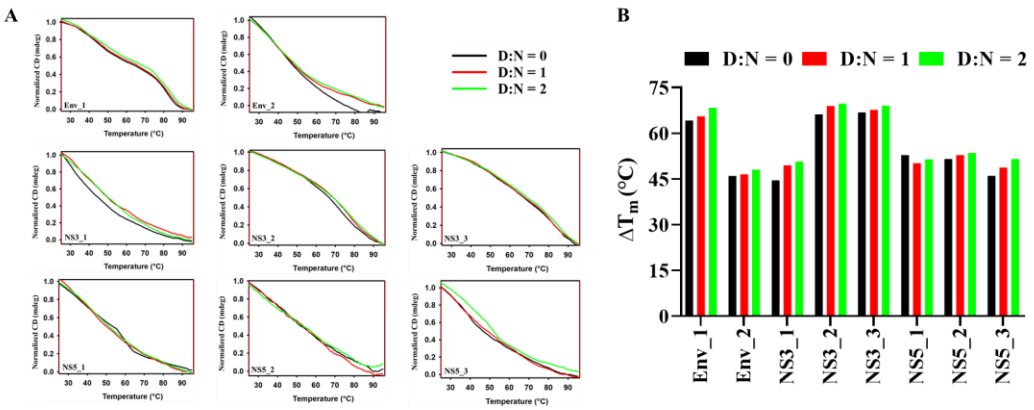

Figure 5.8. CD Melting Assay with increasing BRACO-19 concentration (100 mM K^+). (A) CD Melting spectra of JEV-PGQs. (B) ΔTm values of JEV-PGQs. [(Ligand:RNA) i.e. D:N = 0, D:N = 1 and D:N = 2].

To fully acknowledge the effect of BRACO-19 on PGQ stability, we performed CD Melting Analysis at a lower K^+ concentration (25 mM). We observed an increase in T_m in this case as well, for all the JEV-PGQs, except NS5_1, which could not be determined (5.9. A, B, Table C5). This can be explained by the possible presence of multiple conformations for this sequence at such a low K^+ concentration. CD melting profiles typically assume the presence of a single folded conformation in solution and the presence of multiple conformations can lead to biphasic melting profiles, as observed at D:N = 0[305]. If different conformational species have similar melting temperatures, their melting profiles are bound to overlap and appear as a single phase transition, though with a lower slope, as observed at D:N = 1, and D:N = 2[306].

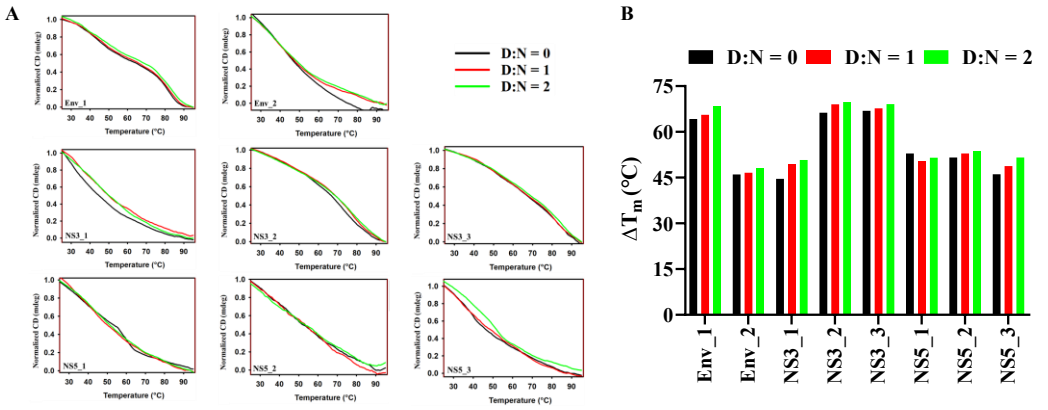

Figure 5.9. CD Melting Assay with increasing BRACO-19 concentration (25 mM K^+). (A) CD Melting spectra of JEV-PGQs. (B) ΔT_m values of JEV-PGQs. [(Ligand:RNA) i.e. D:N = 0, D:N = 1 and D:N = 2].

5.3.7 Binding of BRACO-19 with JEV-PGQs with high affinity

The fluorescence titration assay of ligands with nucleic acids (DNA/RNA) serves as a valuable assay to evaluate the binding affinity of the ligand towards the latter. Small molecules, such as BRACO-19 which exhibit intrinsic fluorescence, attributable to the presence of delocalized π electrons, are significantly affected by the addition of nucleic acids. An observable shift in fluorescence intensity (ΔF) upon titration of RNA is indicative of the binding between the ligand and RNA which can be quantified in terms of dissociation constant (K_d) value. An effective interaction reflects an alteration in fluorescence intensity, characterized by either enhancement or quenching. K_d value is obtained after global curve fitting of the binding curve plotted using ΔF and RNA concentration using a two-site saturation model. The binding affinity is inversely related to the K_d value, and therefore the lower the K_d value higher the binding affinity of the ligand towards RNA. In this study, we performed fluorescence titration assays of BRACO-19 with the selected JEV-PGQs. It is worth mentioning that each of the PGQs displayed higher binding affinity compared to the mutant (Figure 5.10 A, B, Table C6). The contrast in the binding affinity of the different PGQs might arise due to differences in sequence length and composition, folding, and loop length and composition.

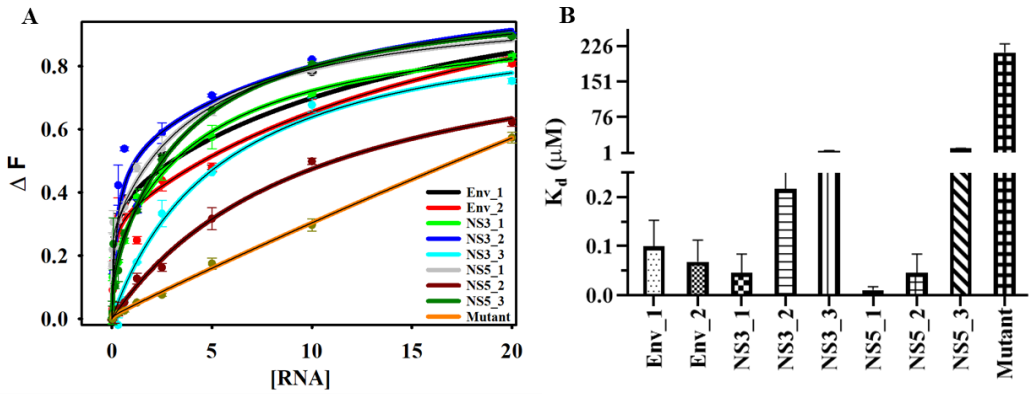

Figure 5.10. Fluorescence titration assay of BRACO-19 with JEV-PGQs. (A) Binding curves of JEV-PGQs with BRACO-19. (B) Bar graph representing the dissociation constant (Kd) values of JEV-PGQs w.r.t. mutant.

ITC is a unique and widely employed technique for studying the interactions and binding affinities of ligands to macromolecules and the characterization of its energetic aspects[132]. ITC is robust, and offers the advantage of providing complete thermodynamic profiling, giving clear information about the binding constants, free binding energy, its enthalpic and entropic components, and the nature of the interacting forces[307,308]. This technique has also been proven valuable in evaluating the energetics of ligand interaction with G-quadruplex structures[309]. Following this notion, we employed ITC to investigate the interaction between JEV-PGQs and the G-quadruplex binding ligand BRACO-19. We selected three PGQs (JEV-PGQ-ENV_2, JEV-PGQ-NS3_2, JEV-PGQ-NS5_1) out of the eight PGQs, exhibiting a conserved ness of >90 % to demonstrate their ability to interact and bind with BRACO-19. The titration of BRACO-19 with JEV-PGQs resulted in highly enthalpy-driven exothermic reaction as observed from their thermograms (Figure 5.11). The enthalpic contribution in these reactions may be ascribed to non-covalent interactions, such as those arising due to the stacking of the ligand (BRACO-19) to the G-quadruplex tetrad structure of the PGQs[310,311]. The negative enthalpy change (ΔH_1) for the PGQs (-2.11 x 10^4 joules/mol for ENV_2, -4.186 x 10^4 joules/mol for NS3_2, and -3.86 x 10^4 joules/mol for NS5_1) depicted their thermodynamic feasibility and selectivity towards the ligand. In contrast, the mutant sequence lacked a putative G-quadruplex forming sequence, precluding its interaction with BRACO-19, as

evident from its positive enthalpy change (ΔH_1 = 17.96 x 10^4 joules/mol). The dissociation constants calculated for JEV-PGQs were higher than the negative mutant control, indicating a higher affinity of G4s towards BRACO-19 (Table C7).

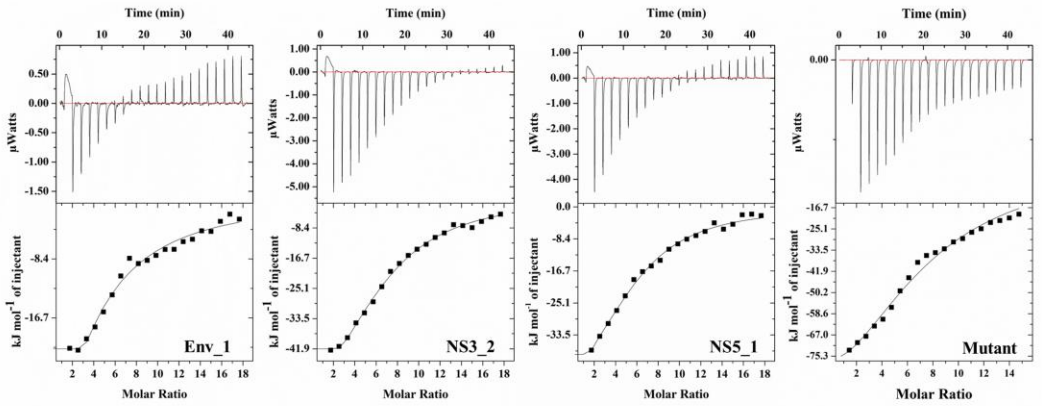

Figure 5.11. ITC thermograms of JEV-PGQs and mutant sequence obtained by titration with BRACO-19.

5.3.8 NMR spectroscopy studies validate the binding of Braco-19 to JEV-PGQs

^{1}H NMR spectroscopy is a valuable technique to examine the binding interactions between ligands and nucleic acids at the atomic level. For a more comprehensive understanding of the interaction between BRACO-19 and JEV-PGQs, as observed from the above experimental results, we conducted RNA titration experiments with BRACO-19, followed by ^{1}H NMR analysis. The NMR proton spectrum of BRACO-19 in general exhibits proton resonances between 6.5 - 8 ppm in the absence of the PGQs. With the subsequent addition of the oligonucleotide to the BRACO-19 solution, in each case, a line broadening of the existing resonance signals was observed within the same range (Figure 5.12). The broadening of the resonance signals of the ligand confirmed the binding of the ligand with the JEV-PGQs[312]. Moreover, notable upfield shifts were also observed in the proton region of BRACO-19, suggesting the presence of π–π interactions between the aromatic surface of the ligand and the G-tetrads of the JEV-PGQs[312,313]. For almost all the PGQs, significant changes in line-broadening began to plateau upon the addition of RNA to the ligand. Collectively, this data supports the interaction of

BRACO-19 and JEV-PGQs resulting in the formation of a complex in which the G-quadruplex structure is stabilized.

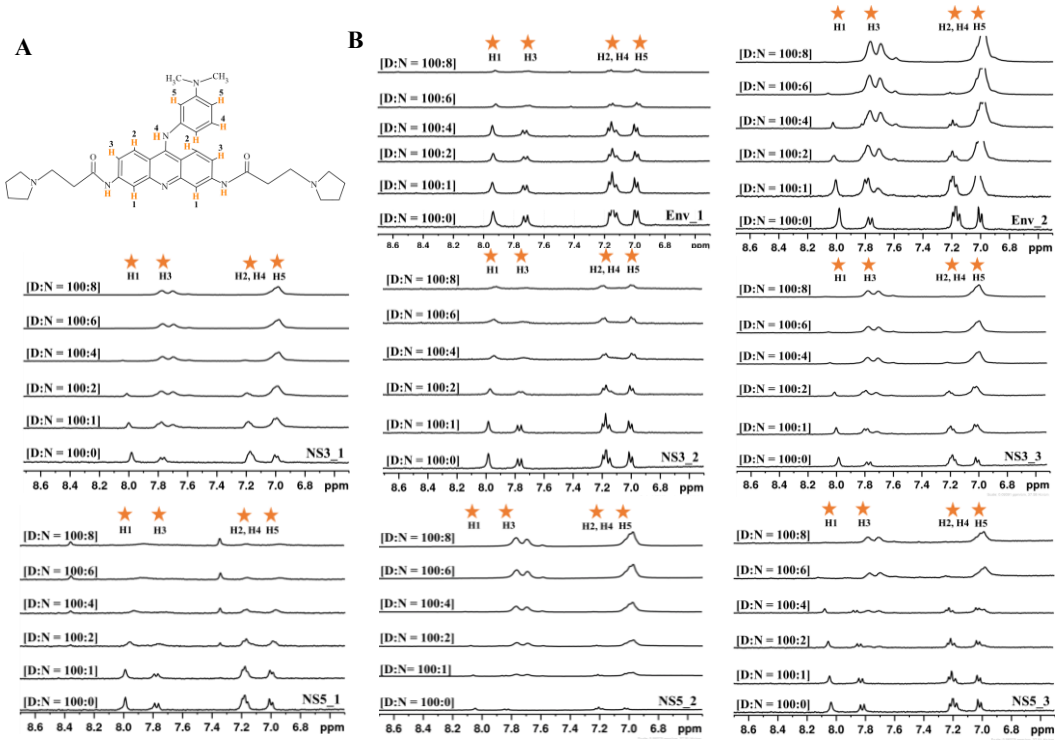

Figure 5.12. NMR Line Broadening Analysis. (A) Structure of BRACO-19 with the allocated aromatic protons showing resonances in 1H NMR spectra. (B) NMR spectra of BRACO-19 with consecutive addition of JEV-PGQ RNA. Orange star marks depict the flattened proton resonances.

5.3.9 Stabilization of JEV-PGQs results in mTFP gene repression

It is plausible to consider the impact of the presence of secondary RNA structures on gene translation[314,315]. Gene reporter assays are usually the methods of choice to elucidate the functional role of RNA GQ structures in vivo. Besides, these assays serve as valuable tools for evaluating small molecules targeting intracellular RNA G-quadruplexes[139]. To assess the effect of BRACO-19 on JEV-PGQ stabilization and its potential as an antiviral agent, we conducted an mTFP (mono teal fluorescence protein) based reporter assay. We selected PGQ motifs present in the JEV genes, i.e. Envelope protein E, NS3, and NS5 as representatives for each gene and cloned them upstream of the mTFP gene in the pCAG-mTFP vector (pCAG-JEV-PGQ-mTFP). HEK293T cells were transfected with these plasmids

and treated with BRACO-19 (5 µM and 10 µM) 6 h post-infection and an untreated control was kept for comparison. The expression of the mTFP gene was monitored 24 h following transfection under the microscope. On visualization, we observed a decrease in mTFP expression in the BRACO-19 treated cells w.r.t to the untreated control, both of which were transfected with constructed plasmids (Figure 5.13 A, B). To ascertain whether the decreased expression stems from the interaction between BRACO-19 and JEV-PGQs, we proceeded to construct a plasmid containing a mutant sequence (pCAG-JEV-Mut-mTFP) incapable of adopting the G-quadruplex structure. HEK293T cells transfected with this plasmid showed no change in expression under the same conditions (Figure 5.13 A, B).

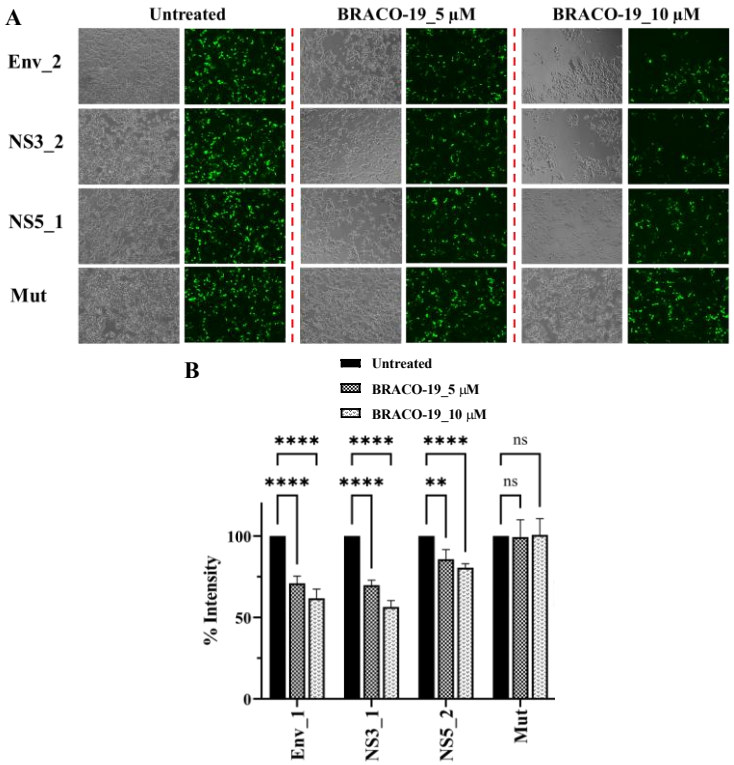

Figure 5.13. mTFP-based reporter assay. (A) Fluorescence microscopy images of untreated and treated HEK293T cells transfected with pCAG-JEV-PGQ-mTFP and pCAG-JEV-Mut-mTFP plasmids. (B) Relative fluorescence intensity of the treated and untreated transfected cells.

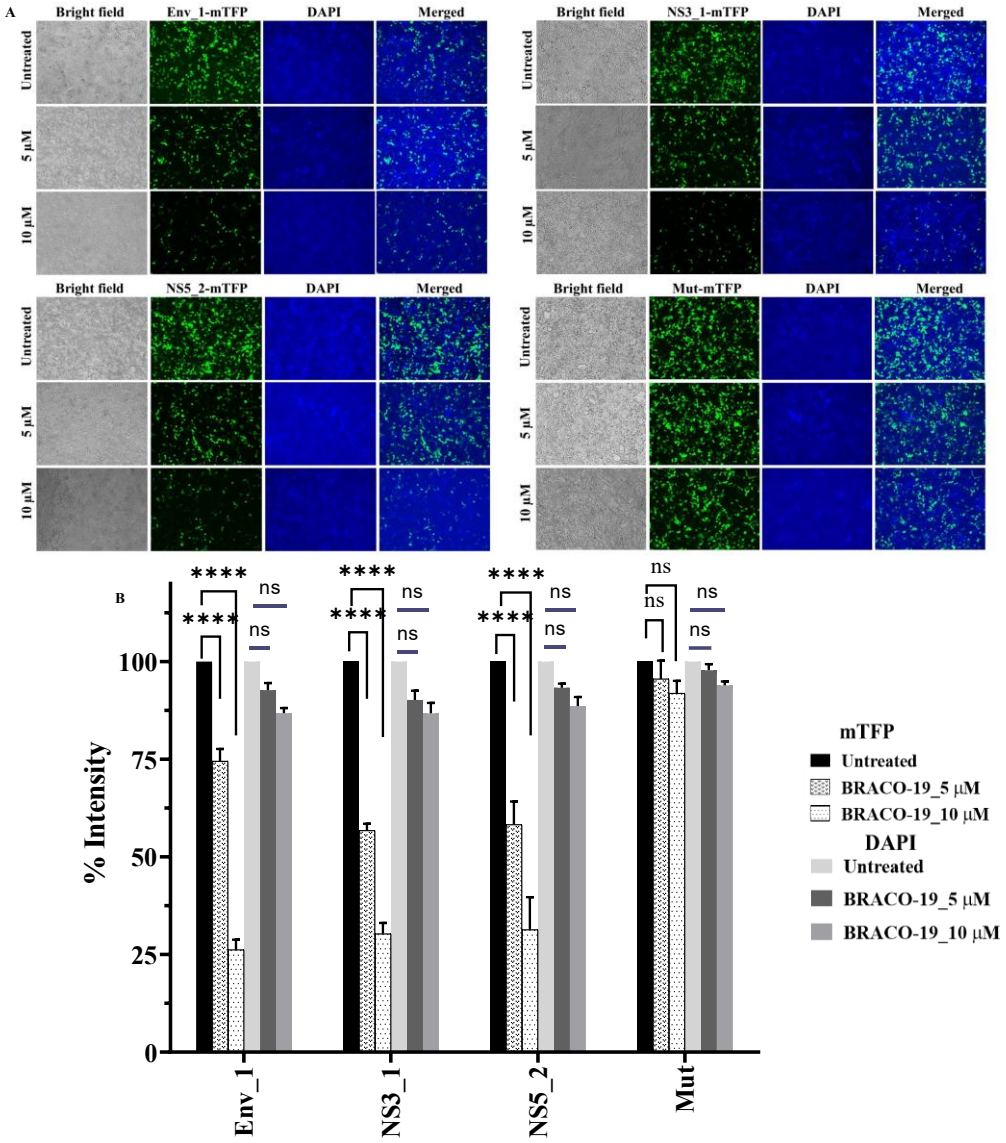

Figure 5.14. mTFP-based reporter assay. (A) Fluorescence microscopy images of untreated and treated HEK293T cells transfected with pCAG-JEV-PGQ-mTFP and pCAG-JEV-Mut-mTFP plasmids. (B) Relative fluorescence intensity of the treated and untreated transformed cells.

All the sets were also subsequently stained with DAPI (4′,6-diamidino-2-phenylindole) to monitor the cell viability upon treatment with BRACO-19 (Figure 5.14 A, B). Therefore, it was judicious to conclude that BRACO-19 substantially affected the expression of mTFP gene through the stabilization of JEV-PGQs, thereby suggesting potential antiviral efficacy.

5.3.10 BRACO-19 exerts potent antiviral effects against JEV

The biophysical experiments suggested that BRACO-19 interacts with and stabilizes the G4 structures derived from the JEV genome. To assess its biological properties and impact on JEV replication, we conducted cell-based experiments. We first evaluated the cytotoxic effect of BRACO-19 on Neuro-2a cells, a mouse neuronal cell line commonly used for JEV studies. The cell viability assay showed no adverse effects at concentrations of 50 μM or lower (Figure 5.15 A); hence, these concentrations were used to test anti-JEV effect. To evaluate the effect of BRACO-19 on JEV-replication in Neuro-2a cells infected with P20778 JEV strain, cellular RNA level was quantified using RT-qPCR after treatment with 0-50 μM ligand concentration. When tested against the virus infection at 1 MOI, it was observed that BRACO-19 reduced the JEV RNA levels at 5, 10, 20, and 50 μM in a dose-dependent manner. The strongest anti-JEV effect was observed for 50 μM BRACO-19. showing the maximal inhibition at 24 h post-infection (Figure 5.15 B). Similarly, infectious virus titers in the culture supernatants at 24 hpi were measured by plaque assay. In response to 50 μM BRACO-19 treatment, the total infectious virus yield showed a significant reduction compared to the untreated control (Figure 5.15 C). Since BRACO-19 affected JEV growth inhibiting the replication of the viral progeny, we sought to determine the impact of the ligand on viral protein levels in virus-infected cells. We selected two of the three viral proteins, NS3 and NS5 as the indicators of viral protein expression. JEV-infected Neura-2a cells were treated with 10, 20 and 50 μM BRACO-19 for 24 h. Cellular NS3 and NS5 protein levels were analyzed by Western blotting at 24 hpi, which was found to reduce the expression of both viral proteins in a dose-dependent manner (Figure 5.15 D). These observations confirmed that BRACO-19 exerts potent antiviral effects against JEV.

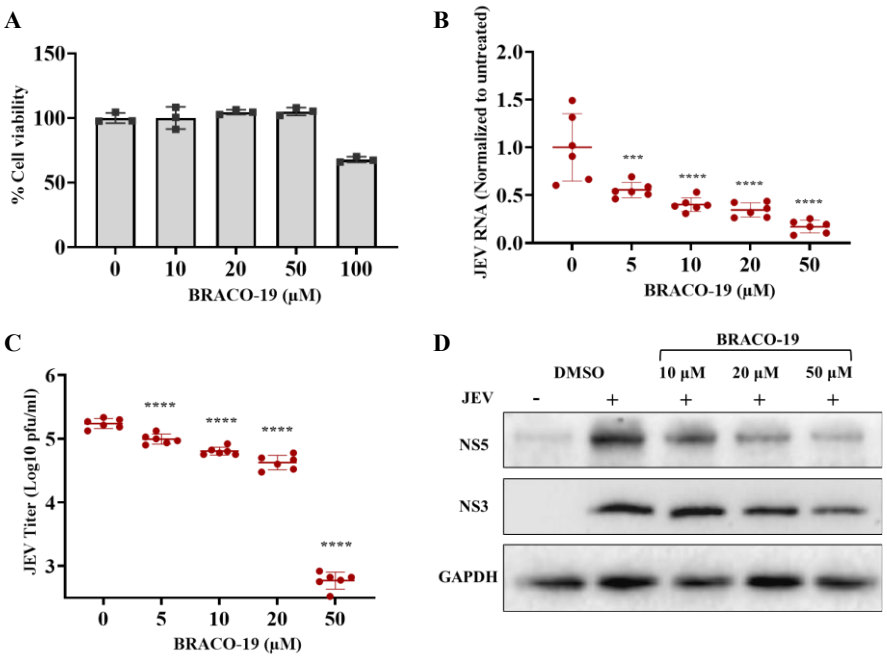

Figure 5.15. Antiviral effect of BRACO-19 on neuronal cells.

5.4 Conclusion

Unlike other viruses, JEV owing to its complex enzootic nature cannot be completely eradicated and thus there is a frequent resurgence of the virus[316]. Currently, only palliative care is available for managing JEV-associated infections, with no specific antiviral therapies approved. Most of the therapeutic strategies aimed at tackling JEV infections include the targeting of viral proteins as it stands out as one of the most appealing antiviral strategies and has been extensively investigated. However, the major challenge is the development of antiviral drug resistance, which is particularly prevalent in viruses that possess RNA-dependent RNA polymerase[317]. It is therefore imperative to devise novel therapeutic strategies to combat JEV infections.

In this work, we first retrieved all the accessible genomes of the Japanese Encephalitis virus (JEV) from the NCBI Database and executed a genome-wide mining study to identify putative G-quadruplex forming motifs through the G4 prediction tool. We obtained eight highly conserved putative G-quadruplexes in the JEV genome, located in the open reading frames of structural (Envelope Protein; E) and non-structural protein (NS3, NS5) coding genes. To validate the formation

of G4 structures by these predicted motifs in vitro, we used an array of biophysical and cell-based tools. 1D ^{1}H NMR and CD Spectroscopy experiments carried out in the presence of potassium ions, confirmed the formation of RNA GQ structures with a parallel topology by all the predicted PGQs. Further validation arrived from the increase in fluorescence emission intensity of ThT on binding with JEV-PGQs. Moreover, well-characterized G4 binders, such as BRACO-19 and TMPyP4 were able to displace ThT associated with G4 structures showcasing their interaction with G4 structures forming in JEV-PGQs. BRACO-19 was selected for further study as it displayed a better percentage displacement. To further assess the interaction of BRACO-19 with JEV-PGQs, we performed a gel retardation assay, which showed retardation in the mobility of bands of all the PGQs w.r.t to the mutant sequence which was incapable of folding into G4 conformation. Fluorescence titration assays were performed utilizing the intrinsic fluorescence ability of BRACO-19, wherein, BRACO-19 exhibited a higher binding affinity towards the PGQs, unlike the mutant. We also carried out an NMR resonance broadening study of BRACO-19 with the JEV-PGQs, where the broadening of characteristic resonance peaks of BRACO-19 and the emergence of new peaks indicated the possible formation of ligand-RNA complexes. To elucidate the binding of BRACO-19 with JEV-PGQs on gene expression, and the antiviral potency of BRACO-19, we conducted mTFP reporter assay studies. The dose-dependent decrease in mTFP gene expression in the presence of the ligand, confirmed the binding of JEV-PGQs with BRACO-19. BRACO-19 was also able to cause suppression of infectious virus yield, viral RNA synthesis as well as NS3 and NS5 protein expression in JEV-infected Neura-2a cells, thereby illustrating its effect on cell-based systems. Collectively, these findings provide the first comprehensive experimental evidence supporting RNA G-quadruplexes as pharmacologically actionable elements within the JEV genome and establish a foundation for developing structure-guided antiviral agents that exploit non-canonical viral RNA architectures. Targeting conserved RNA structural motifs therefore represents a promising strategy to overcome classical resistance

mechanisms and enables the development of broad-spectrum antiviral therapeutics for JEV and related flaviviruses.

CHAPTER 6

CONCLUSION AND FUTURE PERSPECTIVES

Chapter 6

Conclusion and Future Perspectives

6.1 Conclusion of the thesis

This thesis focuses on the structural and functional significance of G-quadruplex (G4) motifs, and focuses on their potential as therapeutic targets within pathogenic bacterial and viral genomes. The emergence and re-emergence of diseases, coupled with the rapid evolution of multidrug-resistant strains and limited efficacy of current antiviral agents, underscore the immediate requirement for novel therapeutic strategies. The work presented in the thesis highlights a focused effort to address both aspects of antimicrobial resistance through targeted intervention.

The current strategies to tackle infections associated with multi-drug-resistant pathogens remain compromised, necessitating the exploration of novel targets. One such promising alternative is non-canonical nucleic acid secondary structure, such as G-quadruplexes (G4s). G4s attract attention as promising targets owing to their evolutionary conservation and involvement in crucial intracellular biological mechanisms. These structures also offer two major advantages including, the regulation of gene expression at transcriptional or post-transcriptional level and the reduced susceptibility to mutation, therefore reducing the likelihood of antimicrobial resistance development. By combining in-silico genome mining, biophysical and cell-based studies, the studies performed in the thesis present G4 structures and G4 binding proteins (G4BPs) as plausible targets for therapeutical intervention in the context of antimicrobial resistance (AMR) and viral pathogenesis. Here, we explored the presence of G-quadruplex motifs in a bacterial and a viral pathogen actively involved in the rise of emerging infectious diseases.

Our initial investigation focused on *Acinetobacter baumannii*, a multidrug-resistant nosocomial pathogen, where we identified eight conserved G4 motifs. To confirm G4 structure formation, an array of biophysical assays were performed. Cellular assays demonstrated that ligand-mediated stabilization of these motifs resulted in altered gene expression, suggesting a direct regulatory role. Moreover, the

recognition and structural validation of stable two-tetrad G4 motifs within the *hfq* gene in *A. baumannii* revealed a unique layer of post-transcriptional regulation via selective recognition by the Hfq protein. This regulatory axis presents a promising avenue for the targeting of G4BPs in wake of alternative antibacterial strategies, in addition to G4s in bacteria.

Expanding the relevance of G4s in viral systems, we explored the presence and significance of RNA G4s (rG4s) in the genome of Japanese Encephalitis Virus (JEV). Bioinformatic predictions identified eight conserved G4 motifs, which were structurally characterized and validated using biophysical experiments. Cellular assays depicted the suppression of viral gene replication and expression upon stabilization of these motifs, reinforcing the potential of viral rG4s as antiviral targets. Collectively, these findings emphasize the evolutionary conservation and structural flexibility of G4s across bacteria; and viral genomes and establish their functional importance in modulation of infection-linked gene networks. The present study provides the framework for development of improved therapeutic strategies to tackle the ongoing challenge of antimicrobial resistance.

6.2 Future Perspectives

Based upon these findings, several avenues warrant further exploration. In *A. baumannii*, the identified G4 motifs are present in essential genes involved in the pathogen's survival and pathogenicity. However, the exact mechanisms elucidating G4 role in the genes harboring them and the functional impact of G4 motif stabilization remains elusive and requires in vivo validation.

In context of viral genomes, in vivo validation in appropriate animal models would be beneficial to establish the translational potential of G4 stabilization as an antiviral strategy. Future strategies focusing on the broader G4 interactome, particularly G4-binding proteins (G4BPs) is also advantageous, which play crucial roles in specific recognition and binding to G4 structures. Targeting of such proteins, either by inhibiting their binding or regulating their activity, may offer an additive or synergistic approach towards G4 stabilization. Moreover, high-throughput screening and development of selective G4-stabilizing or targeting small molecules could lead to the development of novel antimicrobial agents with

reduced risk of resistance. The advancement of ligand development alongside G4BP-targeted interventions present a new hope in the direction of rational design of next-generation antimicrobial and antiviral therapeutics.

Collectively, this thesis builds a foundation for G4 targeting in infectious diseases. It presents a breakthrough in utilization of non-canonical nucleic acid secondary structures for antimicrobial and antiviral intervention, offering new directions in combating AMR and emerging viral threats.

APPENDIX

APPENDIX A

APPENDIX A

Table A1. List of forward and reverse primers used in RT-PCR analysis.

Motif	**Primers**	**Primer Sequence (5'→ 3')**
16s rRNA	Forward Primer	GTGCGTAGGCGGCTTATTA
	Reverse Primer	TCTACCATCCTCTCCCATACTC
AB_PGQ1	Forward Primer	CAAGCGAAAGTCACTCAAGAAG
	Reverse Primer	GCTAAACCTGTAATCGGTAGGG
AB_PGQ2	Forward Primer	GCTTGTCGGTTGTGATTCAAG
	Reverse Primer	ATCGGTGCTGGTTCAATAGG
AB_PGQ3	Forward Primer	CAGCGATTACAAGCAAATGG
	Reverse Primer	AACCACCGGATCATCCATAAC
AB_PGQ4	Forward Primer	ACCGTATGGCAATCGAGATAG
	Reverse Primer	ACCATATCGGCATCAGGTTT
AB_PGQ5	Forward Primer	TCCGGTGTTATCGGTAGATAGT
	Reverse Primer	GGTGAGCACGGCTTAAATTG
AB_PGQ6	Forward Primer	ATCAGAACAACTCGCCCATAG
	Reverse Primer	GAACGTTGGACCTGATCTCTT
AB_PGQ7	Forward Primer	CCGAAAGGTTTATGGCAAGAAG
	Reverse Primer	GGTGCTACCTTATGCATGGTAT
AB_PGQ8	Forward Primer	GGACAAGCCGACAGTGTAAATA
	Reverse Primer	CCGGATATTGTTCTGGTGTATAGG

Table A2. List of predicted PGQ motifs with G-tract ≥3 and loop length of 20 nts.

#	Length (bp)	Start Position	End Position	PG4 Motifs	cG Score	cC Score	Strand
1	36	18498	18533	GGGAGGCAGCAGTGGGGAATATTGGACAATGGGGGG	190	30	+
2	38	54007	54044	GGGCCTGCACTTTCGGGGTCTAAATCTTCGGGAAGGGG	150	80	+
3	33	240570	240602	GGGTTTGAGGGGAAAGGCCTGACGGGAGTTGGG	180	30	+
4	37	310674	310710	GGGTACAAGTGGGTAACTATATGGGCATGAATCAGGG	140	40	+
5	39	334368	334406	GGGGTTCTGGGGATGAGGGGAATTATTCCACAAGAAGGG	170	40	+
6	36	484293	484328	GGGAGGCAGCAGTGGGGAATATTGGACAATGGGGGG	190	30	+
7	36	516667	516702	GGGAGGCAGCAGTGGGGAATATTGGACAATGGGGGG	190	30	+
8	43	589188	589230	GGGATGAACAGGGGCGTCGTATTGGGTTAAATCTGGCCTCGGG	180	70	+
9	31	682812	682842	GGGGCTTATAACGAAGGGTATGGGGCATGGG	150	30	+
10	32	863365	863396	GGGAATTTAGGGATTTGGGAGTGTCAACCGGG	140	30	+

11	37	942586	942622	GGGGTGCAGTTCAGAACGGGAGGGGGACACCTTTGGG	180	60	+
12	36	1225914	1225949	GGGCAAATTGAAGGCGGGTTTGTTCAAGGGATGGGG	170	30	+
13	34	1288250	1288283	GGGAAAGAAGGGCACAGCAGTTCGGGTTTAAGGG	150	40	+
14	44	1359014	1359057	GGGTTTGTTCCCGGGCATCCGATTGCGGGAAGTGAACACACGGG	170	100	+
15	42	1364784	1364825	GGGACTTTATGTTGAGGGGTTCCACCTTGTAATGGGTGAGGG	170	50	+
16	36	1414860	1414895	GGGGTCAGATCAGAACGGGAGGGGGACACCTTCGGG	170	70	+
17	37	1603432	1603468	GGGGTGCAGTTCAGAACGGGAGGGGGACACCTTCGGG	180	70	+
18	37	1794988	1795024	GGGATGATTGTCGGGAATACGGGCAAGATGGCACGGG	170	50	+
19	39	1889611	1889649	GGGGGAATGGGGCTATCGGTCGAAGCTGGGCTTTTAGGG	190	50	+
20	31	1941834	1941864	GGGGGATGGGGTGAGGGGGAAATAATCAGGG	180	10	+

21	35	2322144	2322178	GGGGCAGGTTTTCGGGTAGGTTGGGTCTATGCGGG	180	40	+
22	33	2359599	2359631	GGGCAGCGGTTATTTCAGCGGGTCCGGGCTGGG	160	70	+
23	37	2374784	2374820	GGGGTGCAGTTCAGAACGGGAGTGGGACACCCTTGGG	170	70	+
24	29	3628669	3628697	GGGCTAAAGGGCACGGGTTTATGAGTGGG	140	30	+
25	36	33117	33152	GGGAGGCAGCAGTGGGGAATATTGGACAATGGGGGG	190	30	-
26	18	52887	52904	GGGTTAGGGTTGGGTGGG	120	0	-
27	27	139131	139157	GGGTTTATTGGGCGGCCTTTAGGGGGG	140	30	-
28	36	203095	203130	GGGAGGCAGCAGTGGGGAATATTGGACAATGGGGGG	190	30	-
29	35	226627	226661	GGGCTTTCGGGTCAGGCTGGGCATCGGCAATGGGG	170	70	-
30	41	492439	492479	GGGTGGTACTTGGATGGGTGTTACGCCGCAGGGCCGATGGG	200	70	-

31	37	567435	567471	GGGTATTCGGGTGGCAATTGATGACTTTGGGACAGGG	160	40	-
32	40	593048	593087	GGGATTTGAACTGGAAACAGCGGGGGTACTTAAAGGGGGG	180	40	-
33	28	628777	628804	GGGCGGGTGAGACTCCGTCATTGGGGGG	150	50	-
34	36	669647	669682	GGGAGGCAGCAGTGGGGAATATTGGACAATGGGGGG	190	30	-
35	34	713962	713995	GGGATGGGGATTGGCGGTATTTTGGGTGGTTGGG	190	10	-
36	39	725006	725044	GGGTGGCCCAACTAAAGGGTATTACAACTTGGGCGTGGG	150	70	-
37	36	861056	861091	GGGCTTCATAGGGCAGGGTGCCAGGTAACGCCTGGG	160	80	-
38	44	865391	865434	GGGTATTGGGTCTTCTACATTGTACTGGGGCTTTTTGGACTGGG	160	60	-
39	32	948440	948471	GGGGCGGGCAAATGAAAAAAGCGGGAATGGGG	160	30	-
40	35	1174912	1174946	GGGTTTACTGTATATACGGGTGGGCTAAAGATGGG	140	30	-

41	37	1185418	1185454	GGGGTGCAGTTCAGAACGGGAGGGGGACACCTTCGGG	180	70	-
42	38	1305171	1305208	GGGCAAGGGGATGATGAGCTTACTGGCGGGTTAGAGGG	190	40	-
43	41	1306500	1306540	GGGGGGATTATCACGGATGAATATGGGAATAATGTTACGGG	160	30	-
44	44	1334788	1334831	GGGAAATTCAATTGGCTTTGGGCTTAGTGGCAGCGGGAGAAGGG	190	50	-
45	21	1476883	1476903	GGGCAAATTGGGACAGGGGGG	120	20	-
46	32	1631096	1631127	GGGAAGGGATAGACTGCGTAGTGAGGGCGGGG	180	30	-
47	37	1931547	1931583	GGGATTATTGCTGGGCTTTTAACGGGGATGTTAGGGG	160	30	-
48	44	3346330	3346373	GGGTTCTCATTTCAGGGAACCGAGATGGTGGGTGTAGCAGCGGG	190	70	-
49	27	3364164	3364190	GGGCGTGTTGGGTGCGGGCATGATGGG	160	30	-

Table A3. List of Acinetobacter baumannii strains taken into consideration for PGQ prediction analysis.

***Acinetobacter baumannii* strain**	**Accession ID**
Acinetobacter baumannii NCGM 237 DNA, complete genome	AP013357.1
Acinetobacter baumannii DNA, complete genome, strain: IOMTU 433	AP014649.1
Acinetobacter baumannii NU-60 DNA, complete genome	AP019685.1
Acinetobacter baumannii DNA, complete genome, strain: WP8-W18-ESBL-11	AP022238.1
Acinetobacter baumannii ATCC19606 DNA, complete genome	AP022836.1
Acinetobacter baumannii OCU_Ac16a DNA, complete genome	AP023077.1
Acinetobacter baumannii NIPH17_0019 DNA, complete genome	AP024415.1
Acinetobacter baumannii OCU_Ac18 DNA, complete genome	AP024802.1
Acinetobacter baumannii ATCC 19606 DNA, complete genome	AP025740.1
Acinetobacter baumannii ATCC 17978, complete genome	CP000521.1
Acinetobacter baumannii ACICU, complete genome	CP000863.1
Acinetobacter baumannii AB307-0294, complete genome	CP001172.2
Acinetobacter baumannii AB0057, complete genome	CP001182.2
Acinetobacter baumannii 1656-2, complete genome	CP001921.1
Acinetobacter baumannii MDR-ZJ06, complete genome	CP001937.2
Acinetobacter baumannii TCDC-AB0715, complete genome	CP002522.2
Acinetobacter baumannii MDR-TJ, complete genome	CP003500.1
Acinetobacter baumannii BJAB07104, complete genome	CP003846.1
Acinetobacter baumannii BJAB0715, complete genome	CP003847.1
Acinetobacter baumannii BJAB0868, complete genome	CP003849.1
Acinetobacter baumannii TYTH-1, complete genome	CP003856.1
Acinetobacter baumannii D1279779, complete genome	CP003967.2
Acinetobacter baumannii ZW85-1, complete genome	CP006768.1
Acinetobacter baumannii strain AC29, complete genome	CP007535.2
Acinetobacter baumannii AC30, complete genome	CP007577.1
Acinetobacter baumannii LAC-4, complete genome	CP007712.1
Acinetobacter baumannii strain AB5075-UW, complete genome	CP008706.1
Acinetobacter baumannii strain AB031, complete genome	CP009256.1
Acinetobacter baumannii strain AB030, complete genome	CP009257.1

Acinetobacter baumannii strain AbH12O-A2, complete genome	CP009534.1
Acinetobacter baumannii strain 6200, complete genome	CP010397.1
Acinetobacter baumannii strain XH386, complete genome	CP010779.1
Acinetobacter baumannii strain A1, complete genome	CP010781.1
Acinetobacter baumannii ATCC 17978-mff, complete genome	CP012004.1
Acinetobacter baumannii Ab04-mff, complete genome	CP012006.1
Acinetobacter baumannii strain PR07 genome	CP012035.1
Acinetobacter baumannii strain CA-17 chromosome, complete genome	CP012587.1
Acinetobacter baumannii strain D36, complete genome	CP012952.1
Acinetobacter baumannii strain KBN10P02143 chromosome, complete genome	CP013924.1
Acinetobacter baumannii strain YU-R612, complete genome	CP014215.1
Acinetobacter baumannii strain Ab421_GEIH-2010 genome	CP014266.1
Acinetobacter baumannii strain AB34299 chromosome, complete genome	CP014291.1
Acinetobacter baumannii strain XH858 chromosome, complete genome	CP014528.1
Acinetobacter baumannii strain XH860 chromosome, complete genome	CP014538.1
Acinetobacter baumannii strain XH859 chromosome, complete genome	CP014539.1
Acinetobacter baumannii strain XH857 chromosome, complete genome	CP014540.1
Acinetobacter baumannii strain XH856 chromosome, complete genome	CP014541.1
Acinetobacter baumannii strain ab736, complete genome	CP015121.1
Acinetobacter baumannii strain 3207 chromosome, complete genome	CP015364.1
Acinetobacter baumannii strain ORAB01, complete genome	CP015483.1
Acinetobacter baumannii strain CMC-CR-MDR-Ab4 chromosome, complete genome	CP016295.1
Acinetobacter baumannii strain CMC-MDR-Ab59 chromosome, complete genome	CP016298.1
Acinetobacter baumannii strain CMC-CR-MDR-Ab66 chromosome, complete genome	CP016300.1
Acinetobacter baumannii DU202 chromosome, complete genome	CP017152.1
Acinetobacter baumannii strain KAB01 chromosome, complete genome	CP017642.1
Acinetobacter baumannii strain KAB02 chromosome, complete genome	CP017644.1
Acinetobacter baumannii strain KAB03 chromosome, complete genome	CP017646.1
Acinetobacter baumannii strain KAB04 chromosome, complete genome	CP017648.1
Acinetobacter baumannii strain KAB05 chromosome, complete genome	CP017650.1

Acinetobacter baumannii strain KAB06 chromosome, complete genome	CP017652.1
Acinetobacter baumannii strain KAB07 chromosome, complete genome	CP017654.1
Acinetobacter baumannii strain KAB08 chromosome, complete genome	CP017656.1
Acinetobacter baumannii strain HRAB-85, complete genome	CP018143.1
Acinetobacter baumannii strain AF-401 chromosome, complete genome	CP018254.1
Acinetobacter baumannii strain AF-673 chromosome, complete genome	CP018256.1
Acinetobacter baumannii strain A1296 chromosome, complete genome	CP018332.1
Acinetobacter baumannii strain XDR-BJ83 chromosome, complete genome	CP018421.1
Acinetobacter baumannii strain ATCC 17978 chromosome, complete genome	CP018664.1
Acinetobacter baumannii strain LAC4, complete genome	CP018677.1
Acinetobacter baumannii strain 11510 chromosome	CP018861.2
Acinetobacter baumannii strain AB042 chromosome, complete genome	CP019034.1
Acinetobacter baumannii strain MDR-CQ chromosome, complete genome	CP019114.1
Acinetobacter baumannii strain XH731 chromosome, complete genome	CP019217.1
Acinetobacter baumannii strain 15A5 chromosome, complete genome	CP020574.1
Acinetobacter baumannii strain SSA12 chromosome, complete genome	CP020578.1
Acinetobacter baumannii strain SAA14 chromosome, complete genome	CP020579.1
Acinetobacter baumannii strain SSMA17 chromosome, complete genome	CP020581.1
Acinetobacter baumannii strain JBA13 chromosome, complete genome	CP020584.1
Acinetobacter baumannii strain CBA7 chromosome, complete genome	CP020586.1
Acinetobacter baumannii strain 15A34 chromosome, complete genome	CP020590.1
Acinetobacter baumannii strain SSA6 chromosome, complete genome	CP020591.1
Acinetobacter baumannii strain USA2 chromosome, complete genome	CP020592.1
Acinetobacter baumannii strain USA15 chromosome, complete genome	CP020595.1
Acinetobacter baumannii strain HWBA8 chromosome, complete genome	CP020597.1
Acinetobacter baumannii strain WKA02 chromosome, complete genome	CP020598.1
Acinetobacter baumannii strain XH731 chromosome, complete genome	CP021321.1
Acinetobacter baumannii strain XH386 chromosome, complete genome	CP021326.1
Acinetobacter baumannii strain B8342 chromosome, complete genome	CP021342.1
Acinetobacter baumannii strain B11911 chromosome, complete genome	CP021345.1
Acinetobacter baumannii strain B8300 chromosome, complete genome	CP021347.1
Acinetobacter baumannii strain ZS3 chromosome	CP021496.1
Acinetobacter baumannii strain A85 chromosome, complete genome	CP021782.1

Acinetobacter baumannii strain 7804 chromosome, complete genome	CP022283.1
Acinetobacter baumannii strain 9201 chromosome, complete genome	CP023020.1
Acinetobacter baumannii strain 10324 chromosome, complete genome	CP023022.1
Acinetobacter baumannii strain 10042 chromosome, complete genome	CP023026.1
Acinetobacter baumannii strain 9102 chromosome, complete genome	CP023029.1
Acinetobacter baumannii strain 7847 chromosome, complete genome	CP023031.1
Acinetobacter baumannii strain 5845 chromosome, complete genome	CP023034.1
Acinetobacter baumannii strain XH906 chromosome, complete genome	CP023140.1
Acinetobacter baumannii strain AYP-A2 chromosome, complete genome	CP024124.1
Acinetobacter baumannii strain A388 chromosome, complete genome	CP024418.1
Acinetobacter baumannii strain AbPK1 chromosome, complete genome	CP024576.1
Acinetobacter baumannii strain Ab4977 chromosome, complete genome	CP024611.1
Acinetobacter baumannii strain Ab4653 chromosome, complete genome	CP024612.1
Acinetobacter baumannii strain Ab4568 chromosome, complete genome	CP024613.1
Acinetobacter baumannii isolate SMC_Paed_Ab_BL01 chromosome, complete genome	CP025266.1
Acinetobacter baumannii strain ABNIH28 chromosome, complete genome	CP026125.1
Acinetobacter baumannii strain 810CP chromosome, complete genome	CP026338.1
Acinetobacter baumannii strain AR_0056 chromosome, complete genome	CP026707.1
Acinetobacter baumannii strain AR_0063 chromosome, complete genome	CP026711.1
Acinetobacter baumannii strain WCHAB005133 chromosome, complete genome	CP026750.2
Acinetobacter baumannii strain AR_0078 chromosome, complete genome	CP026761.1
Acinetobacter baumannii strain S1 chromosome	CP026943.1
Acinetobacter baumannii strain AR_0056 chromosome, complete genome	CP027123.1
Acinetobacter baumannii strain AR_0070 chromosome, complete genome	CP027178.1
Acinetobacter baumannii strain AR_0052 chromosome, complete genome	CP027183.1
Acinetobacter baumannii strain WCHAB005078 chromosome, complete genome	CP027246.2
Acinetobacter baumannii strain AR_0083 chromosome, complete genome	CP027528.1
Acinetobacter baumannii strain AR_0088 chromosome, complete genome	CP027530.1
Acinetobacter baumannii strain AR_0102 chromosome, complete genome	CP027607.1
Acinetobacter baumannii strain AR_0101 chromosome, complete genome	CP027611.1
Acinetobacter baumannii strain DS002 chromosome, complete genome	CP027704.2

Acinetobacter baumannii strain NCIMB 8209 chromosome, complete genome	CP028138.1
Acinetobacter baumannii strain DA33098 chromosome, complete genome	CP029569.1
Acinetobacter baumannii strain Aba chromosome, complete genome	CP030083.1
Acinetobacter baumannii strain DA33382 chromosome, complete genome	CP030106.1
Acinetobacter baumannii ACICU chromosome, complete genome	CP031380.1
Acinetobacter baumannii strain LUH 6011 chromosome, complete genome	CP031383.1
Acinetobacter baumannii strain MDR-UNC chromosome, complete genome	CP031444.1
Acinetobacter baumannii WM99c chromosome, complete genome	CP031743.1
Acinetobacter baumannii strain A320 (RUH134) chromosome, complete genome	CP032055.1
Acinetobacter baumannii strain UPAB1 chromosome, complete genome	CP032215.1
Acinetobacter baumannii strain C25 chromosome, complete genome	CP032743.1
Acinetobacter baumannii strain 7835 chromosome, complete genome	CP033243.1
Acinetobacter baumannii strain 2008S11-069 chromosome, complete genome	CP033516.1
Acinetobacter baumannii strain FDAARGOS_540 chromosome, complete genome	CP033754.1
Acinetobacter baumannii strain FDAARGOS_533 chromosome, complete genome	CP033768.1
Acinetobacter baumannii strain MRSN15313 chromosome, complete genome	CP033869.1
Acinetobacter baumannii strain A52 chromosome, complete genome	CP034092.1
Acinetobacter baumannii isolate 09A16CRGN0014 chromosome, complete genome	CP034242.1
Acinetobacter baumannii isolate 09A16CRGN003B chromosome, complete genome	CP034243.1
Acinetobacter baumannii strain ABUH796 chromosome, complete genome	CP035043.1
Acinetobacter baumannii strain ABUH793 chromosome, complete genome	CP035045.1
Acinetobacter baumannii strain ABUH773 chromosome, complete genome	CP035049.1
Acinetobacter baumannii strain ABUH763 chromosome, complete genome	CP035051.1
Acinetobacter baumannii strain 11A14CRGN003 chromosome, complete genome	CP035183.1
Acinetobacter baumannii strain 11A1314CRGN088 chromosome, complete genome	CP035184.1

Acinetobacter baumannii strain 11A1213CRGN055 chromosome, complete genome	CP035185.1
Acinetobacter baumannii strain 11A1213CRGN008 chromosome, complete genome	CP035186.1
Acinetobacter baumannii strain VB23193 chromosome, complete genome	CP035672.1
Acinetobacter baumannii strain VB31459 chromosome, complete genome	CP035930.1
Acinetobacter baumannii strain VB31459 plasmid unnamed1, complete sequence	CP035931.1
Acinetobacter baumannii strain TG60155 chromosome	CP036283.1
Acinetobacter baumannii strain AB053 chromosome	CP037869.1
Acinetobacter baumannii strain AB048 chromosome	CP037870.1
Acinetobacter baumannii strain AB047 chromosome	CP037871.1
Acinetobacter baumannii strain AB046 chromosome	CP037872.1
Acinetobacter baumannii strain EH chromosome, complete genome	CP038258.1
Acinetobacter baumannii strain EC chromosome, complete genome	CP038262.1
Acinetobacter baumannii strain CIAT758 chromosome, complete genome	CP038500.1
Acinetobacter baumannii strain ACN21 chromosome, complete genome	CP038644.1
Acinetobacter baumannii ATCC 17978 substr. PMR-Low chromosome	CP039023.2
Acinetobacter baumannii ATCC 17978 substr. PMR-High chromosome, complete genome	CP039025.2
Acinetobacter baumannii ATCC 17978 substr. Lab-WT chromosome	CP039028.2
Acinetobacter baumannii strain TG31986 chromosome, complete genome	CP039341.1
Acinetobacter baumannii strain TG31302 chromosome, complete genome	CP039343.1
Acinetobacter baumannii strain TG22653 chromosome, complete genome	CP039518.1
Acinetobacter baumannii strain TG22627 chromosome, complete genome	CP039520.1
Acinetobacter baumannii strain TG29392 chromosome, complete genome	CP039930.1
Acinetobacter baumannii strain TG22182 chromosome, complete genome	CP039993.1
Acinetobacter baumannii strain VB958 chromosome, complete genome	CP040040.1
Acinetobacter baumannii strain VB958 plasmid unnamed1, complete sequence	CP040041.1
Acinetobacter baumannii strain VB958 plasmid unnamed2, complete sequence	CP040042.1
Acinetobacter baumannii strain VB1190 chromosome, complete genome	CP040047.1
Acinetobacter baumannii strain VB16141 chromosome, complete genome	CP040050.1

Acinetobacter baumannii strain VB35179 chromosome, complete genome	CP040053.1
Acinetobacter baumannii strain VB35435 chromosome, complete genome	CP040056.1
Acinetobacter baumannii strain SP304 chromosome, complete genome	CP040080.1
Acinetobacter baumannii strain VB33071 chromosome, complete genome	CP040084.1
Acinetobacter baumannii strain VB33071 plasmid unnamed1, complete sequence	CP040085.1
Acinetobacter baumannii strain VB35575 chromosome, complete genome	CP040087.1
Acinetobacter baumannii strain P7774 chromosome, complete genome	CP040259.1
Acinetobacter baumannii strain PB364 chromosome, complete genome	CP040425.1
Acinetobacter baumannii strain 11W359501 chromosome, complete genome	CP041035.1
Acinetobacter baumannii strain CUVET-MIC596 chromosome, complete genome	CP041148.1
Acinetobacter baumannii strain J9 chromosome, complete genome	CP041587.1
Acinetobacter baumannii strain E47 chromosome, complete genome	CP042556.1
Acinetobacter baumannii strain ATCC BAA-1790 chromosome, complete genome	CP042841.1
Acinetobacter baumannii strain ABCR01 chromosome, complete genome	CP042931.1
Acinetobacter baumannii strain PG20180064 chromosome, complete genome	CP043180.1
Acinetobacter baumannii strain N13-03449 chromosome, complete genome	CP043417.1
Acinetobacter baumannii strain 11A1314CRGN089 chromosome, complete genome	CP043418.1
Acinetobacter baumannii strain 11A1213CRGN064 chromosome, complete genome	CP043419.1
Acinetobacter baumannii strain AB043 chromosome, complete genome	CP043910.1
Acinetobacter baumannii strain K09-14 chromosome, complete genome	CP043953.1
Acinetobacter baumannii strain CAM180-1 chromosome, complete genome	CP044356.1
Acinetobacter baumannii strain 31FS3-2 chromosome, complete genome	CP044517.1
Acinetobacter baumannii strain 29FS20 chromosome, complete genome	CP044519.1
Acinetobacter baumannii strain ATCC 19606 chromosome, complete genome	CP045110.1
Acinetobacter baumannii strain AbCAN2 chromosome, complete genome	CP045428.1
Acinetobacter baumannii strain 6507 chromosome, complete genome	CP045528.1
Acinetobacter baumannii strain 5457 chromosome	CP045541.1

Acinetobacter baumannii strain XH1056 chromosome, complete genome	CP045645.1
Acinetobacter baumannii strain XL380 chromosome, complete genome	CP046536.1
Acinetobacter baumannii strain ATCC 19606 chromosome, complete genome	CP046654.1
Acinetobacter baumannii strain A1429 chromosome, complete genome	CP046898.1
Acinetobacter baumannii strain DETAB-P2 chromosome, complete genome	CP047973.1
Acinetobacter baumannii strain D46 chromosome, complete genome	CP048131.1
Acinetobacter baumannii strain ABF9692 chromosome, complete genome	CP048827.1
Acinetobacter baumannii strain D4 chromosome, complete genome	CP048849.1
Acinetobacter baumannii strain Ax270 chromosome, complete genome	CP049240.1
Acinetobacter baumannii strain Ex003 chromosome, complete genome	CP049314.1
Acinetobacter baumannii strain ATCC 17978 chromosome, complete genome	CP049363.1
Acinetobacter baumannii strain VB82 chromosome, complete genome	CP050385.1
Acinetobacter baumannii strain VB473 chromosome, complete genome	CP050388.1
Acinetobacter baumannii strain VB723 chromosome, complete genome	CP050390.1
Acinetobacter baumannii strain VB11737 chromosome, complete genome	CP050400.1
Acinetobacter baumannii strain VB2181 chromosome, complete genome	CP050401.1
Acinetobacter baumannii strain VB2486 chromosome, complete genome	CP050403.1
Acinetobacter baumannii strain PM1912235 chromosome, complete genome	CP050410.1
Acinetobacter baumannii strain PM192696 chromosome, complete genome	CP050412.1
Acinetobacter baumannii strain PM193665 chromosome, complete genome	CP050415.1
Acinetobacter baumannii strain VB2200 chromosome, complete genome	CP050421.1
Acinetobacter baumannii strain PM194188 chromosome, complete genome	CP050425.1
Acinetobacter baumannii strain PM194229 chromosome, complete genome	CP050432.1
Acinetobacter baumannii strain VB7036 chromosome, complete genome	CP050523.1
Acinetobacter baumannii strain VB2139 chromosome, complete genome	CP050526.1
Acinetobacter baumannii strain DT-Ab057 chromosome, complete genome	CP050904.1
Acinetobacter baumannii strain DT-Ab022 chromosome, complete genome	CP050907.1
Acinetobacter baumannii strain DT-Ab020 chromosome, complete genome	CP050911.1
Acinetobacter baumannii strain DT-Ab007 chromosome, complete genome	CP050914.1
Acinetobacter baumannii strain DT-Ab003 chromosome, complete genome	CP050916.1
Acinetobacter baumannii strain A24 chromosome	CP051262.1
Acinetobacter baumannii strain VB2107 chromosome, complete genome	CP051474.1

Acinetobacter baumannii strain Ab-C102 chromosome, complete genome	CP051862.1
Acinetobacter baumannii strain Ab-C63 chromosome, complete genome	CP051866.1
Acinetobacter baumannii strain Ab-D10a-a chromosome, complete genome	CP051869.1
Acinetobacter baumannii strain Ab-B004d-c chromosome, complete genome	CP051875.1
Acinetobacter baumannii ATCC 17978 chromosome, complete genome	CP053098.1
Acinetobacter baumannii strain DT0544C chromosome, complete genome	CP053215.1
Acinetobacter baumannii strain DT01139C chromosome, complete genome	CP053218.1
Acinetobacter baumannii strain MS14413 chromosome, complete genome	CP054302.1
Acinetobacter baumannii strain AB79 chromosome, complete genome	CP054416.1
Acinetobacter baumannii strain YC103 chromosome, complete genome	CP054560.1
Acinetobacter baumannii strain TP1 chromosome, complete genome	CP056784.2
Acinetobacter baumannii ATCC 19606 = CIP 70.34 = JCM 6841 strain ATCC 19606 chromosome, complete genome	CP058289.1
Acinetobacter baumannii strain ATCC BAA1605 chromosome, complete genome	CP058625.1
Acinetobacter baumannii strain M164-3 chromosome, complete genome	CP058729.1
Acinetobacter baumannii strain A118 chromosome, complete genome	CP059039.1
Acinetobacter baumannii strain ATCC 19606 chromosome, complete genome	CP059040.1
Acinetobacter baumannii strain ATCC 17978 chromosome, complete genome	CP059041.1
Acinetobacter baumannii strain AC1633 chromosome, complete genome	CP059300.1
Acinetobacter baumannii strain 2014TJAB1 chromosome, complete genome	CP059349.1
Acinetobacter baumannii strain 2018BJAB2 chromosome, complete genome	CP059350.1
Acinetobacter baumannii strain 2018BJAB1 chromosome, complete genome	CP059351.1
Acinetobacter baumannii strain 2014LNAB1 chromosome, complete genome	CP059352.1
Acinetobacter baumannii strain 2016LNAB1 chromosome, complete genome	CP059353.1
Acinetobacter baumannii strain 2014BJAB1 chromosome, complete genome	CP059354.1
Acinetobacter baumannii strain 2016BJAB1 chromosome, complete genome	CP059355.1
Acinetobacter baumannii strain 2018HBAB1 chromosome, complete genome	CP059356.1
Acinetobacter baumannii strain 2018HLJAB2 chromosome, complete genome	CP059357.1

Acinetobacter baumannii strain 2018HLJAB1 chromosome, complete genome	CP059358.1
Acinetobacter baumannii strain 2018TJAB1 chromosome, complete genome	CP059359.1
Acinetobacter baumannii strain 36-1512 chromosome, complete genome	CP059386.1
Acinetobacter baumannii strain M175-3 chromosome, complete genome	CP059474.1
Acinetobacter baumannii strain 17-84 chromosome, complete genome	CP059479.1
Acinetobacter baumannii strain E-011922 chromosome, complete genome	CP059542.1
Acinetobacter baumannii strain 10_4 chromosome, complete genome	CP059546.1
Acinetobacter baumannii strain 10_3 chromosome, complete genome	CP059547.1
Acinetobacter baumannii strain B9 chromosome, complete genome	CP059548.1
Acinetobacter baumannii strain AbCTX13 chromosome, complete genome	CP059729.1
Acinetobacter baumannii strain TP2 chromosome, complete genome	CP060011.1
Acinetobacter baumannii strain TP3 chromosome, complete genome	CP060013.1
Acinetobacter baumannii strain AbCTX1 chromosome, complete genome	CP060029.1
Acinetobacter baumannii strain XYAB2018 chromosome, complete genome	CP060285.1
Acinetobacter baumannii strain AbCTX9 chromosome, complete genome	CP060504.1
Acinetobacter baumannii strain AbCTX5 chromosome, complete genome	CP060505.1
Acinetobacter baumannii strain abA1 chromosome, complete genome	CP060732.1
Acinetobacter baumannii strain CAb-65 chromosome, complete genome	CP060994.1
Acinetobacter baumannii strain CFSAN093710 chromosome, complete genome	CP061514.1
Acinetobacter baumannii strain CFSAN093709 chromosome, complete genome	CP061517.1
Acinetobacter baumannii strain CFSAN093708 chromosome, complete genome	CP061519.1
Acinetobacter baumannii strain CFSAN093707 chromosome, complete genome	CP061521.1
Acinetobacter baumannii strain CFSAN093706 chromosome, complete genome	CP061523.1
Acinetobacter baumannii strain CFSAN093705 chromosome, complete genome	CP061525.1
Acinetobacter baumannii strain XH1344 chromosome, complete genome	CP061541.1
Acinetobacter baumannii strain E-072658 chromosome, complete genome	CP061705.1
Acinetobacter baumannii strain Res13-Abat-PEA21-P4-01-A chromosome, complete genome	CP062919.1

Acinetobacter baumannii strain SD chromosome, complete genome	CP064292.1
Acinetobacter baumannii strain PartI-Abaumannii-RM8376 isolate ATCC isolate chromosome, complete genome	CP064375.1
Acinetobacter baumannii strain 2016GDAB1 chromosome, complete genome	CP065051.1
Acinetobacter baumannii strain ATCC 17961 chromosome, complete genome	CP065432.1
Acinetobacter baumannii strain FDAARGOS_917 chromosome 1	CP065887.1
Acinetobacter baumannii strain FDAARGOS_1036 chromosome, complete genome	CP066016.1
Acinetobacter baumannii strain G20AB011 chromosome, complete genome	CP066229.1
Acinetobacter baumannii strain G20AB010 chromosome, complete genome	CP066232.1
Acinetobacter baumannii strain G20AB009 chromosome, complete genome	CP066235.1
Acinetobacter baumannii strain G20AB007 chromosome, complete genome	CP066237.1
Acinetobacter baumannii strain FDAARGOS_1360 chromosome, complete genome	CP069840.1
Acinetobacter baumannii strain FDAARGOS_1359 chromosome, complete genome	CP069851.1
Acinetobacter baumannii strain AB5075-VUB-itrA::ISAba13 chromosome, complete genome	CP070358.2
Acinetobacter baumannii strain AB5075-VUB chromosome, complete genome	CP070362.2
Acinetobacter baumannii strain Cl415 chromosome, complete genome	CP071763.1
Acinetobacter baumannii strain GIMC5510:ABT-897-17 chromosome 1	CP071919.1
Acinetobacter baumannii strain KSK1 chromosome, complete genome	CP072122.1
Acinetobacter baumannii strain KSK6 chromosome, complete genome	CP072270.1
Acinetobacter baumannii strain KSK7 chromosome, complete genome	CP072275.1
Acinetobacter baumannii strain KSK10 chromosome, complete genome	CP072280.1
Acinetobacter baumannii strain KSK11 chromosome, complete genome	CP072285.1
Acinetobacter baumannii strain KSK18 chromosome, complete genome	CP072290.1
Acinetobacter baumannii strain KSK19 chromosome, complete genome	CP072295.1
Acinetobacter baumannii strain KSK20 chromosome, complete genome	CP072300.1
Acinetobacter baumannii strain KSK Sensitive chromosome, complete genome	CP072305.1
Acinetobacter baumannii strain KSK2 chromosome, complete genome	CP072398.1

Acinetobacter baumannii strain DETAB-E227 chromosome, complete genome	CP072526.1
Acinetobacter baumannii strain DETAB-P39 chromosome, complete genome	CP073060.1
Acinetobacter baumannii strain ATCC 19606 chromosome, complete genome	CP074585.1
Acinetobacter baumannii strain ATCC 17978 chromosome, complete genome	CP074710.1
Acinetobacter baumannii strain DD520 chromosome, complete genome	CP075321.1
Acinetobacter baumannii strain UC25604 chromosome, complete genome	CP076801.1
Acinetobacter baumannii strain UC24371 chromosome, complete genome	CP076804.1
Acinetobacter baumannii strain UC20804 chromosome, complete genome	CP076807.1
Acinetobacter baumannii strain UC23022 chromosome, complete genome	CP076812.1
Acinetobacter baumannii strain UC21460 chromosome, complete genome	CP076814.1
Acinetobacter baumannii strain UC24137 chromosome, complete genome	CP076817.1
Acinetobacter baumannii strain UC22850 chromosome, complete genome	CP076821.1
Acinetobacter baumannii strain 40288 chromosome, complete genome	CP077801.1
Acinetobacter baumannii strain DETAB-E108 chromosome, complete genome	CP077826.1
Acinetobacter baumannii strain DETAB-E351 chromosome, complete genome	CP077828.1
Acinetobacter baumannii strain DETAB-E51 chromosome, complete genome	CP077830.1
Acinetobacter baumannii strain DETAB-P43 chromosome, complete genome	CP077832.1
Acinetobacter baumannii strain DETAB-P65 chromosome, complete genome	CP077835.1
Acinetobacter baumannii strain DETAB-E159 chromosome, complete genome	CP077837.1
Acinetobacter baumannii strain DETAB-P90 chromosome, complete genome	CP077840.1
Acinetobacter baumannii strain DETAB-E155 chromosome, complete genome	CP077843.1
Acinetobacter baumannii strain DETAB-P24 chromosome, complete genome	CP077846.1

Acinetobacter baumannii strain DETAB-P16 plasmid pDETAB15, complete sequence	CP077849.1
Acinetobacter baumannii strain CNRAB1 chromosome	CP078099.1
Acinetobacter baumannii strain Colony271 chromosome	CP078525.1
Acinetobacter baumannii strain Colony319 chromosome	CP078526.1
Acinetobacter baumannii strain Colony151 chromosome	CP078527.1
Acinetobacter baumannii strain Colony258 chromosome	CP078528.1
Acinetobacter baumannii strain Ab17978UN chromosome	CP079212.1
Acinetobacter baumannii strain Ab17978VU chromosome	CP079213.1
Acinetobacter baumannii strain 17978UN chromosome, complete genome	CP079931.1
Acinetobacter baumannii strain B10 chromosome, complete genome	CP079942.1
Acinetobacter baumannii strain K7-3RD chromosome	CP079945.1
Acinetobacter baumannii strain MRSN 56 chromosome, complete genome	CP080452.1
Acinetobacter baumannii strain ARLG_6420 chromosome, complete genome	CP081137.1
Acinetobacter baumannii strain ARLG_6344 chromosome, complete genome	CP081139.1
Acinetobacter baumannii strain ARLG_6295 chromosome, complete genome	CP081144.1
Acinetobacter baumannii strain Cl300 chromosome, complete genome	CP082952.1
Acinetobacter baumannii strain AB43 chromosome, complete genome	CP083181.1
Acinetobacter baumannii strain LHC22-2 chromosome, complete genome	CP084297.1
Acinetobacter baumannii strain HKU7 chromosome, complete genome	CP084721.1
Acinetobacter baumannii strain HKU6 chromosome, complete genome	CP084724.1
Acinetobacter baumannii strain HKU5 chromosome, complete genome	CP084727.1
Acinetobacter baumannii strain HKU4 chromosome, complete genome	CP084730.1
Acinetobacter baumannii strain HKU3 chromosome, complete genome	CP084733.1
Acinetobacter baumannii strain RCH52 chromosome, complete genome	CP085788.1
Acinetobacter baumannii strain ACI713 chromosome, complete genome	CP086759.1
Acinetobacter baumannii strain OC070 chromosome, complete genome	CP087298.1
Acinetobacter baumannii strain OC061 chromosome, complete genome	CP087300.1
Acinetobacter baumannii strain OC081 chromosome, complete genome	CP087304.1
Acinetobacter baumannii strain OC068 chromosome, complete genome	CP087309.1
Acinetobacter baumannii strain OC059 chromosome, complete genome	CP087312.1

Acinetobacter baumannii strain OC064 chromosome, complete genome	CP087317.1
Acinetobacter baumannii strain OC043 chromosome, complete genome	CP087321.1
Acinetobacter baumannii strain OC073 chromosome, complete genome	CP087325.1
Acinetobacter baumannii strain OC074 chromosome, complete genome	CP087328.1
Acinetobacter baumannii strain LMG994 chromosome, complete genome	CP087331.1
Acinetobacter baumannii strain DB053 chromosome, complete genome	CP087335.1
Acinetobacter baumannii strain DB008 chromosome, complete genome	CP087340.1
Acinetobacter baumannii strain DB007 chromosome, complete genome	CP087344.1
Acinetobacter baumannii strain DB006 chromosome, complete genome	CP087348.1
Acinetobacter baumannii strain DB003 chromosome, complete genome	CP087351.1
Acinetobacter baumannii strain DB002 chromosome, complete genome	CP087354.1
Acinetobacter baumannii strain OC041 chromosome	CP087357.1
Acinetobacter baumannii strain OC008 chromosome	CP087362.1
Acinetobacter baumannii strain DB005 chromosome	CP087365.1
Acinetobacter baumannii strain DB004 chromosome	CP087370.1
Acinetobacter baumannii strain DB001 chromosome	CP087374.1
Acinetobacter baumannii strain SHOU-Ab01 chromosome, complete genome	CP087594.1
Acinetobacter baumannii strain XH1935 chromosome, complete genome	CP088894.1
Acinetobacter baumannii strain DETAB-R21 chromosome, complete genome	CP088895.1
Acinetobacter baumannii strain AB1343 chromosome, complete genome	CP090182.1
Acinetobacter baumannii strain MRSN 56 chromosome, complete genome	CP090606.1
Acinetobacter baumannii strain MRSN 58 chromosome, complete genome	CP090607.1
Acinetobacter baumannii strain MRSN57 chromosome, complete genome	CP091172.1
Acinetobacter baumannii strain AB5116 chromosome, complete genome	CP091173.1
Acinetobacter baumannii strain BM2333 chromosome, complete genome	CP091328.1
Acinetobacter baumannii strain DSM30011-VUB chromosome, complete genome	CP091333.1
Acinetobacter baumannii strain ATCC19606-VUB chromosome, complete genome	CP091334.1
Acinetobacter baumannii strain ATCC17978-VUB chromosome, complete genome	CP091335.1

Acinetobacter baumannii strain AB233-VUB chromosome, complete genome	CP091336.1
Acinetobacter baumannii strain AB232-VUB chromosome, complete genome	CP091337.1
Acinetobacter baumannii strain AB231-VUB chromosome, complete genome	CP091338.1
Acinetobacter baumannii strain AB229-VUB chromosome, complete genome	CP091339.1
Acinetobacter baumannii strain AB227-VUB chromosome, complete genome	CP091340.1
Acinetobacter baumannii strain AB226-VUB chromosome, complete genome	CP091341.1
Acinetobacter baumannii strain AB224-VUB chromosome, complete genome	CP091342.1
Acinetobacter baumannii strain AB222-VUB chromosome, complete genome	CP091343.1
Acinetobacter baumannii strain AB220-VUB chromosome, complete genome	CP091344.1
Acinetobacter baumannii strain AB219-VUB chromosome, complete genome	CP091345.1
Acinetobacter baumannii strain AB217-VUB chromosome, complete genome	CP091346.1
Acinetobacter baumannii strain AB216-VUB chromosome, complete genome	CP091347.1
Acinetobacter baumannii strain AB214-VUB chromosome, complete genome	CP091348.1
Acinetobacter baumannii strain AB213-VUB chromosome, complete genome	CP091349.1
Acinetobacter baumannii strain AB212-VUB chromosome, complete genome	CP091350.1
Acinetobacter baumannii strain AB194-VUB chromosome, complete genome	CP091351.1
Acinetobacter baumannii strain AB193-VUB chromosome, complete genome	CP091352.1

Acinetobacter baumannii strain AB189-VUB chromosome, complete genome	CP091353.1
Acinetobacter baumannii strain AB188-VUB chromosome, complete genome	CP091354.1
Acinetobacter baumannii strain AB187-VUB chromosome, complete genome	CP091355.1
Acinetobacter baumannii strain AB186-VUB chromosome, complete genome	CP091356.1
Acinetobacter baumannii strain AB183-VUB chromosome, complete genome	CP091357.1
Acinetobacter baumannii strain AB181-VUB chromosome, complete genome	CP091358.1
Acinetobacter baumannii strain AB180-VUB chromosome, complete genome	CP091359.1
Acinetobacter baumannii strain AB179-VUB chromosome, complete genome	CP091360.1
Acinetobacter baumannii strain AB177-VUB chromosome, complete genome	CP091361.1
Acinetobacter baumannii strain AB176-VUB chromosome, complete genome	CP091362.1
Acinetobacter baumannii strain AB175-VUB chromosome, complete genome	CP091363.1
Acinetobacter baumannii strain AB173-VUB chromosome, complete genome	CP091364.1
Acinetobacter baumannii strain AB172-VUB chromosome, complete genome	CP091365.1
Acinetobacter baumannii strain AB171-VUB chromosome, complete genome	CP091366.1
Acinetobacter baumannii strain AB169-VUB chromosome, complete genome	CP091367.1
Acinetobacter baumannii strain AB167-VUB chromosome, complete genome	CP091368.1
Acinetobacter baumannii strain AB40-VUB chromosome, complete genome	CP091369.1
Acinetobacter baumannii strain AB39-VUB chromosome, complete genome	CP091370.1
Acinetobacter baumannii strain AB36-VUB chromosome, complete genome	CP091371.1

Acinetobacter baumannii strain AB32-VUB chromosome, complete genome	CP091372.1
Acinetobacter baumannii strain AB21-VUB chromosome, complete genome	CP091373.1
Acinetobacter baumannii strain AB20-VUB chromosome, complete genome	CP091374.1
Acinetobacter baumannii strain AB16-VUB chromosome, complete genome	CP091375.1
Acinetobacter baumannii strain AB14-VUB chromosome, complete genome	CP091376.1
Acinetobacter baumannii strain AB9-VUB chromosome, complete genome	CP091377.1
Acinetobacter baumannii strain AB3-VUB chromosome, complete genome	CP091378.1
Acinetobacter baumannii strain AB329 chromosome, complete genome	CP091452.1
Acinetobacter baumannii strain NCCP 16007 chromosome, complete genome	CP091465.1
Acinetobacter baumannii strain Nord4-2 chromosome, complete genome	CP091596.1
Acinetobacter baumannii strain AB2877 chromosome, complete genome	CP092485.1
Acinetobacter baumannii strain NY5301 chromosome, complete genome	CP094283.1
Acinetobacter baumannii strain AB4451 chromosome, complete genome	CP095091.1
Acinetobacter baumannii strain Z1 chromosome	CP095784.1
Acinetobacter baumannii strain F46 chromosome, complete genome	CP096575.1
Acinetobacter baumannii strain 6080 chromosome, complete genome	CP096681.1
Acinetobacter baumannii strain 5955 chromosome, complete genome	CP096682.1
Acinetobacter baumannii strain 5847 chromosome, complete genome	CP096684.1
Acinetobacter baumannii strain 5846 chromosome, complete genome	CP096686.1
Acinetobacter baumannii strain 5840 chromosome, complete genome	CP096688.1
Acinetobacter baumannii strain 5839 chromosome, complete genome	CP096690.1
Acinetobacter baumannii strain 5779 chromosome, complete genome	CP096692.1
Acinetobacter baumannii strain 5773 chromosome, complete genome	CP096693.1
Acinetobacter baumannii strain 5771 chromosome, complete genome	CP096696.1
Acinetobacter baumannii strain 5769 chromosome, complete genome	CP096698.1
Acinetobacter baumannii strain 5768 chromosome, complete genome	CP096700.1
Acinetobacter baumannii strain 5767 chromosome, complete genome	CP096702.1
Acinetobacter baumannii strain 5765 chromosome, complete genome	CP096704.1
Acinetobacter baumannii strain 5761 chromosome, complete genome	CP096705.1
Acinetobacter baumannii strain 5760 chromosome, complete genome	CP096707.1
Acinetobacter baumannii strain 5759 chromosome, complete genome	CP096710.1
Acinetobacter baumannii strain 5745 chromosome, complete genome	CP096714.1
Acinetobacter baumannii strain 5741 chromosome, complete genome	CP096717.1

Acinetobacter baumannii strain 5740 chromosome, complete genome	CP096720.1
Acinetobacter baumannii strain 5736 chromosome, complete genome	CP096722.1
Acinetobacter baumannii strain 5734 chromosome, complete genome	CP096724.1
Acinetobacter baumannii strain 5732 chromosome, complete genome	CP096727.1
Acinetobacter baumannii strain 5729 chromosome, complete genome	CP096729.1
Acinetobacter baumannii strain 5689 chromosome, complete genome	CP096731.1
Acinetobacter baumannii strain 5685 chromosome, complete genome	CP096734.1
Acinetobacter baumannii strain 5683 chromosome, complete genome	CP096735.1
Acinetobacter baumannii strain 5679 chromosome, complete genome	CP096738.1
Acinetobacter baumannii strain 5672 chromosome, complete genome	CP096740.1
Acinetobacter baumannii strain 5671 chromosome, complete genome	CP096742.1
Acinetobacter baumannii strain 5670 chromosome, complete genome	CP096745.1
Acinetobacter baumannii strain 5669 chromosome, complete genome	CP096747.1
Acinetobacter baumannii strain 5666 chromosome, complete genome	CP096749.1
Acinetobacter baumannii strain 5664 chromosome, complete genome	CP096753.1
Acinetobacter baumannii strain 5663 chromosome, complete genome	CP096755.1
Acinetobacter baumannii strain 5656 chromosome, complete genome	CP096757.1
Acinetobacter baumannii strain 5653 chromosome, complete genome	CP096759.1
Acinetobacter baumannii strain 5651 chromosome, complete genome	CP096762.1
Acinetobacter baumannii strain 5634 chromosome, complete genome	CP096764.1
Acinetobacter baumannii strain 5626 chromosome, complete genome	CP096766.1
Acinetobacter baumannii strain 5388 chromosome, complete genome	CP096768.1
Acinetobacter baumannii strain XH1820 chromosome, complete genome	CP096892.1
Acinetobacter baumannii strain R4-1 chromosome, complete genome	CP097875.1
Acinetobacter baumannii strain R6-1 chromosome, complete genome	CP097878.1
Acinetobacter baumannii strain Cl107 chromosome, complete genome	CP098521.1
Acinetobacter baumannii strain 280820 chromosome, complete genome	CP098791.1
Acinetobacter baumannii strain VB280821 chromosome, complete genome	CP098795.1
Acinetobacter baumannii strain NCCP 15989 chromosome, complete genome	CP099784.1
Acinetobacter baumannii strain NCCP 15992 chromosome, complete genome	CP099786.1
Acinetobacter baumannii strain NCCP 15995 chromosome, complete genome	CP099788.1

Acinetobacter baumannii strain NCCP 15996 chromosome, complete genome	CP099790.1
Acinetobacter baumannii strain NCCP 16006 chromosome, complete genome	CP099793.1
Acinetobacter baumannii strain NCCP 16011 chromosome, complete genome	CP099795.1
Acinetobacter baumannii strain 17978R chromosome, complete genome	CP099855.1
Acinetobacter baumannii strain 17978S chromosome, complete genome	CP099856.1
Acinetobacter baumannii strain A54R chromosome, complete genome	CP099857.1
Acinetobacter baumannii strain A54S chromosome, complete genome	CP099858.1
Acinetobacter baumannii strain F-1629 chromosome, complete genome	CP099969.1
Acinetobacter baumannii strain KBN10P04593 chromosome, complete genome	CP099989.1
Acinetobacter baumannii strain KBN10P05679 chromosome, complete genome	CP100305.1
Acinetobacter baumannii strain CCBH31270 chromosome	CP101887.1
Acinetobacter baumannii strain CCBH31258 chromosome, complete genome	CP101889.1
Acinetobacter baumannii strain AB3927 chromosome, complete genome	CP102831.1
Acinetobacter baumannii strain AB105 chromosome, complete genome	CP103338.1
Acinetobacter baumannii strain AB2369 chromosome, complete genome	CP103413.1
Acinetobacter baumannii strain 2021CK-01408 chromosome, complete genome	CP104335.1
Acinetobacter baumannii strain 2021CK-01409 chromosome, complete genome	CP104340.1
Acinetobacter baumannii strain 2021CK-01300 chromosome, complete genome	CP104342.1
Acinetobacter baumannii strain 2021CK-01332 chromosome, complete genome	CP104347.1
Acinetobacter baumannii strain 2021CK-01333 chromosome, complete genome	CP104350.1
Acinetobacter baumannii strain 2021CK-01335 chromosome, complete genome	CP104351.1
Acinetobacter baumannii strain 2021CK-01407 plasmid unnamed1, complete sequence	CP104448.1

Acinetobacter baumannii strain 37662 chromosome, complete genome	CP104751.1
Acinetobacter baumannii strain Ab-3556 chromosome, complete genome	CP104786.1
Acinetobacter baumannii strain Ab-3557 chromosome, complete genome	CP104907.1
Acinetobacter baumannii strain YZM-0314 chromosome, complete genome	CP104908.1
Acinetobacter baumannii strain YZM-0406 chromosome, complete genome	CP104912.1
Acinetobacter baumannii strain ARC6851 chromosome, complete genome	CP106943.1
Acinetobacter baumannii strain NY13623 chromosome, complete genome	CP106988.1
Acinetobacter baumannii strain GIMC5507:ABT-52Ts18 chromosome	CP107032.1
Acinetobacter baumannii strain GIMC5509:ABT-52Ts19 chromosome	CP107034.1
Acinetobacter baumannii strain 1326359 chromosome, complete genome	CP107577.1
Acinetobacter baumannii strain 1326525-1 chromosome, complete genome	CP107579.1
Acinetobacter baumannii strain 1326525-2 chromosome, complete genome	CP107581.1
Acinetobacter baumannii strain 1326525-3 chromosome, complete genome	CP107583.1
Acinetobacter baumannii strain 1326527-1 chromosome, complete genome	CP107585.1
Acinetobacter baumannii strain 1326527-2 chromosome, complete genome	CP107587.1
Acinetobacter baumannii strain 1326569 chromosome, complete genome	CP107590.1
Acinetobacter baumannii strain 1326580 chromosome, complete genome	CP107593.1
Acinetobacter baumannii strain 1326581-1 chromosome, complete genome	CP107595.1
Acinetobacter baumannii strain 1326581-2 chromosome, complete genome	CP107597.1
Acinetobacter baumannii strain 1326584 chromosome, complete genome	CP107599.1
Acinetobacter baumannii strain 1326589 chromosome, complete genome	CP107601.1
Acinetobacter baumannii strain 1326595 chromosome, complete genome	CP107603.1
Acinetobacter baumannii strain 1326924-1 chromosome, complete genome	CP107605.1
Acinetobacter baumannii strain 1326924-2 chromosome, complete genome	CP107608.1
Acinetobacter baumannii strain 1326924-3 chromosome, complete genome	CP107610.1
Acinetobacter baumannii strain 1326927-1 chromosome, complete genome	CP107612.1
Acinetobacter baumannii strain 1326927-2 chromosome, complete genome	CP107614.1
Acinetobacter baumannii strain 1326932 chromosome, complete genome	CP107616.1
Acinetobacter baumannii strain AB44 chromosome, complete genome	CP107728.1
Acinetobacter baumannii strain Z198 chromosome, complete genome	CP109836.1
Acinetobacter baumannii strain RBH2 chromosome, complete genome	CP110462.1
Acinetobacter baumannii str. AYE, complete genome	CU459141.1
Acinetobacter baumannii SDF, complete genome	CU468230.2

Acinetobacter baumannii strain SGH0701 genomic resistance island AbGRI3 genomic sequence	KX011025.2
Acinetobacter baumannii strain SGH1111 genomic resistance island AbGRI3 genomic sequence	KX011027.1
Acinetobacter baumannii strain IHIT7853 plasmid IHIT7853-OXA-23, complete sequence	KX118105.1
Acinetobacter baumannii genome assembly CIP70.10, chromosome : I	LN865143.1
Acinetobacter baumannii genome assembly R2090, chromosome : I	LN868200.1
Acinetobacter baumannii genome assembly R2091, chromosome : I	LN997846.1
Acinetobacter baumannii strain NCTC13421 genome assembly, chromosome: 1	LS483472.1
Acinetobacter baumannii strain BAL062 genome assembly, chromosome: 1	LT594095.1
Acinetobacter baumannii strain NCTC7364 genome assembly, chromosome: 1	LT605059.1

APPENDIX B

APPENDIX B

Table B1. List of primer sequences used for qRT-PCR.

Gene	**Primers**	**Primer Sequence (5' – 3')**
16s rRNA	Forward Primer	GTGCGTAGGCGGCTTATTA
	Reverse Primer	TCTACCATCCTCTCCCATACTC
Hfq full-length	Forward Primer	AGCTCAGGGTGGTAGTCA
	Reverse Primer	CCACCTTGACCACCGAAG
ΔCTD	Forward Primer	TCTCCGTAAAGAACGCATCC
	Reverse Primer	TGCGTGTTTGTAAACCATTTGA
GRP	Forward Primer	GGTGGTCAAGGTGGCTT
	Reverse Primer	CCTTGATGTCCGCCGAA

Table B2. Structural details of hfq constructs used in qRT-PCR assay.

Construct	**Coding Sequence (CDS)**	**C-terminal Domain**
Hfq full-length	Complete CDS	Included
ΔCTD	CTR truncated	Absent
GRP	Glycine-rich domain only	Only

Table B3. Table depicting the values of thermodynamic parameters obtained through Isothermal Titration Calorimetry (ITC) Analysis of the hfq and mutant sequences with BRACO-19.

Parameters	**hfq_RNA**	***truncated* hfq_RNA**	**hfq_DNA**	***truncated* hfq_DNA**	**Mutant RNA**	**Mutant DNA**	***truncated* Mutant RNA**	***truncated* Mutant DNA**
K_d1 (μM)	0.004	0.870	5.435	0.581	62.893	273.973	518.135	75.188
K_d2 (μM)	10.235	6.803	43.668	4.255	12.578	235.294	0.826	38.760
ΔG1 (cal/mol)	-5.550	-6.051	-5.178	-78.840	7.265×10^6	1.002×10^4	1.577×10^5	0.449
ΔG2 (cal/mol)	-0.112	-2.651	61.210	1.389	-3.838×10^6	-312.850	-65.935	-4.275×10^3
ΔS1 (cal/mol/°C)	21.900	8.140	7.340	-258.000	2.660×10^4	3.670×10^4	5.770×10^5	22.200
ΔS2 (cal/mol/°C)	24.500	30.000	246.000	31.900	-1.40×10^4	-1.130×10^3	-211.000	-1.560×10^4
ΔH1 (cal/mol)	-5.002×10^3	-5.847×10^3	-4.994×10^3	-8.529×10^4	7.930×10^6	1.094×10^7	1.722×10^8	1.004×10^3
ΔH2 (cal/mol)	500.500	-1.901×10^3	6.736×10^4	2.186×10^3	-4.188×10^6	-3.411×10^5	-7.121×10^4	-4.665×10^6

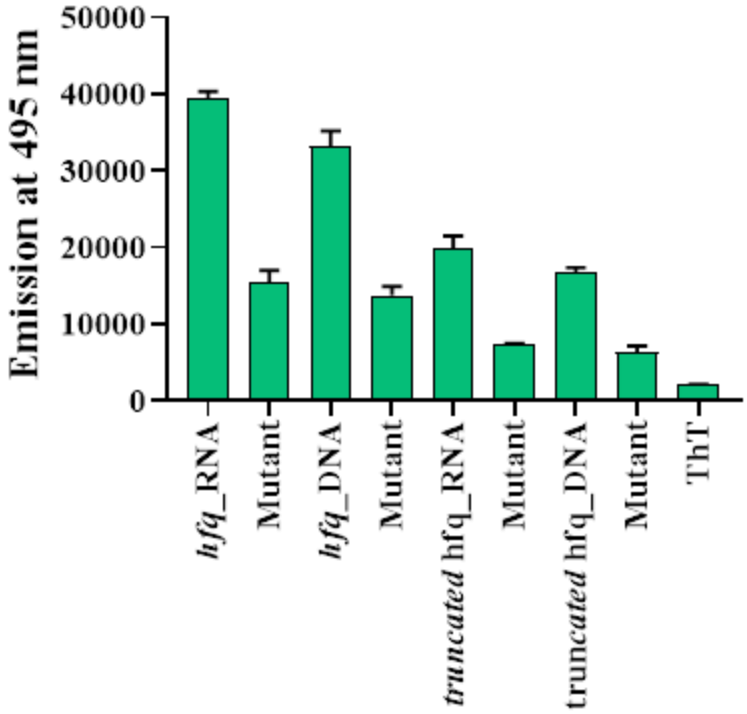

Figure B.1. The fluorescence enhancement of Thioflavin T (ThT) upon the addition of hfq G4 sequences with respect to (w.r.t.) respective mutants and ThT alone.

APPENDIX C

APPENDIX C

Table C1. List of template and primer sequences used for PCR amplification of JEV-PGQs.

Gene	Primers	Primer Sequence (5' – 3')	Template Sequences (5' – 3')
Env_1	Forward	GGCCGGATCCTAATACGACTCAC	GGCCGGATCCTAATACGACTCACTATAGCTCTTGGGTCACAGGAAGGAGGCCTCCA
	Reverse	TGGAGGCCTCCTTCCTGTGAC	
Env_2	Forward	GGCCGGATCCTAATACGACTCAC	GGCCGGATCCTAATACGACTCACTATAGAGCCTGGGACTTTGGCTCCATTGGAGGGGTCTTC
	Reverse	GAAGACCCCTCCAATGGAGCCA	
NS3_1	Forward	GAGATCTCTAATACGACTCAC	GAGATCTCTAATACGACTCACTATAGACCAAGGTGGAATTAGGGGAGGCAGCAAA
	Reverse	TTTGCTGCCTCCCCTAATT	
NS3_2	Forward	GAGATCTCTAATACGACTCAC	GAGATCTCTAATACGACTCACTATAGGCACTGGTTATGGGAGATGGGTTTCCAAGGATGAC
	Reverse	GTCATCCTTGGAAACCCATC	
NS3_3	Forward	GGCCGGATCCTAATACGACTCAC	GGCCGGATCCTAATACGACTCACTATAGAGTCAGGAAAAGGATCCGTGGTTCCAGGCGGGG
	Reverse	CCCCGCCTGGAACCACGGAT	
NS5_1	Forward	GGCCGGATCCTAATACGACTCAC	GGCCGGATCCTAATACGACTCACTATAGGAAAAGGGGAAGGCCCGGGGGCAGGACGCTAAAA
	Reverse	TTTTAGCGTCCTGCCCCCGG	
NS5_2	Forward	GGCCGGATCCTAATACGACTCAC	GGCCGGATCCTAATACGACTCACTATAGGTATTGGGTTAGTGGAGCCGCTGGCAATGTGGTGCAC
	Reverse	GTGCACCACATTGCCAGCGG	
NS5_3	Forward	GAGATCTCTAATACGACTCAC	GAGATCTCTAATACGACTCACTATAGCTAAAGGAAGCAGGGCCATTTGGTTCATGTGGCTTGG
	Reverse	CCAAGCCACATGAACCAAAT	

Table C2. List of primer sequences used for mTFP reporter assay.

Sequence Name	**Primers**	**Primer Sequence (5' – 3')**
JEV-PGQ-Env_2-mTFP	Forward	ATGAGTGAATTCATGCCTGGGACTTTGGCTCCATTGGAGGGGTCTGTGAGCAAGG
	Reverse	CGTCTCGAGCTTGTACAGCTCGTCCATGCC
JEV-PGQ-NS3_2-mTFP	Forward	ATGAGTGAATTCATGACTGGTTATGGGAGATGGGTTTCCAAGGATGGTGAGCAAGG
	Reverse	CGTCTCGAGCTTGTACAGCTCGTCCATGCC
JEV-PGQ-NS5_1-mTFP	Forward	ATGAGTGAATTCATGAAAGGGGAAGGCCCGGGGGCAGGACGGTGAGCAAGG
	Reverse	CGTCTCGAGCTTGTACAGCTCGTCCATGCC
JEV-PGQ-Mut-mTFP	Forward	ATGAGTGAATTCATGCCTTCTACTTTCTCTCCATTTCACTTCTCTGTGAGCAAGG
	Reverse	CGTCTCGAGCTTGTACAGCTCGTCCATGCC

Table C3. List of primer sequences used for qRT-PCR.

Gene	**Primers**	**Primer Sequence (5' – 3')**
JEV	Forward Primer	AGAGCACCAAGGGAATGAAATAGT
	Reverse Primer	AATAAGTTGTAGTTGGGCACTCTG'
GAPDH	Forward Primer	CGTCCCGTAGACAAAATGGT
	Reverse Primer	TTGATGGCAACAATCTCCAC

Table C4. Table displaying the ΔTm values of JEV-PGQs in the BRACO-19 through CD Melting experiment performed in 100 mM K+ containing potassium phosphate buffer.

	Env_1	**Env_2**	**NS3_1**	**NS3_2**	**NS3_3**	**NS5_1**	**NS5_2**	**NS5_3**
ΔT_m	4.2 °C	2.1 °C	8.4 °C	16.8 °C	2.8 °C	11.2 °C	9.7 °C	16.8 °C

Table C5. Table displaying the ΔTm values of JEV-PGQs in the BRACO-19 through CD Melting experiment performed in 25 mM K+ containing potassium phosphate buffer.

	Env_1	**Env_2**	**NS3_1**	**NS3_2**	**NS3_3**	**NS5_1**	**NS5_2**	**NS5_3**
ΔT_m	4.2 °C	2.1 °C	6.2 °C	3.5 °C	2.2 °C	N.D.	2.0 °C	5.5 °C

Table C6. Table depicting the equilibrium dissociation constant (K_d) values of the JEV-PGQs and mutant with BRACO-19 obtained through Fluorescence titration assay.

	Env_1	**Env_2**	**NS3_1**	**NS3_2**	**NS3_3**	**NS5_1**	**NS5_2**	**NS5_3**	**Mutant**
K_{d1} **(μM)**	0.099	2.042	0.045	0.217	5.606	0.0776	0.040	10.178	212.7
K_{d2} **(μM)**	15.107	2.042	4.537	12.393	5.606	4.2669	3.660	10.178	212.1

Table C7. Table depicting the values of thermodynamic parameters obtained through Isothermal Titration Calorimetry Analysis of the JEV-PGQs and Mutant with BRACO-19.

Parameters	Env_2	NS3_2	NS5_1	Mutant
K_{d1} (µM)	0.058	0.008	0.045	28.08
K_{d2} (µM)	85.47	35.7	26.45	99.00
ΔG1(kJ/mol)	-22.79	-42.23	-38.87	162.35
ΔG2(kJ/mol)	-164.75	-70.3	-55.57	-154.275
ΔS1 (joules/mol/deg)	67.6	14.8	10.8	690
ΔS2 (joules/mol/deg)	-518	-164	-108	-481
ΔH1 (joules/mol)	-2.11×10^4	-4.186×10^4	-3.86×10^4	17.96×10^4
ΔH2 (joules/mol)	-17.77×10^4	-7.44×10^4	-5.827×10^4	-16.63×10^4

Table C8. List of Japanese Encephalitis Virus isolates taken into consideration for PGQ prediction analysis.

Strain	Accession ID
Japanese encephalitis virus genomic RNA, complete genome, clone:JEV-AT38	AB196923.1_AS
Japanese encephalitis virus genomic RNA, complete genome, clone:JEV-at229	AB196924.1_AS
Japanese encephalitis virus genomic RNA, complete genome, clone:JEV-rAT	AB196925.1_AS
Japanese encephalitis virus genomic RNA, complete genome, clone:JEV-AT38	AB196926.1_AS
Japanese encephalitis virus RNA, complete genome, strain: JaTAn1/102	AB551991.1_AS
Japanese encephalitis virus RNA, complete genome, strain: JaTAn1/103	AB551991.1_AS
Japanese encephalitis virus RNA, complete genome, strain: JaTAn2/103	AB551992.1_AS
Japanese encephalitis virus RNA, complete genome, strain: JaTAn2/104	AB551992.1_AS
Japanese encephalitis virus JaGAr 01 complete genome	AF069076.1_AS
Japanese encephalitis virus isolate Vellore P20778, complete genome	AF080251.1_AS
Japanese encephalitis virus strain HVI, complete genome	AF098735.1_AS
Japanese encephalitis virus strain TC, complete genome	AF098736.1_AS
Japanese encephalitis virus strain TL, complete genome	AF098737.1_AS
Japanese encephalitis virus isolate CH2195LA, complete genome	AF221499.1_AS

Japanese encephalitis virus isolate CH2195SA, complete genome	AF221500.1_AS
Japanese encephalitis virus strain CH1392 complete genome	AF254452.1_AS
Japanese encephalitis virus strain T1P1 complete genome	AF254453.1_AS
Japanese encephalitis virus strain SA14-14-2, complete genome	AF315119.1_AS
Japanese encephalitis virus attenuated strain SA14-12-1-7, complete genome	AF416457.1_AS
Japanese encephalitis virus strain T1P1-S1, complete genome	AY303791.1_AS
Japanese encephalitis virus strain T1P1-L4, complete genome	AY303792.1_AS
Japanese encephalitis virus strain CJN-S1, complete genome	AY303793.1_AS
Japanese encephalitis virus strain CJN-L1, complete genome	AY303794.1_AS
Japanese encephalitis virus strain ML17 (live vaccine)/Japan/1981/human, complete genome	AY508812.1_AS
Japanese encephalitis virus strain JaOH0566/Japan/1966/human, complete genome	AY508813.1_AS
Japanese encephalitis virus strain HW, complete genome	AY849939.1_AS
Japanese encephalitis virus strain SA(V) genomic RNA, complete genome	D90194.1_AS
Japanese encephalitis virus strain SA(A) genomic RNA, complete genome	D90195.1_AS
Japanese encephalitis virus strain WHe, complete genome	EF107523.1_AS
Japanese encephalitis virus strain Nakayama, complete genome	EF571853.1_AS
Japanese encephalitis virus strain B58, complete genome	FJ185036.1_AS
Japanese encephalitis virus strain GB30, complete genome	FJ185037.1_AS
Japanese encephalitis virus strain NJ 2008, complete genome	GQ918133.2_AS
Japanese encephalitis virus complete genome, genomic RNA, strain Nakayama/MY/2009/P578669	HE861351.1_AS
Japanese encephalitis virus isolate DL04-29, complete genome	JF706272.1_AS
Japanese encephalitis virus isolate Fj02-29, complete genome	JF706273.1_AS
Japanese encephalitis virus isolate GSS, complete genome	JF706275.1_AS
Japanese encephalitis virus isolate HLJ02-134, complete genome	JF706276.1_AS
Japanese encephalitis virus isolate ZMT, complete genome	JF706283.1_AS
Japanese encephalitis virus isolate HB49, complete genome	JF706284.1_AS
Japanese encephalitis virus isolate HB97, complete genome	JF706285.1_AS
Japanese encephalitis virus isolate HYZ, complete genome	JN381853.1_AS
Japanese encephalitis virus isolate DL0445, complete genome	JN381854.1_AS
Japanese encephalitis virus isolate JH0418, complete genome	JN381855.1_AS

Japanese encephalitis virus isolate SH0410, complete genome	JN381856.1 _AS
Japanese encephalitis virus isolate GZ042, complete genome	JN381857.1_AS
Japanese encephalitis virus isolate FJ0394, complete genome	JN381858.1_AS
Japanese encephalitis virus isolate FJ0339, complete genome	JN381859.1_AS
Japanese encephalitis virus isolate CBH, complete genome	JN381860.1_AS
Japanese encephalitis virus isolate YN98A151, complete genome	JN381861.1_AS
Japanese encephalitis virus isolate ZSZ, complete genome	JN381862.1_AS
Japanese encephalitis virus isolate SH3, complete genome	JN381864.1_AS
Japanese encephalitis virus isolate SH045, complete genome	JN381866.1_AS
Japanese encephalitis virus isolate Fj0276, complete genome	JN381867.1_AS
Japanese encephalitis virus isolate CH13, complete genome	JN381870.1_AS
Japanese encephalitis virus isolate YN, complete genome	JN381871.1_AS
Japanese encephalitis virus isolate DH107, complete genome	JN381873.1_AS
Japanese encephalitis virus strain SA14-14-2, complete genome	JN604986.1_AS
Japanese encephalitis virus strain GD, complete genome	JN711458.1_AS
Japanese encephalitis virus strain HN2, complete genome	JN711459.1_AS
Japanese encephalitis virus strain YUNNAN0901, complete genome	JN864064.1_AS
Japanese encephalitis virus strain YUNNAN0901, complete genome	JQ086762.1_AS
Japanese encephalitis virus strain YUNNAN0902, complete genome	JQ086763.1_AS
Japanese encephalitis virus isolate IND-WB-JE1, complete genome	JX050179.1_AS
Japanese encephalitis virus isolate IND-WB-JE2, complete genome	JX072965.1_AS
Japanese encephalitis virus isolate JEV/eq/India/H225/2009, complete genome	JX131374.1_AS
Japanese encephalitis virus strain JE/vaccine/China/Chengdu-Institute-of-Biological-Products-SA14-14-2, complete genome	KC517497.1_AS
Japanese encephalitis virus isolate JEV/SW/GD/01/2009, complete genome	KF297915.1_AS
Japanese encephalitis virus strain RP9-190, complete genome	KF907505.1_AS
Japanese encephalitis virus isolate JEV-hubei, complete genome	KR265316.1_AS
Japanese encephalitis virus isolate Vellore P20778-T, complete genome	KT239164.1_AS
Japanese encephalitis virus strain Anyang-300, complete genome	KT447437.1_AS
Japanese encephalitis virus strain SA14, complete genome	KU323483.1_AS
Japanese encephalitis virus strain SC201301, complete genome	KU363309.1_AS
Japanese encephalitis virus isolate SA-14_CP8, complete genome	KU871338.1_AS
Japanese encephalitis virus isolate SA14_CP12, complete genome	KU871339.1_AS
Japanese encephalitis virus isolate SA-14_CP16, complete genome	KU871340.1_AS

Japanese encephalitis virus isolate SA-14_CP20, complete genome	KU871341.1_AS
Japanese encephalitis virus isolate SA-14_CP24, complete genome	KU871342.1_AS
Japanese encephalitis virus isolate SA-14_CP28_, complete genome	KU871343.1_AS
Japanese encephalitis virus isolate BJ-1_M2R2, complete genome	KU871344.1_AS
Japanese encephalitis virus isolate BJ-1_M14R14, complete genome	KU871345.1_AS
Japanese encephalitis virus isolate BJ-1_M4R4, complete genome	KU871346.1_AS
Japanese encephalitis virus isolate BJ-1_M12R12, complete genome	KU871347.1_AS
Japanese encephalitis virus isolate BJ-1_M10R10, complete genome	KU871348.1_AS
Japanese encephalitis virus isolate BJ-1_M8R8, complete genome	KU871349.1_AS
Japanese encephalitis virus isolate BJ-1_M6R6, complete genome	KU871350.1_AS
Japanese encephalitis virus isolate BJ-1__BCP8, complete genome	KU871351.1_AS
Japanese encephalitis virus isolate BJ-1__BCP12_OFR, complete genome	KU871352.1_AS
Japanese encephalitis virus isolate BJ-1_BCP28, complete genome	KU871353.1_AS
Japanese encephalitis virus isolate BJ-1__BCP16, complete genome	KU871354.1_AS
Japanese encephalitis virus isolate BJ-1_BCP24, complete genome	KU871355.1_AS
Japanese encephalitis virus isolate BJ-1_BCP4, complete genome	KU871356.1_AS
Japanese encephalitis virus isolate BJ-1_BCP20, complete genome	KU871357.1_AS
Japanese encephalitis virus isolate BJ-1_CP4, complete genome	KU871358.1_AS
Japanese encephalitis virus isolate BJ-1_CP28, complete genome	KU871359.1_AS
Japanese encephalitis virus isolate BJ-1_CP8, complete genome	KU871360.1_AS
Japanese encephalitis virus isolate BJ-1_CP12, complete genome	KU871361.1_AS
Japanese encephalitis virus isolate BJ-1_CP16, complete genome	KU871362.1_AS
Japanese encephalitis virus isolate BJ-1_CP20, complete genome	KU871363.1_AS
Japanese encephalitis virus isolate BJ-1_CP24, complete genome	KU871364.1_AS
Japanese encephalitis virus isolate BJ-1_BP4, complete genome	KU871365.1_AS
Japanese encephalitis virus isolate BJ-1_BP8, complete genome	KU871366.1_AS
Japanese encephalitis virus isolate BJ-1_BP12, complete genome	KU871367.1_AS
Japanese encephalitis virus isolate BJ-1_BP16, complete genome	KU871368.1_AS
Japanese encephalitis virus isolate BJ-1_BP20, complete genome	KU871369.1_AS
Japanese encephalitis virus isolate BJ-1_BP24, complete genome	KU871370.1_AS
Japanese encephalitis virus isolate BJ-1_BP28, complete genome	KU871371.1_AS
Japanese encephalitis virus isolate JEV/SC/2016-2, complete genome	KX779520.1_AS
Japanese encephalitis virus isolate JEV/SC/2016-1, complete genome	KX779521.1_AS
Japanese encephalitis virus isolate JEV/SC/2016-3, complete genome	KX779522.1_AS
Japanese encephalitis virus isolate C17, complete genome	KX945367.1_AS

Japanese encephalitis virus isolate JEV/sw/GD/2008, complete genome	KX965684.1_AS
Japanese encephalitis virus Bo/Kochi/211/2018 RNA, complete genome	LC705012.1 _AS
Japanese encephalitis virus (strain JaOArS982), complete genome	M18370.1_AS
Japanese encephalitis SA-14 virus, complete genome	M55506.1_AS
Japanese encephalitis virus isolate FC792, complete genome	MF002373.1_AS
Japanese encephalitis virus strain JEV/sw/GD/2008, complete genome	MF326270.1_AS
Japanese encephalitis virus isolate SA14, complete genome	MH258848.1_AS
Japanese encephalitis virus isolate SA14-14-2 MSV, complete genome	MH258849.1_AS
Japanese encephalitis virus isolate SA14-14-2-PHK17, complete genome	MH258850.1_AS
Japanese encephalitis virus isolate SA14-14-2 PSV, complete genome	MH258851.1_AS
Japanese encephalitis virus isolate SA14-14-2, complete genome	MH258852.1_AS
Japanese encephalitis virus isolate SA14-14-2 WSV, complete genome	MH258853.1_AS
Japanese encephalitis virus strain N28, complete genome	MH753126.1_AS
Japanese encephalitis virus strain SH1, complete genome	MH753128.1_AS
Japanese encephalitis virus strain SH15, complete genome	MH753130.1_AS
Japanese encephalitis virus strain SH19, complete genome	MH753131.1_AS
Japanese encephalitis virus strain SH18, complete genome	MH753132.1_AS
Japanese encephalitis virus strain SA14-14-2, complete genome	MK585066.1_AS
Japanese encephalitis virus isolate JEV1805M, complete genome	MN639770.1_AS
Japanese encephalitis virus isolate SA14 clone TJE302, complete genome	MT764727.1_AS
Japanese encephalitis virus strain SA14-14-2 vaccine clone JE697, complete genome	MT764728.1_AS
Japanese encephalitis virus strain SA14-5-3 clone TJE565, complete genome	MT764729.1_AS
Japanese encephalitis virus strain SA14-2-8 clone TJE2330, complete genome	MT764730.1_AS
Japanese encephalitis virus strain SA14 clone TJE2350, complete genome	MT764731.1_AS
Japanese encephalitis virus strain SA14-4-2 clone TJE2359, complete genome	MT764732.1_AS
Japanese encephalitis virus strain SA14-2-8 clone TJE2365, complete genome	MT764733.1_AS
Japanese encephalitis virus, genome	NC_001437.1_AS
Japanese encephalitis virus strain Vellore P20778, complete genome	OK257213.1_AS

Japanese encephalitis virus strain Vellore P20779, complete genome	OK257214.1_AS
Japanese encephalitis virus strain Vellore P20780, complete genome	OK257215.1_AS
Japanese encephalitis virus strain p3, complete genome	U47032.1_AS
Japanese encephalitis virus FU strain, complete genome	AF217620.1_AS
Japanese encephalitis virus isolate LN0716, complete genome	JN381849.1_AS
Japanese encephalitis virus strain DH10M865, complete genome	KT229572.1_AS
Japanese encephalitis virus strain YNTC07172, complete genome	KT957419.1_AS
Japanese encephalitis virus strain JEV/mosq/YN/2016, complete genome	MH385014.1_AS
Japanese encephalitis virus isolate JEV_ASSAM_03, complete genome	MZ702743.1_AS
Japanese encephalitis virus isolate LFM, complete genome	JN381863.1_AS
Japanese encephalitis virus isolate CZX, complete genome	JN381865.1_AS
Japanese encephalitis virus isolate TLA, complete genome	JN381868.1_AS
Japanese encephalitis virus strain Beijing-015, complete genome	KY885009.1_AS
Japanese encephalitis virus (strain Beijing-1), complete genome	L48961.1_AS
Japanese encephalitis virus JEV/sw/Bali/93/2017 RNA, complete genome	LC461961.1_AS
Japanese encephalitis virus isolate YLG, complete genome	JF706280.1_AS
Japanese encephalitis virus strain GP78, complete genome	AF075723.1
Japanese encephalitis virus isolate 014178, complete genome	EF623987.1
Japanese encephalitis virus isolate 057434, complete genome	EF623988.1
Japanese encephalitis virus isolate 04940-4, complete genome	EF623989.1
Japanese encephalitis virus isolate 04940-4, complete genome	EF623989.1
Japanese encephalitis virus strain KPP82-39-214CT, complete genome	GQ902063.1
Japanese encephalitis virus isolate IGIB-NIV-2009-01, complete genome	JN644310.1_AS
Japanese encephalitis virus genomic RNA, complete genome, clone:JEV-AT36	AB196923.1
Japanese encephalitis virus genomic RNA, complete genome, clone:JEV-at227	AB196924.1
Japanese encephalitis virus genomic RNA, complete genome, clone:JEV-rAT	AB196925.1
Japanese encephalitis virus genomic RNA, complete genome, clone:JEV-AT36	AB196926.1
AF045551.2 Japanese encephalitis virus strain K94P05, complete genome	AF045551.2

Japanese encephalitis virus JaGAr 01 complete genome	AF069076.1
Japanese encephalitis virus isolate Vellore P20778, complete genome	AF080251.1
Japanese encephalitis virus strain HVI, complete genome	AF098735.1
Japanese encephalitis virus strain TC, complete genome	AF098736.1
Japanese encephalitis virus strain TL, complete genome	AF098737.1
Japanese encephalitis virus isolate CH2195LA, complete genome	AF221499.1
Japanese encephalitis virus isolate CH2195SA, complete genome	AF221500.1
Japanese encephalitis virus strain CH1392 complete genome	AF254452.1
Japanese encephalitis virus strain T1P1 complete genome	AF254453.1
Japanese encephalitis virus strain SA14-14-2, complete genome	AF315119.1
Japanese encephalitis virus attenuated strain SA14-12-1-7, complete genome	AF416457.1
Japanese encephalitis virus strain T1P1-S1, complete genome	AY303791.1
Japanese encephalitis virus strain T1P1-L4, complete genome	AY303792.1
Japanese encephalitis virus strain CJN-S1, complete genome	AY303793.1
Japanese encephalitis virus strain CJN-L1, complete genome	AY303794.1
Japanese encephalitis virus strain CC27-L1, complete genome	AY303795.1
Japanese encephalitis virus strain CC27-L3, complete genome	AY303796.1
Japanese encephalitis virus strain CC27-S6, complete genome	AY303797.1
Japanese encephalitis virus strain CC27-S8, complete genome	AY303798.1
Japanese encephalitis virus strain ML17 (live vaccine)/Japan/1981/human, complete genome	AY508812.1
Japanese encephalitis virus strain JaOH0566/Japan/1966/human, complete genome	AY508813.1
Japanese encephalitis virus strain HW, complete genome	AY849939.1
Japanese encephalitis virus strain SA(V) genomic RNA, complete genome	D90194.1
Japanese encephalitis virus strain SA(A) genomic RNA, complete genome	D90195.1
Japanese encephalitis virus strain WHe, complete genome	EF107523.1
Japanese encephalitis virus strain SH0601, complete genome	EF543861.1
Japanese encephalitis virus strain B58, complete genome	FJ185036.1
Japanese encephalitis virus strain GB30, complete genome	FJ185037.1
Japanese encephalitis virus strain GB30, complete genome	FJ185037.1
Japanese encephalitis virus strain NJ 2008, complete genome	GQ918133.2
Japanese encephalitis virus isolate 47, complete genome	JF706269.1

Japanese encephalitis virus isolate DL04-29, complete genome	JF706272.1
Japanese encephalitis virus isolate Fj02-29, complete genome	JF706273.1
Japanese encephalitis virus isolate GSS, complete genome	JF706275.1
Japanese encephalitis virus isolate HLJ02-134, complete genome	JF706276.1
Japanese encephalitis virus isolate YLG, complete genome	JF706280.1
Japanese encephalitis virus isolate ZMT, complete genome	JF706283.1
Japanese encephalitis virus isolate HB49, complete genome	JF706284.1
Japanese encephalitis virus isolate HB97, complete genome	JF706285.1
Japanese encephalitis virus isolate HYZ, complete genome	JN381853.1
Japanese encephalitis virus isolate DL0445, complete genome	JN381854.1
Japanese encephalitis virus isolate JH0418, complete genome	JN381855.1
Japanese encephalitis virus isolate SH0410, complete genome	JN381856.1
Japanese encephalitis virus isolate GZ042, complete genome	JN381857.1
Japanese encephalitis virus isolate FJ0394, complete genome	JN381858.1
Japanese encephalitis virus isolate FJ0339, complete genome	JN381859.1
Japanese encephalitis virus isolate CBH, complete genome	JN381860.1
Japanese encephalitis virus isolate YN98A151, complete genome	JN381861.1
Japanese encephalitis virus isolate ZSZ, complete genome	JN381862.1
Japanese encephalitis virus isolate SH3, complete genome	JN381864.1
Japanese encephalitis virus isolate CZX, complete genome	JN381865.1
Japanese encephalitis virus isolate SH045, complete genome	JN381866.1
Japanese encephalitis virus isolate Fj0276, complete genome	JN381867.1
Japanese encephalitis virus isolate TLA, complete genome	JN381868.1
Japanese encephalitis virus isolate LYZ, complete genome	JN381869.1
Japanese encephalitis virus isolate YN, complete genome	JN381871.1
Japanese encephalitis virus isolate Ha3, complete genome	JN381872.1
Japanese encephalitis virus isolate DH107, complete genome	JN381873.1
Japanese encephalitis virus strain SA14-14-2, complete genome	JN604986.1
Japanese encephalitis virus strain GD, complete genome	JN711458.1
Japanese encephalitis virus strain HN2, complete genome	JN711459.1
Japanese encephalitis virus isolate IND-WB-JE1, complete genome	JX050179.1
Japanese encephalitis virus isolate IND-WB-JE2, complete genome	JX072965.1
Japanese encephalitis virus isolate JEV/eq/India/H225/2009, complete genome	JX131374.1
Japanese encephalitis virus strain JE/vaccine/China/Chengdu-Institute-of-Biological-Products-SA14-14-2, complete genome	KC517497.1

Japanese encephalitis virus isolate JEV/SW/GD/01/2009, complete genome	KF297915.1
Japanese encephalitis virus strain RP9-190, complete genome	KF907505.1
Japanese encephalitis virus isolate JEV/SW/IVRI/395A/2014, complete genome	KP164498.2
Japanese encephalitis virus isolate JEV-hubei, complete genome	KR265316.1
Japanese encephalitis virus isolate Vellore P20778-T, complete genome	KT239164.1
Japanese encephalitis virus strain Anyang-300, complete genome	KT447437.1
Japanese encephalitis virus strain SA14, complete genome	KU323483.1
Japanese encephalitis virus strain SC201301, complete genome	KU363309.1
Japanese encephalitis virus isolate SA-14_CP8, complete genome	KU871338.1
Japanese encephalitis virus isolate SA14_CP12, complete genome	KU871339.1
Japanese encephalitis virus isolate SA-14_CP16, complete genome	KU871340.1
Japanese encephalitis virus isolate SA-14_CP20, complete genome	KU871341.1
Japanese encephalitis virus isolate SA-14_CP24, complete genome	KU871342.1
Japanese encephalitis virus isolate SA-14_CP28_, complete genome	KU871343.1
Japanese encephalitis virus isolate BJ-1_M2R2, complete genome	KU871344.1
Japanese encephalitis virus isolate BJ-1_M14R14, complete genome	KU871345.1
Japanese encephalitis virus isolate BJ-1_M4R4, complete genome	KU871346.1
Japanese encephalitis virus isolate BJ-1_M12R12, complete genome	KU871347.1
Japanese encephalitis virus isolate BJ-1_M10R10, complete genome	KU871348.1
Japanese encephalitis virus isolate BJ-1_M8R8, complete genome	KU871349.1
Japanese encephalitis virus isolate BJ-1_M6R6, complete genome	KU871350.1
Japanese encephalitis virus isolate BJ-1__BCP8, complete genome	KU871351.1
Japanese encephalitis virus isolate BJ-1__BCP12_OFR, complete genome	KU871352.1
Japanese encephalitis virus isolate BJ-1_BCP28, complete genome	KU871353.1
Japanese encephalitis virus isolate BJ-1__BCP16, complete genome	KU871354.1
Japanese encephalitis virus isolate BJ-1_BCP24, complete genome	KU871355.1
Japanese encephalitis virus isolate BJ-1_BCP4, complete genome	KU871356.1
Japanese encephalitis virus isolate BJ-1_BCP20, complete genome	KU871357.1
Japanese encephalitis virus isolate BJ-1_CP4, complete genome	KU871358.1
Japanese encephalitis virus isolate BJ-1_CP28, complete genome	KU871359.1
Japanese encephalitis virus isolate BJ-1_CP8, complete genome	KU871360.1
Japanese encephalitis virus isolate BJ-1_CP12, complete genome	KU871361.1
Japanese encephalitis virus isolate BJ-1_CP16, complete genome	KU871362.1

Japanese encephalitis virus isolate BJ-1_CP20, complete genome	KU871363.1
Japanese encephalitis virus isolate BJ-1_CP24, complete genome	KU871364.1
Japanese encephalitis virus isolate BJ-1_BP4, complete genome	KU871365.1
Japanese encephalitis virus isolate BJ-1_BP8, complete genome	KU871366.1
Japanese encephalitis virus isolate BJ-1_BP12, complete genome	KU871367.1
Japanese encephalitis virus isolate BJ-1_BP16, complete genome	KU871368.1
Japanese encephalitis virus isolate BJ-1_BP20, complete genome	KU871369.1
Japanese encephalitis virus isolate BJ-1_BP24, complete genome	KU871370.1
Japanese encephalitis virus isolate BJ-1_BP28, complete genome	KU871371.1
Japanese encephalitis virus isolate JEV/SC/2016-2, complete genome	KX779520.1
Japanese encephalitis virus isolate JEV/SC/2016-1, complete genome	KX779521.1
Japanese encephalitis virus isolate JEV/SC/2016-3, complete genome	KX779522.1
Japanese encephalitis virus isolate C17, complete genome	KX945367.1
Japanese encephalitis virus isolate JEV/sw/GD/2008, complete genome	KX965684.1
Japanese encephalitis virus strain Beijing-015, complete genome	KY885009.1
Japanese encephalitis virus (strain Beijing-1), complete genome	L48961.1
Japanese encephalitis virus strain Ling, complete genome	L78128.1
Japanese encephalitis virus JEV/sw/Mindanao/K4/2018 RNA, complete genome	LC461960.1
Japanese encephalitis virus Bo/Kochi/211/2018 RNA, complete genome	LC705012.1
Japanese encephalitis virus (strain JaOArS982), complete genome	M18370.1
Japanese encephalitis SA-14 virus, complete genome	M55506.1
Japanese encephalitis virus strain JEV/sw/GD/2008, complete genome	MF326270.1
Japanese encephalitis virus isolate SA14, complete genome	MH258848.1
Japanese encephalitis virus isolate SA14-14-2 MSV, complete genome	MH258849.1
Japanese encephalitis virus isolate SA14-14-2-PHK17, complete genome	MH258850.1
Japanese encephalitis virus isolate SA14-14-2 PSV, complete genome	MH258851.1
Japanese encephalitis virus isolate SA14-14-2, complete genome	MH258852.1
Japanese encephalitis virus isolate SA14-14-2 WSV, complete genome	MH258853.1
Japanese encephalitis virus strain N28, complete genome	MH753126.1
Japanese encephalitis virus strain SH1, complete genome	MH753128.1
Japanese encephalitis virus strain SH15, complete genome	MH753130.1
Japanese encephalitis virus strain SH19, complete genome	MH753131.1
Japanese encephalitis virus strain SH18, complete genome	MH753132.1
Japanese encephalitis virus strain SA14-14-2, complete genome	MK585066.1

Japanese encephalitis virus isolate JEV1805M, complete genome	MN639770.1
Japanese encephalitis virus isolate SA14 clone TJE302, complete genome	MT764727.1
Japanese encephalitis virus strain SA14-14-2 vaccine clone JE697, complete genome	MT764728.1
Japanese encephalitis virus strain SA14-5-3 clone TJE565, complete genome	MT764729.1
Japanese encephalitis virus strain SA14-2-8 clone TJE2330, complete genome	MT764730.1
Japanese encephalitis virus strain SA14 clone TJE2350, complete genome	MT764731.1
Japanese encephalitis virus strain SA14-4-2 clone TJE2359, complete genome	MT764732.1
Japanese encephalitis virus strain SA14-2-8 clone TJE2365, complete genome	MT764733.1
Japanese encephalitis virus, genome	NC_001437.1
Japanese encephalitis virus strain Vellore P20778, complete genome	OK257213.1
Japanese encephalitis virus strain Vellore P20779, complete genome	OK257214.1
Japanese encephalitis virus strain Vellore P20780, complete genome	OK257215.1
Japanese encephalitis virus strain p3, complete genome	U47032.1
Japanese encephalitis virus isolate LFM, complete genome	JN381863.1
Japanese encephalitis virus FU strain, complete genome	AF217620.1
Japanese encephalitis virus strain GZ, complete genome	KC915016.1
Japanese encephalitis virus isolate JEV/SW/GZ/09/2004, complete genome	KF297916.1
Japanese encephalitis virus strain YUNNAN0901, complete genome	JN864064.1
Japanese encephalitis virus strain YUNNAN0901, complete genome	JQ086762.1
Japanese encephalitis virus strain YUNNAN0902, complete genome	JQ086763.1
Japanese encephalitis virus isolate FC792, complete genome	MF002373.1
Japanese encephalitis virus RNA, complete genome, strain: JaTAn1/75	AB551990.1
Japanese encephalitis virus isolate BL06-50, complete genome	JF706270.1
Japanese encephalitis virus strain K87P39, complete genome	AY585242.1_AS
Japanese encephalitis virus CNU/LP2, complete genome	AY585243.1_AS
Japanese encephalitis virus isolate HEN0701, complete genome	FJ495189.1_AS
Japanese encephalitis virus clone CNU/LP2x, complete genome	GQ199609.1_AS
Japanese encephalitis virus isolate Ha3, complete genome	JN381872.1_AS

Japanese encephalitis virus strain GZ, complete genome	KC915016.1_AS
Japanese encephalitis virus isolate JEV/SW/GZ/09/2004, complete genome	KF297916.1_AS
Japanese encephalitis virus isolate ZJ82-6, complete genome	KY650724.1_AS
Japanese encephalitis virus isolate ZJ83-8, complete genome	KY650725.1_AS
Japanese encephalitis virus strain Nakayama, complete genome	EF571853.1
Japanese encephalitis virus complete genome, genomic RNA, strain Nakayama/MY/2009/P578667	HE861351.1
Japanese encephalitis virus isolate GSBY0804, complete genome	JN381844.1
Japanese encephalitis virus isolate GSBY0827, complete genome	JN381845.1
Japanese encephalitis virus isolate SCCZ, complete genome	KU351667.1
Japanese encephalitis virus genomic RNA, complete genome, strain: JEV/sw/Mie/40/2005	AB241118.1
Japanese encephalitis virus genomic RNA, complete genome, strain: JEV/sw/Mie/41/2002	AB241119.1
Japanese encephalitis virus genomic RNA, complete genome, strain: JEV/eq/Tottori/2004	AB594829.1
Japanese encephalitis virus genomic RNA, complete genome, strain: Sw/Mie/51/2007	AB698905.1
Japanese encephalitis virus genomic RNA, complete genome, strain: Sw/Mie/84/2006	AB698906.1
Japanese encephalitis virus genomic RNA, complete genome, strain: Sw/Tokyo/373/2006	AB698907.1
Japanese encephalitis virus genomic RNA, complete genome, strain: Sw/Tokyo/602/2006	AB698908.1
Japanese encephalitis virus genomic RNA, complete genome, strain: Sw/Mie/34/2005	AB698909.1
Japanese encephalitis virus genomic RNA, complete genome, strain: JEV/Bo/Miyazaki/1/2010	AB830335.1
Japanese encephalitis virus strain SH17M-07, complete genome	EU429297.1
Japanese encephalitis virus strain XJP613, complete genome	EU693899.1
Japanese encephalitis virus strain XJ69, complete genome	EU880214.1
Japanese encephalitis virus strain SC04-17, complete genome	GU187972.1
Japanese encephalitis virus strain 131V, complete genome	GU205163.1
Japanese encephalitis virus strain 90VN70, complete genome	HM228921.1
Japanese encephalitis virus isolate GZ56, complete genome	HM366552.1

Japanese encephalitis virus isolate SX09S-01, complete genome	HQ893545.1
Japanese encephalitis virus isolate TC2009-3, complete genome	JF499788.1
Japanese encephalitis virus isolate YL2009-4, complete genome	JF499789.1
Japanese encephalitis virus isolate TC2009-1, complete genome	JF499790.1
Japanese encephalitis virus isolate YN0911, complete genome	JF706267.1
Japanese encephalitis virus isolate YN0967, complete genome	JF706268.1
Japanese encephalitis virus isolate BL06-54, complete genome	JF706271.1
Japanese encephalitis virus isolate HN06129, complete genome	JF706277.1
Japanese encephalitis virus isolate YN05124, complete genome	JF706281.1
Japanese encephalitis virus isolate SD0810, complete genome	JF706286.1
Japanese encephalitis virus isolate HN0411, complete genome	JN381831.1
Japanese encephalitis virus isolate GX0523/44, complete genome	JN381832.1
Japanese encephalitis virus isolate GSBY0861, complete genome	JN381833.1
Japanese encephalitis virus isolate YN82BN8219, complete genome	JN381834.1
Japanese encephalitis virus isolate GX0519, complete genome	JN381835.1
Japanese encephalitis virus isolate YN0623, complete genome	JN381836.1
Japanese encephalitis virus isolate HN0626, complete genome	JN381837.1
Japanese encephalitis virus isolate SC0415, complete genome	JN381838.1
Japanese encephalitis virus isolate SC0412, complete genome	JN381839.1
Japanese encephalitis virus isolate HN0421, complete genome	JN381841.1
Japanese encephalitis virus isolate GSBY0816, complete genome	JN381842.1
Japanese encephalitis virus isolate GS07TS11, complete genome	JN381843.1
Japanese encephalitis virus isolate SH80, complete genome	JN381848.1
Japanese encephalitis virus isolate LN0716, complete genome	JN381849.1
Japanese encephalitis virus isolate SH53, complete genome	JN381850.1
Japanese encephalitis virus isolate YN79Bao83, complete genome	JN381851.1
Japanese encephalitis virus isolate YN05155, complete genome	JN381852.1
Japanese encephalitis virus isolate HL2010-2, complete genome	JQ031753.1
Japanese encephalitis virus strain JEV/CNS769/Laos/2009, complete genome	KC196115.1
Japanese encephalitis virus isolate SCYA201201, complete genome	KM658163.1
Japanese encephalitis virus strain DH10M978, complete genome	KT229573.1
Japanese encephalitis virus strain YN09M57, complete genome	KT229574.1
Japanese encephalitis virus strain DHL10M62, complete genome	KT229575.1
Japanese encephalitis virus strain DHL10M62, complete genome	KT229575.1
Japanese encephalitis virus strain YNTC07172, complete genome	KT957419.1

Japanese encephalitis virus strain YNTC07018, complete genome	KT957420.1
Japanese encephalitis virus isolate SCMY, complete genome	KU351668.1
Japanese encephalitis virus clone SCYA201201-1, complete genome	KU508408.1
Japanese encephalitis virus clone SCYA201201-86, complete genome	KU508409.1
Japanese encephalitis virus isolate ZJ10-7, complete genome	KY650726.1
Japanese encephalitis virus isolate ZJ10-10, complete genome	KY650727.1
Japanese encephalitis virus JEV/MQ/Yamaguchi/804/2016 RNA, complete genome	LC461957.1
Japanese encephalitis virus sw/Kochi/167/2013 RNA, complete genome	LC708273.1
Japanese encephalitis virus sw/Kochi/230/2013 RNA, complete genome	LC708274.1
Japanese encephalitis virus sw/Kochi/240/2017 RNA, complete genome	LC708276.1
Japanese encephalitis virus clone SCYA201201-0901, complete genome	MF124315.1
Japanese encephalitis virus clone SCYA201201-0901-SN5, complete genome	MF124316.1
Japanese encephalitis virus isolate JNSBr/01/2017, complete genome	MK495877.1
Japanese encephalitis virus isolate Pig/India-Assam/36/2015-JEV, complete genome	MT232844.1
Japanese encephalitis virus isolate 0945054, complete genome	MT859415.1
Japanese encephalitis virus clone JEV-0945054-RV, complete genome	MT859416.1
Japanese encephalitis virus isolate HEN0701, complete genome	FJ495189.1
Japanese encephalitis virus strain XZ0938, complete genome	HQ652538.1
Japanese encephalitis virus isolate GSBY0801, complete genome	JF706274.1
Japanese encephalitis virus isolate LN02-102, complete genome	JF706278.1
Japanese encephalitis virus isolate GSBY0810, complete genome	JN381840.1
Japanese encephalitis virus isolate SH03105, complete genome	JN381846.1
Japanese encephalitis virus isolate SH03103, complete genome	JN381847.1
Japanese encephalitis virus strain SD12, complete genome	MH753127.1
Japanese encephalitis virus strain SH7, complete genome	MH753129.1
Japanese encephalitis virus strain SH2, complete genome	MH753133.1
Japanese encephalitis virus isolate SD12-F120, complete genome	MN544779.1
Japanese encephalitis virus isolate SD12-F120-VC, complete genome	MN544780.1
Japanese encephalitis virus strain NX1889, complete genome	MT134112.1
Japanese encephalitis virus strain JEV-SC-2020-1, complete genome	OK423757.1
Japanese encephalitis virus isolate HB49, complete genome	JF915894.1
Japanese encephalitis virus isolate ME802, complete genome	KY927819.1

Japanese encephalitis virus genomic RNA, complete genome, clone:JEV-AT32	AB196923.1
Japanese encephalitis virus genomic RNA, complete genome, clone:JEV-at223	AB196924.1
Japanese encephalitis virus genomic RNA, complete genome, clone:JEV-AT32	AB196926.1
Japanese encephalitis virus clone 13OK206 envelope protein mRNA, partial cds	KM079174.1
Japanese encephalitis virus RNA, complete genome, strain: JaTAn1/76	AB551990.1
Japanese encephalitis virus RNA, complete genome, strain: JaTAn1/92	AB551991.1
Japanese encephalitis virus RNA, complete genome, strain: JaTAn1/93	AB551991.1
Japanese encephalitis virus RNA, complete genome, strain: JaTAn2/93	AB551992.1
Japanese encephalitis virus RNA, complete genome, strain: JaTAn2/94	AB551992.1
Japanese encephalitis virus strain K87P39, complete genome	AY585242.1
Japanese encephalitis virus CNU/LP2, complete genome	AY585243.1
Japanese encephalitis virus clone CNU/LP2x, complete genome	GQ199609.1
Japanese encephalitis virus clone CNU/LP2x, complete genome	GQ199609.1
Japanese encephalitis virus complete genome, genomic RNA, strain Nakayama/MY/2009/P578663	HE861351.1
Japanese encephalitis virus isolate CH13, complete genome	JN381870.1
Japanese encephalitis virus isolate ZJ82-6, complete genome	KY650724.1
Japanese encephalitis virus isolate ZJ83-8, complete genome	KY650725.1
Japanese encephalitis virus RNA, complete genome, strain: JaTAn1/98	AB551991.1
Japanese encephalitis virus RNA, complete genome, strain: JaTAn1/99	AB551991.1
Japanese encephalitis virus RNA, complete genome, strain: JaTAn2/99	AB551992.1
Japanese encephalitis virus RNA, complete genome, strain: JaTAn2/100	AB551992.1
Japanese encephalitis virus JEV/sw/Bali/93/2017 RNA, complete genome	LC461961.1
Japanese encephalitis virus genomic RNA, complete genome, clone:JEV-AT34	AB196923.1
Japanese encephalitis virus genomic RNA, complete genome, clone:JEV-at225	AB196924.1
Japanese encephalitis virus genomic RNA, complete genome, clone:JEV-AT34	AB196926.1
Japanese encephalitis virus strain B-0860/82, complete genome	GQ902058.1
Japanese encephalitis virus strain 1070/82 (Subin), complete genome	GQ902059.1

Japanese encephalitis virus strain 3KP"U"CV569, complete genome	GQ902060.1
Japanese encephalitis virus strain B-1381-85, complete genome	GQ902061.1
Japanese encephalitis virus strain 4790-85, complete genome	GQ902062.1
Japanese encephalitis virus complete genome, genomic RNA, strain Nakayama/MY/2009/P578665	HE861351.1
Japanese encephalitis virus isolate M28, complete genome	JF706279.1
Japanese encephalitis virus strain M28, complete genome	KT957422.1
Japanese encephalitis virus strain BN82215, complete genome	KT957423.1
Japanese encephalitis virus isolate 639A37Cx-tri, complete genome	KY927815.1
Japanese encephalitis virus isolate C081, complete genome	KY927816.1
Japanese encephalitis virus JEV/sw/Thailand/185/2017 RNA, complete genome	LC461958.1
Japanese encephalitis virus strain JEV/mosq/YN/2016, complete genome	MH385014.1
Japanese encephalitis virus genomic RNA, complete genome, clone:JEV-AT31	AB196923.1
Japanese encephalitis virus genomic RNA, complete genome, clone:JEV-at222	AB196924.1
Japanese encephalitis virus genomic RNA, complete genome, clone:JEV-AT31	AB196926.1
Japanese encephalitis virus complete genome, genomic RNA, strain Nakayama/MY/2009/P578662	HE861351.1
Japanese encephalitis virus genomic RNA, complete genome, strain: JEV/sw/Mie/40/2004	AB241118.1
Japanese encephalitis virus RNA, complete genome, strain: JaTAn1/90	AB551991.1
Japanese encephalitis virus RNA, complete genome, strain: JaTAn1/91	AB551991.1
Japanese encephalitis virus RNA, complete genome, strain: JaTAn2/91	AB551992.1
Japanese encephalitis virus RNA, complete genome, strain: JaTAn2/92	AB551992.1
Japanese encephalitis virus genomic RNA, complete genome, strain: JEV/eq/Tottori/2003	AB594829.1
Japanese encephalitis virus genomic RNA, complete genome, strain: Sw/Mie/51/2006	AB698905.1
Japanese encephalitis virus genomic RNA, complete genome, strain: Sw/Mie/84/2005	AB698906.1
Japanese encephalitis virus genomic RNA, complete genome, strain: Sw/Tokyo/373/2005	AB698907.1

Japanese encephalitis virus genomic RNA, complete genome, strain: Sw/Tokyo/602/2005	AB698908.1
Japanese encephalitis virus genomic RNA, complete genome, strain: Sw/Mie/34/2004	AB698909.1
Japanese encephalitis virus genomic RNA, complete genome, strain: JEV/Bo/Miyazaki/1/2009	AB830335.1
Japanese encephalitis virus genomic RNA, complete genome, strain: JEV/Bo/Aichi/1/2010	AB853904.1
Japanese encephalitis virus strain KV1899, complete genome	AY316157.1
Japanese encephalitis virus strain JX61, complete genome	GU556217.1
Japanese encephalitis virus isolate HN0621, complete genome	JN381830.1
Japanese encephalitis virus isolate K10CT661 polyprotein mRNA, partial cds	JX018150.1
Japanese encephalitis virus isolate K10CT662 polyprotein mRNA, partial cds	JX018151.1
Japanese encephalitis virus isolate K10CB663 polyprotein mRNA, partial cds	JX018152.1
Japanese encephalitis virus isolate K10CP371 polyprotein mRNA, partial cds	JX018153.1
Japanese encephalitis virus isolate K10CT372 polyprotein mRNA, partial cds	JX018154.1
Japanese encephalitis virus isolate K10CT611 polyprotein mRNA, partial cds	JX018155.1
Japanese encephalitis virus isolate K10CT612 polyprotein mRNA, partial cds	JX018156.1
Japanese encephalitis virus isolate K10CT613 polyprotein mRNA, partial cds	JX018157.1
Japanese encephalitis virus isolate K10CT621 polyprotein mRNA, partial cds	JX018158.1
Japanese encephalitis virus isolate K10CT622 polyprotein mRNA, partial cds	JX018159.1
Japanese encephalitis virus isolate K10CT623 polyprotein mRNA, partial cds	JX018160.1
Japanese encephalitis virus isolate K10CT631 polyprotein mRNA, partial cds	JX018161.1

Japanese encephalitis virus isolate K10CT632 polyprotein mRNA, partial cds	JX018162.1
Japanese encephalitis virus isolate K10CT633 polyprotein mRNA, partial cds	JX018163.1
Japanese encephalitis virus isolate K10CT671 polyprotein mRNA, partial cds	JX018164.1
Japanese encephalitis virus isolate K10CT672 polyprotein mRNA, partial cds	JX018165.1
Japanese encephalitis virus isolate K10CT673 polyprotein mRNA, partial cds	JX018166.1
Japanese encephalitis virus isolate K10CP674 polyprotein mRNA, partial cds	JX018167.1
Japanese encephalitis virus isolate K10CT675 polyprotein mRNA, partial cds	JX018168.1
Japanese encephalitis virus strain DH10M865, complete genome	KT229572.1
Japanese encephalitis virus JEV/Mo/Kagawa/NIID09/2020 RNA, complete genome	LC623822.1
Japanese encephalitis virus JEV-seal-UT1-2020 RNA, complete genome	LC687612.1
Japanese encephalitis virus Bo/Kochi/132/2018 DNA, complete genome	LC704880.1
Japanese encephalitis virus sw/Kochi/231/2017 RNA, complete genome	LC708275.1
Japanese encephalitis virus strain seal/china/anheal/2017, complete genome	MH165313.1
Japanese encephalitis virus strain ZJ/52/14, complete genome	MK558811.1
Japanese encephalitis virus strain TC4E10_18-9E-Y-T-Cxt-Y-5-11, complete genome	MT254426.1
Japanese encephalitis virus isolate GZDJ1609, complete genome	MT560941.1
Japanese encephalitis virus isolate JEV_ASSAM_03, complete genome	MZ702743.1
Japanese encephalitis virus strain Muar, complete genome	HM596272.1
Japanese encephalitis virus isolate Tengah, complete genome	KM677246.1
Japanese encephalitis virus genomic RNA, complete genome, strain: JEV/Bo/Miyazaki/1/2012	AB830335.1
Japanese encephalitis virus genomic RNA, complete genome, strain: JEV/eq/Tottori/2006	AB594829.1
Japanese encephalitis virus genomic RNA, complete genome, strain: JEV/sw/Mie/40/2007	AB241118.1

Japanese encephalitis virus genomic RNA, complete genome, strain: JEV/sw/Mie/41/2003	AB241119.1
Japanese encephalitis virus genomic RNA, complete genome, strain: Sw/Mie/51/2009	AB698905.1
Japanese encephalitis virus genomic RNA, complete genome, strain: Sw/Mie/84/2008	AB698906.1
Japanese encephalitis virus genomic RNA, complete genome, strain: Sw/Tokyo/373/2008	AB698907.1
Japanese encephalitis virus genomic RNA, complete genome, strain: Sw/Tokyo/602/2007	AB698908.1
Japanese encephalitis virus genomic RNA, complete genome, strain: Sw/Mie/34/2007	AB698909.1
Japanese encephalitis virus genomic RNA, complete genome, strain: JEV/Bo/Aichi/1/2012	AB853904.1
Japanese encephalitis virus isolate YN83-Meng83-54, complete genome	JF706282.1
Japanese encephalitis virus strain DH10M585, complete genome	KT957421.1
Japanese encephalitis virus strain JEV/sw-22-00722-11/Qld/2022, complete genome	ON624132.1
Japanese encephalitis virus genomic RNA, complete genome, clone:JEV-AT35	AB196923.1
Japanese encephalitis virus genomic RNA, complete genome, clone:JEV-at226	AB196924.1
Japanese encephalitis virus genomic RNA, complete genome, clone:JEV-AT35	AB196926.1
Japanese encephalitis virus RNA, complete genome, strain: JaTAn1/78	AB551990.1
Japanese encephalitis virus RNA, complete genome, strain: JaTAn1/96	AB551991.1
Japanese encephalitis virus RNA, complete genome, strain: JaTAn1/97	AB551991.1
Japanese encephalitis virus RNA, complete genome, strain: JaTAn2/97	AB551992.1
Japanese encephalitis virus RNA, complete genome, strain: JaTAn2/98	AB551992.1
Japanese encephalitis virus complete genome, genomic RNA, strain Nakayama/MY/2009/P578666	HE861351.1
Japanese encephalitis virus genomic RNA, complete genome, strain: JEV/sw/Mie/40/2006	AB241118.1
Japanese encephalitis virus genomic RNA, complete genome, strain: JEV/eq/Tottori/2005	AB594829.1

Japanese encephalitis virus genomic RNA, complete genome, strain: Sw/Mie/51/2008	AB698905.1
Japanese encephalitis virus genomic RNA, complete genome, strain: Sw/Mie/84/2007	AB698906.1
Japanese encephalitis virus genomic RNA, complete genome, strain: Sw/Tokyo/373/2007	AB698907.1
Japanese encephalitis virus genomic RNA, complete genome, strain: Sw/Mie/34/2006	AB698909.1
Japanese encephalitis virus genomic RNA, complete genome, strain: JEV/Bo/Miyazaki/1/2011	AB830335.1
Japanese encephalitis virus genomic RNA, complete genome, strain: JEV/Bo/Aichi/1/2011	AB853904.1
Japanese encephalitis virus isolate C14-B3, complete genome	KY927817.1
Japanese encephalitis virus isolate D03-B9, complete genome	KY927818.1
Japanese encephalitis virus RNA, complete genome, strain: JaTAn1/94	AB551991.1
Japanese encephalitis virus RNA, complete genome, strain: JaTAn1/95	AB551991.1
Japanese encephalitis virus RNA, complete genome, strain: JaTAn2/95	AB551992.1
Japanese encephalitis virus RNA, complete genome, strain: JaTAn2/96	AB551992.1
Japanese encephalitis virus genomic RNA, complete genome, clone:JEV-AT33	AB196923.1
Japanese encephalitis virus genomic RNA, complete genome, clone:JEV-at224	AB196924.1
Japanese encephalitis virus genomic RNA, complete genome, clone:JEV-AT33	AB196926.1
Japanese encephalitis virus complete genome, genomic RNA, strain Nakayama/MY/2009/P578664	HE861351.1
Japanese encephalitis virus RNA, complete genome, strain: JaTAn1/77	AB551990.1
Japanese encephalitis virus strain SH0601, complete genome	EF543861.1_AS
Japanese encephalitis virus strain KPP82-39-214CT, complete genome	GQ902063.1_AS
Japanese encephalitis virus RNA, complete genome, strain: JaTAn1/79	AB551990.1_AS
Japanese encephalitis virus RNA, complete genome, strain: JaTAn1/100	AB551991.1_AS
Japanese encephalitis virus RNA, complete genome, strain: JaTAn1/101	AB551991.1_AS
Japanese encephalitis virus RNA, complete genome, strain: JaTAn2/101	AB551992.1_AS
Japanese encephalitis virus RNA, complete genome, strain: JaTAn2/102	AB551992.1_AS
Japanese encephalitis virus strain GP78, complete genome	AF075723.1_AS
Japanese encephalitis virus strain CC27-L1, complete genome	AY303795.1_AS

Japanese encephalitis virus strain CC27-L3, complete genome	AY303796.1_AS
Japanese encephalitis virus strain CC27-S6, complete genome	AY303797.1_AS
Japanese encephalitis virus strain CC27-S8, complete genome	AY303798.1_AS
Japanese encephalitis virus isolate 014178, complete genome	EF623987.1_AS
Japanese encephalitis virus isolate 057434, complete genome	EF623988.1_AS
Japanese encephalitis virus isolate 04940-4, complete genome	EF623989.1_AS
Japanese encephalitis virus complete genome, genomic RNA, strain Nakayama/MY/2009/P578668	HE861351.1_AS
Japanese encephalitis virus isolate 47, complete genome	JF706269.1_AS
Japanese encephalitis virus isolate LYZ, complete genome	JN381869.1_AS
Japanese encephalitis virus isolate IGIB-NIV-2009-01, complete genome	JN644310.1
Japanese encephalitis virus isolate JEV/SW/IVRI/395A/2014, complete genome	KP164498.2_AS
Japanese encephalitis virus strain Ling, complete genome	L78128.1_AS
Japanese encephalitis virus JEV/sw/Mindanao/K4/2018 RNA, complete genome	LC461960.1_AS
Japanese encephalitis virus isolate JNSBr/01/2017, complete genome	MK495877.1_AS
Japanese encephalitis virus genomic RNA, complete genome, strain: JEV/Bo/Miyazaki/1/2013	AB830335.1_AS
Japanese encephalitis virus strain XJ69, complete genome	EU880214.1_AS
Japanese encephalitis virus JEV/MQ/Yamaguchi/804/2016 RNA, complete genome	LC461957.1_AS
Japanese encephalitis virus JEV/Mo/Kagawa/NIID09/2020 RNA, complete genome	LC623822.1_AS
Japanese encephalitis virus JEV-seal-UT1-2020 RNA, complete genome	LC687612.1_AS
Japanese encephalitis virus Bo/Kochi/132/2018 DNA, complete genome	LC704880.1_AS
Japanese encephalitis virus sw/Kochi/167/2013 RNA, complete genome	LC708273.1_AS
Japanese encephalitis virus sw/Kochi/230/2013 RNA, complete genome	LC708274.1_AS
Japanese encephalitis virus sw/Kochi/231/2017 RNA, complete genome	LC708275.1_AS
Japanese encephalitis virus sw/Kochi/240/2017 RNA, complete genome	LC708276.1_AS
Japanese encephalitis virus strain seal/china/anheal/2017, complete genome	MH165313.1_AS
Japanese encephalitis virus strain ZJ/52/14, complete genome	MK558811.1_AS
Japanese encephalitis virus strain NX1889, complete genome	MT134112.1 _AS
Japanese encephalitis virus isolate GZDJ1609, complete genome	MT560941.1_AS

Japanese encephalitis virus strain JEV-SC-2020-1, complete genome	OK423757.1_AS
Japanese encephalitis virus genomic RNA, complete genome, clone:JEV-AT37	AB196923.1_AS
Japanese encephalitis virus genomic RNA, complete genome, clone:JEV-at228	AB196924.1_AS
Japanese encephalitis virus genomic RNA, complete genome, clone:JEV-AT37	AB196926.1_AS

Table C9. Predicted G-quadruplex motifs in the Japanese Encephalitis Virus Reference genome (NC_001437.1) with G-tract ≥2 and Loop length = 7 and their Functional annotation.

#	Length (bp)	Start Position	End Position	PGQ Motifs	cG Score	cC Score	Gene
1	21	711	731	GGACGGTGCACGCGGACCAGG	100	60	locus_tag="JEVgp1" Product="membrane glycoprotein precursor prM" protein_id="NP_775664.1"
2	20	1275	1294	GGGTGGGGCAACGGATGTGG	120	20	locus_tag="JEVgp1" product="envelope protein E" protein_id="NP_775666.1"
3	17	1743	1759	GGGTCACAGGAAGGAGG	90	20	locus_tag="JEVgp1" product="envelope protein E" protein_id="NP_775666.1"
4	18	1919	1936	GGCGGACACTGGCCACGG	80	60	locus_tag="JEVgp1" product="envelope protein E" protein_id="NP_775666.1"
5	24	2251	2274	GGGACTTTGGCTCCATTGGAGGGG	110	40	locus_tag="JEVgp1" product="envelope protein E" protein_id="NP_775666.1"
6	19	2552	2570	GGAAGCCTGGGTGGACAGG	100	30	locus_tag="JEVgp1" product="non-structural protein NS1" protein_id="NP_775667.1"
7	26	3344	3369	GGACTGTGGCAAGAGAGGCCCTTCGG	110	60	locus_tag="JEVgp1" product="non-structural protein NS1" protein_id="NP_775667.1"

8	19	3459	3477	GGCTGCTGGTACGGAATGG	90	30	locus_tag="JEVgp1" product="non-structural protein NS1" protein_id="NP_775667.1"
9	19	4269	4287	GGTGGCTTGGCCGAGTTGG	100	30	locus_tag="JEVgp1" product="non-structural protein NS2b" protein_id="NP_775669.1"
10	15	4845	4859	GGAGGCCCATGGAGG	80	30	locus_tag="JEVgp1" product="non-structural protein NS3" protein_id="NP_775670.1"
11	17	5519	5535	GGTGGAATTAGGGGAGG	100	0	locus_tag="JEVgp1" product="non-structural protein NS3" protein_id="NP_775670.1"
12	20	6239	6258	GGTGTGGCTGGCCTACAAGG	90	40	locus_tag="JEVgp1" product="non-structural protein NS3" protein_id="NP_775670.1"
13	24	6689	6712	GGGTATAGGGAAGATGGGTCTTGG	120	10	locus_tag="JEVgp1" product="non-structural protein NS4a" protein_id="NP_775671.1"
14	19	6748	6766	GGGCGGCAGAGGTTCCTGG	100	40	locus_tag="JEVgp1" product="non-structural protein NS4a" protein_id="NP_775671.1"
15	14	6893	6906	GGTTGGAGTGGTGG	90	0	locus_tag="JEVgp1" product="2k protein" protein_id="NP_775672.1"
16	19	7506	7524	GGGGTATTGGTGACGGCGG	110	20	locus_tag="JEVgp1" product="non-structural protein NS4b" protein_id="NP_775673.1"

17	20	7675	7694	GGGGAAGGCCCGGGGGCAGG	130	40	locus_tag="JEVgp1" product="RNA-dependent RNA polymerase NS5" protein_id="NP_775674.1"
18	17	7917	7933	GGGTGTGGGCGTGGAGG	120	10	locus_tag="JEVgp1" product="RNA-dependent RNA polymerase NS5" protein_id="NP_775674.1"
19	27	8338	8364	GGGTTAGTGGAGCCGCTGGCAATGTGG	130	40	locus_tag="JEVgp1" product="RNA-dependent RNA polymerase NS5" protein_id="NP_775674.1"
20	24	8938	8961	GGAGCACGGCTCGTGAGGCTGTGG	120	50	locus_tag="JEVgp1" product="RNA-dependent RNA polymerase NS5" protein_id="NP_775674.1"
21	27	9090	9116	GGAAGCAGGGCCATTTGGTTCATGTGG	110	40	locus_tag="JEVgp1" product="RNA-dependent RNA polymerase NS5" protein_id="NP_775674.1"
22	13	9192	9204	GGAGGTGGAGTGG	90	0	locus_tag="JEVgp1" product="RNA-dependent RNA polymerase NS5" protein_id="NP_775674.1"
23	18	9481	9498	GGGGGAGTGGACAGGTGG	120	10	locus_tag="JEVgp1" product="RNA-dependent RNA polymerase NS5" protein_id="NP_775674.1"
24	21	9554	9574	GGAGGCTGAGGGGGTCATTGG	120	20	locus_tag="JEVgp1" product="RNA-dependent RNA polymerase NS5" protein_id="NP_775674.1"

25	24	10740	10763	GGTGTAAGGACTAGAGGTTAGAGG	110	10	-
26	12	10815	10826	GGAGGTGGAAGG	80	0	-
27	25	260	284	GGCTTGGGCCGTGGGGGCTCAACGG	130	60	-
28	18	1245	1262	GGAAGTGGAGGGCTGTGG	110	10	locus_tag="JEVgp1" product="RNA-dependent RNA polymerase NS5" protein_id="NP_775674.1"
29	20	2269	2288	GGCCATGGTGGTGACGTTGG	100	30	locus_tag="JEVgp1" product="RNA-dependent RNA polymerase NS5" protein_id="NP_775674.1"
30	19	2656	2674	GGAGTTCCGGGACAGGGGG	110	30	locus_tag="JEVgp1" product="RNA-dependent RNA polymerase NS5" protein_id="NP_775674.1"
31	19	3943	3961	GGCTGTGGCTGGACGCAGG	100	40	locus_tag="JEVgp1" product="non-structural protein NS4b" protein_id="NP_775673.1"
32	25	5017	5041	GGTTATGGGAGATGGGTTTCCGAGG	120	20	locus_tag="JEVgp1" product="non-structural protein NS3" protein_id="NP_775670.1"
33	23	5390	5412	GGAAAAGGATCCGTGGTTCCAGG	90	40	locus_tag="JEVgp1" product="non-structural protein NS3" protein_id="NP_775670.1"

34	21	6409	6429	GGCGGGAACGATGGCCCAAGG	100	50	locus_tag="JEVgp1" product="non-structural protein NS2b" protein_id="NP_775669.1"
35	16	6986	7001	GGCATGGTGACGGAGG	90	20	locus_tag="JEVgp1" product="non-structural protein NS2a" protein_id="NP_775668.1"
36	22	7048	7069	GGCGGCATTCAGGATTCCGTGG	90	50	locus_tag="JEVgp1" product="non-structural protein NS2a" protein_id="NP_775668.1"
37	21	7530	7550	GGAATCGTAGGGGCGGAAGGG	120	20	locus_tag="JEVgp1" product="non-structural protein NS1" protein_id="NP_775667.1"
38	20	7751	7770	GGTCCGGCTATGGTATGCGG	90	40	locus_tag="JEVgp1" product="non-structural protein NS1" protein_id="NP_775667.1"

REFERENCES

[1] Z. Zhang, X. He, G. Yuan, Formation and recognition of G-quadruplex relevant for pilin antigenic variation in Neisseria gonorrhoeae, Can. J. Chem. 90 (2012) 34–38. https://doi.org/10.1139/v11-092.

[2] P. Majee, A. Pattnaik, B.R. Sahoo, U. Shankar, A.K. Pattnaik, A. Kumar, D. Nayak, Inhibition of Zika virus replication by G-quadruplex-binding ligands, Molecular Therapy - Nucleic Acids 23 (2021) 691–701. https://doi.org/10.1016/j.omtn.2020.12.030.

[3] T.M. Rivers, Viruses and Koch's Postulates, J Bacteriol 33 (1937) 1–12. https://doi.org/10.1128/jb.33.1.1-12.1937.

[4] C. Miller, 1.5 Theories in Science, (2020). https://pressbooks.bccampus.ca/humanbiology053/chapter/1-5-theories-in-science/ (accessed August 15, 2025).

[5] S. Falkow, Molecular Koch's postulates applied to microbial pathogenicity, Rev Infect Dis 10 Suppl 2 (1988) S274-276. https://doi.org/10.1093/cid/10.supplement_2.s274.

[6] N.I. Nii-Trebi, Emerging and Neglected Infectious Diseases: Insights, Advances, and Challenges, Biomed Res Int 2017 (2017) 5245021. https://doi.org/10.1155/2017/5245021.

[7] Institute of Medicine (US) Committee on Emerging Microbial Threats to Health, Emerging Infections: Microbial Threats to Health in the United States, National Academies Press (US), Washington (DC), 1992. http://www.ncbi.nlm.nih.gov/books/NBK234855/ (accessed August 15, 2025).

[8] WHO EMRO | Emerging diseases | Health topics, World Health Organization - Regional Office for the Eastern Mediterranean (n.d.). http://www.emro.who.int/health-topics/emerging-diseases/index.html (accessed July 4, 2025).

[9] Global Tuberculosis Report 2023, (n.d.). https://www.who.int/teams/global-programme-on-tuberculosis-and-lung-health/tb-reports/global-tuberculosis-report-2023 (accessed July 4, 2025).

[10] Emerging Infectious Diseases - CDC, Emerging Infectious Diseases Journal (n.d.). https://wwwnc.cdc.gov/eid (accessed July 4, 2025).

[11] D.V. Parums, A Review of the Resurgence of Measles, a Vaccine-Preventable Disease, as Current Concerns Contrast with Past Hopes for Measles Elimination, Med Sci Monit 30 (2024) e944436-1-e944436-10. https://doi.org/10.12659/MSM.944436.

[12] S. Rebaudet, G. Bulit, J. Gaudart, E. Michel, P. Gazin, C. Evers, S. Beaulieu, A.A. Abedi, L. Osei, R. Barrais, K. Pierre, S. Moore, J. Boncy, P. Adrien, F.D. Guillaume, E. Beigbeder, R. Piarroux, The case-area targeted rapid response strategy to control cholera in Haiti: a four-year implementation study, PLOS Neglected Tropical Diseases 13 (2019) e0007263. https://doi.org/10.1371/journal.pntd.0007263.

[13] N.D. Wolfe, C.P. Dunavan, J. Diamond, Origins of major human infectious diseases, Nature 447 (2007) 279–283. https://doi.org/10.1038/nature05775.

[14] J.A. Patz, P. Daszak, G.M. Tabor, A.A. Aguirre, M. Pearl, J. Epstein, N.D. Wolfe, A.M. Kilpatrick, J. Foufopoulos, D. Molyneux, D.J. Bradley, Unhealthy Landscapes: Policy Recommendations on Land Use Change and Infectious Disease Emergence, Environ Health Perspect 112 (2004) 1092–1098. https://doi.org/10.1289/ehp.6877.
[15] R.E. Baker, A.S. Mahmud, I.F. Miller, M. Rajeev, F. Rasambainarivo, B.L. Rice, S. Takahashi, A.J. Tatem, C.E. Wagner, L.-F. Wang, A. Wesolowski, C.J.E. Metcalf, Infectious disease in an era of global change, Nat Rev Microbiol 20 (2022) 193–205. https://doi.org/10.1038/s41579-021-00639-z.
[16] G.P. Wormser, R.L. Colebunders, Control of Communicable Diseases Manual, 19th Edition Edited by David L. Heymann Washington, DC: American Public Health Association, 2008. 746 pp. $45.00 (hardcover), Clinical Infectious Diseases 49 (2009) 1292–1293. https://doi.org/10.1086/605668.
[17] J. Davies, D. Davies, Origins and Evolution of Antibiotic Resistance, Microbiology and Molecular Biology Reviews 74 (2010) 417–433. https://doi.org/10.1128/mmbr.00016-10.
[18] Antimicrobial resistance, (n.d.). https://www.who.int/news-room/fact-sheets/detail/antimicrobial-resistance (accessed July 5, 2025).
[19] A. resistance, What causes AMR?, (2017). https://www.amr.gov.au/about-amr/what-causes-amr (accessed July 7, 2025).
[20] G. Pierre, The leading causes of antimicrobial resistance in India, GARDP (2023). https://gardp.org/over-prescription-self-medication-and-regulatory-gaps-leading-causes-of-antimicrobial-resistance-in-india/ (accessed July 7, 2025).
[21] Causes of Antimicrobial (Drug) Resistance | NIAID: National Institute of Allergy and Infectious Diseases, (2011). https://www.niaid.nih.gov/research/antimicrobial-resistance-causes (accessed July 7, 2025).
[22] H. Endale, M. Mathewos, D. Abdeta, Potential Causes of Spread of Antimicrobial Resistance and Preventive Measures in One Health Perspective-A Review, IDR 16 (2023) 7515–7545. https://doi.org/10.2147/IDR.S428837.
[23] C.J.L. Murray, K.S. Ikuta, F. Sharara, L. Swetschinski, G. Robles Aguilar, A. Gray, C. Han, C. Bisignano, P. Rao, E. Wool, S.C. Johnson, A.J. Browne, M.G. Chipeta, F. Fell, S. Hackett, G. Haines-Woodhouse, B.H. Kashef Hamadani, E.A.P. Kumaran, B. McManigal, S. Achalapong, R. Agarwal, S. Akech, S. Albertson, J. Amuasi, J. Andrews, A. Aravkin, E. Ashley, F.-X. Babin, F. Bailey, S. Baker, B. Basnyat, A. Bekker, R. Bender, J.A. Berkley, A. Bethou, J. Bielicki, S. Boonkasidecha, J. Bukosia, C. Carvalheiro, C. Castañeda-Orjuela, V. Chansamouth, S. Chaurasia, S. Chiurchiù, F. Chowdhury, R. Clotaire Donatien, A.J. Cook, B. Cooper, T.R. Cressey, E. Criollo-Mora, M. Cunningham, S. Darboe, N.P.J. Day, M. De Luca, K. Dokova, A. Dramowski, S.J. Dunachie, T. Duong Bich, T. Eckmanns, D. Eibach, A. Emami, N. Feasey, N. Fisher-Pearson, K. Forrest, C. Garcia, D. Garrett, P. Gastmeier, A.Z. Giref, R.C. Greer, V. Gupta, S. Haller, A.

Haselbeck, S.I. Hay, M. Holm, S. Hopkins, Y. Hsia, K.C. Iregbu, J. Jacobs, D. Jarovsky, F. Javanmardi, A.W.J. Jenney, M. Khorana, S. Khusuwan, N. Kissoon, E. Kobeissi, T. Kostyanev, F. Krapp, R. Krumkamp, A. Kumar, H.H. Kyu, C. Lim, K. Lim, D. Limmathurotsakul, M.J. Loftus, M. Lunn, J. Ma, A. Manoharan, F. Marks, J. May, M. Mayxay, N. Mturi, T. Munera-Huertas, P. Musicha, L.A. Musila, M.M. Mussi-Pinhata, R.N. Naidu, T. Nakamura, R. Nanavati, S. Nangia, P. Newton, C. Ngoun, A. Novotney, D. Nwakanma, C.W. Obiero, T.J. Ochoa, A. Olivas-Martinez, P. Olliaro, E. Ooko, E. Ortiz-Brizuela, P. Ounchanum, G.D. Pak, J.L. Paredes, A.Y. Peleg, C. Perrone, T. Phe, K. Phommasone, N. Plakkal, A. Ponce-de-Leon, M. Raad, T. Ramdin, S. Rattanavong, A. Riddell, T. Roberts, J.V. Robotham, A. Roca, V.D. Rosenthal, K.E. Rudd, N. Russell, H.S. Sader, W. Saengchan, J. Schnall, J.A.G. Scott, S. Seekaew, M. Sharland, M. Shivamallappa, J. Sifuentes-Osornio, A.J. Simpson, N. Steenkeste, A.J. Stewardson, T. Stoeva, N. Tasak, A. Thaiprakong, G. Thwaites, C. Tigoi, C. Turner, P. Turner, H.R. van Doorn, S. Velaphi, A. Vongpradith, M. Vongsouvath, H. Vu, T. Walsh, J.L. Walson, S. Waner, T. Wangrangsimakul, P. Wannapinij, T. Wozniak, T.E.M.W. Young Sharma, K.C. Yu, P. Zheng, B. Sartorius, A.D. Lopez, A. Stergachis, C. Moore, C. Dolecek, M. Naghavi, Global burden of bacterial antimicrobial resistance in 2019: a systematic analysis, The Lancet 399 (2022) 629–655. https://doi.org/10.1016/S0140-6736(21)02724-0.

[24] S.K. Ahmed, S. Hussein, K. Qurbani, R.H. Ibrahim, A. Fareeq, K.A. Mahmood, M.G. Mohamed, Antimicrobial resistance: Impacts, challenges, and future prospects, Journal of Medicine, Surgery, and Public Health 2 (2024) 100081. https://doi.org/10.1016/j.glmedi.2024.100081.

[25] Antimicrobial resistance and its impact on cancer care | UICC, (n.d.). https://www.uicc.org/what-we-do/thematic-areas/antimicrobial-resistance-amr (accessed July 5, 2025).

[26] Drug-Resistant Infections: A Threat to Our Economic Future, (n.d.). https://www.worldbank.org/en/topic/health/publication/drug-resistant-infections-a-threat-to-our-economic-future (accessed July 5, 2025).

[27] R. Price, O'Neill report on antimicrobial resistance: funding for antimicrobial specialists should be improved, Eur J Hosp Pharm 23 (2016) 245–247. https://doi.org/10.1136/ejhpharm-2016-001013.

[28] K. Bush, P.A. Bradford, β-Lactams and β-Lactamase Inhibitors: An Overview, Cold Spring Harb Perspect Med 6 (2016) a025247. https://doi.org/10.1101/cshperspect.a025247.

[29] S. Kumar, M.M. Mukherjee, M.F. Varela, Modulation of Bacterial Multidrug Resistance Efflux Pumps of the Major Facilitator Superfamily, Int J Bacteriol 2013 (2013) 204141. https://doi.org/10.1155/2013/204141.

[30] J.M.A. Blair, M.A. Webber, A.J. Baylay, D.O. Ogbolu, L.J.V. Piddock, Molecular mechanisms of antibiotic resistance, Nat Rev Microbiol 13 (2015) 42–51. https://doi.org/10.1038/nrmicro3380.

[31] M.S. Ramirez, M.E. Tolmasky, Aminoglycoside modifying enzymes, Drug Resist Updat 13 (2010) 151–171. https://doi.org/10.1016/j.drup.2010.08.003.

[32] A. Robicsek, J. Strahilevitz, G.A. Jacoby, M. Macielag, D. Abbanat, C. Hye Park, K. Bush, D.C. Hooper, Fluoroquinolone-modifying enzyme: a new adaptation of a common aminoglycoside acetyltransferase, Nat Med 12 (2006) 83–88. https://doi.org/10.1038/nm1347.
[33] S. Schwarz, C. Kehrenberg, B. Doublet, A. Cloeckaert, Molecular basis of bacterial resistance to chloramphenicol and florfenicol, FEMS Microbiology Reviews 28 (2004) 519–542. https://doi.org/10.1016/j.femsre.2004.04.001.
[34] J.M. Blair, G.E. Richmond, L.J. Piddock, Multidrug Efflux Pumps in Gram-Negative Bacteria and Their Role in Antibiotic Resistance, Future Microbiology 9 (2014) 1165–1177. https://doi.org/10.2217/fmb.14.66.
[35] A. Kumar, H.P. Schweizer, Bacterial resistance to antibiotics: Active efflux and reduced uptake, Advanced Drug Delivery Reviews 57 (2005) 1486–1513. https://doi.org/10.1016/j.addr.2005.04.004.
[36] P.A. Lambert, Cellular impermeability and uptake of biocides and antibiotics in Gram-positive bacteria and mycobacteria, J Appl Microbiol 92 Suppl (2002) 46S-54S.
[37] C.M. Bébéar, S. Pereyre, Mechanisms of drug resistance in Mycoplasma pneumoniae, Curr Drug Targets Infect Disord 5 (2005) 263–271. https://doi.org/10.2174/1568005054880109.
[38] W.R. Miller, J.M. Munita, C.A. Arias, Mechanisms of antibiotic resistance in enterococci, Expert Review of Anti-Infective Therapy 12 (2014) 1221–1236. https://doi.org/10.1586/14787210.2014.956092.
[39] R.A. Weinstein, S.K. Fridkin, Vancomycin-Intermediate and -Resistant Staphylococcus aureus: What the Infectious Disease Specialist Needs to Know, Clinical Infectious Diseases 32 (2001) 108–115. https://doi.org/10.1086/317542.
[40] B.P. Howden, J.K. Davies, P.D.R. Johnson, T.P. Stinear, M.L. Grayson, Reduced Vancomycin Susceptibility in Staphylococcus aureus, Including Vancomycin-Intermediate and Heterogeneous Vancomycin-Intermediate Strains: Resistance Mechanisms, Laboratory Detection, and Clinical Implications, Clin Microbiol Rev 23 (2010) 99–139. https://doi.org/10.1128/CMR.00042-09.
[41] G. CORNAGLIA, A. MAZZARIOL, R. FONTANA, G. SATTA, Diffusion of Carbapenems Through the Outer Membrane of Enterobacteriaceae and Correlation of Their Activities with Their Periplasmic Concentrations, Microbial Drug Resistance 2 (1996) 273–276. https://doi.org/10.1089/mdr.1996.2.273.
[42] J.W. Chow, D.M. Shlaes, Imipenem resistance associated with the loss of a 40 kDa outer membrane protein in Enterobacter aerogenes, Journal of Antimicrobial Chemotherapy 28 (1991) 499–504. https://doi.org/10.1093/jac/28.4.499.
[43] A. Thiolas, C. Bornet, A. Davin-Régli, J.-M. Pagès, C. Bollet, Resistance to imipenem, cefepime, and cefpirome associated with mutation in Omp36 osmoporin of *Enterobacter aerogenes*, Biochemical and Biophysical Research Communications 317 (2004) 851–856. https://doi.org/10.1016/j.bbrc.2004.03.130.

[44] M.J. Gill, S. Simjee, K. Al-Hattawi, B.D. Robertson, C.S.F. Easmon, C.A. Ison, Gonococcal Resistance to β-Lactams and Tetracycline Involves Mutation in Loop 3 of the Porin Encoded at thepenB Locus, Antimicrobial Agents and Chemotherapy 42 (1998) 2799–2803. https://doi.org/10.1128/aac.42.11.2799.
[45] T.-F. Mah, Biofilm-Specific Antibiotic Resistance, Future Microbiology 7 (2012) 1061–1072. https://doi.org/10.2217/fmb.12.76.
[46] S.M. Soto, Role of efflux pumps in the antibiotic resistance of bacteria embedded in a biofilm, Virulence 4 (2013) 223–229. https://doi.org/10.4161/viru.23724.
[47] H. Van Acker, P. Van Dijck, T. Coenye, Molecular mechanisms of antimicrobial tolerance and resistance in bacterial and fungal biofilms, Trends in Microbiology 22 (2014) 326–333. https://doi.org/10.1016/j.tim.2014.02.001.
[48] A. Beceiro, M. Tomás, G. Bou, Antimicrobial Resistance and Virulence: a Successful or Deleterious Association in the Bacterial World?, Clin Microbiol Rev 26 (2013) 185–230. https://doi.org/10.1128/CMR.00059-12.
[49] W. Reygaert, Methicillin-resistant Staphylococcus aureus (MRSA): molecular aspects of antimicrobial resistance and virulence, Clin Lab Sci 22 (2009) 115–119.
[50] C.P. Randall, K.R. Mariner, I. Chopra, A.J. O'Neill, The Target of Daptomycin Is Absent from Escherichia coli and Other Gram-Negative Pathogens, Antimicrobial Agents and Chemotherapy 57 (2013) 637–639. https://doi.org/10.1128/aac.02005-12.
[51] G. Cox, G.D. Wright, Intrinsic antibiotic resistance: Mechanisms, origins, challenges and solutions, International Journal of Medical Microbiology 303 (2013) 287–292. https://doi.org/10.1016/j.ijmm.2013.02.009.
[52] S. Stefani, F. Campanile, M. Santagati, M.L. Mezzatesta, V. Cafiso, G. Pacini, Insights and clinical perspectives of daptomycin resistance in *Staphylococcus aureus*: A review of the available evidence, International Journal of Antimicrobial Agents 46 (2015) 278–289. https://doi.org/10.1016/j.ijantimicag.2015.05.008.
[53] S.-J. Yang, B.N. Kreiswirth, G. Sakoulas, M.R. Yeaman, Y.Q. Xiong, A. Sawa, A.S. Bayer, Enhanced Expression of dltABCD Is Associated with the Development of Daptomycin Nonsusceptibility in a Clinical Endocarditis Isolate of Staphylococcus aureus, The Journal of Infectious Diseases 200 (2009) 1916–1920. https://doi.org/10.1086/648473.
[54] N.N. Mishra, A.S. Bayer, C. Weidenmaier, T. Grau, S. Wanner, S. Stefani, V. Cafiso, T. Bertuccio, M.R. Yeaman, C.C. Nast, S.-J. Yang, Phenotypic and Genotypic Characterization of Daptomycin-Resistant Methicillin-Resistant Staphylococcus aureus Strains: Relative Roles of mprF and dlt Operons, PLOS ONE 9 (2014) e107426. https://doi.org/10.1371/journal.pone.0107426.
[55] G.M. Eliopoulos, G.M. Eliopoulos, M.C. Roberts, Tetracycline Therapy: Update, Clinical Infectious Diseases 36 (2003) 462–467. https://doi.org/10.1086/367622.

[56] M.C. Roberts, Resistance to macrolide, lincosamide, streptogramin, ketolide, and oxazolidinone antibiotics, Mol Biotechnol 28 (2004) 47–62. https://doi.org/10.1385/MB:28:1:47.
[57] P.M. Hawkey, Mechanisms of quinolone action and microbial response, Journal of Antimicrobial Chemotherapy 51 (2003) 29–35. https://doi.org/10.1093/jac/dkg207.
[58] L.S. Redgrave, S.B. Sutton, M.A. Webber, L.J.V. Piddock, Fluoroquinolone resistance: mechanisms, impact on bacteria, and role in evolutionary success, Trends in Microbiology 22 (2014) 438–445. https://doi.org/10.1016/j.tim.2014.04.007.
[59] M.E. Poey, E. de Los Santos, D. Aznarez, C.X. García-Laviña, M. Laviña, Genetics of resistance to trimethoprim in cotrimoxazole resistant uropathogenic Escherichia coli: integrons, transposons, and single gene cassettes, Front Microbiol 15 (2024) 1395953. https://doi.org/10.3389/fmicb.2024.1395953.
[60] M. Galgano, F. Pellegrini, E. Catalano, L. Capozzi, L. Del Sambro, A. Sposato, M.S. Lucente, V.I. Vasinioti, C. Catella, A.E. Odigie, M. Tempesta, A. Pratelli, P. Capozza, Acquired Bacterial Resistance to Antibiotics and Resistance Genes: From Past to Future, Antibiotics 14 (2025) 222. https://doi.org/10.3390/antibiotics14030222.
[61] P. Huovinen, L. Sundström, G. Swedberg, O. Sköld, Trimethoprim and sulfonamide resistance, Antimicrobial Agents and Chemotherapy 39 (1995) 279–289. https://doi.org/10.1128/aac.39.2.279.
[62] G. Vedantam, G.G. Guay, N.E. Austria, S.Z. Doktor, B.P. Nichols, Characterization of Mutations Contributing to Sulfathiazole Resistance in Escherichia coli, Antimicrobial Agents and Chemotherapy 42 (1998) 88–93. https://doi.org/10.1128/aac.42.1.88.
[63] N.A. Villagra, J.A. Fuentes, M.R. Jofré, A.A. Hidalgo, P. García, G.C. Mora, The carbon source influences the efflux pump-mediated antimicrobial resistance in clinically important Gram-negative bacteria, Journal of Antimicrobial Chemotherapy 67 (2012) 921–927. https://doi.org/10.1093/jac/dkr573.
[64] S. Wang, X. Sun, Q. Yuan, Strategies for enhancing microbial tolerance to inhibitors for biofuel production: A review, Bioresource Technology 258 (2018) 302–309. https://doi.org/10.1016/j.biortech.2018.03.064.
[65] L.J.V. Piddock, Clinically Relevant Chromosomally Encoded Multidrug Resistance Efflux Pumps in Bacteria, Clinical Microbiology Reviews 19 (2006) 382–402. https://doi.org/10.1128/cmr.19.2.382-402.2006.
[66] K. Poole, Efflux pumps as antimicrobial resistance mechanisms, Annals of Medicine 39 (2007) 162–176. https://doi.org/10.1080/07853890701195262.
[67] H.J. Field, R.A. Vere Hodge, Recent developments in anti-herpesvirus drugs, British Medical Bulletin 106 (2013) 213–249. https://doi.org/10.1093/bmb/ldt011.
[68] N. Kumar, S. Sharma, R. Kumar, V.K. Meena, S. Barua, Evolution of drug resistance against antiviral agents that target cellular factors, Virology 600 (2024) 110239. https://doi.org/10.1016/j.virol.2024.110239.

[69] K.K. Irwin, N. Renzette, T.F. Kowalik, J.D. Jensen, Antiviral drug resistance as an adaptive process, Virus Evol 2 (2016) vew014. https://doi.org/10.1093/ve/vew014.
[70] A.N. Matthew, F. Leidner, G.J. Lockbaum, M. Henes, J. Zephyr, S. Hou, N.R. Desaboini, J. Timm, L.N. Rusere, D.A. Ragland, J.L. Paulsen, K. Prachanronarong, D.I. Soumana, E.A. Nalivaika, N.K. Yilmaz, A. Ali, C.A. Schiffer, Drug design strategies to avoid resistance in direct-acting antivirals and beyond, Chem Rev 121 (2021) 3238–3270. https://doi.org/10.1021/acs.chemrev.0c00648.
[71] D.Z.H. Aw, D.X. Zhang, M. Vignuzzi, Strategies and efforts in circumventing the emergence of antiviral resistance against conventional antivirals, Npj Antimicrob Resist 3 (2025) 54. https://doi.org/10.1038/s44259-025-00125-z.
[72] T. Nora, C. Charpentier, O. Tenaillon, C. Hoede, F. Clavel, A.J. Hance, Contribution of Recombination to the Evolution of Human Immunodeficiency Viruses Expressing Resistance to Antiretroviral Treatment, Journal of Virology 81 (2007) 7620–7628. https://doi.org/10.1128/jvi.00083-07.
[73] A. Vere Hodge, H.J. Field, General Mechanisms of Antiviral Resistance, Genetics and Evolution of Infectious Disease (2011) 339–362. https://doi.org/10.1016/B978-0-12-384890-1.00013-3.
[74] V.N. Potaman, R.R. Sinden, DNA: Alternative Conformations and Biology, in: Madame Curie Bioscience Database [Internet], Landes Bioscience, 2013. https://www.ncbi.nlm.nih.gov/books/NBK6545/ (accessed July 17, 2025).
[75] Different form of DNA, (n.d.). http://www.bch.cuhk.edu.hk/vr_biomolecules/different-form-of-dna.html (accessed July 17, 2025).
[76] A.H.-J. Wang, G.J. Quigley, F.J. Kolpak, J.L. Crawford, J.H. van Boom, G. van der Marel, A. Rich, Molecular structure of a left-handed double helical DNA fragment at atomic resolution, Nature 282 (1979) 680–686. https://doi.org/10.1038/282680a0.
[77] S. Ravichandran, V.K. Subramani, K.K. Kim, Z-DNA in the genome: from structure to disease, Biophys Rev 11 (2019) 383–387. https://doi.org/10.1007/s12551-019-00534-1.
[78] T. Hermann, D.J. Patel, RNA bulges as architectural and recognition motifs, Structure 8 (2000) R47–R54. https://doi.org/10.1016/S0969-2126(00)00110-6.
[79] P.B. Moore, Structural motifs in RNA, Annu Rev Biochem 68 (1999) 287–300. https://doi.org/10.1146/annurev.biochem.68.1.287.
[80] C.M. Knobler, W.M. Gelbart, How and why RNA genomes are (partially) ordered in viral capsids, Current Opinion in Virology 52 (2022) 203–210. https://doi.org/10.1016/j.coviro.2021.11.014.
[81] A. Varshavsky, Discovering the RNA Double Helix and Hybridization, Cell 127 (2006) 1295–1297. https://doi.org/10.1016/j.cell.2006.12.008.

[82] P. Svoboda, A.Di. Cara, Hairpin RNA: a secondary structure of primary importance, Cell Mol Life Sci 63 (2006) 901–908. https://doi.org/10.1007/s00018-005-5558-5.
[83] Riboswitches, RNA Regulation | Learn Science at Scitable, (n.d.). https://www.nature.com/scitable/topicpage/riboswitches-a-common-rna-regulatory-element-14262702/ (accessed December 1, 2025).
[84] A. Serganov, D.J. Patel, Ribozymes, riboswitches and beyond: regulation of gene expression without proteins, Nat Rev Genet 8 (2007) 776–790. https://doi.org/10.1038/nrg2172.
[85] L.R. Ganser, M.L. Kelly, D. Herschlag, H.M. Al-Hashimi, The roles of structural dynamics in the cellular functions of RNAs, Nat Rev Mol Cell Biol 20 (2019) 474–489. https://doi.org/10.1038/s41580-019-0136-0.
[86] I. Bang, Chemische und physiologische Studien über die Guanylsäure., 32 (1901) 201–213. https://doi.org/10.1515/bchm2.1901.32.3-4.201.
[87] M. Gellert, M.N. Lipsett, D.R. Davies, HELIX FORMATION BY GUANYLIC ACID, Proc Natl Acad Sci U S A 48 (1962) 2013–2018. https://doi.org/10.1073/pnas.48.12.2013.
[88] D. Sen, W. Gilbert, Formation of parallel four-stranded complexes by guanine-rich motifs in DNA and its implications for meiosis, Nature 334 (1988) 364–366. https://doi.org/10.1038/334364a0.
[89] T.M. Bryan, P. Baumann, G-Quadruplexes: From Guanine Gels to Chemotherapeutics, Mol Biotechnol 49 (2011) 198–208. https://doi.org/10.1007/s12033-011-9395-5.
[90] T. van Mourik, A.J. Dingley, Characterization of the monovalent ion position and hydrogen-bond network in guanine quartets by DFT calculations of NMR parameters, Chemistry 11 (2005) 6064–6079. https://doi.org/10.1002/chem.200500198.
[91] Y. Chen, D. Yang, Sequence, Stability, Structure of G-Quadruplexes and Their Drug Interactions, Curr Protoc Nucleic Acid Chem CHAPTER (2012) Unit17.5. https://doi.org/10.1002/0471142700.nc1705s50.
[92] S. Neidle, S. Balasubramanian, Quadruplex Nucleic Acids, Royal Society of Chemistry, 2006.
[93] V. Esposito, A. Galeone, L. Mayol, G. Oliviero, A. Virgilio, L. Randazzo, A topological classification of G-quadruplex structures, Nucleosides Nucleotides Nucleic Acids 26 (2007) 1155–1159. https://doi.org/10.1080/15257770701527059.
[94] X. Cang, J. Šponer, T.E. Cheatham, Explaining the varied glycosidic conformational, G-tract length and sequence preferences for anti-parallel G-quadruplexes, Nucleic Acids Res 39 (2011) 4499–4512. https://doi.org/10.1093/nar/gkr031.
[95] A.T. Phan, Human telomeric G-quadruplex: structures of DNA and RNA sequences, The FEBS Journal 277 (2010) 1107–1117. https://doi.org/10.1111/j.1742-4658.2009.07464.x.
[96] Y. Wang, D.J. Patel, Solution structure of the *Tetrahymena* telomeric repeat d(T2G4)4 G-tetraplex, Structure 2 (1994) 1141–1156. https://doi.org/10.1016/S0969-2126(94)00117-0.

[97] J. Dai, M. Carver, C. Punchihewa, R.A. Jones, D. Yang, Structure of the Hybrid-2 type intramolecular human telomeric G-quadruplex in K+ solution: insights into structure polymorphism of the human telomeric sequence, Nucleic Acids Res 35 (2007) 4927–4940. https://doi.org/10.1093/nar/gkm522.
[98] V. Brázda, J. Kolomazník, J. Lýsek, M. Bartas, M. Fojta, J. Šťastný, J.-L. Mergny, G4Hunter web application: a web server for G-quadruplex prediction, Bioinformatics 35 (2019) 3493–3495. https://doi.org/10.1093/bioinformatics/btz087.
[99] S.K. Mishra, A. Tawani, A. Mishra, A. Kumar, G4IPDB: A database for G-quadruplex structure forming nucleic acid interacting proteins, Sci Rep 6 (2016) 38144. https://doi.org/10.1038/srep38144.
[100] P. Lejault, J. Mitteaux, F.R. Sperti, D. Monchaud, How to untie G-quadruplex knots and why?, Cell Chemical Biology 28 (2021) 436–455. https://doi.org/10.1016/j.chembiol.2021.01.015.
[101] S. Pandey, P. Agarwala, S. Maiti, Effect of loops and G-quartets on the stability of RNA G-quadruplexes, J Phys Chem B 117 (2013) 6896–6905. https://doi.org/10.1021/jp401739m.
[102] S. Ceschi, E. Largy, V. Gabelica, C. Sissi, A two-quartet G-quadruplex topology of human KIT2 is conformationally selected by a perylene derivative, Biochimie 179 (2020) 77–84. https://doi.org/10.1016/j.biochi.2020.09.015.
[103] D.-H. Zhang, T. Fujimoto, S. Saxena, H.-Q. Yu, D. Miyoshi, N. Sugimoto, Monomorphic RNA G-Quadruplex and Polymorphic DNA G-Quadruplex Structures Responding to Cellular Environmental Factors, Biochemistry 49 (2010) 4554–4563. https://doi.org/10.1021/bi1002822.
[104] M.M. Fay, S.M. Lyons, P. Ivanov, RNA G-quadruplexes in biology: principles and molecular mechanisms, J Mol Biol 429 (2017) 2127–2147. https://doi.org/10.1016/j.jmb.2017.05.017.
[105] S. Pandey, P. Agarwala, S. Maiti, Targeting RNA G-Quadruplexes for Potential Therapeutic Applications, in: A.L. Garner (Ed.), RNA Therapeutics, Springer International Publishing, Cham, 2018: pp. 177–206. https://doi.org/10.1007/7355_2016_22.
[106] H. Shu, R. Zhang, K. Xiao, J. Yang, X. Sun, G-Quadruplex-Binding Proteins: Promising Targets for Drug Design, Biomolecules 12 (2022) 648. https://doi.org/10.3390/biom12050648.
[107] R.K. Thakur, P. Kumar, K. Halder, A. Verma, A. Kar, J.-L. Parent, R. Basundra, A. Kumar, S. Chowdhury, Metastases suppressor NM23-H2 interaction with G-quadruplex DNA within c-MYC promoter nuclease hypersensitive element induces c-MYC expression, Nucleic Acids Research 37 (2009) 172–183. https://doi.org/10.1093/nar/gkn919.
[108] M. Melko, B. Bardoni, The role of G-quadruplex in RNA metabolism: Involvement of FMRP and FMR2P, Biochimie 92 (2010) 919–926. https://doi.org/10.1016/j.biochi.2010.05.018.
[109] P. Herviou, M. Le Bras, L. Dumas, C. Hieblot, J. Gilhodes, G. Cioci, J.-P. Hugnot, A. Ameadan, F. Guillonneau, E. Dassi, A. Cammas, S. Millevoi,

hnRNP H/F drive RNA G-quadruplex-mediated translation linked to genomic instability and therapy resistance in glioblastoma, Nat Commun 11 (2020) 2661. https://doi.org/10.1038/s41467-020-16168-x.
[110] B. Herdy, C. Mayer, D. Varshney, G. Marsico, P. Murat, C. Taylor, C. D'Santos, D. Tannahill, S. Balasubramanian, Analysis of NRAS RNA G-quadruplex binding proteins reveals DDX3X as a novel interactor of cellular G-quadruplex containing transcripts, Nucleic Acids Research 46 (2018) 11592–11604. https://doi.org/10.1093/nar/gky861.
[111] E. Tosoni, I. Frasson, M. Scalabrin, R. Perrone, E. Butovskaya, M. Nadai, G. Palù, D. Fabris, S.N. Richter, Nucleolin stabilizes G-quadruplex structures folded by the LTR promoter and silences HIV-1 viral transcription, Nucleic Acids Res 43 (2015) 8884–8897. https://doi.org/10.1093/nar/gkv897.
[112] M. Scalabrin, I. Frasson, E. Ruggiero, R. Perrone, E. Tosoni, S. Lago, M. Tassinari, G. Palù, S.N. Richter, The cellular protein hnRNP A2/B1 enhances HIV-1 transcription by unfolding LTR promoter G-quadruplexes, Sci Rep 7 (2017) 45244. https://doi.org/10.1038/srep45244.
[113] D. Ji, M. Juhas, C.M. Tsang, C.K. Kwok, Y. Li, Y. Zhang, Discovery of G-quadruplex-forming sequences in SARS-CoV-2, Brief Bioinform (2020) bbaa114. https://doi.org/10.1093/bib/bbaa114.
[114] A.B. Lorusso, J.A. Carrara, C.D.N. Barroso, F.F. Tuon, H. Faoro, Role of Efflux Pumps on Antimicrobial Resistance in Pseudomonas aeruginosa, Int J Mol Sci 23 (2022) 15779. https://doi.org/10.3390/ijms232415779.
[115] A. Sharma, Current Trends and Future Prospects of Antiviral Therapeutics, Infectious Diseases: Prevention and Control 2023 (2023). https://www.scitechnol.com/abstract/current-trends-and-future-prospects-of-antiviral-therapeutics-23556.html (accessed July 21, 2025).
[116] Y.-H. Yang, J. Buttery, Antimicrobial resistance: a global one-health problem for all ages, World J Pediatr 14 (2018) 521–522. https://doi.org/10.1007/s12519-018-0194-y.
[117] W.H. Organization, Global antimicrobial resistance and use surveillance system (GLASS) report 2022, World Health Organization, 2022.
[118] The true death toll of COVID-19 estimating global excess mortality, (n.d.). https://www.who.int/data/stories/the-true-death-toll-of-covid-19-estimating-global-excess-mortality (accessed July 21, 2025).
[119] S.K. Mishra, A. Kumar, G4IPDB: A database for G-quadruplex structure forming nucleic acid interacting proteins, Scientific Reports (2016). https://doi.org/10.1038/srep38144.
[120] O. Kikin, L. D'Antonio, P.S. Bagga, QGRS Mapper: a web-based server for predicting G-quadruplexes in nucleotide sequences, Nucleic Acids Res 34 (2006) W676-682. https://doi.org/10.1093/nar/gkl253.
[121] Y. Yu, Y. Ouyang, W. Yao, shinyCircos: an R/Shiny application for interactive creation of Circos plot, Bioinformatics 34 (2018) 1229–1231. https://doi.org/10.1093/bioinformatics/btx763.
[122] G.E. Crooks, G. Hon, J.-M. Chandonia, S.E. Brenner, WebLogo: a sequence logo generator, Genome Res 14 (2004) 1188–1190. https://doi.org/10.1101/gr.849004.

[123] NMR for Functional & Structural Biology Research, (n.d.). https://www.bruker.com/en/landingpages/bbio/nmr-for-functional-and-structural-biology-research.html (accessed July 26, 2025).
[124] S. Lee, The Power of 1D NMR in Molecular Analysis, (n.d.). https://www.numberanalytics.com/blog/power-of-1d-nmr-in-molecular-analysis (accessed July 26, 2025).
[125] D. Marion, An Introduction to Biological NMR Spectroscopy*, Molecular & Cellular Proteomics 12 (2013) 3006–3025. https://doi.org/10.1074/mcp.O113.030239.
[126] M. Adrian, B. Heddi, A.T. Phan, NMR spectroscopy of G-quadruplexes, Methods 57 (2012) 11–24. https://doi.org/10.1016/j.ymeth.2012.05.003.
[127] D.J. Patel, A.E. Tonelli, Assignment of the proton nmr chemical shifts of the T□N3H and G□N1H proton resonances in isolated AT and GC Watson-Crick base pairs in double-stranded deoxy oligonucleotides in aqueous solution, Biopolymers 13 (1974) 1943–1964. https://doi.org/10.1002/bip.1974.360131003.
[128] C. Lin, J. Dickerhoff, D. Yang, NMR Studies of G-Quadruplex Structures and G-Quadruplex-Interactive Compounds, Methods Mol Biol 2035 (2019) 157–176. https://doi.org/10.1007/978-1-4939-9666-7_9.
[129] Circular Dichroism, Chemistry LibreTexts (2013). https://chem.libretexts.org/Bookshelves/Physical_and_Theoretical_Chemistry_Textbook_Maps/Supplemental_Modules_(Physical_and_Theoretical_Chemistry)/Spectroscopy/Electronic_Spectroscopy/Circular_Dichroism (accessed July 26, 2025).
[130] B. Onel, G. Wu, D. Sun, C. Lin, D. Yang, Electrophoretic Mobility Shift Assay and Dimethyl Sulfate Footprinting for Characterization of G-Quadruplexes and G-Quadruplex-Protein Complexes, Methods Mol Biol 2035 (2019) 201–222. https://doi.org/10.1007/978-1-4939-9666-7_11.
[131] D.E. Wolf, Fundamentals of fluorescence and fluorescence microscopy, Methods Cell Biol 114 (2013) 69–97. https://doi.org/10.1016/B978-0-12-407761-4.00004-X.
[132] P. B, M. Ca, V. A, R. A, M. L, G. C, Thermodynamic analysis of quadruplex DNA-drug interaction, Nucleosides, Nucleotides & Nucleic Acids 26 (2007). https://doi.org/10.1080/15257770701499069.
[133] D. Mr, G. J, H. Ee, Isothermal titration calorimetry for measuring macromolecule-ligand affinity, Journal of Visualized Experiments : JoVE (2011). https://doi.org/10.3791/2796.
[134] W.H.J. Ward, G.A. Holdgate, 7 Isothermal Titration Calorimetry in Drug Discovery, in: F.D. King, A.W. Oxford (Eds.), Progress in Medicinal Chemistry, Elsevier, 2001: pp. 309–376. https://doi.org/10.1016/S0079-6468(08)70097-3.
[135] A. Velazquez-Campoy, S.A. Leavitt, E. Freire, Characterization of protein-protein interactions by isothermal titration calorimetry, Methods Mol Biol 1278 (2015) 183–204. https://doi.org/10.1007/978-1-4939-2425-7_11.

[136] Isothermal Titration Calorimetry (ITC) | Center for Macromolecular Interactions, (n.d.). https://cmi.hms.harvard.edu/isothermal-titration-calorimetry (accessed July 28, 2025).
[137] A. Saponaro, Isothermal Titration Calorimetry: A Biophysical Method to Characterize the Interaction between Label-free Biomolecules in Solution, Bio Protoc 8 (2018) e2957. https://doi.org/10.21769/BioProtoc.2957.
[138] Gene reporter assays | BMG LABTECH, (n.d.). https://www.bmglabtech.com/en/blog/gene-reporter-assays/ (accessed July 29, 2025).
[139] K. Halder, M. Benzler, J.S. Hartig, Reporter assays for studying quadruplex nucleic acids, Methods 57 (2012) 115–121. https://doi.org/10.1016/j.ymeth.2012.02.005.
[140] L. Benov, Improved Formazan Dissolution for Bacterial MTT Assay, Microbiology Spectrum 9 (2021) e01637-21. https://doi.org/10.1128/spectrum.01637-21.
[141] E. Grela, J. Kozłowska, A. Grabowiecka, Current methodology of MTT assay in bacteria – A review, Acta Histochemica 120 (2018) 303–311. https://doi.org/10.1016/j.acthis.2018.03.007.
[142] M.V. Berridge, P.M. Herst, A.S. Tan, Tetrazolium dyes as tools in cell biology: new insights into their cellular reduction, Biotechnol Annu Rev 11 (2005) 127–152. https://doi.org/10.1016/S1387-2656(05)11004-7.
[143] H. Wang, H. Cheng, F. Wang, D. Wei, X. Wang, An improved 3-(4,5-dimethylthiazol-2-yl)-2,5-diphenyl tetrazolium bromide (MTT) reduction assay for evaluating the viability of *Escherichia coli* cells, Journal of Microbiological Methods 82 (2010) 330–333. https://doi.org/10.1016/j.mimet.2010.06.014.
[144] J. Carmichael, W.G. DeGraff, A.F. Gazdar, J.D. Minna, J.B. Mitchell, Evaluation of a tetrazolium-based semiautomated colorimetric assay: assessment of chemosensitivity testing, Cancer Res 47 (1987) 936–942.
[145] A.K. Witte, P. Mester, S. Fister, B. Süß, M. Wagner, P. Rossmanith, PCR-Stop analysis as a new tool for qPCR assay validation, Sci Rep 8 (2018) 8275. https://doi.org/10.1038/s41598-018-26116-x.
[146] Quantitative PCR and Digital PCR Detection Methods, (n.d.). https://www.sigmaaldrich.com/IN/en/technical-documents/technical-article/genomics/qpcr/quantitative-pcr-and-digital-pcr-detection-methods?srsltid=AfmBOorc4mI-qL5ScfsfRSuzwptInCyUbRtSLWV7SEOziVVRyICALgGl (accessed July 30, 2025).
[147] The Role of Bacterial Biofilms in Antimicrobial Resistance, ASM.Org (n.d.). https://asm.org:443/articles/2023/march/the-role-of-bacterial-biofilms-in-antimicrobial-re (accessed July 29, 2025).
[148] L.B. Rice, Federal Funding for the Study of Antimicrobial Resistance in Nosocomial Pathogens: No ESKAPE, The Journal of Infectious Diseases 197 (2008) 1079–1081. https://doi.org/10.1086/533452.
[149] Z. Shamsizadeh, M. Nikaeen, B. Nasr Esfahani, S.H. Mirhoseini, M. Hatamzadeh, A. Hassanzadeh, Detection of antibiotic resistant *Acinetobacter*

baumannii in various hospital environments: potential sources for transmission of Acinetobacter infections, Environ Health Prev Med 22 (2017) 44. https://doi.org/10.1186/s12199-017-0653-4.
[150] D.J. Weber, D. Anderson, W.A. Rutala, The role of the surface environment in healthcare-associated infections, Curr Opin Infect Dis 26 (2013) 338–344. https://doi.org/10.1097/QCO.0b013e3283630f04.
[151] A. Al Atrouni, M.-L. Joly-Guillou, M. Hamze, M. Kempf, Reservoirs of Non-baumannii Acinetobacter Species, Front Microbiol 7 (2016) 49. https://doi.org/10.3389/fmicb.2016.00049.
[152] I. Roca, P. Espinal, X. Vila-Farrés, J. Vila, The *Acinetobacter baumannii* Oxymoron: Commensal Hospital Dweller Turned Pan-Drug-Resistant Menace, Front Microbiol 3 (2012) 148. https://doi.org/10.3389/fmicb.2012.00148.
[153] S.B. Almasaudi, Acinetobacter spp. as nosocomial pathogens: Epidemiology and resistance features, Saudi Journal of Biological Sciences 25 (2018) 586–596. https://doi.org/10.1016/j.sjbs.2016.02.009.
[154] K. Montefour, J. Frieden, S. Hurst, C. Helmich, D. Headley, M. Martin, D.A. Boyle, *Acinetobacter baumannii*: an emerging multidrug-resistant pathogen in critical care, Crit Care Nurse 28 (2008) 15–25; quiz 26.
[155] Acinetobacter infection: Treatment and prevention - UpToDate, (n.d.). https://www.uptodate.com/contents/acinetobacter-infection-treatment-and-prevention/print (accessed July 3, 2022).
[156] N. Kosiol, S. Juranek, P. Brossart, A. Heine, K. Paeschke, G-quadruplexes: a promising target for cancer therapy, Molecular Cancer 20 (2021) 40. https://doi.org/10.1186/s12943-021-01328-4.
[157] J.A. Kulkarni, D. Witzigmann, S.B. Thomson, S. Chen, B.R. Leavitt, P.R. Cullis, R. van der Meel, The current landscape of nucleic acid therapeutics, Nat. Nanotechnol. 16 (2021) 630–643. https://doi.org/10.1038/s41565-021-00898-0.
[158] E. Ruggiero, S.N. Richter, G-quadruplexes and G-quadruplex ligands: targets and tools in antiviral therapy, Nucleic Acids Res 46 (2018) 3270–3283. https://doi.org/10.1093/nar/gky187.
[159] H. Eichner, J. Karlsson, E. Loh, The emerging role of bacterial regulatory RNAs in disease, Trends in Microbiology 0 (2022). https://doi.org/10.1016/j.tim.2022.03.007.
[160] N. Jain, S.K. Mishra, U. Shankar, A. Jaiswal, T.K. Sharma, P. Kodgire, A. Kumar, G-quadruplex stabilization in the ions and maltose transporters gene inhibit Salmonella enterica growth and virulence, Genomics 112 (2020) 4863–4874. https://doi.org/10.1016/j.ygeno.2020.09.010.
[161] U. Shankar, N. Jain, S.K. Mishra, T.K. Sharma, A. Kumar, Conserved G-Quadruplex Motifs in Gene Promoter Region Reveals a Novel Therapeutic Approach to Target Multi-Drug Resistance Klebsiella pneumoniae, Front Microbiol 11 (2020) 1269. https://doi.org/10.3389/fmicb.2020.01269.
[162] A. Verma, K. Halder, R. Halder, V.K. Yadav, P. Rawal, R.K. Thakur, F. Mohd, A. Sharma, S. Chowdhury, Genome-wide computational and expression analyses reveal G-quadruplex DNA motifs as conserved cis-regulatory

elements in human and related species, J Med Chem 51 (2008) 5641–5649. https://doi.org/10.1021/jm800448a.
[163] N. Beaume, R. Pathak, V.K. Yadav, S. Kota, H.S. Misra, H.K. Gautam, S. Chowdhury, Genome-wide study predicts promoter-G4 DNA motifs regulate selective functions in bacteria: radioresistance of D. radiodurans involves G4 DNA-mediated regulation, Nucleic Acids Res 41 (2013) 76–89. https://doi.org/10.1093/nar/gks1071.
[164] R. Perrone, E. Lavezzo, E. Riello, R. Manganelli, G. Palù, S. Toppo, R. Provvedi, S.N. Richter, Mapping and characterization of G-quadruplexes in Mycobacterium tuberculosis gene promoter regions, Sci Rep 7 (2017) 5743. https://doi.org/10.1038/s41598-017-05867-z.
[165] N. Smargiasso, V. Gabelica, C. Damblon, F. Rosu, E. De Pauw, M.-P. Teulade-Fichou, J.A. Rowe, A. Claessens, Putative DNA G-quadruplex formation within the promoters of Plasmodium falciparum var genes, BMC Genomics 10 (2009) 362. https://doi.org/10.1186/1471-2164-10-362.
[166] R. Garg, J. Aggarwal, B. Thakkar, Genome-wide discovery of G-quadruplex forming sequences and their functional relevance in plants, Sci Rep 6 (2016) 28211. https://doi.org/10.1038/srep28211.
[167] V. Yadav, Hemansi, N. Kim, N. Tuteja, P. Yadav, G Quadruplex in Plants: A Ubiquitous Regulatory Element and Its Biological Relevance, Front Plant Sci 8 (2017) 1163. https://doi.org/10.3389/fpls.2017.01163.
[168] G. Biffi, D. Tannahill, J. Miller, W.J. Howat, S. Balasubramanian, Elevated Levels of G-Quadruplex Formation in Human Stomach and Liver Cancer Tissues, PLoS One 9 (2014) e102711. https://doi.org/10.1371/journal.pone.0102711.
[169] R. Simone, R. Balendra, T.G. Moens, E. Preza, K.M. Wilson, A. Heslegrave, N.S. Woodling, T. Niccoli, J. Gilbert-Jaramillo, S. Abdelkarim, E.L. Clayton, M. Clarke, M. Konrad, A.J. Nicoll, J.S. Mitchell, A. Calvo, A. Chio, H. Houlden, J.M. Polke, M.A. Ismail, C.E. Stephens, T. Vo, A.A. Farahat, W.D. Wilson, D.W. Boykin, H. Zetterberg, L. Partridge, S. Wray, G. Parkinson, S. Neidle, R. Patani, P. Fratta, A.M. Isaacs, G-quadruplex-binding small molecules ameliorate C9orf72 FTD/ALS pathology in vitro and in vivo, EMBO Mol Med 10 (2018) 22–31. https://doi.org/10.15252/emmm.201707850.
[170] P. Yadav, N. Kim, M. Kumari, S. Verma, T.K. Sharma, V. Yadav, A. Kumar, G-Quadruplex Structures in Bacteria: Biological Relevance and Potential as an Antimicrobial Target, J Bacteriol 203 (n.d.) e00577-20. https://doi.org/10.1128/JB.00577-20.
[171] N. Jain, U. Shankar, A. Kumar, Conserved G-Quadruplex Motifs Regulate Gene Expression in Neisseria meningitidis, ACS Infect. Dis. 8 (2022) 728–743. https://doi.org/10.1021/acsinfecdis.1c00383.
[172] S.K. Mishra, U. Shankar, N. Jain, K. Sikri, J.S. Tyagi, T.K. Sharma, J.-L. Mergny, A. Kumar, Characterization of G-Quadruplex Motifs in espB, espK, and cyp51 Genes of Mycobacterium tuberculosis as Potential Drug Targets, Mol Ther Nucleic Acids 16 (2019) 698–706. https://doi.org/10.1016/j.omtn.2019.04.022.

[173] S.K. Mishra, N. Jain, U. Shankar, A. Tawani, T.K. Sharma, A. Kumar, Characterization of highly conserved G-quadruplex motifs as potential drug targets in Streptococcus pneumoniae, Sci Rep 9 (2019) 1791. https://doi.org/10.1038/s41598-018-38400-x.
[174] L.L. Prister, S. Yin, L.A. Cahoon, H.S. Seifert, Altering the Neisseria gonorrhoeae pilE Guanine Quadruplex Loop Bases Affects Pilin Antigenic Variation, Biochemistry 59 (2020) 1104–1112. https://doi.org/10.1021/acs.biochem.9b01038.
[175] I.T. Holder, J.S. Hartig, A Matter of Location: Influence of G-Quadruplexes on Escherichia coli Gene Expression, Chemistry & Biology 21 (2014) 1511–1521. https://doi.org/10.1016/j.chembiol.2014.09.014.
[176] Z.A.E. Waller, B.J. Pinchbeck, B.S. Buguth, T.G. Meadows, D.J. Richardson, A.J. Gates, Control of bacterial nitrate assimilation by stabilization of G-quadruplex DNA, Chem. Commun. 52 (2016) 13511–13514. https://doi.org/10.1039/C6CC06057A.
[177] U. Shankar, S.K. Mishra, N. Jain, A. Tawani, P. Yadav, A. Kumar, Ni+2 permease system of Helicobacter pylori contains highly conserved G-quadruplex motifs, Infection, Genetics and Evolution 101 (2022) 105298. https://doi.org/10.1016/j.meegid.2022.105298.
[178] U. Shankar, N. Jain, P. Majee, P. Kodgire, T.K. Sharma, A. Kumar, Exploring Computational and Biophysical Tools to Study the Presence of G-Quadruplex Structures: A Promising Therapeutic Solution for Drug-Resistant Vibrio cholerae, Frontiers in Genetics 11 (2020). https://www.frontiersin.org/articles/10.3389/fgene.2020.00935 (accessed November 7, 2022).
[179] P. Majee, A. Pattnaik, B.R. Sahoo, U. Shankar, A.K. Pattnaik, A. Kumar, D. Nayak, Inhibition of Zika virus replication by G-quadruplex-binding ligands, Mol Ther Nucleic Acids 23 (2021) 691–701. https://doi.org/10.1016/j.omtn.2020.12.030.
[180] C. Lalitha, T. Raman, S.S. Rathore, M. Ramar, A. Munusamy, J. Ramakrishnan, ASK2 Bioactive Compound Inhibits MDR Klebsiella pneumoniae by Antibiofilm Activity, Modulating Macrophage Cytokines and Opsonophagocytosis, Frontiers in Cellular and Infection Microbiology 7 (2017). https://www.frontiersin.org/articles/10.3389/fcimb.2017.00346 (accessed October 5, 2022).
[181] G. Kerbauy, A.C.P. Vivan, G.C. Simões, A.S. Simionato, M. Pelisson, E.C. Vespero, S.F. Costa, C.G.T. de J. Andrade, D.M. Barbieri, J.C.P. Mello, A.T. Morey, L.M. Yamauchi, S.F. Yamada-Ogatta, A.G. de Oliveira, G. Andrade, Effect of a Metalloantibiotic Produced by Pseudomonas aeruginosa on Klebsiella pneumoniae Carbapenemase (KPC)-producing K. pneumoniae, Current Pharmaceutical Biotechnology 17 (n.d.) 389–397.
[182] M. Vt, P. At, Bulges in G-quadruplexes: broadening the definition of G-quadruplex-forming sequences, Journal of the American Chemical Society 135 (2013). https://doi.org/10.1021/ja310251r.

[183] J. Jana, S. Mohr, Y.M. Vianney, K. Weisz, Structural motifs and intramolecular interactions in non-canonical G-quadruplexes, RSC Chem. Biol. 2 (2021) 338–353. https://doi.org/10.1039/D0CB00211A.
[184] J. Jana, K. Weisz, Thermodynamic Stability of G-Quadruplexes: Impact of Sequence and Environment, Chembiochem 22 (2021) 2848–2856. https://doi.org/10.1002/cbic.202100127.
[185] S. Amrane, M. Adrian, B. Heddi, A. Serero, A. Nicolas, J.-L. Mergny, A.T. Phan, Formation of Pearl-Necklace Monomorphic G-Quadruplexes in the Human CEB25 Minisatellite, J. Am. Chem. Soc. 134 (2012) 5807–5816. https://doi.org/10.1021/ja208993r.
[186] R.W. Harkness, A.K. Mittermaier, G-register exchange dynamics in guanine quadruplexes, Nucleic Acids Res 44 (2016) 3481–3494. https://doi.org/10.1093/nar/gkw190.
[187] K.-I. Oh, J. Kim, C.-J. Park, J.-H. Lee, Dynamics Studies of DNA with Non-canonical Structure Using NMR Spectroscopy, Int J Mol Sci 21 (2020) 2673. https://doi.org/10.3390/ijms21082673.
[188] J.T. Grün, C. Hennecker, D.-P. Klötzner, R.W. Harkness, I. Bessi, A. Heckel, A.K. Mittermaier, H. Schwalbe, Conformational Dynamics of Strand Register Shifts in DNA G-Quadruplexes, J. Am. Chem. Soc. 142 (2020) 264–273. https://doi.org/10.1021/jacs.9b10367.
[189] W. Yuan, L. Wan, H. Peng, Y. Zhong, W. Cai, Y. Zhang, W. Ai, J. Wu, The influencing factors and functions of DNA G-quadruplexes, Cell Biochem Funct 38 (2020) 524–532. https://doi.org/10.1002/cbf.3505.
[190] C. Liu, B. Zhou, Y. Geng, D.Y. Tam, R. Feng, H. Miao, N. Xu, X. Shi, Y. You, Y. Hong, B.Z. Tang, P.K. Lo, V. Kuryavyi, G. Zhu, A chair-type G-quadruplex structure formed by a human telomeric variant DNA in K+ solution, Chem. Sci. 10 (2018) 218–226. https://doi.org/10.1039/C8SC03813A.
[191] K.W. Lim, S. Amrane, S. Bouaziz, W. Xu, Y. Mu, D.J. Patel, K.N. Luu, A.T. Phan, Structure of the Human Telomere in K+ Solution: A Stable Basket-Type G-Quadruplex with Only Two G-Tetrad Layers, J. Am. Chem. Soc. 131 (2009) 4301–4309. https://doi.org/10.1021/ja807503g.
[192] S. Bielskutė, J. Plavec, P. Podbevšek, Oxidative lesions modulate G-quadruplex stability and structure in the human BCL2 promoter, Nucleic Acids Research 49 (2021) 2346–2356. https://doi.org/10.1093/nar/gkab057.
[193] Y. Ma, K. Iida, K. Nagasawa, Topologies of G-quadruplex: Biological functions and regulation by ligands, Biochemical and Biophysical Research Communications 531 (2020) 3–17. https://doi.org/10.1016/j.bbrc.2019.12.103.
[194] R. del Villar-Guerra, J.O. Trent, J.B. Chaires, G-quadruplex secondary structure from circular dichroism spectroscopy, Angew Chem Int Ed Engl 57 (2018) 7171–7175. https://doi.org/10.1002/anie.201709184.
[195] S. Burge, G.N. Parkinson, P. Hazel, A.K. Todd, S. Neidle, Quadruplex DNA: sequence, topology and structure, Nucleic Acids Res 34 (2006) 5402–5415. https://doi.org/10.1093/nar/gkl655.

[196] J. Carvalho, J.A. Queiroz, C. Cruz, Circular Dichroism of G-Quadruplex: a Laboratory Experiment for the Study of Topology and Ligand Binding, J. Chem. Educ. 94 (2017) 1547–1551. https://doi.org/10.1021/acs.jchemed.7b00160.
[197] V. Víglaský, L. Bauer, K. Tlučková, Structural Features of Intra- and Intermolecular G-Quadruplexes Derived from Telomeric Repeats, Biochemistry 49 (2010) 2110–2120. https://doi.org/10.1021/bi902099u.
[198] D. Sun, L.H. Hurley, Biochemical Techniques for the Characterization of G-Quadruplex Structures: EMSA, DMS Footprinting, and DNA Polymerase Stop Assay, Methods Mol Biol 608 (2010) 65–79. https://doi.org/10.1007/978-1-59745-363-9_5.
[199] P.A. Rachwal, T. Brown, K.R. Fox, Effect of G-Tract Length on the Topology and Stability of Intramolecular DNA Quadruplexes, Biochemistry 46 (2007) 3036–3044. https://doi.org/10.1021/bi062118j.
[200] S.-T.D. Hsu, P. Varnai, A. Bugaut, A.P. Reszka, S. Neidle, S. Balasubramanian, A G-Rich Sequence within the c-kit Oncogene Promoter Forms a Parallel G-Quadruplex Having Asymmetric G-Tetrad Dynamics, J. Am. Chem. Soc. 131 (2009) 13399–13409. https://doi.org/10.1021/ja904007p.
[201] M. Read, R.J. Harrison, B. Romagnoli, F.A. Tanious, S.H. Gowan, A.P. Reszka, W.D. Wilson, L.R. Kelland, S. Neidle, Structure-based design of selective and potent G quadruplex-mediated telomerase inhibitors, Proceedings of the National Academy of Sciences 98 (2001) 4844–4849. https://doi.org/10.1073/pnas.081560598.
[202] S. Burge, G.N. Parkinson, P. Hazel, A.K. Todd, S. Neidle, Quadruplex DNA: sequence, topology and structure, Nucleic Acids Res 34 (2006) 5402–5415. https://doi.org/10.1093/nar/gkl655.
[203] C. R. Buchholz, W.C. K. Pomerantz, 19 F NMR viewed through two different lenses: ligand-observed and protein-observed 19 F NMR applications for fragment-based drug discovery, RSC Chemical Biology 2 (2021) 1312–1330. https://doi.org/10.1039/D1CB00085C.
[204] B. Machireddy, H.-J. Sullivan, C. Wu, Binding of BRACO19 to a Telomeric G-Quadruplex DNA Probed by All-Atom Molecular Dynamics Simulations with Explicit Solvent, Molecules 24 (2019) 1010. https://doi.org/10.3390/molecules24061010.
[205] R. Malhotra, C. Rarhi, K.V. Diveshkumar, P. Bommisetti, S.P.P. Pany, S. Roy, P.I. Pradeepkumar, M. Kundu, Pyridopyrimidinone Derivatives as DNAG-Quadruplex-Stabilizing Agents: Design, Synthesis and Biophysical Studies, ChemistrySelect 2 (2017) 5206–5213. https://doi.org/10.1002/slct.201700677.
[206] S. Shi, S. Gao, T. Cao, J. Liu, X. Gao, J. Hao, C. Lv, H. Huang, J. Xu, T. Yao, Targeting Human Telomeric G-Quadruplex DNA and Inhibition of Telomerase Activity With [(dmb)2Ru(obip)Ru(dmb)2]4+, PLOS ONE 8 (2013) e84419. https://doi.org/10.1371/journal.pone.0084419.
[207] A. Marchand, F. Rosu, R. Zenobi, V. Gabelica, Thermal Denaturation of DNA G-Quadruplexes and Their Complexes with Ligands: Thermodynamic

Analysis of the Multiple States Revealed by Mass Spectrometry, J. Am. Chem. Soc. 140 (2018) 12553–12565. https://doi.org/10.1021/jacs.8b07302.
[208] Y. Katsuda, S.-I. Sato, L. Asano, Y. Morimura, T. Furuta, H. Sugiyama, M. Hagihara, M. Uesugi, A Small Molecule That Represses Translation of G-Quadruplex-Containing mRNA, J Am Chem Soc 138 (2016) 9037–9040. https://doi.org/10.1021/jacs.6b04506.
[209] A. Gedefie, W. Demsis, M. Ashagrie, Y. Kassa, M. Tesfaye, M. Tilahun, H. Bisetegn, Z. Sahle, *Acinetobacter baumannii* Biofilm Formation and Its Role in Disease Pathogenesis: A Review, Infect Drug Resist 14 (2021) 3711–3719. https://doi.org/10.2147/IDR.S332051.
[210] J.A. Gaddy, L.A. Actis, Regulation of *Acinetobacter baumannii* biofilm formation, Future Microbiol 4 (2009) 273–278. https://doi.org/10.2217/fmb.09.5.
[211] V. Cepas, Y. López, E. Muñoz, D. Rolo, C. Ardanuy, S. Martí, M. Xercavins, J.P. Horcajada, J. Bosch, S.M. Soto, Relationship Between Biofilm Formation and Antimicrobial Resistance in Gram-Negative Bacteria, Microbial Drug Resistance 25 (2019) 72–79. https://doi.org/10.1089/mdr.2018.0027.
[212] P. Bowler, C. Murphy, R. Wolcott, Biofilm exacerbates antibiotic resistance: Is this a current oversight in antimicrobial stewardship?, Antimicrobial Resistance & Infection Control 9 (2020) 162. https://doi.org/10.1186/s13756-020-00830-6.
[213] J.L. Mergny, C. Hélène, G-quadruplex DNA: a target for drug design, Nat Med 4 (1998) 1366–1367. https://doi.org/10.1038/3949.
[214] G.M. Cerqueira, A.Y. Peleg, Insights into *Acinetobacter baumannii* pathogenicity, IUBMB Life 63 (2011) 1055–1060. https://doi.org/10.1002/iub.533.
[215] L.A. Ronish, E. Lillehoj, J.K. Fields, E.J. Sundberg, K.H. Piepenbrink, The structure of PilA from *Acinetobacter baumannii* AB5075 suggests a mechanism for functional specialization in Acinetobacter type IV pili, J Biol Chem 294 (2019) 218–230. https://doi.org/10.1074/jbc.RA118.005814.
[216] S. Abdollahi, Z. Raoufi, M.H. Fakoor, Physicochemical and structural characterization, epitope mapping and vaccine potential investigation of a new protein containing Tetratrico Peptide Repeats of *Acinetobacter baumannii*: An in-silico and in-vivo approach, Mol Immunol 140 (2021) 22–34. https://doi.org/10.1016/j.molimm.2021.10.004.
[217] M. Sumyk, S. Himpich, W.E. Foong, A. Herrmann, K.M. Pos, H.-K. Tam, Binding of Tetracyclines to *Acinetobacter baumannii* TetR Involves Two Arginines as Specificity Determinants, Front Microbiol 12 (2021) 711158. https://doi.org/10.3389/fmicb.2021.711158.
[218] Y. Zhao, M. Lei, Y. Wu, C. Wang, Z. Zhang, F. Deng, H. Wang, Molecular cloning and expression of the complete DNA sequence encoding NAD+-dependent acetaldehyde dehydrogenase fromAcinetobacter sp. strain HBS-2, Ann. Microbiol. 59 (2009) 97–104. https://doi.org/10.1007/BF03175605.
[219] C. Nardella, D. Boi, M.L. di Salvo, A. Barile, J. Stetefeld, A. Tramonti, R. Contestabile, Isolation of a Complex Formed Between *Acinetobacter*

baumannii HemA and HemL, Key Enzymes of Tetrapyrroles Biosynthesis, Front Mol Biosci 6 (2019) 6. https://doi.org/10.3389/fmolb.2019.00006.
[220] N.-H. Le, K. Peters, A. Espaillat, J.R. Sheldon, J. Gray, G. Di Venanzio, J. Lopez, B. Djahanschiri, E.A. Mueller, S.W. Hennon, P.A. Levin, I. Ebersberger, E.P. Skaar, F. Cava, W. Vollmer, M.F. Feldman, Peptidoglycan editing provides immunity to *Acinetobacter baumannii* during bacterial warfare, Science Advances 6 (2020) eabb5614. https://doi.org/10.1126/sciadv.abb5614.
[221] P.K. Sahu, P.S. Iyer, M.B. Gaikwad, S.C. Talreja, K.R. Pardesi, B.A. Chopade, An MFS Transporter-Like ORF from MDR *Acinetobacter baumannii* AIIMS 7 Is Associated with Adherence and Biofilm Formation on Biotic/Abiotic Surface, Int J Microbiol 2012 (2012) 490647. https://doi.org/10.1155/2012/490647.
[222] X. Shao, W. Zhang, M.I. Umar, H.Y. Wong, Z. Seng, Y. Xie, Y. Zhang, L. Yang, C.K. Kwok, X. Deng, RNA G-Quadruplex Structures Mediate Gene Regulation in Bacteria, mBio 11 (2020) e02926-19. https://doi.org/10.1128/mBio.02926-19.
[223] S. Burge, G.N. Parkinson, P. Hazel, A.K. Todd, S. Neidle, Quadruplex DNA: sequence, topology and structure, Nucleic Acids Res 34 (2006) 5402–5415. https://doi.org/10.1093/nar/gkl655.
[224] D. Varshney, J. Spiegel, K. Zyner, D. Tannahill, S. Balasubramanian, The regulation and functions of DNA and RNA G-quadruplexes, Nature Reviews Molecular Cell Biology 21 (2020). https://doi.org/10.1038/s41580-020-0236-x.
[225] Z. Zhang, J. Dai, E. Veliath, R.A. Jones, D. Yang, Structure of a two-G-tetrad intramolecular G-quadruplex formed by a variant human telomeric sequence in K+ solution: insights into the interconversion of human telomeric G-quadruplex structures, Nucleic Acids Res 38 (2010) 1009–1021. https://doi.org/10.1093/nar/gkp1029.
[226] H.-L. Bao, H. Liu, Y. Xu, Hybrid-type and two-tetrad antiparallel telomere DNA G-quadruplex structures in living human cells, Nucleic Acids Research 47 (2019) 4940–4947. https://doi.org/10.1093/nar/gkz276.
[227] P. Basu, I. Kejnovská, M. Gajarský, D. Šubert, T. Mikešová, D. Renčiuk, L. Trantírek, J.-L. Mergny, M. Vorlíčková, RNA G-quadruplex formation in biologically important transcribed regions: can two-tetrad intramolecular RNA quadruplexes be formed?, Nucleic Acids Res 52 (2024) 13224–13242. https://doi.org/10.1093/nar/gkae927.
[228] M. Qin, Z. Chen, Q. Luo, Y. Wen, N. Zhang, H. Jiang, H. Yang, Two-quartet G-quadruplexes formed by DNA sequences containing four contiguous GG runs, J Phys Chem B 119 (2015) 3706–3713. https://doi.org/10.1021/jp512914t.
[229] E.-A. Raiber, R. Kranaster, E. Lam, M. Nikan, S. Balasubramanian, A non-canonical DNA structure is a binding motif for the transcription factor SP1 in vitro, Nucleic Acids Res 40 (2012) 1499–1508. https://doi.org/10.1093/nar/gkr882.

[230] G. Marsico, V.S. Chambers, A.B. Sahakyan, P. McCauley, J.M. Boutell, M.D. Antonio, S. Balasubramanian, Whole genome experimental maps of DNA G-quadruplexes in multiple species, Nucleic Acids Res 47 (2019) 3862–3874. https://doi.org/10.1093/nar/gkz179.
[231] O.E. Ahuatzin-Flores, E. Torres, E. Chávez-Bravo, *Acinetobacter baumannii*, a Multidrug-Resistant Opportunistic Pathogen in New Habitats: A Systematic Review, Microorganisms 12 (2024) 644. https://doi.org/10.3390/microorganisms12040644.
[232] A. Sharma, V. Dubey, R. Sharma, K. Devnath, V.K. Gupta, J. Akhter, T. Bhando, A. Verma, K. Ambatipudi, M. Sarkar, R. Pathania, The unusual glycine-rich C terminus of the *Acinetobacter baumannii* RNA chaperone Hfq plays an important role in bacterial physiology, J Biol Chem 293 (2018) 13377–13388. https://doi.org/10.1074/jbc.RA118.002921.
[233] T.J. Soper, K. Doxzen, S.A. Woodson, Major role for mRNA binding and restructuring in sRNA recruitment by Hfq, RNA 17 (2011) 1544–1550. https://doi.org/10.1261/rna.2767211.
[234] A. Sett, P.K. Maiti, K. Garg, A. Hussain, S. Saini, S. Pandey, R. Pathania, 'GGFGGQ' repeats in Hfq of *Acinetobacter baumannii* are essential for nutrient utilization and virulence, J Biol Chem 300 (2024) 107895. https://doi.org/10.1016/j.jbc.2024.107895.
[235] H.A. Vincent, C.A. Henderson, T.J. Ragan, A. Garza-Garcia, P.D. Cary, D.M. Gowers, M. Malfois, P.C. Driscoll, F. Sobott, A.J. Callaghan, Characterization of Vibrio cholerae Hfq Provides Novel Insights into the Role of the Hfq C-Terminal Region, J Mol Biol 420 (2012) 56–69. https://doi.org/10.1016/j.jmb.2012.03.028.
[236] M. Sarshar, D. Scribano, A.T. Palamara, C. Ambrosi, A. Masotti, The *Acinetobacter baumannii* model can explain the role of small non-coding RNAs as potential mediators of host-pathogen interactions, Front. Mol. Biosci. 9 (2022). https://doi.org/10.3389/fmolb.2022.1088783.
[237] H.-Y. Kuo, H.-H. Chao, P.-C. Liao, L. Hsu, K.-C. Chang, C.-H. Tung, C.-H. Chen, M.-L. Liou, Functional Characterization of *Acinetobacter baumannii* Lacking the RNA Chaperone Hfq, Front Microbiol 8 (2017) 2068. https://doi.org/10.3389/fmicb.2017.02068.
[238] A. Santiago-Frangos, J.R. Jeliazkov, J.J. Gray, S.A. Woodson, Acidic C-terminal domains autoregulate the RNA chaperone Hfq, eLife 6 (2017) e27049. https://doi.org/10.7554/eLife.27049.
[239] E. Sonnleitner, K. Prindl, U. Bläsi, The Pseudomonas aeruginosa CrcZ RNA interferes with Hfq-mediated riboregulation, PLOS ONE 12 (2017) e0180887. https://doi.org/10.1371/journal.pone.0180887.
[240] V.J. Parekh, F. Wien, W. Grange, T.A. De Long, V. Arluison, R.R. Sinden, Crucial Role of the C-Terminal Domain of Hfq Protein in Genomic Instability, Microorganisms 8 (2020) 1598. https://doi.org/10.3390/microorganisms8101598.
[241] P. Rawal, V.B.R. Kummarasetti, J. Ravindran, N. Kumar, K. Halder, R. Sharma, M. Mukerji, S.K. Das, S. Chowdhury, Genome-wide prediction of

G4 DNA as regulatory motifs: Role in Escherichia coli global regulation, Genome Res 16 (2006) 644–655. https://doi.org/10.1101/gr.4508806.
[242] J. Trouillon, K. Han, I. Attrée, S. Lory, The core and accessory Hfq interactomes across Pseudomonas aeruginosa lineages, Nat Commun 13 (2022) 1258. https://doi.org/10.1038/s41467-022-28849-w.
[243] M. Hayashi-Nishino, A. Fukushima, K. Nishino, Impact of Hfq on the Intrinsic Drug Resistance of Salmonella Enterica Serovar Typhimurium, Front. Microbiol. 3 (2012). https://doi.org/10.3389/fmicb.2012.00205.
[244] E. Ruhland, M. Siemers, R. Gerst, F. Späth, L.N. Vogt, M.T. Figge, K. Papenfort, K.S. Fröhlich, The global RNA–RNA interactome of Klebsiella pneumoniae unveils a small RNA regulator of cell division, Proceedings of the National Academy of Sciences 121 (2024) e2317322121. https://doi.org/10.1073/pnas.2317322121.
[245] V.J. Parekh, B.A. Niccum, R. Shah, M.A. Rivera, M.J. Novak, F. Geinguenaud, F. Wien, V. Arluison, R.R. Sinden, Role of Hfq in Genome Evolution: Instability of G-Quadruplex Sequences in E. coli, Microorganisms 8 (2020) 28. https://doi.org/10.3390/microorganisms8010028.
[246] D. Sun, L.H. Hurley, Biochemical Techniques for the Characterization of G-Quadruplex Structures: EMSA, DMS Footprinting, and DNA Polymerase Stop Assay, Methods Mol Biol 608 (2010) 65–79. https://doi.org/10.1007/978-1-59745-363-9_5.
[247] L.M. Hellman, M.G. Fried, Electrophoretic Mobility Shift Assay (EMSA) for Detecting Protein-Nucleic Acid Interactions, Nat Protoc 2 (2007) 1849–1861. https://doi.org/10.1038/nprot.2007.249.
[248] V. Víglaský, L. Bauer, K. Tlučková, Structural Features of Intra- and Intermolecular G-Quadruplexes Derived from Telomeric Repeats, Biochemistry 49 (2010) 2110–2120. https://doi.org/10.1021/bi902099u.
[249] J. Dai, T.S. Dexheimer, D. Chen, M. Carver, A. Ambrus, R.A. Jones, D. Yang, An Intramolecular G-Quadruplex Structure with Mixed Parallel/Antiparallel G-strands Formed in the Human BCL-2 Promoter Region in Solution, J Am Chem Soc 128 (2006) 1096–1098. https://doi.org/10.1021/ja055636a.
[250] J.-L. Mergny, L. Lacroix, Analysis of thermal melting curves, Oligonucleotides 13 (2003) 515–537. https://doi.org/10.1089/154545703322860825.
[251] Small-molecule–induced DNA damage identifies alternative DNA structures in human genes | Nature Chemical Biology, (n.d.). https://www.nature.com/articles/nchembio.780 (accessed June 24, 2025).
[252] A.K. Verma, E. Khan, S.K. Mishra, N. Jain, A. Kumar, Piperine Modulates Protein Mediated Toxicity in Fragile X-Associated Tremor/Ataxia Syndrome through Interacting Expanded CGG Repeat (r(CGG)exp) RNA, ACS Chem. Neurosci. 10 (2019) 3778–3788. https://doi.org/10.1021/acschemneuro.9b00282.
[253] S. Neidle, Quadruplex Nucleic Acids as Novel Therapeutic Targets, J Med Chem 59 (2016) 5987–6011. https://doi.org/10.1021/acs.jmedchem.5b01835.

[254] H. Xu, M. Di Antonio, S. McKinney, V. Mathew, B. Ho, N.J. O'Neil, N.D. Santos, J. Silvester, V. Wei, J. Garcia, F. Kabeer, D. Lai, P. Soriano, J. Banáth, D.S. Chiu, D. Yap, D.D. Le, F.B. Ye, A. Zhang, K. Thu, J. Soong, S.-C. Lin, A.H.C. Tsai, T. Osako, T. Algara, D.N. Saunders, J. Wong, J. Xian, M.B. Bally, J.D. Brenton, G.W. Brown, S.P. Shah, D. Cescon, T.W. Mak, C. Caldas, P.C. Stirling, P. Hieter, S. Balasubramanian, S. Aparicio, CX-5461 is a DNA G-quadruplex stabilizer with selective lethality in BRCA1/2 deficient tumours, Nat Commun 8 (2017) 14432. https://doi.org/10.1038/ncomms14432.

[255] T. Santos, G.F. Salgado, E.J. Cabrita, C. Cruz, G-Quadruplexes and Their Ligands: Biophysical Methods to Unravel G-Quadruplex/Ligand Interactions, Pharmaceuticals 14 (2021) 769. https://doi.org/10.3390/ph14080769.

[256] T.B. Updegrove, A. Zhang, G. Storz, Hfq: the flexible RNA matchmaker, Curr Opin Microbiol 30 (2016) 133–138. https://doi.org/10.1016/j.mib.2016.02.003.

[257] S.A. Woodson, S. Panja, A. Santiago-Frangos, Proteins That Chaperone RNA Regulation, Microbiol Spectr 6 (2018). https://doi.org/10.1128/microbiolspec.RWR-0026-2018.

[258] A. Santiago-Frangos, S.A. Woodson, Hfq chaperone brings speed dating to bacterial sRNA, Wiley Interdiscip Rev RNA 9 (2018) e1475. https://doi.org/10.1002/wrna.1475.

[259] A. Singh, N. Jain, U. Shankar, T.K. Sharma, A. Kumar, Characterization of G-quadruplex structures in genes involved in survival and pathogenesis of *Acinetobacter baumannii* as a potential drug target, Int J Biol Macromol 269 (2024) 131806. https://doi.org/10.1016/j.ijbiomac.2024.131806.

[260] P. Kharel, S. Balaratnam, N. Beals, S. Basu, The role of RNA G-quadruplexes in human diseases and therapeutic strategies, Wiley Interdiscip Rev RNA 11 (2020) e1568. https://doi.org/10.1002/wrna.1568.

[261] C.K. Kwok, G. Marsico, S. Balasubramanian, Detecting RNA G-Quadruplexes (rG4s) in the Transcriptome, Cold Spring Harb Perspect Biol 10 (2018) a032284. https://doi.org/10.1101/cshperspect.a032284.

[262] G. Mirihana Arachchilage, A.C. Dassanayake, S. Basu, A potassium ion-dependent RNA structural switch regulates human pre-miRNA 92b maturation, Chem Biol 22 (2015) 262–272. https://doi.org/10.1016/j.chembiol.2014.12.013.

[263] S. Millevoi, H. Moine, S. Vagner, G-quadruplexes in RNA biology, Wiley Interdiscip Rev RNA 3 (2012) 495–507. https://doi.org/10.1002/wrna.1113.

[264] M.J. Morris, Y. Negishi, C. Pazsint, J.D. Schonhoft, S. Basu, An RNA G-Quadruplex Is Essential for Cap-Independent Translation Initiation in Human VEGF IRES, J. Am. Chem. Soc. 132 (2010) 17831–17839. https://doi.org/10.1021/ja106287x.

[265] S. Kumari, A. Bugaut, J.L. Huppert, S. Balasubramanian, An RNA G-quadruplex in the 5' UTR of the NRAS proto-oncogene modulates translation, Nat Chem Biol 3 (2007) 218–221. https://doi.org/10.1038/nchembio864.

[266] J.C. Grigg, N. Shumayrikh, D. Sen, G-Quadruplex Structures Formed by Expanded Hexanucleotide Repeat RNA and DNA from the Neurodegenerative Disease-Linked C9orf72 Gene Efficiently Sequester and Activate Heme, PLOS ONE 9 (2014) e106449. https://doi.org/10.1371/journal.pone.0106449.
[267] E. Ruggiero, S.N. Richter, Viral G-quadruplexes: New frontiers in virus pathogenesis and antiviral therapy, Annu Rep Med Chem 54 (2020) 101–131. https://doi.org/10.1016/bs.armc.2020.04.001.
[268] S. Amrane, C. Jaubert, A. Bedrat, T. Rundstadler, P. Recordon-Pinson, C. Aknin, A. Guédin, A. De Rache, L. Bartolucci, I. Diene, F. Lemoine, O. Gascuel, G. Pratviel, J.-L. Mergny, M.-L. Andreola, Deciphering RNA G-quadruplex function during the early steps of HIV-1 infection, Nucleic Acids Res 50 (2022) 12328–12343. https://doi.org/10.1093/nar/gkac1030.
[269] S.-R. Wang, Q.-Y. Zhang, J.-Q. Wang, X.-Y. Ge, Y.-Y. Song, Y.-F. Wang, X.-D. Li, B.-S. Fu, G.-H. Xu, B. Shu, P. Gong, B. Zhang, T. Tian, X. Zhou, Chemical Targeting of a G-Quadruplex RNA in the Ebola Virus L Gene, Cell Chemical Biology 23 (2016) 1113–1122. https://doi.org/10.1016/j.chembiol.2016.07.019.
[270] S.-R. Wang, Y.-Q. Min, J.-Q. Wang, C.-X. Liu, B.-S. Fu, F. Wu, L.-Y. Wu, Z.-X. Qiao, Y.-Y. Song, G.-H. Xu, Z.-G. Wu, G. Huang, N.-F. Peng, R. Huang, W.-X. Mao, S. Peng, Y.-Q. Chen, Y. Zhu, T. Tian, X.-L. Zhang, X. Zhou, A highly conserved G-rich consensus sequence in hepatitis C virus core gene represents a new anti–hepatitis C target, Sci Adv 2 (2016) e1501535. https://doi.org/10.1126/sciadv.1501535.
[271] C. Jaubert, A. Bedrat, L. Bartolucci, C. Di Primo, M. Ventura, J.-L. Mergny, S. Amrane, M.-L. Andreola, RNA synthesis is modulated by G-quadruplex formation in Hepatitis C virus negative RNA strand, Sci Rep 8 (2018) 8120. https://doi.org/10.1038/s41598-018-26582-3.
[272] A.M. Fleming, Y. Ding, A. Alenko, C.J. Burrows, Zika Virus Genomic RNA Possesses Conserved G-Quadruplexes Characteristic of the Flaviviridae Family, ACS Infect Dis 2 (2016) 674–681. https://doi.org/10.1021/acsinfecdis.6b00109.
[273] G-quadruplexes regulate Epstein-Barr virus–encoded nuclear antigen 1 mRNA translation | Nature Chemical Biology, (n.d.). https://www.nature.com/articles/nchembio.1479 (accessed December 28, 2023).
[274] A. Kabbara, B. Vialet, J. Marquevielle, P. Bonnafous, C.D. Mackereth, S. Amrane, RNA G-quadruplex forming regions from SARS-2, SARS-1 and MERS coronoviruses, Front Chem 10 (2022) 1014663. https://doi.org/10.3389/fchem.2022.1014663.
[275] G. Liu, W. Du, X. Sang, Q. Tong, Y. Wang, G. Chen, Y. Yuan, L. Jiang, W. Cheng, D. Liu, Y. Tian, X. Fu, RNA G-quadruplex in TMPRSS2 reduces SARS-CoV-2 infection, Nat Commun 13 (2022) 1444. https://doi.org/10.1038/s41467-022-29135-5.
[276] R. Perrone, E. Butovskaya, D. Daelemans, G. Palù, C. Pannecouque, S.N. Richter, Anti-HIV-1 activity of the G-quadruplex ligand BRACO-19, J

Antimicrob Chemother 69 (2014) 3248–3258. https://doi.org/10.1093/jac/dku280.
[277] H. Cui, L. Zhang, G-Quadruplexes Are Present in Human Coronaviruses Including SARS-CoV-2, Front Microbiol 11 (2020) 567317. https://doi.org/10.3389/fmicb.2020.567317.
[278] RNA G-quadruplex formed in SARS-CoV-2 used for COVID-19 treatment in animal models | Cell Discovery, (n.d.). https://www.nature.com/articles/s41421-022-00450-x (accessed December 28, 2023).
[279] M. Zou, J.-Y. Li, M.-J. Zhang, J.-H. Li, J.-T. Huang, P.-D. You, S.-W. Liu, C.-Q. Zhou, G-quadruplex binder pyridostatin as an effective multi-target ZIKV inhibitor, Int J Biol Macromol 190 (2021) 178–188. https://doi.org/10.1016/j.ijbiomac.2021.08.121.
[280] M.D. Mileno, Japanese Encephalitis Vaccine, R I Med J (2013) 103 (2020) 49–50.
[281] S. Kumar, A. Verma, P. Yadav, S.K. Dubey, E.I. Azhar, S.S. Maitra, V.D. Dwivedi, Molecular pathogenesis of Japanese encephalitis and possible therapeutic strategies, Arch Virol 167 (2022) 1739–1762. https://doi.org/10.1007/s00705-022-05481-z.
[282] Y. Zhu, Z. He, Z. Qi, Virus-host Interactions in Early Japanese Encephalitis Virus Infection, Virus Research 331 (2023) 199120. https://doi.org/10.1016/j.virusres.2023.199120.
[283] K.B. Sharma, S. Vrati, M. Kalia, Pathobiology of Japanese encephalitis virus infection, Mol Aspects Med 81 (2021) 100994. https://doi.org/10.1016/j.mam.2021.100994.
[284] Japanese encephalitis — the prospects for new treatments | Nature Reviews Neurology, (n.d.). https://www.nature.com/articles/nrneurol.2018.30 (accessed January 12, 2024).
[285] S.K. Prajapat, L. Mishra, S. Khera, S.D. Owusu, K. Ahuja, P. Sharma, E. Choudhary, S. Chhabra, N. Kumar, R. Singh, P.S. Kaushal, D. Mahajan, A. Banerjee, R.K. Motiani, S. Vrati, M. Kalia, Methotrimeprazine is a neuroprotective antiviral in JEV infection via adaptive ER stress and autophagy, EMBO Mol Med 16 (2024) 185–217. https://doi.org/10.1038/s44321-023-00014-w.
[286] A. Abiri, M. Lavigne, M. Rezaei, S. Nikzad, P. Zare, J.-L. Mergny, H.-R. Rahimi, Unlocking G-Quadruplexes as Antiviral Targets, Pharmacol Rev 73 (2021) 897–923. https://doi.org/10.1124/pharmrev.120.000230.
[287] R. Assenberg, E. Mastrangelo, T.S. Walter, A. Verma, M. Milani, R.J. Owens, D.I. Stuart, J.M. Grimes, E.J. Mancini, Crystal Structure of a Novel Conformational State of the Flavivirus NS3 Protein: Implications for Polyprotein Processing and Viral Replication, Journal of Virology 83 (2009) 12895–12906. https://doi.org/10.1128/jvi.00942-09.
[288] H. Malet, M.-P. Egloff, B. Selisko, R.E. Butcher, P.J. Wright, M. Roberts, A. Gruez, G. Sulzenbacher, C. Vonrhein, G. Bricogne, J.M. Mackenzie, A.A. Khromykh, A.D. Davidson, B. Canard, Crystal structure of the RNA

polymerase domain of the West Nile virus non-structural protein 5, J Biol Chem 282 (2007) 10678–10689. https://doi.org/10.1074/jbc.M607273200.
[289] I. Frasson, M. Nadai, S.N. Richter, Conserved G-Quadruplexes Regulate the Immediate Early Promoters of Human Alphaherpesviruses, Molecules 24 (2019) 2375. https://doi.org/10.3390/molecules24132375.
[290] E. Butovskaya, B. Heddi, B. Bakalar, S.N. Richter, A.T. Phan, Major G-Quadruplex Form of HIV-1 LTR Reveals a (3 + 1) Folding Topology Containing a Stem-Loop, J Am Chem Soc 140 (2018) 13654–13662. https://doi.org/10.1021/jacs.8b05332.
[291] S. Bidula, V. Brázda, Genomic Analysis of Non-B Nucleic Acids Structures in SARS-CoV-2: Potential Key Roles for These Structures in Mutability, Translation, and Replication?, Genes 14 (2023) 157. https://doi.org/10.3390/genes14010157.
[292] G. Nicoletto, S.N. Richter, I. Frasson, Presence, Location and Conservation of Putative G-Quadruplex Forming Sequences in Arboviruses Infecting Humans, International Journal of Molecular Sciences 24 (2023) 9523. https://doi.org/10.3390/ijms24119523.
[293] A. Guédin, P. Alberti, J.-L. Mergny, Stability of intramolecular quadruplexes: sequence effects in the central loop, Nucleic Acids Res 37 (2009) 5559–5567. https://doi.org/10.1093/nar/gkp563.
[294] A. Bedrat, L. Lacroix, J.-L. Mergny, Re-evaluation of G-quadruplex propensity with G4Hunter, Nucleic Acids Res 44 (2016) 1746–1759. https://doi.org/10.1093/nar/gkw006.
[295] A. Randazzo, G.P. Spada, M.W. da Silva, Circular dichroism of quadruplex structures, Top Curr Chem 330 (2013) 67–86. https://doi.org/10.1007/128_2012_331.
[296] S. Xu, Q. Li, J. Xiang, Q. Yang, H. Sun, A. Guan, L. Wang, Y. Liu, L. Yu, Y. Shi, H. Chen, Y. Tang, Thioflavin T as an efficient fluorescence sensor for selective recognition of RNA G-quadruplexes, Sci Rep 6 (2016) 24793. https://doi.org/10.1038/srep24793.
[297] A. Renaud de la Faverie, A. Guédin, A. Bedrat, L.A. Yatsunyk, J.-L. Mergny, Thioflavin T as a fluorescence light-up probe for G4 formation, Nucleic Acids Res 42 (2014) e65. https://doi.org/10.1093/nar/gku111.
[298] P.L.T. Tran, E. Largy, F. Hamon, M.-P. Teulade-Fichou, J.-L. Mergny, Fluorescence intercalator displacement assay for screening G4 ligands towards a variety of G-quadruplex structures, Biochimie 93 (2011) 1288–1296. https://doi.org/10.1016/j.biochi.2011.05.011.
[299] D. Monchaud, M.-P. Teulade-Fichou, G4-FID: a fluorescent DNA probe displacement assay for rapid evaluation of quadruplex ligands, Methods Mol Biol 608 (2010) 257–271. https://doi.org/10.1007/978-1-59745-363-9_15.
[300] H.-J. Sullivan, C. Readmond, C. Radicella, V. Persad, T.J. Fasano, C. Wu, Binding of Telomestatin, TMPyP4, BSU6037, and BRACO19 to a Telomeric G-Quadruplex–Duplex Hybrid Probed by All-Atom Molecular Dynamics Simulations with Explicit Solvent, ACS Omega 3 (2018) 14788–14806. https://doi.org/10.1021/acsomega.8b01574.

[301] M.M. Garner, A. Revzin, A gel electrophoresis method for quantifying the binding of proteins to specific DNA regions: application to components of the Escherichia coli lactose operon regulatory system., Nucleic Acids Res 9 (1981) 3047–3060.
[302] K. Paeschke, T. Simonsson, J. Postberg, D. Rhodes, H.J. Lipps, Telomere end-binding proteins control the formation of G-quadruplex DNA structures in vivo, Nat Struct Mol Biol 12 (2005) 847–854. https://doi.org/10.1038/nsmb982.
[303] M.F. Carey, C.L. Peterson, S.T. Smale, Experimental strategies for the identification of DNA-binding proteins, Cold Spring Harb Protoc 2012 (2012) 18–33. https://doi.org/10.1101/pdb.top067470.
[304] J. Carvalho, J.A. Queiroz, C. Cruz, Circular Dichroism of G-Quadruplex: a Laboratory Experiment for the Study of Topology and Ligand Binding, J. Chem. Educ. 94 (2017) 1547–1551. https://doi.org/10.1021/acs.jchemed.7b00160.
[305] E.E. Merkina, K.R. Fox, Kinetic Stability of Intermolecular DNA Quadruplexes, Biophys J 89 (2005) 365–373. https://doi.org/10.1529/biophysj.105.061259.
[306] P.A. Rachwal, K.R. Fox, Quadruplex melting, Methods 43 (2007) 291–301. https://doi.org/10.1016/j.ymeth.2007.05.004.
[307] B. Pagano, C.A. Mattia, C. Giancola, Applications of Isothermal Titration Calorimetry in Biophysical Studies of G-quadruplexes, Int J Mol Sci 10 (2009) 2935–2957. https://doi.org/10.3390/ijms10072935.
[308] O. Callies, A.H. Daranas, Application of isothermal titration calorimetry as a tool to study natural product interactions, Nat. Prod. Rep. 33 (2016) 881–904. https://doi.org/10.1039/C5NP00094G.
[309] B. Pagano, C. Giancola, Energetics of quadruplex-drug recognition in anticancer therapy, Curr Cancer Drug Targets 7 (2007) 520–540. https://doi.org/10.2174/156800907781662257.
[310] H. Alniss, B. Zamiri, M. Khalaj, C.E. Pearson, R.B. Macgregor, Thermodynamic and spectroscopic investigations of TMPyP4 association with guanine- and cytosine-rich DNA and RNA repeats of C9orf72, Biochemical and Biophysical Research Communications 495 (2018) 2410–2417. https://doi.org/10.1016/j.bbrc.2017.12.108.
[311] A. Tawani, S.K. Mishra, A. Kumar, Structural insight for the recognition of G-quadruplex structure at human c-myc promoter sequence by flavonoid Quercetin, Sci Rep 7 (2017) 3600. https://doi.org/10.1038/s41598-017-03906-3.
[312] A.T. Phan, V. Kuryavyi, H.Y. Gaw, D.J. Patel, Small-molecule interaction with a five-guanine-tract G-quadruplex structure from the human MYC promoter, Nat Chem Biol 1 (2005) 167–173. https://doi.org/10.1038/nchembio723.
[313] M.P. Foster, C.A. McElroy, C.D. Amero, Solution NMR of large molecules and assemblies, Biochemistry 46 (2007) 331–340. https://doi.org/10.1021/bi0621314.

[314] T. Endoh, Y. Kawasaki, N. Sugimoto, Suppression of Gene Expression by G-Quadruplexes in Open Reading Frames Depends on G-Quadruplex Stability, Angewandte Chemie International Edition 52 (2013) 5522–5526. https://doi.org/10.1002/anie.201300058.
[315] T. Endoh, Y. Kawasaki, N. Sugimoto, Stability of RNA quadruplex in open reading frame determines proteolysis of human estrogen receptor α, Nucleic Acids Research 41 (2013) 6222–6231. https://doi.org/10.1093/nar/gkt286.
[316] S. Joe, A.A.A. Salam, U. Neogi, N.B. N, P.P. Mudgal, Antiviral drug research for Japanese encephalitis: an updated review, Pharmacol Rep 74 (2022) 273–296. https://doi.org/10.1007/s43440-022-00355-2.
[317] E. Ruggiero, S.N. Richter, Targeting G-quadruplexes to achieve antiviral activity, Bioorg Med Chem Lett 79 (2023) 129085. https://doi.org/10.1016/j.bmcl.2022.129085.